

Effects of impurities and local behavior
characterization using active thermography on solid
oxide electrolysis cells

Présentée le 30 avril 2021

Faculté des sciences et techniques de l'ingénieur
Groupe SCI STI JVH
Programme doctoral en énergie

pour l'obtention du grade de Docteur ès Sciences

par

Guillaume JEANMONOD

Acceptée sur proposition du jury

Prof. F. Maréchal, président du jury
Dr J. Van Herle, directeur de thèse
Prof. P. Shearing, rapporteur
Prof. R. Walker, rapporteur
Prof. S. Haussener, rapporteuse

*Toutes les grandes personnes ont d'abord été des enfants,
mais peu d'entre elles s'en souviennent.*

— Antoine de Saint-Exupéry

Acknowledgements

Generally, I have a tendency to get excited and amazed by my surroundings and I want to believe that this is what led me to try out the sweet and sour taste of PhD thesis. I found the recipe for a PhD thesis to be quite interesting. You begin spending quite some time looking for the right materials — questions that haven't been answered yet, questions that you aren't yet qualified to answer. Over the years, you add cups of guesswork, pints of ups and down, tablespoons of frustrations, a pinch of being overwhelmed, a teaspoon of being fed up; you also add gallons of new encounters, good exchanges, support, and the cherry on top — satisfaction. I would like to give credit to the people who contributed to the sweet and helped me through the sour.

I've tried to be as exhaustive as possible when writing these acknowledgments but I have to say that my brain is sometimes whimsy and may have incidentally omitted someone.

I would like to first thank my thesis director, Dr. Jan Van herle, who believed in me from the beginning and gave me the freedom to explore the research path I wanted. Although this may have been scary at first, I am grateful looking back. Maybe more importantly, I have appreciated the work atmosphere that he has created and fostered within GEM and the importance he put into social events.

Particularly during the last months, I realized that one of the hardest part of my thesis was dealing with my uncertainties regarding the quality and relevance of my work. For clearing up my doubts and providing constructive criticism, I would like to deeply thank the members of my thesis exam jury: Prof. Prof. Robert Walker, Sophia Haussener, Prof. Paul Shearing, and Prof. François Maréchal.

I would like to acknowledge all of my coworkers at GEM and who, over the years, have become my dear friends: Dr. Stefan Diethelm for his availability and sharing his endless scientific and general knowledge with me, Priscilla for taking the time to teach me all I know about DRT, Manuel for introducing me to materials science (or at least trying), Ligang for being a fun travel partner and a good advisor, Giorgio for providing me with critical feedback on my thesis, Philippe for bringing a touch of extravaganza to the lab, David for his practical advice and social support, Steve for his technical support and great cheese, Arata for his time spent discussing modeling and electrochemistry with me,

Acknowledgements

Mar for always being joyful and supportive, Hugh for pushing me to be creative, Chantal for her administrative support and being my first "desk-mate", and also Hamza, Thierry, Tafarel, Hossein the 1st, Hossein the 2nd, Samaneh, Audrey, Thibault, and Nicola.

My acknowledgments also go to all of the partners from ECo and AdAstra projects (particularly Megha); and also to the European Union Horizon 2020 program (FCH JU program) for funding my research.

I would never have participated in so many amazing thesis public defenses, fun christmas parties, and relaxing lunch breaks if it wasn't for our sister lab, IPESE, and its wonderful members, past and present: Nils, Sébastien, Paul, Franscesca, Maziar, Julia, Sophia, Ti-Vi, Luise, Rafael, Alessio, Hür, Raluca, Stefano, Dilan, Ivan, Frédéric, Xiang, Franscesco, Victor, Elfie, Alberto, Raman, and Sylvie. These moments would not have been the same without Riccardo, Cecilia, Bonnie, and Nadja.

I am very grateful towards the team of EPFL Valais/Wallis: Cédric, Jean, Filipe, Stéphane, Robin, Patrick, Laurent, Annabelle, Fabbio, Annik, Séverine, Angela, Palmira, and the team of the EDEY program: Cécile and Mario; all of whom we often tend to forget but whose work and support was essential during my journey.

I would like to thanks my old-time friends: Randy, Gabriella, Romain, Alexandra, Jean-Pablo, Marine, Max, Nathalie, Félix, Damien, Cyril, Elliott, Sarah, Frederike, Baptiste, Vincent, Adrien, with whom I share great memories and who gave my "a brain" a break through sport, yachting on the Aar, weddings, cheering around a Fondue or a torée, or simply by solving a murder.

I am particularly grateful to my parents, Corinne and Claude-Alain, who have been nothing but supportive and caring throughout my entire life. I feel very lucky to be surrounded by such loving family members: Julia, Raphaël, Thomas, Gaëlle, Léa, Zoé (my goddaughter ☺), Thierry, Patou, Gérard, Patricia, Dominique, Jaqueline, Grégoire, Lucien, Paul, Marco, Guignolet, Catherine, the cats Réglisse, Pipeau, and last but not least Raskolnikov 🐾. Woe betide me if I forget the McClungs 🍀 Andrea, Maddi, Laren, Darlene, and Bob.

I can't end these acknowledgments without mentioning Katie who entered my life right after I started my thesis and will remain for at least 89 years after my PhD graduation. Thank you for being the first person to read (and also proofread) my whole thesis and having supported and taken care of me, particularly during the last months when I would otherwise have barely taken the time to eat ❤️.

Vevey, March 4, 2021

🌿 *Guillaume Jeanmonod* 🌿

Abstract

Ambitious policies are needed from every country to drastically curtail the anthropogenic emission of greenhouse gases responsible for the on-going modification of the earth's climate. A quick transition towards a society fully based on renewable materials and energy sources is necessary. Power-to-gas via solid oxide electrolysis cells (SOECs) is a promising solution to accommodate the variability inherent in renewable electricity production. Despite evidence of a high sensitivity to impurities during electrolysis, however, the literature available on the effects of contaminants in the reactant is rather sparse.

This thesis therefore aims to identify and determine the effects of the potential harmful impurities to which a solid oxide electrolysis cell can be exposed. The effects of SO₂ and HCl, the two most critical impurities identified for Ni-YSZ electrodes, on the performance and durability were investigated using electrochemical impedance spectroscopy and the analysis of the distribution of relaxation time (DRT). The results indicate that the operation in electrolysis mode reduces the tolerance to impurities. Exposure to HCl and SO₂ deteriorated the charge transfer processes at the triple phase boundary, whereas only SO₂ limited the catalytic reactions. Durability testing performed in galvanostatic operation with impurities showed a voltage runaway behavior after approximately 200 h. Shorter experiments may thus greatly underestimate the impact of impurities. A low-frequency pseudo-inductive hook appeared in the electrochemical impedance spectra during the poisoning experiments, which was attributed to the Ni-YSZ electrode. Two processes were identified as possible causes of the observed pseudo-inductive hook: 1) a two-step reaction mechanism involving an intermediate species, or 2) the development of an electronic conductivity in the electrolyte. The former appeared to be the most likely explanation.

This thesis also proposes and assesses the use of active thermography as a novel method to characterize in operando the local behavior of solid oxide cells (SOCs), thereby overcoming the limitation of typical measurements that only provide spatially averaged values. The proposed method consists of stimulating the solid oxide cell with a sinusoidal (lock-in thermography) or pulse (pulse thermography) current perturbation and analyzing the local thermal response using Fourier transforms. As a preliminary step and to support experimental work, a numerical parametric investigation was performed on lock-in thermography results using a pseudo 2-D model. Analysis of the 1st harmonic revealed that,

Abstract

in addition to the heat generated by the electrochemical reaction and the Joule effect, the modulation of the local reactant composition also contributed to the thermal response. Analysis of the 2nd harmonic allowed the visual local non-uniformities not visible in the 1st harmonic. Lock-in thermography measurements performed on the developed test bench were in good agreement with the numerical simulations, thus validating the feasibility of the method. Lock-in thermography was found to be more adapted to SOC applications than pulse thermography, as a lower noise level can be achieved while maintaining a reasonably low current modulation. When CO₂ was added to the reactant, the thermal response was modified, thereby demonstrating the sensitivity of active thermography to the reactant composition. Lock-in thermography measurements taken during an SO₂-poisoning experiment evidenced a spatially non-uniform deactivation process. By combining these results with DRT analysis, a detailed degradation mechanism was proposed, thereby demonstrating the complementary and added benefits of active thermography.

The outcomes of this thesis are expected to provide new pathways for the analysis of fuel cells and electrolyzers as well as guidelines for the design of power-to-gas systems especially regarding the required CO₂ quality.

Keywords: Solid oxide cell, fuel cell, electrolysis, active thermography, poisoning, sulfur, chlorine, degradation, impedance spectroscopy.

Résumé

Des décisions politiques ambitieuses sont nécessaires de la part de chaque pays pour réduire de manière drastique les émissions anthropiques de gaz à effet de serre responsables de l'actuel dérèglement du climat terrestre. Une transition rapide vers une société entièrement basée sur les matériaux et les sources d'énergie renouvelables est nécessaire. La conversion de l'électricité au gaz via des cellules électrolyses à oxyde solide (SOECs) est une solution prometteuse pour compenser la variabilité inhérente à la production d'électricité renouvelable. Cependant, malgré les évidences d'une grande sensibilité aux impuretés pendant l'électrolyse, la littérature disponible sur les effets des contaminants dans le réactif est plutôt rare.

Cette thèse vise donc à identifier et à déterminer les effets des impuretés potentiellement nocives auxquelles une cellule d'électrolyse à oxyde solide peut être exposée. Les effets du SO_2 et HCl , les deux impuretés les plus critiques identifiées pour les électrodes à base de Ni-YSZ, sur la performance et la durabilité ont été étudiés en utilisant la spectroscopie d'impédance électrochimique et l'analyse de la distribution du temps de relaxation. Les résultats indiquent que le fonctionnement en électrolyse réduit la tolérance aux impuretés. L'exposition au HCl et SO_2 a détérioré les processus de transfert de charge à la frontière de la triple phase, alors que seul le SO_2 a limité les réactions catalytiques. Les essais de durabilité effectués en fonctionnement galvanostatique avec des impuretés ont montré un comportement d'emballement du voltage après environ 200 h. Des expériences plus courtes peuvent donc sous-estimer considérablement l'impact des impuretés. Un crochet pseudo-inductif à basse fréquence est apparu dans les spectres d'impédance électrochimique pendant les expériences d'empoisonnement, ce qui a été attribué à l'électrode Ni-YSZ. Deux processus ont été identifiés comme causes possibles du crochet pseudo-inductif observé : 1) un mécanisme de réaction en deux étapes impliquant une espèce intermédiaire, ou 2) le développement d'une conductivité électronique dans l'électrolyte. Le premier semble être l'explication la plus probable.

Cette thèse propose et évalue également l'utilisation de la thermographie active comme une nouvelle méthode pour caractériser in operando le comportement local des cellules à oxyde solide (SOCs), surmontant ainsi la limitation des mesures classiques qui ne fournissent que des valeurs moyennées dans l'espace. La méthode proposée consiste à stimuler la cellule à oxyde solide avec un courant sinusoïdale (thermographie lock-in) ou

Résumé

pulsée (thermographie à impulsions) et à analyser la réponse thermique locale à l'aide de transformées de Fourier. Dans un premier temps et pour supporter le travail expérimental, une étude paramétrique numérique a été réalisée sur les résultats de la thermographie lock-in à l'aide d'un modèle pseudo 2-D. L'analyse de la 1^{ère} harmonique a révélé qu'en plus de la chaleur générée par la réaction électrochimique et l'effet Joule, la modulation de la composition local du réactif a également contribué à la réponse thermique. L'analyse de la 2^{ième} harmonique a permis de mettre en évidence les non-uniformités locales non visibles sur la 1^{ère} harmonique. Les mesures de thermographie lock-in effectuées sur le banc d'essai développé dans cette thèse étaient en bon accord avec les simulations numériques, validant ainsi la faisabilité de la méthode. La thermographie lock-in s'est avérée plus adaptée aux cellules à oxyde solide que la thermographie à impulsions, car il est possible d'obtenir un niveau de bruit plus faible tout en maintenant une modulation de courant raisonnablement faible. Lorsque du CO₂ a été ajouté au réactif, la réponse thermique a été modifiée, démontrant ainsi la sensibilité de la thermographie active à la composition du réactif. Les mesures de thermographie de active prises au cours d'une expérience d'empoisonnement au SO₂ ont mis en évidence un processus de désactivation spatialement non uniforme. En combinant ces résultats avec l'analyse DRT, un mécanisme de dégradation détaillé a été proposé, démontrant ainsi les avantages complémentaires et supplémentaires de la thermographie active.

Les résultats de cette thèse devraient fournir de nouvelles pistes pour l'analyse des piles à combustible et des électrolyseurs ainsi que des lignes directrices pour la conception de systèmes de conversion de l'énergie en gaz, notamment en ce qui concerne la qualité requise du CO₂.

Mots-clés : Cellule à oxyde solide, pile à combustible, électrolyse, thermographie active, empoisonnement, soufre, chlore, dégradation, spectroscopie d'impédance.

Zusammenfassung

Die internationale Gemeinschaft muss ehrgeizige Maßnahmen ergreifen, um den vom Menschen verursachten Ausstoß von Treibhausgasen, die für die anhaltende Veränderung des Erdklimas verantwortlich sind, drastisch zu reduzieren. Ein schneller Übergang zu einer Gesellschaft, die sich vollständig auf erneuerbare Energiequellen stützt, ist notwendig. Power-to-Gas über Festoxid-Elektrolysezellen (SOECs) ist eine vielversprechende Lösung, um die Variabilität der erneuerbaren Stromerzeugung auszugleichen. Trotz der Hinweise auf eine hohe Empfindlichkeit gegenüber Verunreinigungen während der Elektrolyse ist die verfügbare Literatur zu den Auswirkungen von Verunreinigungen im Reaktanten eher spärlich.

Diese Arbeit zielt daher darauf ab die Auswirkungen von potenziell schädlichen Verunreinigungen, denen eine Festoxidelektrolysezelle während ihres Einsatzes ausgesetzt sein kann, zu identifizieren und zu bestimmen. Die Auswirkung auf die Leistung und Haltbarkeit einer Zelle durch Verunreinigung von SO_2 und HCl , den zwei kritischsten Substanzen, die für Ni-YSZ-Elektroden identifiziert wurden, wurde mit Hilfe der elektrochemischen Impedanzspektroskopie und der Analyse der Verteilung der Relaxationszeit untersucht. Die Ergebnisse zeigen, dass der Elektrolyse-Betrieb die Toleranz gegenüber Verunreinigungen verringert. Verunreinigung mit HCl und SO_2 verschlechterte die Ladungsübertragungsprozesse an der Dreiphasengrenze, während nur SO_2 die katalytischen Reaktionen einschränkte. Haltbarkeitstests mit Verunreinigungen im galvanostatischen Betrieb zeigten nach etwa 200 Stunden ein Spannungsausfallverhalten. Während der Vergiftungsexperimente trat in den elektrochemischen Impedanzspektren ein niederfrequenter pseudoinduktiver Ausschlag auf, der der Ni-YSZ-Elektrode zugeschrieben wurde. Zwei Prozesse wurden als mögliche Ursachen für den beobachteten pseudoinduktiven Ausschlag identifiziert: 1) ein zweistufiger Reaktionsmechanismus, an dem eine intermediäre Spezies beteiligt ist, oder 2) die Entwicklung einer elektronischen Leitfähigkeit im Elektrolyten. Ersteres schien die wahrscheinlichste Erklärung zu sein.

In dieser Arbeit wird auch die Verwendung der aktiven Hermographie als neuartige Methode zur Charakterisierung des lokalen Verhaltens von Festoxid-Elektrolysezellen (SOCs) während des Betriebs vorgeschlagen und bewertet. Dadurch werden die Einschränkungen klassischer Messverfahren, die nur räumlich gemittelte Werte liefern, überwunden. Das vorgeschlagene Verfahren besteht darin, die Festoxidzelle mit einer sinusförmigen-

(Lock-In-Thermografie) oder Puls- (Impulsthermografie) Stromstörung zu stimulieren und die lokale thermische Reaktion unter Verwendung von Fourier-Transformationen zu analysieren. Als Vorstufe und zur Unterstützung der experimentellen Arbeit wurde eine numerische parametrische Untersuchung der Ergebnisse der Lock-In-Thermografie unter Verwendung eines Pseudo-2-D-Modells durchgeführt. Die Analyse der 1. Harmonischen ergab, dass zusätzlich zu der durch die elektrochemische Reaktion und den Joule-Effekt erzeugten Wärme auch die Modulation der lokalen Reaktantenzusammensetzung zur thermischen Reaktion beiträgt. Die Analyse der 2. Harmonischen zeigte die lokalen Ungleichmäßigkeiten auf, die in der 1. Harmonischen nicht sichtbar waren. Die Lock-In-Thermografiemessungen stimmten gut mit den numerischen Simulationen überein und bestätigten somit die Machbarkeit der neuartigen Methode. Es wurde festgestellt, dass die Lock-In-Thermografie besser an FOE-Anwendungen angepasst ist als Impulsthermografie, da ein niedrigerer Geräuschpegel erreicht werden kann, während eine einigermaßen niedrige Strommodulation aufrechterhalten wird. Wenn dem Reaktanten CO_2 zugesetzt wurde, wurde die thermische Reaktion modifiziert, wodurch die Empfindlichkeit der aktiven Thermografie gegenüber der Reaktantenzusammensetzung demonstriert wurde. Lock-in-Thermografiemessungen, die während eines SO_2 -Vergiftungsexperiments durchgeführt wurden, zeigten einen räumlich ungleichmäßigen Deaktivierungsprozess. Durch die Kombination dieser Ergebnisse mit der Analyse der Verteilung der Relaxationszeit wurde ein detaillierter Degradierungs-Mechanismus ermittelt, der die komplementären und zusätzlichen Vorteile der aktiven Thermografie demonstriert.

Die Ergebnisse dieser Arbeit sollen neue Wege für die Analyse von Brennstoffzellen und Elektrolysezellen sowie Leitsätze für die Entwicklung von Power-to-Gas-Systemen aufzeigen, insbesondere hinsichtlich der erforderlichen CO_2 -Qualität.

Schlüsselwörter: Festoxidzelle, Brennstoffzelle, Elektrolyse, aktive Thermografie, Vergiftung, Schwefel, Chlor, Degradierung, Impedanzspektroskopie.

Riassunto

Politiche ambientali ambiziose da parte di ogni paese sono fondamentali per ridurre drasticamente le emissioni di gas a effetto serra responsabili del cambiamento climatico e garantire una rapida transizione verso una società completamente basata su materiali e fonti di energia rinnovabili. L'uso di celle elettrolitiche ad ossidi solidi (SOEC) che convertono l'energia elettrica in gas, offre una soluzione promettente per compensare la natura fluttuante della produzione di elettricità da fonti rinnovabili. Nonostante sia evidente che questi dispositivi elettrochimici siano altamente suscettibili alle impurità presenti nel reagente durante il funzionamento in elettrolisi, la letteratura disponibile a proposito degli effetti dei contaminanti è piuttosto scarsa.

Questa tesi ha lo scopo di identificare e determinare gli effetti dannosi causati dalle potenziali impurità a cui una cella elettrolitica a ossidi solidi può essere esposta. Gli effetti che SO_2 e HCl , identificate come le due impurità più critiche per gli elettrodi Ni/YSZ , inducono sulle prestazioni e la durata dei dispositivi in esame, sono stati studiati utilizzando la spettroscopia d'impedenza elettrochimica e l'analisi della distribuzione dei tempi di rilassamento (DRT). I risultati indicano che il funzionamento in elettrolisi riduce la tolleranza alle impurità. L'esposizione all' HCl e alla SO_2 è responsabile del deterioramento dei processi di trasferimento di carica, mentre unicamente alla SO_2 è imputabile una limitazione delle reazioni catalitiche. Test di durata eseguiti in funzionamento galvanostatico in presenza di impurità nei reagenti hanno mostrato una perdita del potenziale di cella dopo circa 200 ore di funzionamento. Esperimenti più brevi possono quindi sottostimare notevolmente l'impatto delle impurità. Un arco pseudo-induttivo a bassa frequenza è apparso negli spettri di impedenza elettrochimica durante gli esperimenti di avvelenamento, arco che è stato attribuito all'elettrodo Ni/YSZ . Due processi sono stati identificati come possibili cause di questo effetto pseudo-induttivo: 1) un meccanismo di reazione a due fasi che prevede la formazione di una specie intermedia o 2) lo sviluppo di una conduttività elettronica nell'elettrolita. Il primo sembra essere la spiegazione più probabile.

Questa tesi propone e valuta anche l'uso della termografia attiva come un nuovo metodo per caratterizzare in-operando il comportamento locale delle celle ad ossidi solidi, superando così la limitazione delle misure standard che forniscono solo valori mediati sulla superficie della cella. Il metodo proposto consiste nello stimolare la cella ad ossidi

solidi con una perturbazione di corrente sinusoidale (termografia lock-in) o ad impulsi (termografia a impulsi) e analizzare la risposta termica locale utilizzando la trasformata di Fourier. Come passo preliminare e per supportare il lavoro sperimentale, è stata eseguita un'indagine parametrica sui risultati della termografia lock-in utilizzando un modello numerico pseudo-2D che descrive la fisica del processo in esame. L'analisi della prima armonica ha rivelato che, oltre al calore generato dalla reazione elettrochimica e dall'effetto Joule, anche la variazione della composizione locale del reagente contribuisce alla risposta termica. L'analisi della seconda armonica ha permesso di visualizzare le disomogeneità locali non visibili nella prima armonica. Le misure di termografia lock-in eseguite sul banco di prova, ideato e realizzato in questa tesi, sono in accordo con le simulazioni numeriche, convalidando così l'efficacia del metodo. La termografia lock-in si è rivelata più adatta alle applicazioni SOC rispetto alla termografia a impulsi, poiché è possibile ottenere un livello di rumore inferiore mantenendo una modulazione di corrente ragionevolmente bassa. Quando la CO_2 è stata aggiunta al flusso in ingresso nella cella, la risposta termica è risultata altamente modificata, dimostrando così la sensibilità della termografia attiva alla composizione del reagente. Le misure di termografia lock-in ottenute durante un esperimento di avvelenamento con SO_2 hanno evidenziato un processo di disattivazione spazialmente non uniforme. Combinando questi risultati con l'analisi DRT, è stato proposto un meccanismo di degradazione dettagliato, dimostrando così i vantaggi complementari e aggiuntivi della termografia attiva.

I risultati di questa tesi dovrebbero fornire nuovi percorsi per l'analisi delle celle a combustibile e degli elettrolizzatori, nonché linee guida per la progettazione di sistemi power-to-gas, soprattutto per quanto riguarda la qualità di CO_2 richiesta.

Parola chiave: Cella a ossido solido, cella a combustibile, elettrolisi, termografia attiva, avvelenamento, zolfo, cloro, degradazione, spettroscopia di impedenza.

Table of Contents

Acknowledgements	i
Abstract/Résumé/Zusammenfassung/Riassunto	iii
List of Figures	xv
List of Tables	xxi
Nomenclature & Acronyms	xxv
1 Introduction	1
1.1 A short history of climate change	1
1.2 Chemical energy storage in the context of energy transition	2
1.3 SOEC working principle	3
1.4 SOEC degradation	8
1.4.1 H ₂ -electrode	8
1.4.2 Electrolyte	10
1.4.3 O ₂ -electrode	10
1.5 Characterization methods	11
1.5.1 Current–voltage characterization	12
1.5.2 Microstructure characterization	14
1.5.3 Optical characterization	15
1.5.4 Raman and infrared spectroscopy	15
1.5.5 Thermal/infrared imaging	16
1.5.6 Active thermography	19
1.6 Thesis objectives	22
I H₂-electrode poisoning	23
2 Literature Review	25
2.1 Impurities in CO ₂ sources	25
2.2 Literature on SOC contaminants	26
2.2.1 Sulfur compounds	30

Table of Contents

2.2.2	Chlorine compounds	31
2.2.3	Silicon compounds	34
2.2.4	Tar	36
2.2.5	Miscellaneous	39
2.3	Conclusions	41
3	Experimental method	45
3.1	Test rig	45
3.2	Control, acquisition, and characterization	46
3.3	Data analysis procedure	47
4	Effect of HCl	53
4.1	Effect of polarization and HCl concentration	54
4.1.1	Open circuit condition	54
4.1.2	Under polarization	56
4.2	Durability	59
4.3	Conclusion	63
5	Effect of SO₂	65
5.1	The effect of polarization and SO ₂ concentration	66
5.1.1	Open-circuit conditions	66
5.1.2	Under polarization (0.25 Acm ⁻²)	71
5.2	Effect on Durability	73
5.2.1	Voltage "runaway"	76
5.2.2	Low-frequency hook	76
5.3	Conclusion	79
II	Active thermography	81
6	Introduction and basic principles	83
6.1	Thermal radiation	83
6.2	Thermography	85
6.3	Active thermography	87
6.3.1	Fourier analysis	89
6.4	Conclusion	95
7	Numerical investigation	97
7.1	Model description	97
7.1.1	Thermal model	98
7.1.2	Electrochemical model	104
7.2	LT sensitivity analysis	107
7.2.1	Frequency dependency	111
7.2.2	Dependency on the MIC thermal conductivity	113

7.2.3	SOFC operation	114
7.2.4	SOEC operation	114
7.2.5	Dependency on the convection coefficient	115
7.2.6	Dependency on flow rate and reactant utilization	122
7.2.7	Dependency on the thermal conductivity of the GDL	128
7.2.8	Local defect identification	130
7.2.9	Local power density estimation	135
7.3	Conclusion	139
8	Test bench description	141
8.1	Test bench	141
8.2	Control and data acquisition	145
8.3	Camera calibration	146
8.4	SOC preparation and assembly	149
9	Experimental results	151
9.1	Model-based interpretation of experimental LT	152
9.1.1	Electrolysis	152
9.1.2	Fuel cell	155
9.1.3	Intermediate discussion	158
9.2	Pulse thermography	159
9.3	Electrolysis and Co-electrolysis	160
9.4	SO ₂ poisoning	167
9.4.1	Proposed SO ₂ degradation mechanism	169
9.5	Conclusion	174
10	Concluding remarks & outlook	177
10.1	Concluding remarks	177
10.1.1	Part I	177
10.1.2	Part II	179
10.2	Outlook	181
A	Reversible R_s increase	183
B	Electronic conductivity of YSZ	185
C	Analytical Fourier Transform	189
D	LT defect	195
E	LT data analysis results	199
	Bibliography	203

Table of Contents

Publications & Conferences	243
Curriculum Vitae	245

List of Figures

1.1	Schematic representation of the power-to-X concept. Reprinted from [1].	4
1.2	Schematic representation of the working principal of a SOFC and SOEC.	5
1.3	Typical current density–voltage (J–V) curve for a solid oxide electrolysis cell (SOEC). Regions where activation, ohmic, or concentration losses dominate are highlighted.	12
1.4	Schematic representation of a typical impedance spectra of an SOC in a Nyquist diagram.	13
1.5	Real-time monitoring of the formation of a crack originating from a hot spot and leading to complete cell failure . First column: raw thermal image, second column: emissivity corrected image, third column: pixel based temperature distribution. Reprinted with permission from [2] ©The Optical Society.	18
1.6	LT measurements on a PEM fuel cell taken at a polarization of 0.1 A cm^{-2} with an excitation frequency of 0.07 Hz. The thermogram (a) represents the steady state temperature field, the amplitogram is the amplitude of the sinusoidal temperature evolution (b), and the phase shift (c) is the phase difference between the current sent to the peltier element and the temperature response. Reprinted with permission [3]	21
3.1	Schematic representation of the SOC assembly with (a) central and (b) twisted lead wire configuration. The flange, the gold current lead wires, the glass sealant, and the SOC are colored in grey, yellow, blue, and green and black, respectively. The mica gasket, the alumina felt, and the Ni current collector are represented by green horizontal strips, black diagonal strips, and grey cross strips, respectively. The alumina tube in the gas inlet is represented in black.	46
3.2	Schematic Bode representation of the electrochemical impedance spectrum with the definition of the serial (R_s), polarization (R_p), and total cell resistance (R_{tot}). Z is the complex electrochemical impedance.	47
3.3	A series connection of resistor (R) and capacitor (C) connected in parallel ($//$), representing the concept of DRT.	48
3.4	Schematic representation of the electric circuit used for DRT comparison	49

List of Figures

3.5	Nyquist (a) and Bode (b) representation of the impedance spectra of the circuit defined in Table 3.1 showing a low frequency hook. The analytical and numerical DRT of the spectra is presented together with the Bode representation in (b).	50
4.1	Time evolution of the cell voltage when exposed to 0 to 10 ppmv of HCl in open-circuit conditions, the horizontal black dashed line is the initial cell voltage	54
4.2	(a) and (b) electrochemical impedance spectra taken at OCV after exposure to 0.5, 1, 5, and 10 ppmv of HCl, (c) corresponding distribution of relaxation time, and (d) resistance associated with peaks P1–P6 in function of the HCl concentration . The exposure durations are indicated in parentheses.	55
4.3	Time evolution of the cell voltage when exposed to 0 to 10 ppmv of HCl polarized at 0.25 A cm^{-2} , the horizontal black dashed line is the initial cell voltage	56
4.4	(a) and (b) electrochemical impedance spectra taken at 0.25 A cm^{-2} after exposure to 0.5, 1, 5, and 10 ppmv of HCl, (c) corresponding distribution of relaxation time, and (d) resistances associated to peak P1–P6 as a function of the HCl concentration. The exposure durations are indicated in parentheses.	57
4.5	Time evolution of the cell voltage when exposed to 0 to 10 ppmv of HCl polarized at 0.5 A cm^{-2} , the horizontal black dashed line is the initial cell voltage	58
4.6	(a) and (b) electrochemical impedance spectra taken at OCV after exposure to 0.5, 1, 5, and 10 ppmv of HCl and (c) corresponding distribution of relaxation time. The exposure durations are indicated in parentheses.	59
4.7	Time evolution of (a) the cell voltage and (b) R_s and R_p during the durability test at a constant polarization of 0.5 A cm^{-2} , where the numbers in the plot area are the HCl content in ppmv	60
4.8	Evolution of the DRT during a) exposure to 1 ppmv of HCl and recovery and b) exposure to 2 ppmv of HCl. The time at which the EIS were recorded are indicated in parentheses.	61
4.9	Evolution of the EI taken at 0.5 A cm^{-2} during exposure to HCl and recovery in HCl-free mixture. The time at which the EI were recorded are indicated in parentheses.	63
5.1	Schematic representation of the SOEC voltage time evolution during poisoning by SO_2	66
5.2	Time evolution of the cell voltage when exposed to various concentrations of SO_2 and during recovery , respectively, at (a) and (b) OCV and (c) and (d) 0.25 A cm^{-2} , respectively.	67

5.3	Ni coverage and reduction of the CO content with respect to the SO ₂ content. The reduction of the CO content was computed based on the equivalent composition corresponding to the initial OCV measured. The red data points were extrapolated.	69
5.4	(a) and (b) electrochemical impedance spectra taken at OCV after exposure to 0.5, 1, 2, and 5 ppmv of SO ₂ followed by a recovery period without SO ₂ , (c) corresponding DRT, and (d) relative increase of R_p function of the surface coverage . The exposure/recovery durations are indicated in parentheses.	70
5.5	(a) and (b) electrochemical impedance spectra taken at 0.25 Acm ⁻² after exposure to 0.5, 1, and 2 ppmv of SO ₂ followed by a recovery period without SO ₂ and (c) corresponding DRT and (d) relative increase of R_p as a function of the surface coverage. The exposure/recovery durations are indicated in parentheses.	72
5.6	Time evolution of (a) the cell voltage and temperature and (b) of R_s and R_p during the long-term stability test, where the numbers at the top of the graphic indicate the SO ₂ concentration in ppmv.	73
5.7	Time evolution of the DRT during the long term stability test, where the arrows represent the observed trends.	74
5.8	(a) and (b) electrochemical impedance spectra taken at 0.5 Acm ⁻² during the first exposure to 1 ppmv of SO ₂ followed by a recovery period without SO ₂ and (c) corresponding DRT.	75
5.9	Electrochemical impedance spectra taken at 0.5 Acm ⁻² during the exposure to (a) 1 ppmv, (b) 2 ppmv, and (c) 0.5 ppmv of SO ₂ followed by a recovery period without SO ₂ . The time from the beginning of the test at which the impedance spectra were measured is indicated in between parentheses.	77
5.10	(a) and (b) electrochemical impedance spectra at 0.5 Acm ⁻² taken during the recovery following the exposure to 0.5 ppmv of SO ₂ and (c) the corresponding DRT. Black arrows represent the observed trends of the time-evolution from the last measurement taken with 0.5 ppmv of SO ₂ (2289 h) until the end of the recovery period (2480 h)	78
6.1	Black body spectral radiance computed with equation (6.3) at varying temperatures and the four different spectral ranges used for thermal imaging.	87
6.2	(a) and (c) are the temporal representation of a cosine and pulse signal whereas (b) and (d) are the norm of their respective Fourier transform for positive frequency only. In both cases, the norm of the Fourier transform is symmetric with respect to $f = 0$ at negative frequencies.	91
6.3	Schematic representation of the LT and EI procedure.	94
7.1	Schematic representation of the discretization domain.	98
7.2	Definition of the view factor parameters. Reproduced from [4].	101

List of Figures

7.3	Convergence of \dot{Q}_{rad}^{wall} with N	101
7.4	Schematic representation of the phase shift between a sinusoidal signal and response, here, the current density and temperature, respectively. The resulting effect of the phase shift on the real and imaginary part of the response is also presented. The phase is positive in the counter-clockwise direction.	108
7.4	Dependency of the SOC's thermal response on the steady-state current density. From the left to the right column : $\ \hat{T}_{SOC}\ ^I$, $\ \hat{T}_{SOC}^{rel}\ ^I$, and ϕ_{SOC}^I . Each line corresponds to a different current density.	110
7.5	Dependency of $\ T_{MIC}\ ^I$, $\ T_R\ ^I$, $\ T_A\ ^I$, and \dot{Q}_{rx} on the excitation frequency at 0 Acm^{-2}	112
7.6	Dependency of $\ j\ ^I$ and ϕ_j^I on the excitation frequency at 0 Acm^{-2}	112
7.7	Dependency of the SOC thermal response on λ_{MIC} at 0 Acm^{-2} . From the left to the right column : $\ \hat{T}_{SOC}\ ^I$, $\ \hat{T}_{SOC}^{rel}\ ^I$, and ϕ_{SOC}^I . Each line corresponds to a different value of λ_{MIC}	113
7.8	Schematic representation of \dot{Q}_{rx} as function of the SOC's voltage.	116
7.9	Dependency of h_R^c on c_{H_2} for a $\text{H}_2\text{O} / \text{H}_2$ mixture at 750°C	116
7.10	Dependency of $\ \hat{T}_{SOC}\ ^I$ on h_R^c at -0.3 Acm^{-2} . The first column corresponds to a spatially constant h_R^c computed based on the inlet composition ($3330 \text{ Wm}^{-2} \text{ K}^{-1}$) and the three other columns correspond to a different values of Nu_R and thus h_R^c	117
7.11	Spatial distribution of a) the steady-state value and b) modulation amplitude (Δh_R^c) of h_R^c	118
7.12	Dependency of ϕ_{SOC}^I on h_R^c at various current densities. The first column corresponds to a spatially constant h_R^c computed based on the inlet composition ($3330 \text{ Wm}^{-2} \text{ K}^{-1}$) and the three other columns correspond to different values of Nu_R and thus h_R^c	120
7.13	Dependency of $\ \hat{T}_{SOC}^{rel}\ ^I$ on h_R^c at various current densities. The first column corresponds to a spatially constant h_R^c computed based on the inlet composition ($3330 \text{ Wm}^{-2} \text{ K}^{-1}$) and the three other columns correspond to different values of Nu_R and thus h_R^c	121
7.14	Dependency of the $\ \hat{T}_{SOC}^{rel}\ ^I$ and ϕ_{SOC}^I on the reactant (U_R) and air (U_A) flow rate at 0 Acm^{-2}	122
7.15	Dependency of the thermal response of the SOC on the U_R and RU in electrolysis operation.	124
7.16	Dependency of the SOC thermal response on U_R and RU in fuel cell operation.	125
7.17	Thermal response of the SOC at $\text{RU} = 0.87$ in (a)–(c) fuel cell and (d)–(f) in electrolysis operation.	127

7.18	Effect of high RU on the local current density, (a) phase shift between the local and applied current density modulation in fuel cell operation at $RU = 0.87$ and (b) local and total current density modulation from the steady state-value.	127
7.19	Dependency of the thermal response of the SOC to the λ_{GDL} at 0 Acm^{-2}	130
7.20	Simulated EI spectra for the three different defect location at various current densities in a) Nyquist and b) Bode representation	131
7.21	Thermal response of an SOC at 0 Acm^{-2} containing a defective area defined by a supplementary local resistance ASR_{def} . From the left to right column: $\ \hat{T}_{SOC}\ ^I$, $\ \hat{T}_{SOC}^{rel}\ ^I$, and ϕ_{SOC}^I . Each line corresponds to the ASR_{def} being added at different values of x^*	132
7.22	The thermal response of the SOC containing a defective area defined by a supplementary local resistance ASR_{def} . From left to right columns: $\ \hat{T}_{SOC}\ ^I$, $\ \hat{T}_{SOC}^{rel}\ ^I$, and ϕ_{SOC}^I . Each line corresponds to different applied current density.	133
7.23	Thermal response of an SOC containing a defective area defined by a supplementary local resistance ASR_{def} . From left to right columns: $\ \hat{T}_{SOC}\ ^{II}$, $\ \hat{T}_{SOC}^{rel}\ ^{II}$, and ϕ_{SOC}^{II} . Each line corresponds to different applied current density.	134
7.24	ϵ_Q for various current densities under reference conditions.	137
7.25	ϵ_Q for various current densities under reference conditions.	138
8.1	(a) schematic and (b) photograph of the test bench dedicated to active thermography experiments.	142
8.2	CAD of the test bench showing a cut through the set-up (a) and a close-up view of the SOC frame (b).	143
8.3	Photograph of (a) the SOC assembly in the homemade furnace and (b) SOC assembly positioned above the camera with part of the insulation removed.	143
8.4	EIS measurements at 0 Acm^{-2} in a 50/50 vol% $\text{H}_2/\text{H}_2\text{O}$ at $12 \text{ Nm l min}^{-1} \text{ cm}^{-2}$ with different current and voltage measurements configuration. The untwisted, twisted, and co-axial configuration are defined in Figures 3.1 (a), (b), and 8.2 (b), respectively.	145
8.5	Quantum efficiency of the Allied Vision Manta G-223B (grey) and G-223B NIR (purple). Adapted from [5]	146
8.6	Results of the least-squares fitting used for the camera calibration including the upper and lower prediction bounds.	148
8.7	Photographs of (a) the SOC-gold-mesh assembly, (b) of the Ni-foam with the NiO paste deposited, (c) the glass sealing positioning, (d) the mica gasket.	150
9.1	Colorized temperature field of the SOC.	152

List of Figures

9.2	Thermal response at -0.2 A cm^{-2} to a 1 A perturbation at various frequencies. The reactant and air flow from left to right. Images (a)–(d) and (e)–(f) are simulation results obtained with λ_{GDL} set to 3.5 and $0.35 \text{ W m}^{-1} \text{ K}^{-1}$, respectively, whereas images (i)–(aj) are experimental data.	153
9.3	Thermal response of the SOC at -0.4 A cm^{-2} to a 1 A perturbation at various frequencies. The reactant and air flow from left to right. Images (a)–(d) are simulation results obtained with λ_{GDL} set to $0.35 \text{ W m}^{-1} \text{ K}^{-1}$ whereas images (e)–(p) are experimental data.	156
9.4	Thermal response of the SOC at 0.1 A cm^{-2} to a 0.5 A perturbation at various frequencies. The reactant and air flow from left to right. Images (a)–(b) are simulation results obtained with λ_{GDL} set to $0.35 \text{ W m}^{-1} \text{ K}^{-1}$ whereas images (e)–(p) are experimental data.	157
9.5	Frequency content of the pulse excitation signal sent (continuous) and recorded (sampled).	159
9.6	SOC thermal response to a 1.5 A current pulse perturbation in fuel cell operation. The reactant and air flow from left to right.	160
9.7	SOC's current voltage–characterization for the reactant compositions defined in Table 9.1	161
9.8	Dependency of the h_R^c on c_{CO} for a CO_2 / CO mixture at 750°C	161
9.9	$\hat{T}_{SOC}^{''I}$ averaged perpendicularly to the flow for (a) CE30 and (b) SE80 reactant mixtures.	162
9.10	$\hat{T}_{SOC}^{''I}$ at -0.1 A cm^{-2} and 1 A perturbation for the reactant mixture defined in Table 9.1	164
9.11	$\hat{T}_{SOC}^{''I}$ at -0.1 A cm^{-2} and 1 A perturbation for the reactant mixture defined in Table 9.1	165
9.12	$\hat{T}_{SOC}^{''I}$ at -0.3 A cm^{-2} and 1 A perturbation for the reactant mixture defined in Table 9.1	166
9.13	$\hat{T}_{SOC}^{''I}$ at -0.3 A cm^{-2} and 1 A perturbation for the reactant mixture defined in Table 9.1	166
9.14	Time evolution of the V_{SOC} operated at -0.2 A cm^{-2} in a 65/25/10 $\text{H}_2\text{O}/\text{CO}_2/\text{H}_2$ vol% mixture with the addition of 1 ppmv of SO_2 and during the recovery period in an SO_2 -free atmosphere	167
9.15	(a) The time evolution of the DRT during the initial degradation step (reproduction of Figure 5.7 and (b) current density distribution computed with the model described in Chapter 7 for a 90/10 vol% $\text{H}_2\text{O}/\text{H}_2$ mixture at -0.2 A cm^{-2} and a $\text{RU} = 0.13$	170
9.16	Thermal response of the SOC at -0.2 A cm^{-2} to a 1 A perturbation at various frequencies when exposed to 1 ppmv of SO_2 and during recovery. The reactant and air flow from left to right.	172

9.17	Difference between the value of \hat{T}_{SOC}^I measured at 0.01 Hz before and (a)–(d) during SO ₂ poisoning (2 h–20 h) and during (e)–(f) recovery (20 h–120 h). \hat{T}_{SOC}^I was averaged perpendicularly to the flow in three regions of interest (b) and (e) A1, (c) and (f) A2, and (d) and (g) A3 as defined in (a). The reactant and air flow from left to right.	173
B.1	YSZ ionic, electron, and hole conductivity at 800 °C function of the oxygen partial pressure at which the YSZ is at equilibrium with. The red rectangle correspond the typical range of oxygen partial pressure experienced during the poisoning experiments performed in this thesis. Reproduced from Schefold et al. [6].	186
D.1	The thermal response of the SOC containing a defective area defined by a supplementary local resistance ASR_{def} at $x^* = 0.1$ – 0.12 . From left to right columns: $\ \hat{T}_{SOC}\ ^I$, $\ \hat{T}_{SOC}^{rel}\ ^I$, and ϕ_{SOC}^I . Each line corresponds to a different applied current density.	196
D.2	The thermal response of the SOC containing a defective area defined by a supplementary local resistance ASR_{def} at $x^* = 0.5$ – 0.52 . From left to right columns: $\ \hat{T}_{SOC}\ ^I$, $\ \hat{T}_{SOC}^{rel}\ ^I$, and ϕ_{SOC}^I . Each line corresponds to a different applied current density.	197
D.3	The thermal response of the SOC containing a defective area defined by a supplementary local resistance ASR_{def} at $x^* = 0.9$ – 0.92 . From left to right column: $\ \hat{T}_{SOC}\ ^I$, $\ \hat{T}_{SOC}^{rel}\ ^I$, and ϕ_{SOC}^I . Each line corresponds to a different applied current density.	198
E.1	The ϕ_{SOC}^I for eight frequencies as well as Z and ϕ in a Bode plot.	200
E.2	The $\ \hat{T}_{SOC}\ ^I$ for eight frequencies as well as Z' and Z'' in a Bode plot.	201

List of Tables

1.1	Definition of typical types of over-potential	7
2.1	Typical biogas composition [7]	27
2.2	Generic impurities likely to be found in a captured CO ₂ stream from various sources [8]	28
2.3	Captured CO ₂ composition from various sources. Data are compiled from [8–11].	29
2.4	Summarized literature review on sulfur poisoning	32
2.5	Summarized literature review on chlorine poisoning	35
2.6	Summarized literature review on silicon poisoning	37
2.7	Summarized literature review on tar poisoning	38
2.8	Summarized literature review on heavy metals and phosphor poisoning .	40
2.9	Summary and effect of the principal impurities impacting Ni-based composites SOC H ₂ -electrode	43
3.1	Parameters of the electric circuit defined in Figure 3.4	49
3.2	Attribution of the DRT peaks to processes according to Caliendo et al. [12]	51
5.1	ΔV measured from the initial (recovered) voltage, S_i , S_f , and Δt as defined in Figure 5.1, when the SOECs were polarized at a current density j and exposed to various concentrations of SO ₂	70
6.1	Summary of infrared imaging technologies	85
6.2	Data processing for pulse thermography	89
7.1	Parameters used for the reference case	108
8.1	Values of the fitting parameters obtained by regression	148
9.1	Reactant composition in electrolysis (SE80) and co-electrolysis (CE15 and CE30) operation. The air flow was always 200 Nmlmin ⁻¹	161

Nomenclature & Acronyms

Latin letters

\dot{Q}	Heating power	W m^{-2}
A	Area	m^2
ASR	Area specific resistance	Ωcm^2
C	Capacitance	F
c	Speed of light	m s^{-1}
c_x	Volume fraction of component x	–
E	Hemispherical emissive power	W m^{-2}
E_N	Nernst potential	V
F	Faraday constant	C mol^{-1}
f	Frequency	Hz
F_{1-2}	View factor	–
g	Gibbs free energy	kJ mol^{-1}
H	Height	m
h	Enthalpy	kJ mol^{-1}
h	Planck constant	J s
h^c	Convective heat transfer coefficient	$\text{W m}^{-2} \text{K}^{-1}$
I	Grey level	–
I	Spectral intensity	$\text{W}^2 \text{m}^{-1} \text{sr}^{-1} \mu\text{m}^{-1}$
J	Total current density	A cm^{-2}
j	Local current density	A cm^{-2}
k_B	Boltzmann constant	J K^{-1}
L	Inductance	H
N	Number of cycles	–
n	Refractive index or number of frame per cycle	–
Nu	Nusselt number	–
p	Pressure	Pa
QE	Quantum efficiency	–
R	Ideal gas constant	$\text{J mol}^{-1} \text{K}^{-1}$
R	Resistance	Ωcm^2
Re	Reynolds number	–
RU	Reactant utilization	–
S	Slope	–

List of Tables

s	Entropy	$\text{kJ mol}^{-1} \text{K}^{-1}$
T	Period	s^{-1}
T	Temperature	K
t	Time	s
U	Flow rate	NmL/min
V	Voltage	V
v	Volume	m^3
W	Width	m
x^*	Dimensionless position	—
Z	Electrochemical impedance	Ωcm^2
z	Number of electrons exchanged	—

Greek letters

α	Absorbance	—
Δ	Difference	—
δ	Delta function	—
ϵ	Emittance	—
ϵ_{el}	Electric efficiency	—
η	Overpotential	V
γ	Distribution function of relaxation time	$\Omega \text{cm}^2 \text{s}$
λ	Wavelength	μm
λ_x	Thermal conductivity of material x	$\text{W m}^{-1} \text{K}^{-1}$
ν	Stoichiometric coefficient	—
ω	Pulsation	rad s^{-1}
ϕ	Phase	rad
ρ	Density	kg m^{-3}
ρ	Reflectance	—
σ	Stefan-Boltzmann constant	$\text{W}^2 \text{m}^{-1} \text{K}^{-4}$
τ	Transmittance	—

Subscript

act	Activation
bb	Black body
$conc$	Concentration
$conv$	Convection
DS	Dark signal
f	Formation or final
gb	Grey body
i	Initial (Part I) or intergration (Part II)
ohm	Ohmic
p	Polarization
r	Reaction
s	Serial
sen	Sensor

tn Thermo-neutral

tot Total

Superscript

' Real component

" Imaginary component

0 Reference conditions

ss Single sided

th Theoric value

Others

$\hat{}$ Fourier transform of a variable

\mathfrak{F} Fourier transform function

\mathfrak{F}_d Discrete Fourier transform function

$\| \cdot \|$ Norm

Acronyms

AT Active thermography

CCD Charge-coupled device

CMOS Complementary metal oxide semi-conductor

D4 Octamethylcyclotetrasiloxane

D5 Decamethylcyclopentasiloxane

DFT Discrete Fourier transform

DRT Distribution of relaxation time

DSNU Dark signal non-uniformity

EEC Electric equivalent circuit

EIS Electro-chemical impedance spectroscopy

ESEM Environmental SEM

ETIS Electro-thermal impedance spectroscopy

FFT Fast Fourier transform

FIB Focused ion-beam

FTIR Infrared Fourier transform spectroscopy

GDC Gadolinia doped ceria

GDL Gas diffusion layer

HHW Half height width

HOSM High order statistical method

LSC Lanthanum strontium cobaltite

LSCF Lanthanum strontium cobalt ferite

LSCM Lanthanum strontium chromo-manganite

LSM Lanthanum strontium manganite

LT Lock-in thermography

LWIR Long-wave infrared

MIC Metallic interconnect

MWIR Mid-wave infrared

NETD Noise equivalent temperature difference

List of Tables

NIR	Near infrared
OCC	Open circuit conditions
PCA	Principal component analysis
PCT	Principal component thermography
PEM	Polymer electrolyte fuel cell
ppm	part per million
ppmv	part per million of a volume basis
ppmw	part per million of a weight basis
PPT	Pulse phase thermography
PRNU	Photon-response non-uniformity
PT	Pulse thermography
RWGS	Reverse water-gas shift reaction
ScSZ	Scandia stabilized zirconia
SEM	Scanning electron microscopy
SoA	State of the Art
SOC	Solide oxide cell
SOEC	Solide oxide electrolysis cell
SOFC	Solide oxide fuel cell
SWIR	Short-wave infrared
TEM	Transmission electron microscopy
TEOS	Tetraethyl orthosilicate
TPB	Triple phase boundary
TSR	Thermographic signa reconstruction
YSZ	Yttria stabilized zirconia

CHAPTER 1

Introduction

This chapter uses text and information published in Jeanmonod et al. [13].

1.1 A short history of climate change

Since the pioneering work by Arrhenius [14] in 1896, an increase in atmospheric CO₂ has been known to cause an increase of the global mean temperature of the Earth. In the 1930s, Guy Stewart Callendar observed an increase of the atmospheric CO₂ concentration that he linked with a global temperature increase, attributable to the raising fossil fuel consumption [15]. In the late 1950s and early 1960s, large-scale and long-term monitoring of the atmospheric CO₂ were put in place [16]. Data recorded over eight years showed that the atmospheric CO₂ concentration follows daily and yearly cycles as well as continuously increasing trend, thus confirming Callendar's claim [17]. In the 1970s, the observed CO₂ increase was acknowledged to be related to human activities [17, 18]. In 1981, Hansen et al. [19] modeled the global temperature increase by the end of the 21st century and its consequences considering no, a slow, or a fast growth of the global energy consumption with and without phaseout of coal by 2000 or 2020. A global warming of at least 2°C was found in all cases but the no-growth or coal phaseout cases. This temperature increase was demonstrated to be sufficient to lead to a rapid melting of the Antarctica ice sheet and thus a rapid rise of the sea level with potentially dramatic consequences for coastal cities. Furthermore, they also predicted an increase in drought-prone regions and radical local climate modification. In 1985, the World Meteorological Organization (WMO), the United Nation Environment Programme (UNEP), and the International Science Council (ICSU) concluded that the doubling of the atmospheric CO₂ may occur before the mid-21st century, making climate change a much greater threat than expected at that time [20]. The WMO and UNEP managed to raise countries' awareness on climate change, leading to the creation of the International Panel on Climate Change (IPCC) in 1988, which aims to evaluate the impact of human activities on the climate. In 1992, the United Nation Framework Convention of Climate Change (UNFCCC) was created, in which signatories acknowledged the role of human activities on the increased greenhouse effect [21]. The UNFCCC led to the Kyoto protocol in 1997 and the Paris Agreement in 2015. Signatories of the Paris agreement is to limit

the global temperature increase to less than 2 °C and as close as possible to 1.5 °C above the pre-industrial level. If the 2 °C limit is not met, there is a high risk for a dangerous climate destabilization [22, 23]. The 2019 emission gap report made by the UNEP reveals that with the current nationally determined contributions (NDCs), a 2 °C target is way out of reach; the world is moving towards a 3.2 °C global temperature increase [24]. To reach the 2 °C and 1.5 °C target, the NDCs would need to be three and five times more ambitious, respectively.

1.2 Chemical energy storage in the context of energy transition

A key aspect of reaching the target stipulated in the Paris Agreement is the decarbonization of the energy and transport sector [25]. Renewable energy production must thus be extensively promoted. The cost of renewable energy has been drastically reduced in the past years and now easily competes with fossil fuels [24]. To accommodate for the variability inherent in renewable electricity production (e.g., photovoltaic panels and wind turbines) and the consequent mismatch between the production and consumption, the grid flexibility must be improved [26, 27]. One solution is to store and redistribute the excess renewable energy to match the demand [28–30].

Fast- and short-term balancing of the electrical grid at the order of seconds to minutes can be achieved using super-capacitors and flywheels; for longer-term balancing at the scale of minutes to hours, batteries (e.g., flow batteries, Li-ion, NaS, NiCd [31]) are the major available technologies; the balancing at the scale of days to weeks currently depends highly on pumped hydro power plants (PHP) [32–34], which are, limited by geographic location and capacity [35]. No mature technology has yet been developed to store electricity for several months (i.e., for seasonal storage) at the TWh scale [34, 36].

The "power-to-X" concept, which consists of converting power to either gases (e.g., H₂ or CH₄), liquid fuels (e.g., methanol or dimethyl ether), or other chemicals (e.g. solvent, formic acid, or waxes) [37], has recently gained interest as a method for substituting fossil resources and storing excess renewable electricity [38]. A schematic representation of the power-to-X concept is presented in 1.1. In the context of seasonal storage of renewable energies, "power-to-gas" (PtG), which uses excess electricity to produce hydrogen or syngas (a mixture of hydrogen and carbon monoxide) via electrolysis, is a promising candidate [39, 40]. Syngas or hydrogen mixed with carbon dioxide can be further transformed into methane to facilitate large-scale storage and transport by using the existing natural gas infrastructure [41–43]. These pathways are referred to as "power-to-methane" (PtM). PtM is of particular interest in Europe, as the European gas grid has been estimated to have the capacity to store the current annual European renewable energy production (1100 TWh) [44]. In this sense, the natural gas grid can be seen as a

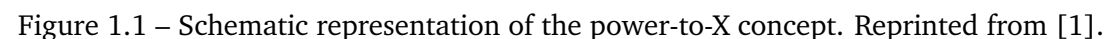
chemical battery distributed over the entire continent. Furthermore, the methane produced can be converted back to electricity using, for example, a solid oxide fuel cell [45] or used as a substitute of conventional fuel, for example in the transport industry [33, 46].

The CO₂ required to perform co-electrolysis can be extracted from various sources. Non-renewable sources mainly involve flue gases from conventional power plants and cement plants containing between 10 to 20 vol% of CO₂ [47]; however, renewable sources, e.g., biomass (including biogas), are more attractive to store renewable electricity using PtG [37, 48]. The CO₂ fraction in the streams converted from biomass can vary from 8 vol% in flue gases to approximately 40 vol% in raw biogas, and even reach 100 vol% in fermentation processes [47], which allow less energy-intensive or even the avoidance of CO₂ capture (CC) [42]. Renewable-power driven PtM can be employed to upgrade biogas to methane suitable for grid injection [49] with or without carbon capture (CC) [50, 51].

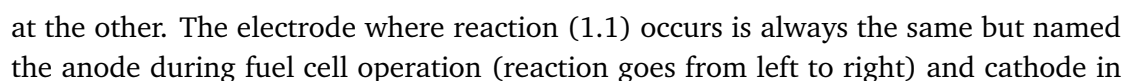
PtM's system performance is mainly dependant on the performance of the electrolyzer used [52]. Compared with an alkaline or a proton-exchange membrane electrolyzer, a solid oxide electrolyzer (SOE) is advantageous due to (1) a higher electrical efficiency [53] of steam electrolysis (SE) rather than liquid-water electrolysis, (2) the possibility of CO₂ electrolysis to produce CO [54], (3) direct syngas production by co-electrolysis (CE) of steam and CO₂ [55], and (4) heat-integration opportunity with other industrial processes. The system-performance bottleneck of steam electrolysis is the significant amount of heat required for steam generation [56]. However, for SOE-based PtM, this heat requirement can be supported (up to 80 % [56]) by the heat released from the exothermic methanation reaction. Furthermore, properly selecting the SOE design points may allow for a thermally self-sufficient PtM system that requires no electrical heating [52].

1.3 SOEC working principle

A solid oxide cell (SOC) is an electrochemical device that operates at high temperatures (i.e., typically between 600 °C and 900 °C) and can convert hydrogen- and carbon-based fuel into electricity and heat, releasing H₂O and/or CO₂. As such, they would then be referred to as solid oxide fuel cell (SOFC). Like rechargeable batteries, SOCs are reversible and can convert H₂O and CO₂ into H₂ and CO, respectively, in that case they would be referred to as a solid oxide electrolysis cell (SOEC). SOCs are composed of two porous electrodes separated by a dense electrolyte where oxygen ions are transported. A schematic representation of an SOFC and SOEC is presented in Figure 1.2 where the interconnect represents metallic plates that physically separates two repeat elements in a stack assembly but provides an electronic connection.



The reduction/oxidation (red/ox) process taking place in SOC can be split in two-half reactions:



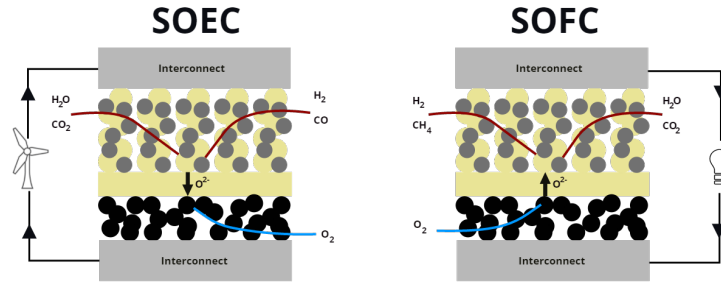


Figure 1.2 – Schematic representation of the working principal of a SOFC and SOEC.

electrolysis mode (reaction goes from right to left). To avoid any confusion, the electrode where reaction (1.1) happens is always referred to as the H_2 -electrode whereas the electrode where reaction (1.2) is referred to as the O_2 -electrode.

In the presence of carbonaceous reactant, the reaction :



can also take place at the H_2 -electrode. In addition to electrochemical reaction, catalytic reactions may also take place. They will depend on the fuel used but the most common ones are the steam methane reforming (SMR), water gas shift (WGS) and the Boudouard reactions defined in equations (1.4), (1.5), and (1.6), respectively.



The overall reactions for H_2 and CO conversion are given by equation (1.7) and (1.8), respectively.



The enthalpy of reaction $\Delta_r h^0$, corresponding to the energy needed/released by the reaction, is defined as:

$$\Delta_r h^0 = \sum_{product} \nu \Delta_f h^0 - \sum_{reactant} \nu \Delta_f h^0 \quad (1.9)$$

where h is the enthalpy, ν is the stoichiometric coefficients, the subscripts r and f stand for "reaction" and "formation" respectively, and the superscript 0 indicates that

the value is referenced to the standard pressure p_0 (10^5 Pa) and here to a temperature of 298 K. In fuel cell operation, reactions (1.7) and (1.8) go from left to right and the standard reaction enthalpy for gaseous species is $\Delta_r h_{H_2/H_2O}^0 = -241.826 \text{ kJ mol}^{-1}$ and $\Delta_r h_{CO/CO_2}^0 = -282.964 \text{ kJ mol}^{-1}$, respectively. Both reaction enthalpies are negative indicating that heat is released and that the reactions are exothermic. In electrolysis however, the reactions (1.8) and (1.7) go from right to left and the reaction enthalpies are positive; thus, the reactions are endothermic.

The enthalpy of reaction is related to the Gibbs free energy of reaction, $\Delta_r g^0$, and the entropy of reaction, $\Delta_r s^0$, as expressed by equation (1.10) where T^0 corresponds to the reference temperature at which $\Delta_r h^0$, $\Delta_r g^0$, and $\Delta_r s^0$ are computed. In fuel cell mode, $\Delta_r g^0$ represents the maximum work/electricity that can be extracted and $T\Delta_r s^0$ represents the an avoidable heat loss. Reciprocally, $\Delta_r g^0$ also represents the minimum work that needs to be provided to the system to perform electrolysis.

$$\Delta_r h^0 = \Delta_r g^0 + T^0 \Delta_r s^0 \quad (1.10)$$

In a galvanic cell, this work is related to the reversible transport of charges from one electrode to the other through a potential expressed by the Nernst equation [61]:

$$\Delta_r g^0 = -zFE_N^0, \quad (1.11)$$

where E_N^0 is the Nernst potential in standard condition, z is the number of electrons involved in the reaction, and F the Faraday constant, equal to 96485 C mol^{-1} .

When the temperature, pressure, and concentration differ from the reference conditions the Nernst potential for an ideal mixture is given by [62]:

$$E_N = E_N^0 + \frac{RT}{zF} \left[\sum_{product} \nu_i \ln \left(\frac{p_i}{p^0} \right) - \sum_{reactant} \nu_i \ln \left(\frac{p_i}{p^0} \right) \right] \quad (1.12)$$

where $p_i = c_i \cdot p_t$, and c_i are the partial pressure and molar fraction of the reactant/product i , respectively, p_t is the mixture pressure, $R = 8.314 \text{ J mol}^{-1} \text{ K}^{-1}$ is the ideal gas constant, and T the operating temperature.

For both reactions (1.7) and (1.8), E_N and $\Delta_r g$ decrease with the temperature [61]. As the temperature increases, a larger share of $\Delta_r h$ is released/provided as heat during SOFC/SOEC operation, respectively. As electricity is the desired output in fuel cell operation, this release of heat is generally detrimental to fuel cell operation. However, this addition of heat could be advantageous in electrolysis mode as less electrical power is needed to produce the same amount of H_2 and/or CO [63].

1.3. SOEC working principle

When a current is drawn/applied, the voltage measured on the SOC deviates from E_N . The operating SOC voltage as function of the current density j can be expressed as:

$$V_{SOC}(j) = E_N + \sum_k \eta_k(j), \quad (1.13)$$

where η_k is the over-potential related to a specific process. Generally, three types of over-potential are considered and briefly defined in Table 1.1.

Table 1.1 – Definition of typical types of over-potential

η_{act}	The activation over-potential is representative of the kinetics of the electrochemical reaction and is linked to the activation energy, which corresponds to energy that must be provided for a chemical reaction to happen.
η_{ohm}	The ohmic over-potential represents the losses related to the conduction of ions and electrons. The main contributors are generally related to the electrolyte ionic conductivity and the contact with the interconnect especially in a stack assembly configuration.
η_{conc}	The concentration over-potential is related to the limitation of the gas transport which leads to a depletion of the reactant at the electrochemically active sites.

The over-potentials result in irreversible heat dissipation, analogously to Joule heat in a resistor. The electrolysis of H_2O and/or CO_2 is an endothermic process, but if the current is increased, the over-potentials and the corresponding heat generated also increases. When a certain voltage is reached, the electric power input compensates exactly for the enthalpy of reaction. This particular voltage is referred to as the thermoneutral voltage V_{tn} and defined by equation (1.14), where $\Delta_r h$ is the reaction enthalpy at the operating temperature and pressure expressed in $Jmol^{-1}$. In electrolysis mode, V_{tn} corresponds to the limit between global endothermic ($V_{SOC} < V_{tn}$) and exothermic ($V_{SOC} > V_{tn}$) operation.

$$V_{tn} = -\frac{\Delta_r h}{zF} \quad (1.14)$$

The theoretical electric efficiency of an SOEC ϵ_{el}^{th} is defined as the ratio between the enthalpy of reaction (product) and the Gibbs free energy of reaction (input), which can then also be expressed in term of voltage using relation (1.12) and (1.14) as expressed by equation (1.15).

$$\epsilon_{el}^{th} = \frac{product}{input} = \frac{\Delta_r h}{\Delta_r g} = \frac{V_{tn}}{E_N} \quad (1.15)$$

The effective electric efficiency, which takes into account the contribution of the over-potentials is computed by substituting E_N for V_{SOC} in equation (1.15),

$$\epsilon_{el} = \frac{V_{tn}}{V_{SOC}}. \quad (1.16)$$

When V_{SOC} is between E_N and V_{tn} , $\epsilon_{el} > 1$. This number has to be considered carefully as it only considers the electric input and does not take into account the external heat input necessary below V_{tn} to keep the SOEC's temperature constant due to the endothermic operation. When $V_{SOC} = V_{tn}$, $\epsilon_{el} = 1$ and the SOEC is thermally stable if it is perfectly insulated; ϵ_{el} then decreases with increasing V_{SOC} as the SOEC is operated exothermically.

In fuel cell operation, the numerator and denominator of equations (1.15) and (1.16) have to be inverted as the desired product is electricity. As operation in fuel cell mode can only be exothermic, $\epsilon_{el} < 1$.

1.4 SOEC degradation

The longterm degradation of an SOEC is mostly related to an increase of the ohmic losses [64–68]. The degradation observed in electrolysis mode is usually higher than in fuel cell mode [57, 69], and the degradation rate tends to increase as the current density rises [70, 71] and as the temperature is lowered [69, 72]. Also, degradation during co-electrolysis (electrolysis of a $\text{CO}_2/\text{H}_2\text{O}$ mixture) is often more severe than in electrolysis (only H_2O) operation [71]. Ebbesen et al. [73] observed that by cleaning the inlet gases the degradation can be extensively reduced, indicating that impurities are a key parameters for SOEC durability. Interestingly, the performance of an SOEC can be partially recovered if it is alternately operated in fuel cell and electrolysis mode [74–76]. Reversible SOCs are thus very promising for grid balancing applications [76].

Locally resolved electrochemical impedance (EI) measurements, have shown that SOC degradation is a local phenomenon [77]. Microstructural observations performed on specimens sampled from different SOC locations (e.g., gas inlet, and outlet) also a different evolution from the initial microstructure which is generally more severe at the inlet [78, 79].

Multiple processes can be responsible for the SOC's performance degradation that originate from physical and chemical modifications of the electrodes and the electrolyte [57, 80]. In the following sub-sections, the major degradation processes regarding commonly used SOEC materials are reviewed with respect to their location: H_2 -electrode, electrolyte, or O_2 -electrode.

1.4.1 H_2 -electrode

Most commonly, the H_2 -electrode is a cermet composed of a mixture of NiO and ZrO_2 stabilized in cubic form with about 8 % Y_2O_3 (YSZ) [81]. The nickel oxide is then reduced to metallic Ni for proper operation. This type of electrode is commonly referred to as Ni –YSZ. In this case, the mixed ionic-electronic conduction necessary to an electrode

is obtained by mixing a purely electronic (Ni) and a purely ionic (YSZ) conductor. A critical parameter that defines the electrochemical performance of such an electrode is the triple-phase boundary (TPB), which is a collection of the three dimensional lines where Ni, YSZ, and the reactant meet [82].

The degradation mechanisms of Ni–YSZ electrodes are generally related to the TPBs and most particularly to the Ni phase. During electrolysis operation, Ni is extremely mobile. Various researchers observed the depletion of Ni in the vicinity of the electrolyte [83, 84], the agglomeration or coarsening of Ni particles [84], a loss of percolation of the Ni network [85], and the detachment of Ni from YSZ [85]. Electrodes with larger Ni particles [86, 87] and operated at higher current density favored Ni mobility [83]. Hubert et al. [69] observed that the YSZ backbone is a key parameter of the Ni-network stability. The microstructural transformation extends to about $5\mu\text{m}$ from the electrolyte [78, 82, 88], which also corresponds to the electrochemically active thickness of the electrode [87]. Also, Ni depletion was found to be slightly more pronounced at the reactant and air inlet, possibly due to the higher local current density and steam content [78]

Chen et al. [83] and, later, Tao et al. [85] attributed the detachment of Ni particles and the percolation lost to the formation of ZrO_2 nanoparticles. Monaco et al. [87] suggested another mechanism related to an accumulation of vacancies, which destabilizes the Ni particles and is the precursor to the observed Ni depletion. Mogensen et al. [89] suggested that the detached particles are then less stable and could be transported as nickel hydroxyl compounds ($\text{Ni}(\text{OH})_x$). However, the volatilization of $\text{Ni}(\text{OH})_x$ is unlikely to be solely responsible for the extent of the observed Ni depletion and it was suggested that other volatile species form in the presence of external contaminants e.g., NiSH or NiPH_2 [90]. Recent observations, have led to the consideration of the electrowetting theory as the driving mechanism for Ni depletion [91]. As the wetting properties of Ni on YSZ are highly dependant on the local oxygen partial pressure, the modification of the dihedral angle between Ni and YSZ would then be responsible for the observed Ni mobility [91, 92].

Nickel catalysts are known for their susceptibility to coking, which may also occur in Ni-based H_2 -electrodes in the presence of carbonaceous species. Carbon deposition in a Ni–YSZ electrode has been observed during electrolysis of CO_2 [93] and has occurred in the presence of steam during the co-electrolysis of CO_2 and H_2O [94]. Substituting Ni with Cu or strontium-doped lanthanum chromo-manganite (LSCM) and YSZ with gadolinia-doped ceria (GDC) was found to be a promising solution to effectively reduce coking [95, 96].

Ni–YSZ electrodes are also sensitive to various contaminants such as sulphur, and silicon compounds, and tars, which mostly deteriorate the TPB. A detailed description of the effect of various contaminants is presented in chapter 2.

1.4.2 Electrolyte

The electrolyte material is often YSZ for its compatibility with Ni–YSZ electrode but also because of its good ionic conductivity and stability [97]. Depending on the air electrode, GDC is used as a barrier layer with YSZ to avoid any mixing/interaction and the formation of secondary phases. These interactions are discussed in section 1.4.3. An alternative to YSZ is scandia-stabilised zirconia (ScSZ), which is more expensive but also more conductive than YSZ [81].

During longterm operation, voids in the grains and at the grain boundaries of the YSZ electrolyte have been observed especially near the H₂-electrode for the former and near the GDC barrier layer for the latter [84, 88, 98]. The formation of pores in the grain likely originates from the kinetic demixing of the electrolyte [84, 98] whereas intergranular pore formation has been attributed to the buildup of a high local partial pressure of oxygen [99]. Intergranular pore formation may result in the formation and propagation of cracks within the electrolyte [100].

At the interface between the electrolyte and the barrier layer, a dense zone resulting from the inter diffusion between YSZ and GDC with SrZrO₃ inclusions is generally formed, which limits the transport of oxygen ions [84, 88, 98]. The strontium has been determined to originate from the O₂-electrode, which suggests that the GDC barrier layer is partially permeable.

1.4.3 O₂-electrode

The O₂-electrode is either composed of a mixed ionic-electronic conductor, generally lanthanum strontium cobalt ferrite (LSCF), or occasionally lanthanum strontium cobaltite (LSC) or lanthanum strontium ferrite (LSF), or a composite made of an electronic and an ionic conductor, mostly lanthanum strontium manganite (LSM) mixed with YSZ, referred to as LSM–YSZ.

O₂-electrodes are prone to delamination when operated in electrolysis mode [57]. Often times, the O₂-electrode delamination does not extend to the entire electrode. Zheng et al. [79] observed that delamination of the air electrode occurred preferentially at the reactant and air inlet with LSM and LSC whereas LSCF showed no sign of delamination. Schefold et al. [67] observed local delamination of the LSCF O₂-electrode after 23000 h of operation, which was attributed to longterm operation and related to local inhomogeneities originating from the manufacturing, or due to local operating conditions (e.g., higher current density). The mechanism behind O₂-electrode delamination is generally attributed to the build up of oxygen pressure due to a limited oxygen flux at the O₂-electrode [101]. Increased polarization or reduced electrochemical activity of the O₂-electrode thus increases the risk of delamination [102].

A major issue with LSCF is its chemical incompatibility with YSZ, leading to the formation of a SrZrO_3 or $\text{La}_2\text{Zr}_2\text{O}_7$ insulating phase [103]. A well-established coping strategy is the addition of a dense GDC barrier layer to avoid direct contact between LSCF and the YSZ electrolyte [104, 105]. Even with a barrier layer, SrZrO_3 has been found in pristine cells, indicating that SrZrO_3 formation occurs before operation and is promoted by the high sintering temperature [88]. More additional buildup of SrZrO_3 is then formed during electrolysis than fuel cell operation [106]. The presence of SrZrO_3 has also been linked to a higher risk of delamination [107].

The O_2 -electrode degradation is also often related to contaminants. Chromium evaporated from metallic components can interact with LSM and LSCF based O_2 -electrodes and deposit as SrCrO_4 or Cr_2O_3 [108, 109]. Boron can evaporate from boro-silicate glass sealing and form lanthanum borates when interacting with LSM, which then decomposes the electrode, reducing its activity and promoting delamination [110]. Boron has a similar effect on LSCF and leads to the decomposition of the electrode by forming LaBO_3 [111]. LSCF and LSM can also react with S compounds to form SrSO_4 [112, 113]. Kushi [114] observed a concentration of S at the interface between the LSCF O_2 -electrode and the electrolyte in electrolysis mode whereas it was almost homogeneously distributed after fuel cell operation, suggesting that SOECs are more sensitive to the presence of S-compounds. The high concentration of S at the electrode–electrolyte interface is due to the preferential formation of SrSO_4 where the partial pressure of oxygen is high. The formation of SrSO_4 accelerates the delamination of the LSM electrode by reducing the electrochemical activity of the O_2 -electrode, likely allowing for the buildup of a high oxygen partial pressure at the interface with the electrolyte. Silicon compounds can form a thin continuous insulating layer on top of the air electrode but the effect is likely less important than that of sulphur [113].

In general, LSCF O_2 -electrodes are more stable than LSM–YSZ electrodes, but this may only be related to the additional GDC barrier layer needed with LSCF [100].

1.5 Characterization methods

Degradation in a SOC is generally defined as an increase (SOEC) or decrease (SOFC) of the cell voltage at constant current and is usually expressed as mVkh^{-1} or $\%\text{kh}^{-1}$. Despite its relevance in terms of performance quantification, the degradation rate defined in this manner does not provide detailed information on the underlying mechanisms. Multiple methods have been used to get a better insight into the degradation mechanisms occurring in SOCs and are briefly presented in this section.

1.5.1 Current–voltage characterization

The simplest characterization method consists of recording the cell voltage (V_{SOC}) or current density (J) while linearly modulating J or V_{SOC} , respectively. This gives a J – V curve, as presented schematically in Figure 1.3 for electrolysis operation. Three regions can be defined where specific over-potential dominates: at low current density, activation losses dominate; as the current density increases, ohmic losses take over; and when the current density becomes high, performances are limited by the low concentration of reactant on active sites, due to diffusion limitations.

In this thesis, reactant is used as a generic term to refer to the flow on the H_2 -electrode, which is then used independently on whether the SOC is operated in fuel cell or electrolysis mode. The reactant utilization corresponds to the ratio of the electrochemically converted species, \dot{N}_{Far} , to the reactive species that enter the SOC, \dot{N}_{react} , as expressed by equation (1.17). The \dot{N}_{Far} can be computed using Faraday's law as expressed by equation (1.18), where i_{tot} is the applied current. The \dot{N}_{react} corresponds to the molar flow rate of reactive species, i.e., that can be electrochemically converted, which thus depends on the reactant composition and the operating mode of the SOC. In electrolysis mode the reactive species includes H_2O and CO_2 , whereas in fuel cell mode they are usually H_2 and CO . A $RU = 1$ indicates that the totality of the reactant has been converted.

$$RU = \frac{\dot{N}_{Far}}{\dot{N}_{react}} \quad (1.17)$$

$$\dot{N}_{Far} = \frac{i_{tot}}{zF} \quad (1.18)$$

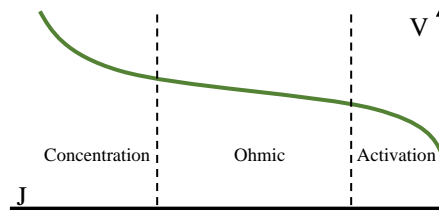


Figure 1.3 – Typical current density–voltage (J – V) curve for a solid oxide electrolysis cell (SOEC). Regions where activation, ohmic, or concentration losses dominate are highlighted.

A more informative method is electrochemical impedance spectroscopy (EIS) [115]. This method comprises computing the complex impedance of the electrochemical system at different frequencies. Under a constant bias, a small sinusoidal current excitation, typically around $10\text{--}40\text{ mA/cm}^2$, is applied to the cell. The voltage and current responses are recorded simultaneously for multiple excitation frequencies usually ranging from tens of millihertz to hundreds of kilohertz. The perturbation is assumed to be small enough so

that the relation between the current and the voltage is linear. The impedance Z of the system is computed for each frequency:

$$Z(\omega) = \hat{V}_{SOC}(\omega) / \hat{I}(\omega), \quad (1.19)$$

where $\hat{V}_{SOC}(\omega)$ and $\hat{I}(\omega)$ are the Fourier transform of the voltage and the current, respectively, recorded in the time domain, and Z is the complex impedance that can be represented in polar coordinates by the phase ϕ and the amplitude $\|Z\|$. To compare different SOC geometries, it is usual to use the current density rather than the current and thus multiply Z by the SOC active area.

The phase ϕ gives information on the nature of the impedance:

Inductive: $\phi > 0$

Resistive: $\phi = 0$

Capacitive: $\phi < 0$

Figure 1.4 shows a schematic Nyquist representation of the impedance response of a SOC where Z' and Z'' are the real and imaginary part of the complex impedance Z . The high- and low-frequency intercepts correspond to the serial (R_s) and total (R_{tot}) SOC resistance. The total cell resistance is often referred to as the area-specific resistance (ASR), which is expressed in Ωcm^2 and corresponds to the local slope of the j - V curve at the current density at which the EIS was taken. The serial resistance encompasses all of the ohmic-type contributions, which are mostly related to the electrolyte and the contact between the electrodes and the current collector. The difference between R_{tot} and R_s is the polarization resistance (R_p), which includes all of the electrochemical processes.

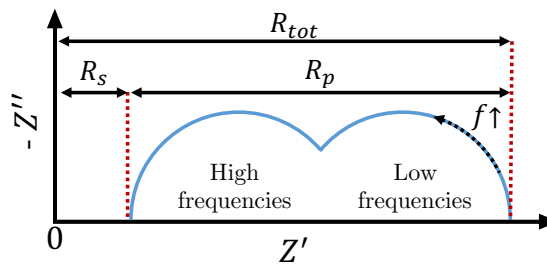


Figure 1.4 – Schematic representation of a typical impedance spectra of an SOC in a Nyquist diagram.

Based on the hypothesis that every process occurring in a fuel or electrolysis cell has a different time constant, two main methods are used to de-convolute the different contributions that compose the impedance spectra. The first is an equivalent electrical circuit (EEC), which consists of an electrical circuit defined *a priori* composed of ideal and

non-ideal elements fitted to the impedance measurement. The second is the distribution of relaxation time (DRT), which supposes an infinite number of parallel capacitors and resistors all connected in series [116]. Every capacitor–resistance subsystem has a different relaxation time. This infinite distribution of electrical elements is then discretized and fit to the impedance measurement by attributing a specific weight to each discrete element. The largest weights are then identified. Each of them is assumed to correspond to a distinct mechanism with an associated resistance and relaxation time (or frequency). EEC and DRT can also be conjugated to make the EEC method less arbitrary. The DRT results can be used to define the number of elements needed in the electric circuit and provide initial values as well as an additional quality criterion for the EEC fitting [117, 118].

The attribution of the correct process to the DRT peaks is not a trivial task and necessitates a vast sensitivity analysis [118]. Boukamp [119] derived an analytical solution of the DRT of a finite-length-Warburg element, which physically corresponds to the solution of a finite-length diffusion problem. The DRT of this process is composed of a main lobe accompanied by an infinite number of lower-amplitude side lobes at lower relaxation times. The secondary peaks could thus be erroneously attributed to a different process or overlap with other processes, making the interpretation of DRT difficult. Additionally, when two processes possess a relaxation time too similar, it can be impossible to deconvolute them [120].

1.5.2 Microstructure characterization

Electron microscopy is the most commonly used post-test analysis. Scanning electron microscopy (SEM) is a widely used method to characterize the micro-structure of SOCs [97–99, 121]. The sample preparation usually involves impregnating the sample in a resin, cutting the sample perpendicularly to the electrode–electrolyte layers to reveal all of the layers at once, polishing the sample to obtain a perfectly flat surface, and coating the sample with a conductive material (generally carbon) to avoid any charging effects during SEM observation. The last step is not always necessary as the charging effect can also be used advantageously to discriminate between percolated and non-percolated Ni [122]. SEM is commonly associated with energy dispersive X-ray microanalysis (EDX), provides detailed information on the local composition of the sample with a precision on the order of 1 at% [123]. As SEM is a destructive analysis method, a reference sample is needed to evaluate the micro structural evolution after operation.

SEM can be coupled with a focused ion beam (FIB), allowing for the 3D reconstruction of the microstructure and the precise evaluation of properties such as volume fraction of pores and electrode components, the tortuosity, the TPB length, or the dihedral angle between two phases [78, 91, 106, 124–126]. The 3D reconstruction procedure comprises taking a SEM image of the microstructure before removing a thin slice of material using an FIB. This process is then repeated until the desired sample size is reached. This method

remains still relatively local, as the typical volume is on the order of 1 to $50\mu\text{m}^3$ [127].

When a higher resolution is needed, transmission electron microscopy (TEM) can be used to reach resolutions lower than 0.5 nm [128]. Using TEM, The et al. [84] observed the presence of nano-sized pores in the YSZ electrolyte of two cells operated for 6100 and 9000 h, respectively, which would not have been seen otherwise. Combining TEM with EDX, they could precisely locate the presence of SrZrO_3 in the pores of the barrier layer between the O_2 -electrode and the electrolyte. TEM also provides the opportunity to analyze the diffraction patterns allowing to identify local crystal structures [88, 129].

SEM and TEM are generally performed at ambient temperature under a high vacuum, but a low-pressure atmosphere can be tolerated. Using an environmental TEM (ETEM), Jeangros et al. [130] observed in situ the reduction and oxidation of Ni particles from a Ni-YSZ electrode sample by switching between an O_2 and H_2 atmosphere at temperatures ranging from 250 °C to 500 °C. ETEM observations allowed them to attribute the activation of the NiO reduction to the transfer of oxygen to the YSZ backbone. Environmental SEM (ESEM) was used by Poitel et al. [131] to monitor the behavior of a CeCo interconnect protective coating. The time evolution of the grain growth was monitored bringing more understanding to the oxide formation and helped define areas of interest for more in-depth TEM observation.

1.5.3 Optical characterization

Optical methods such as raman spectroscopy, infrared spectroscopy, and thermal imaging are promising characterization techniques as they allow for in operando visualization of chemical and physical processes [132].

1.5.4 Raman and infrared spectroscopy

Raman spectroscopy provides local information on the composition, structure, and temperature of a material and potential adsorbate whereas infrared spectroscopy provides essentially the composition of surface and gas species [132, 133].

Raman spectroscopy applied to an operating SOFC has allowed the identification of YSZ temperature related structural modification which could then be used backward to evaluate the specimen temperature with a 25 °C accuracy [134]. Also, species bonded or deposited on the electrodes can be identified. Kirtley et al. [135] attributed a temperature-sensitive Raman peak to the presence of Ni- CH_x bonds (likely Ni- CH_2), shedding new lights on the CH_4 oxidation steps in Ni-YSZ electrodes. [136] observed the deposition of highly ordered carbon on an SOC H_2 -electrode when dry methane or methanol was used. In both cases, the deposition rate was similar at the beginning, suggesting that the

same deposition mechanism takes place. The Raman carbon signal saturated faster with methane than methanol, indicating that despite a similar kinetic the amount of deposited carbon depends on the reactant composition.

Raman spectroscopy is limited to superficial measurements due to the low penetration depth of the laser excitation (typically <50 nm) and may not allow for the visualization of the electrochemically active sites [135]. Using a specifically designed SOC composed of an optically transparent mono-crystalline YSZ electrolyte support (250 μm thick), Agarkov et al. [137] accessed the H_2 -electrode–electrolyte interface and monitored the kinetics of NiO reduction, thereby overcoming the laser depth limitation. In a later work, they added a GDC interlayer and investigated the GDC–YSZ interface [138]. They associated the increase of a specific Raman peak in function of the applied current to the deviation of the local chemical potential at the GDC–YSZ interface from its equilibrium value. The method was also extended to H_2 -electrode supported SOCs opening new opportunities for interfacial reaction investigations [139].

Fourier transform infrared spectroscopy (FTIR) generally requires an infrared light source; however, due to the high operating temperature, the SOC itself can be used as an infrared source. FTIR applied to an operating SOFC has clarified the intermediate species involved in electrochemical reactions. Using FTIR spectroscopy on an SOFC H_2 -electrode operated with CH_4 , Pomfret et al. [140] observed the presence of a $\text{CO}_{2,\text{ads}}$ intermediate on Ni–YSZ due to the oxidation of CH_4 . Lu et al. [141] used FTIR spectroscopy to investigate the gas/solid interaction of a samarium strontium cobaltite (SSC) O_2 -electrode. By varying the atmosphere composition and the SOC potential, two to three different di-oxygen species characterized by a specific wave number range were identified. By coupling FTIR with chronopotentiometry measurements, Kirtley et al. [135] could discriminate between carbon deposited near or far from active sites and evidenced a fuel dependency of the carbon deposition process.

1.5.5 Thermal/infrared imaging

Infrared thermography offers a high spatial and thermal resolution [142] that can be used to validate SOC models ([143], [144]), and identify anomalies such as inhomogeneities or delamination and monitor their evolution in real time [145]. The pictures in Figure 1.5 have been taken by Montanini et al. [2] using an InSb camera (81920 pixels) sensitive to mid-wave infrared (MWIR) spectrum. They were able to identify a hot spot from which a crack originated and to monitor in real time the failure of a button-type cell with 2.5 cm^2 of active area.

Thanks to their high operating temperature, SOCs also emit light in the near- infrared (NIR) which can be measured and used to evaluate the sample temperature. The main advantages of using NIR instead of MWIR are lower cost and a higher spatial resolution.

Pomfret et al. [146] successfully monitored the cooling resulting from the nickel oxide reduction on the fuel electrode of a pellet-type SOC (1 mm thick electrode support of 2.5 cm diameter) using an Si-CCD camera. They achieved a temperature and spatial resolution of 0.1 K and 0.1 mm, respectively.

The infrared emitted by a material are not only dependent on its temperature but also on its emissivity. Infrared imaging can thus be used to detect changes in the chemical structure of a material. Using an Si-CCD camera with a resolution of 5 megapixels, Geller et al. [147] observed the reduction of ceria caused by the change in its emissivity with a spatial resolution of $10\mu\text{m}$. These results were then confirmed by near-ambient pressure X-ray photo-electron microscopy. Often, the emissivity of a material also depends on the temperature. Jasiński et al. [148] evaluated the temperature dependency of a Ni–YSZ H_2 -electrode emittance using a commercial 90 mm diameter SOC, which is the largest SOC ever used in thermal imaging. They observed a decrease in emittance from 0.66 to 0.46 as the SOC temperature was increased from 880 K to 1200 K. The emittance of a specimen can be locally different, which may lead to erroneous temperature evaluation. Tachikawa et al. [149] proposed a corrective method based on the simultaneous monitoring of NIR and visible light emissions. They successfully corrected in operando the local emittance variation caused by the deposition of carbon.

An SOC's thermal behavior is also dependant on the polarization and the reactant composition. When an SOC was polarized in fuel cell mode, Jasiński et al. [148] observed an inhomogeneous temperature increase of the SOC depending on the operating temperature and the radial position, thus demonstrating the potential of infrared imaging to spatially resolve the electrochemical behavior of an SOC. Cumming and Elder [143] compared the thermal behavior of an SOC during j - V measurements during the electrolysis of steam, a mixture of steam and CO_2 , and CO_2 . In the three cases, the temperature first decreased and then increased as the voltage and current increased, confirming the transition from endothermic to exothermic operation as the SOC voltage passes the thermoneutral voltage. The endothermic–exothermic transition occurred at different SOC voltages depending on the CO_2 content which is in agreement with thermodynamic predictions. The determination of the thermoneutral voltage using infrared imaging could thus be used to estimate the reactant composition.

Generally, a chemical reaction either releases (exothermic) or absorbs (endothermic) heat. This characteristic can be advantageously used to investigate catalytic reactions [133, 150, 151]. Kirtley et al. [152] demonstrated that the spatial distribution of the dry methane reforming reaction ($\text{CH}_4 + \text{CO}_2 \rightleftharpoons 2\text{CO} + 2\text{H}_2$) occurring in an SOFC fed by a mixture of CH_4 and CO_2 can be accurately mapped thanks to the cooling resulting from the endothermic nature of the reaction. Thermal imaging allows for both spatial and temporal monitoring of an SOC temperature field, which can then be related to the evolution of the local catalytic properties. Reeping et al. [153] observed a modification

Chapter 1. Introduction

of the SOC temperature when CH_3Cl was added to the reactant stream. The observed heating was attributed to the deactivation of the catalytic activity subsequent to the poisoning of the nickel site by chlorine resulting in a reduction of cooling from reforming reactions. Pomfret et al. [154] observed a larger performance degradation and regions with more intense cooling when an SOFC was run with dry ethanol compared with humidified ethanol. Post-mortem analysis of these cold regions showed that they were responsible for the larger degradation encountered by the SOFC.

Thermal gradients can generate an undesired level of mechanical stress that needs to be accurately estimated to avoid the mechanical failure of the SOC. Infrared thermal imaging has been successfully combined with synchrotron imaging by Robinson et al. [155], who showed that thermal gradients induce non-uniform thermal expansion and lead to an increased stress level when compared with linear thermal expansion models. Added to residual stresses from sintering and assembly, these thermal stresses may be critical and lead to the failure of the SOC [156].

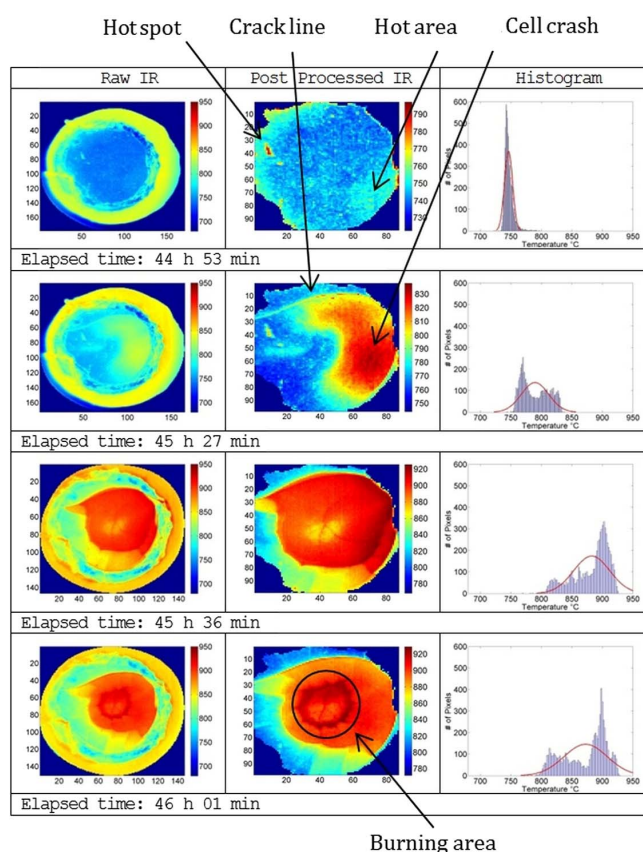


Figure 1.5 – Real-time monitoring of the formation of a crack originating from a hot spot and leading to complete cell failure . First column: raw thermal image, second column: emissivity corrected image, third column: pixel based temperature distribution. Reprinted with permission from [2] ©The Optical Society.

1.5.6 Active thermography

The infrared imaging techniques presented in section 1.5.5 are all passive methods; however, based on an extensive literature search, they represent the only thermography methods that have been applied to SOC. The sensitivity of thermography can, however, be greatly improved by using active thermography [144]. Active thermography consists of applying an external stimulus and measuring the thermal response of the system. Any region that has a different thermal behavior can then be identified. Additionally active thermography is usually less sensitive to emissivity variations, heating heterogeneities, reflections, and noise than passive thermography [157].

A wide variety of external stimulation sources that heat or cool the system can be used such as halogen lamps, lasers, heat guns, electrical currents, vibrations, or convective cooling [157]. The two main active thermography methods are pulse thermography (PT), in which the sample is excited by a pulse signal, and lock-in thermography (LT), in which the sample is excited by a periodic signal (generally a pulse train or a sine wave). Both methods can work either in transmission (source and camera on opposite side of the sample) or reflective (camera and heat source on the same side of the sample) mode.

Active thermal imaging has mainly been used as a non-destructive test for material inspection [158]. Extensive work has been performed on defect detection in composites such as honeycombs or fiber-reinforced polymers, especially in the aeronautical and naval industries [159–162]. Meola and Toscano [161] quantified the porosity in fiber-reinforced composite polymer using flash PT. Furthermore, delamination of layers and fiber orientation has also been observed. Lateral heat diffusion allows for the detection of defects smaller than the camera resolution. Using PT, Broberg [163] was able to detect 5 to 10 μm wide cracks using a camera with a spatial resolution of only 0.1–0.2 mm. Nevertheless, the maximum spatial resolution is limited by the wave length sensitivity of the camera sensor due to diffraction limits. Using an solid immersion lens or a shorter wavelength sensor offers the possibility go beyond this limitation and improve the spatial resolution.

Active thermography has been used in quality inspections of ceramic materials. Using LT on ceramic tiles, Calado et al. [164] determined the porosity of samples and identified delaminated areas. PT using a flash lamp has been used ex situ on SOC cells for quality control [165]. PT was found particularly effective for identifying delamination and can thus be used as complementary measurement to radiography and computed tomography for the control of SOC integrity.

Electrically driven systems can also be analyzed using active thermography. LT, has been used to detect defects in microelectronics. LT can increase the thermal sensitivity by a factor of 100 compared with passive measurements, allowing the visualization of weak

heat sources (≤ 1 mW of dissipated power) [166, 167]. Schmidt et al. [167] identified two hot spots when performing LT with a current excitation on micro-electronic devices that they attributed to the presence of short-circuits. SEM analysis confirmed the presence of the two short-circuits which were caused by a $20\mu\text{m}$ aluminium particle and an incompletely etched element (about $1\mu\text{m}$ wide). Furthermore, they demonstrated that the depth of a defect can be estimated by analyzing the phase shift between the current excitation and the thermal response.

Active thermography can be used to determine local electrical and electrochemical properties of energy conversion devices. By mapping the local j - V characteristic of a photovoltaic cell using LT, Breitenstein [168] effectively discriminated heat sources originating from the diffusion (electron/hole flux through the p-n junction) or recombination (electron-hole recombination in the depletion region) current and reconstructed the spatial distribution of the two processes. In their later work, they demonstrated that the local efficiency and saturation current at the grain boundaries can also be determined using LT [169, 170]. LT has also been applied to investigate the degradation of a Li-ion pouch cell, where comparison between LT measurements taken before and after the aging process showed a modification of the local thermal behavior that was attributable to the formation of gas pockets [171]. Using LT to diagnose a solid-state battery after break down, Sulas et al. [172] precisely localized a point heat source, attributable to the formation of dendrites in the solid electrolyte. LT has been found useful for identifying weak design features and thus provides valuable insights for the optimization the solid-state battery.

LT has been used to investigate PEM fuel cells, with different methods to generate the thermal excitation signals. Engebretsen et al. [173] has proposed the use of electro-thermal impedance spectroscopy (ETIS) to characterize an operating PEM fuel cell. This method consists of applying a sinusoidal current at various frequencies and monitoring the thermal response of the fuel cell. The amplitude ratio and phase shift between the current perturbation and thermal response is then computed. Using ETIS allowed for the compensation of steady state artifacts e.g., the narcissus effect, as well as emissivity non-homogeneity, which are a recurrent issue in steady-state thermographic measurements. Rasha et al. [3] used a Peltier element to generate a sinusoidal heat perturbation at the back of the PEM sample while the camera was located on the opposite site. They observed the water distribution inside the channel at various operating conditions and at different depths by modifying the excitation frequency, even without an optical access, thus demonstrating the capability LT to spot sub-surface features. As an illustration, the results of one LT measurement taken by Rasha et al. [3] on a PEM fuel cell, with a serpentine flow field are presented in Figure 1.6. The thermogram presented in Figure 1.6a is the steady state temperature field, which is rather blurry likely due to the lateral heat diffusion in the end plates. The ampligram shown in Figure 1.6 (b) corresponds to the local amplitude of the thermal response. Regions of higher and lower amplitude reflecting

heat transfer inhomogeneities can be identified. Figure 1.6 (c) corresponds to the phase shift between the thermal response of the PEM active area and the surroundings. The presence of liquid water in the channel increases the thermal conductivity, leading to a negative phase shift. Red and yellow areas thus corresponds to the presence of water in the channel. The channel (dark) and land (green) area can also be distinguished.

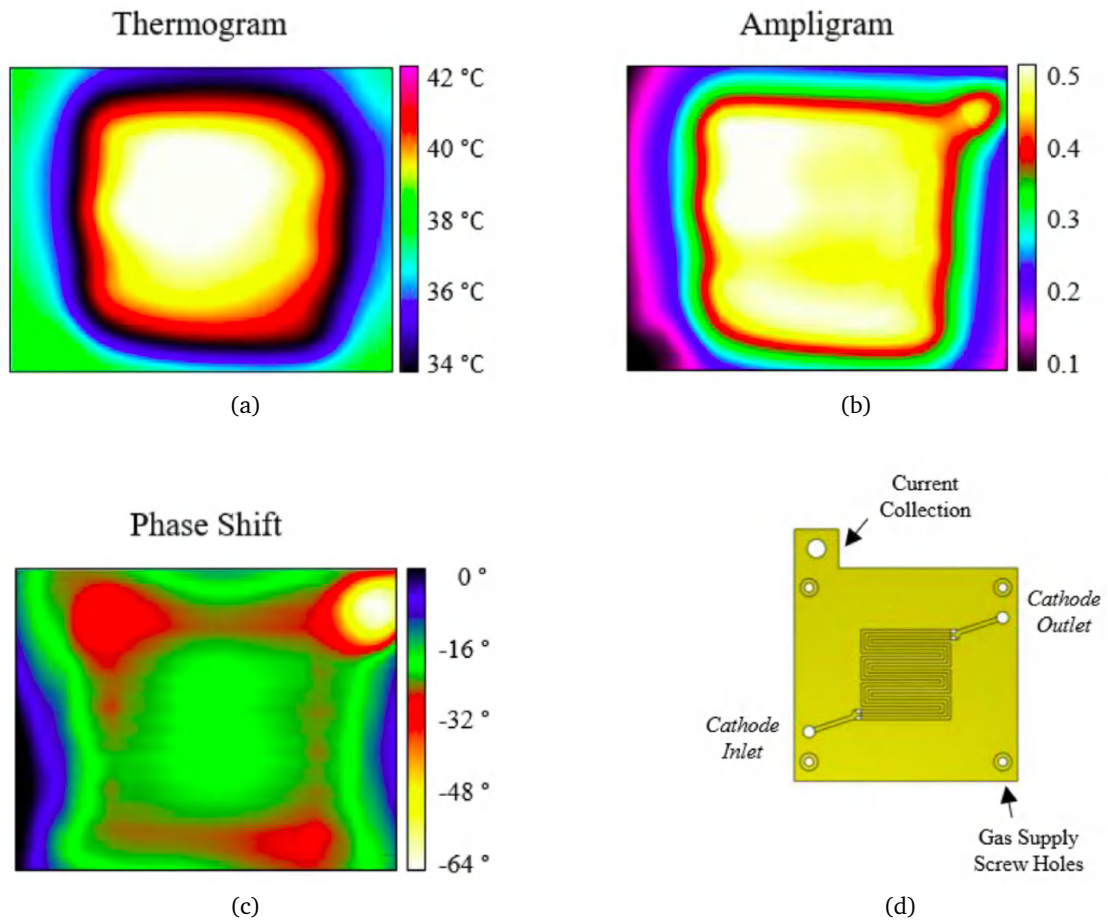


Figure 1.6 – LT measurements on a PEM fuel cell taken at a polarization of 0.1 Acm^{-2} with an excitation frequency of 0.07 Hz. The thermogram (a) represents the steady state temperature field, the ampligram is the amplitude of the sinusoidal temperature evolution (b), and the phase shift (c) is the phase difference between the current sent to the peltier element and the temperature response. Reprinted with permission [3] .

1.6 Thesis objectives

This thesis is based on two central observations made on the available literature.

Observation 1 *The effect of impurities in the reactant stream is very well documented in fuel cell mode but it is rather sparse for electrolysis operation despite evidence of a potentially higher sensitivity.*

Part I of this thesis addresses the following research questions:

- To which impurities are an SOECs the most likely to be confronted with?
- What are the effects of impurities on the performance and durability of an SOEC?
- Are SOECs more or less tolerant to impurities than SOFCs?

Observation 2 *The degradation/performance of an SOC is not spatially homogeneous but "classical" in-situ characterization methods (i.e., EIS and J–V) do not address it properly.*

Part II of this thesis addresses the following research questions:

- Can active thermography be used to evaluate in operando the local performances of an SOC at a global scale?
- Can active thermography be used to monitor the degradation of an SOC, e.g., in the presence of impurities ?

Answers to these questions will allow for more targeted and finer investigations of SOECs and help bring them a step closer to market readiness. The outcomes and outlooks arising from the research performed in this Thesis are presented in Chapter 10.

PART

I

H₂-ELECTRODE POISONING

CHAPTER 2

Literature Review

This chapter aims to detail the potential impurities in the CO₂ stream that may be detrimental to the performance and durability of an SOEC. The impurities present in CO₂ captured from various sources are identified; the effects of a multitude of contaminants on a Ni-based H₂-electrode of an SOC are then reviewed. Due to the lack of literature on the effects of various contaminants on SOECs, the results obtained on SOFCs are used to evaluate the potential threats of various chemical species on SOECs with a special focus on Ni-YSZ H₂-electrodes. This assumption is justified as the sensitivity of SOCs to impurities is likely higher when operated in electrolysis compared with fuel cell mode due to a driving force oriented towards the TPBs [73]. The possible poisoning compounds present in the CO₂ stream are then identified and two are selected for experimental testing.

Section 2.2.1 contains part of the introduction published in Jeanmonod et al. [174].

Contributions to the Field

Determined the main chemical species that can affect a Ni-containing H₂-electrode and thus threaten the lifetime and performance of an SOC operated in co-electrolysis.

2.1 Impurities in CO₂ sources

The CO₂ necessary for PtM or PtL can be extracted from fossil power plants, industrial processes (e.g., cement plants), biomass conversion plants (e.g., biogas or ethanol production), or directly from the air [47].

Last and Schmick [8] provided a list of the wide variety of possible impurities (excluding air compounds and water) that can be present in captured CO₂ from various sources and is reported in Table 2.2. Sulfur and organic compounds are present in every sources in one or multiple forms. This table is not exhaustive; Apps [175] reported finding 30 elements present in flue gases from coal-fired power plants, apart from carbon,

including various metals (Cd, Co, Cr, Cu, Ga, Hg, Mn, Mo, Ni, Pb, V, and Zn), halogens (Cl and F), metalloids (As, B, Ge, and Sb), and non-metals (O, N, S, P, and Se). Volatile organic compounds (e.g., benzene, phenol, toluene, and naphthalene) can potentially be present in captured CO₂ at concentrations below 1 ppmw [175].

Porter et al. [10] provided a detailed overview of the quantity of various impurities present in a CO₂ stream from pre- and post-combustion CC from coal power plants as well as from a few other industrial plants. These data are combined with those reported by Lee et al. [11], Last and Schmick [8], and Lepaumier et al. [176] in Table 2.5. The main impurity in captured CO₂ is generally N₂, except in the case of oxyfuel combustion, where O₂ and Ar can be dominant. Other impurities include NO_x, sulfur compounds, H₂O, CO, hydrocarbons, various metals, chlorine compounds, and NH₃, all ranging from 0 to 1000 ppm.

The use of biogenic CO₂ for PtG applications is particularly attractive as it can close the carbon cycle and significantly reduce the emissions of greenhouse gases (GHG) [177]. Reiter and Lindorfer [47] found that biogas upgrading and bioethanol production were the most suitable CO₂ source for PtG due to their biogenic origins and limited capture costs. Injecting biogas into the natural gas grid requires prior upgrading of the biogas, which is usually performed by CO₂ capture [178]. The typical composition of the biogas is presented in Table 2.1, but these values are highly dependant on the type of biomass used [7]; further, few researchers have investigated the composition of CO₂ captured from biogenic sources. Various solvents used for CO₂ capture can remove sulfur compounds [179], suggesting that traces of any compounds in Table 2.1 could potentially be found in the captured CO₂. The extraction of CO₂ can actually concentrate impurities in the CO₂ stream. Lee et al. [11] estimated that even after reducing the SO₂ concentration in the flue gases below 10 ppm, 34 to 135 ppm could be found in the CO₂ stream.

2.2 Literature on SOC contaminants

The effects of various impurities on the lifetime and performance of SOFCs have been studied extensively, notably in the frame of using coal syngas [180, 181] or biomass-derived chemicals [182, 183] as a potential fuel. A summary of the major impurities found in literature and their effects on Ni-based SOFC's H₂-electrode is reported in Table 2.9; more details are presented in the following sections. This literature review is focused on Ni-YSZ electrodes.

Table 2.1 – Typical biogas composition [7]

	mol%		ppm(mol)
CH ₄	50–60	H ₂ S	20–850
CO ₂	40–50	Terpenes	0–500
H ₂ O	1–7	NH ₃	0–308
N ₂	1–3	C ₆ H ₆ , C ₇ H ₈ , C ₈ H ₁₀	0–7
H ₂	0.1–1.5	Cl-compounds	0.1–5
CO	0–1	F-compounds	0–1.5
O ₂	0.1–0.5	D4 ^a , D5 ^b	0.1–0.5
		HCN	0–0.003

^a Octamethylcyclotetrasiloxane.

^b Decamethylcyclopentasiloxane.

Table 2.2 – Generic impurities likely to be found in a captured CO₂ stream from various sources [8]

	Combustion	Wells / Geothermal	Fermentation	Hydrogen/ Ammonia production	Phosphate rock processing	Coal gasification	Ethylene oxide production	Acid neutralization processes
Aldehydes	•	•	•	•		•	•	
Amines	•			•				
Benzene	•	•	•	•		•	•	•
CO	•	•	•	•	•	•	•	•
COS		•	•	•	•	•		•
Cyclopathic hydrocarbons	•	•		•		•	•	
(CH ₃) ₂ S		•	•		•	•		•
Ethanol	•	•	•	•		•	•	
Ether		•	•	•		•	•	
Ethyl acetate		•	•			•	•	
Ethyl benzene		•		•		•	•	
Ethylene oxide						•	•	
Halocarbons	•					•	•	
Hydrogen cyanide	•					•		
Hydrogen sulfide	•	•	•	•	•	•	•	•
Ketones	•	•	•	•		•	•	
Mercaptans	•	•	•	•	•	•	•	
Mercury	•					•		
Nitrogen oxide	•		•	•		•	•	•
Phosphine					•			
Radon		•			•			•
Sulfur dioxide	•	•	•	•	•	•		•
Toluene		•	•	•		•	•	
Vinyle chloride	•					•	•	
Volatile hydrocarbons	•	•	•	•		•	•	
Xylene		•	•	•		•	•	

Table 2.3 – Captured CO₂ composition from various sources. Data are compiled from [8–11].

		Oxyfuel combustion	Pre-combustion	Post-combustion					
		Coal	Coal	Coal	Refinery stack	Cement plant	Cement kiln ^f	Coke production ^f	Lime production ^f
CO ₂	vol%	74.8 – > 99.9	95 – > 99	99.7 – 99.8	99.6	99.8	99	99.4	99.52
N ₂	vol%	Trace – 15.49	0.0195 – < 1	0.045 ^c – 0.18	0.29	0.0893			
O ₂	vol%	0.001 – 6		0.0061 – 0.015	0.0035	0.0035			
Ar	vol%	Trace – 5	0.0001 – 0.15	22 – 210	0.0011	0.00011			
NO _x	ppmv	0 – 2500	400	1.5 – 50	2.5	0.86	3187 ^f	1616	1056
SO ₂	ppmv	0 – 29000	25 – 50	< 0.1 – 1652 ^{e,f}	1.3	< 0.1	3033 ^f	2083	1169
SO ₃	ppmv	0.1 – 20		10 ^d – 318 ^{e,f}					55
H ₂ S	ppmv		0.2 – 34000						
H ₂ O	ppmv	0 – 1000	0.1 – 600	100 – 640	640	640			
CO	ppmv	< 2 – 162	0 – 2000	10	1.2	1.2	2517	1100	3143
H ₂	ppmv		20 – 30000						
CH ₄	ppmv		0 – 112					566	
Cl ^a	ppmv		17.5	0.85 – 515	0.41	0.41	80.3	32.76	
Hg	ppmv	3.5e ⁻⁷ – 1e ⁻⁴	6.8e ⁻⁷ – 2.2e ⁻³	6.9e ⁻⁴ – 2.8e ⁻³		7.3e ⁻⁴	5.5e ⁻²		
As	ppmv	2.9e ⁻⁷	0.0033–0.01	0.0022 – 0.0055	0.29	0.0029			
Se	ppmv	1e ⁻³ – 7.4e ⁻³	0.01 – 0.0244	0.0122 – 0.017	1.2	0.0088			
Ni	ppmv		0.009	0.002					
Mn	ppmv			0.0309					
Pb	ppmv		0.0045	0.0011					
OC ^b	ppmv		0.0148	0.0202			81 ^g	196.2 ^g	

^a Used to refer to any Cl compounds in literature but mostly found in the form of HCl.

^b Various type of volatile organic compounds, including benzene, toluene, and naphthalene.

^c Includes Ar.

^d Includes SO₂.

^e Theoretical value estimated by [11].

^f Data from [8] converted from ppmw to ppmv assuming ideal gas behavior and that the molar weight of the CO₂ containing stream is the one from CO₂.

^g In ppmw.

2.2.1 Sulfur compounds

Sulfur has a known affinity for nickel and tends to be chemisorbed on Ni or even forms nickel sulfide, depending on the sulfur concentration, leading to the deactivation of Ni's catalytic properties [184, 185]. The vulnerability of Ni-based SOFC anodes towards various sulfur compounds such as C_4H_4S [183], CH_3SH , COS [186], and especially H_2S [187–190] is well documented. A selection of relevant publications on sulfur poisoning, including the involved experimental conditions and main conclusions, is reported in Table 2.4.

Sulfur has been found to impact the electrochemical performance of SOFCs by reducing the catalytic reactions, such as the steam methane reforming (SMR, (2.1)) and the reverse water–gas shift reaction (RSWG, (2.2)) [191, 192], and by limiting the charge transfer processes at the triple phase boundary (TPB) [193–195].



Thermodynamic computations show that nickel sulfide ($Ni_3S_2(l)$) only forms at H_2S concentrations greater than 1 %; at lower H_2S concentrations, the adsorption of sulfur on nickel is preferred [189, 196]. The adsorption process can be described as:



where S_{ad} represents the sulfur adsorbed on nickel. Generally, when the sulfur supply is cut, the SOFC performance recovers partially or completely [190, 197]. Furthermore, the behavior during poisoning and recovery is dependant on the operating conditions. Generally, an increase of the operating temperature [187] or current density [190] improves the SOFC's tolerance to sulfur, whereas an increase of the sulfur concentration [187, 197, 198] and the presence of CO/CO_2 as reactant instead of solely H_2/H_2O [199] were found to reduce the sulfur tolerance. Although H_2S is the most commonly used compound for sulfur tolerance experiments on SOFCs, Jablonski et al. [192] observed a higher rate of deactivation when a nickel catalyst was exposed to SO_2 rather than H_2S , suggesting that the sulfur species may have a direct impact on a SOFC's tolerance to sulfur. A similar impact on the initial voltage drop has been reported when using sulfur compounds other than H_2S , suggesting that sulfur compounds tend to decompose into H_2S , as it is favored thermodynamically [186, 200]. Furthermore, Madi et al. [201] observed a similar behavior for H_2S and C_4H_4S and reported that the same relationship (developed by Hansen [202]) holds between the Ni surface coverage by sulfur and the initial voltage drop for H_2S and C_4H_4S . In the longer term, the SOC tolerance

to sulfur may be dependent on the sulfur compound, as reported by Haga et al. [186] who observed a larger degradation when the SOC was exposed to CH_3SH rather than H_2S .

Few researchers have investigated the effects of impurities on SOECs. Of these, Kushi [114] found that an SOC's O_2 electrode was more sensitive to SO_2 under electrolysis than under fuel cell operation. Zheng et al. [203] investigated the effect of SO_2 on a composite LSCM and GDC H_2 -electrode during electrolysis of simulated flue gases. No significant impact on the SOEC performance was reported below 15 ppm of SO_2 ; electrolysis activity even improved when O_2 was also present. Ebbesen et al. [73] mitigated the degradation of an SOEC, composed of an Ni-YSZ H_2 -electrode by cleaning the inlet gases. The degradation observed without the gas cleaning device was thus attributed to the presence of impurities in the inlet gases. H_2S was found in the ppb level in the supply gases (without the gas cleaning device), but the role of H_2S in the degradation was not clearly assessed. Skafte et al. [204] found that 5 to 20 ppb of H_2S were sufficient to drastically degrade the performance of the Ni-YSZ H_2 -electrode of an SOEC operated with a CO/CO_2 mixture. When the SOEC was exposed to 20 ppb of H_2S , it showed a sharp voltage increase when the thermoneutral voltage was reached. When H_2S was removed, the SOC never recovered but the degradation decreased. The drastic voltage increase was hypothetically attributed to coking.

2.2.2 Chlorine compounds

The effect of chlorine on an SOFC's Ni cermet electrode has been widely studied using various compounds ranging from simple diatomic molecules, such as Cl_2 [205, 206] or HCl [181, 197, 205–215], to more complex molecules containing carbon atoms, such as CH_3Cl [206, 213, 216], and $\text{C}_2\text{H}_3\text{Cl}$ [206]. A summary of relevant experimental investigations with their relevant conclusions is presented in Table 2.5.

When chlorine is added to the fuel stream, a sudden drop of the SOFC performances has been generally observed, followed by either continuously degrading or constant performances [206, 208]. Even though this behavior is similar to sulfur poisoning, higher chlorine concentration can be tolerated by the SOFC; a negligible to modest impact has been reported up to a concentration of 50 ppm [207, 211, 213] and substantial degradation tends to occur only above 100 ppm [205, 215]. When chlorine is removed from the fuel stream, the cell recovery potential is dependant on the chlorine concentration to which the cell was exposed. Marina et al. [208] observed a completely reversible degradation with 50 ppm of HCl in simulated coal syngas. Madi et al. [215] observed a partial recovery of SOFC performances after stopping the HCl exposure, given that the HCl content was lower than 200 ppmv. At higher concentrations, the SOFC performances continued to degrade even in a Cl -free atmosphere. EIS measurements have shown that the charge transfer [214, 215] and gas conversion impedances [206, 215] are both affected by chlorine, but only the gas conversion impedance recovers [215].

Table 2.4 – Summarized literature review on sulfur poisoning

Reference	HE	T °C	Impurity ppm	Duration			Fuel mixture				Observations
				≤ 100 h	100–500 h	> 500 h	H ₂	H ₂ O	CO _x	C _x H _y	
Matsuzaki and Yasuda [187]	Ni–YSZ	800 to 1000	H ₂ S	0.05 to 15	•		•	•			Sulfur poisoning was fully reversible Increasing the operating temperature greatly improves the tolerance
Xia and Birss [220]	Ni–YSZ	800	H ₂ S	10	•		•	•			Increasing the current density reduces the tolerance Exposition of the H ₂ -electrode to air improves the recovery potential
Sasaki et al. [189]	Ni–YSZ or Ni–ScSZ	850 to 1000	H ₂ S	0 to 20	•		•	•	•		The degradation induced by sulfur is composed of an initial step degradation followed by a metastable voltage evolution. Increasing the H ₂ S concentration, decreasing the temperature and/or the H ₂ /CO ratio, and using YSZ rather than ScSZ reduces the tolerance.
Zha et al. [190]	Ni–YSZ	700 to 900	H ₂ S	0.18 to 50	•		•	•			Higher operating temperature and current density improves the SOFC tolerance and accelerates the recovery process. Adsorbed sulfur is likely electrochemically oxidized during recovery.
Cheng et al. [221]	Ni–YSZ	800	H ₂ S	<0.05 to 10	•		•				Galvanostatic or potentiostatic operation has no influence on the tolerance but a higher current density is beneficial.
Rasmussen and Hagen [193]	Ni–YSZ	850	H ₂ S	2 to 100		•	•	•			Sulfur is chemisorbed on Ni progressively from the inlet to the outlet. Sulfur-induced degradation is reversible and the initial voltage drop became saturated around 40 ppm.
Li et al. [180]	Ni–YSZ	800	H ₂ S	12.5	•		•	•	•		Addition of CO, CO ₂ , and H ₂ O increases the effect of H ₂ S, but CO ₂ , and H ₂ O likely improve the recovery.
Hagen et al. [222]	Ni–YSZ or Ni–ScYSZ	850	H ₂ S	2 to 24		•	•	•		•	The deactivation of the SMR reaction was similar for Ni–YSZ and Ni–ScYSZ. The Ni–YSZ electrode continuously deteriorates when exposed to 2 ppm of H ₂ S due to the loss of Ni percolation, whereas the performances of the Ni–ScYSZ electrode remained almost constant with up to 10 ppm of H ₂ S.
Kromp et al. [195]	Ni–YSZ	800	H ₂ S	0.1 to 0.5	•		•	•	•		The polarization remained stable during 100 h with 0.1 ppm but doubled when the H ₂ S concentration was increased to 0.5 ppm DRT analysis showed that sulfur limited the the WGS reaction and the electrochemical oxidation of the fuel.
Hagen [199]	Ni–YSZ	750 850	H ₂ S	2 to 92	•		•	•	•		The electrochemical oxidation of H ₂ is less impacted than the WGS reaction A greater poisoning effect is present at lower temperature.
Hauch et al. [223]	Ni–YSZ or Ni–ScYSZ	850	H ₂ S	2		•	•	•		•	The overpotential plays a key role on sulfur tolerance independently of the electrode material. Irreversible long-term degradation is likely triggered by the combination of a high local O ₂ partial pressure and continuous supply of sulfur.
Madi et al. [183]	Ni–YSZ	700 750	C ₄ H ₄ S	1 to 15	•		•		•		Thiophene concentration above 1 ppm increased the degradation at 700 °C but not at 750 °C. The performance slightly improves at the beginning of the exposure due to the reforming of thiophene which increases the H ₂ and CO concentration.

Haga et al. [205] attributed the partial recovery of the SOFC to reversibly adsorbed Cl on Ni; irreversible degradation was attributed to the formation of NiCl_2 , which possesses a lower melting point than Ni, subsequent sublimation of NiCl_2 , and redistribution of Ni. Post-test microstructural composition analysis using EDS [208, 214], XRD [209, 214], XPS [209], and AES [208] on SOFCs exposed to 20 to 160 ppm of HCl showed no evidence of a solid phase containing chlorine. Furthermore, the formation of NiCl_2 is thermodynamically unfavored in SOFC operating conditions [208, 209, 213, 214]. The formation of NiCl_2 is thus unlikely to occur during Cl-poisoning. However, Xu et al. [209] claimed that adsorbed Cl may still lower the melting point and enhance the sublimation of Ni, leading to a long-term modification of the Ni particles, but to a lesser extent than what was reported by Haga et al. [205].

Adsorbed Cl on Ni can reduce its catalytic properties [217]. Using in-operando Raman spectroscopy, Reeping and Walker [218] observed a large amount of deposited carbon when a CH_4 mixture was used as a fuel. When 110 ppm CH_3Cl was added to the fuel gas mixture, the carbon deposition was completely suppressed, suggesting the deactivation of the catalytic activity of Ni. In later research, Reeping [219] observed that by adding 110 ppm of either HCl or CH_3Cl , carbon deposition mitigation was achieved more quickly when the fuel was pure methane rather than 50 % CH_4 /50 % CO_2 . This may support the hypothesis made by Madi et al. [215] suggesting the competitive adsorption of CO and Cl. Marina et al. [208] observed a saturation of the relative ASR increase at HCl concentration above 100 ppm of HCl, which they attributed to a coverage saturation. This further supports adsorption of chlorine compounds as the main degradation mechanism during chlorine exposure [214].

The form of the chlorine compounds influences the extent of the poisoning. Li et al. [206] investigated the effect of Cl_2 , HCl, CH_3Cl , and $\text{C}_2\text{H}_3\text{Cl}$ at concentrations below 10 ppm in H_2 in galvanostatic operation (0.25 A cm^{-2}). They observed that at 750 °C, the effect of chlorine compounds can be ranked as: $\text{Cl}_2 > \text{CH}_3\text{Cl} > \text{C}_2\text{H}_3\text{Cl} > \text{HCl}$. When the temperature was increased to 850 °C, CH_3Cl and $\text{C}_2\text{H}_3\text{Cl}$ became more detrimental than Cl_2 and the ranking was then: $\text{C}_2\text{H}_3\text{Cl} > \text{CH}_3\text{Cl} > \text{Cl}_2 > \text{HCl}$. Nevertheless, increasing the operating temperature generally mitigates the effect of chlorine poisoning [208, 211]. Haga et al. [205] observed that the poisoning effect of 100 ppm of Cl_2 was similar to that of 200 ppm of HCl in 3 %-humidified hydrogen at 800 °C. When comparing the impact of different chlorine compounds, the amount of Cl atoms per mole of compounds should thus also be considered. If the dissociative adsorption of Cl on Ni is considered, one mole of Cl_2 generates twice as much adsorbed Cl_{ad} than HCl as evidenced by (2.4) and (2.5).



An increase of the current density shows either no [181, 208, 214] or a detrimental [215, 219] effect on the chlorine-induced degradation.

2.2.3 Silicon compounds

The effects of silicon compounds have been mainly investigated in the frame of using biogas [207, 224] or coal-derived syngas [181] as fuel for an SOFC. The principal studies on the effect of Si-compounds and their main conclusions are reported in Table 2.6. Octamethylcyclotetrasiloxane (D4) [224], decamethylcyclopentasiloxane (D5) [186, 207] or tetraethyl orthosilicate (TEOS) [181] have been used as representative silicon compounds found in biogas or coal-derived syngas. In the presence of steam, they decompose into Si(OH)_4 (plus additional non-Si containing byproducts) that eventually deposit as SiO_2 , as:



which deteriorates the performances and can lead to the failure of the SOFC [186].

Using X-ray spectroscopy, Madi et al. [225] reported a gradient of deposited Si from the feed gas inlet to the outlet and from the current-collector–electrode interface to the electrode–electrolyte interface in both single cell and short-stack configurations. The authors suggested that Si deposits at the current-collector–electrode interface and is partially vaporized in the form of Si(OH)_4 , which is transported in gaseous phase in the porous H_2 -electrode towards the electrolyte. Kuramoto et al. [181] also reported a peak of Si at the current-collector–electrode interface, but found an additional peak between the electrode support and active region. They thus argued that Si is deposited in the form of SiO_2 and then reduced to SiO(g) that is transported in the electrode support and finally re-oxidized to SiO_2 in the vicinity of the TPBs.

The main impact of Si deposition is the limiting of the gas–solid reaction at the TPB that translates into an increase of the mid- to high-frequency region of the electrochemical impedance spectra [207, 225]. The degradation rate has been found to increase with the Si content [181, 207]. The evolution of the degradation rate with respect to the Si content is non-linear and shows signs of saturation as the concentration of Si increases [225].

A thorough literature search presented no publications on the effect of silicon-containing reactant feed on SOEC's H_2 -electrode, but Hauch et al. [226] observed the deposition of SiO_2 in the H_2 -electrode of an SOC operated in electrolysis despite the fact that clean gases were used. The presence of silica was attributed to the evaporation of Si(OH)_4 from the glass sealing, which deposited in the vicinity of the TPBs; in fuel cell operation, SiO_2 deposited mainly at the electrode surface. This difference in behavior was attributed

Table 2.5 – Summarized literature review on chlorine poisoning

Reference	HE	T °C	Impurity ppm	Duration			Fuel mixture				Observations
				≤ 100 h	100–500 h	> 500 h	H ₂	H ₂ O	CO _x	C _x H _y	
Buchinger et al. [211]	Ni-YSZ	750, 800	HCl	47.5	•		•	•	•	•	A higher temperature mitigates degradation.
Trembly et al. [214]	Ni-YSZ + Ni-GDC	800, 900	Cl ₂	20, 160	•		•	•	•		The ohmic and charge transfer resistance were impacted. No trace of a secondary Cl phase was found. The degradation was attributed to Cl adsorption. The current density has no effect.
Haga et al. [205]	Ni-ScSZ	800, 850	Cl ₂ , HCl	5 to 1000	•		•	•			A degradation was visible beginning at 5 ppm. Cl ₂ and HCl have comparable effects. The partial recovery was attributed to desorption of Cl. The permanent degradation was attributed to NiCl ₂ evaporation.
Marina et al. [208]	Ni-YSZ	650 to 850	HCl	50 to 800	•		•	•	•		Chlorine poisoning is reversible. A higher temperature is beneficial but the current density shows no effect. A saturation is reached at 100 ppm. No evidence of a Cl phase.
Li et al. [206]	Ni-YSZ	750, 850	Cl ₂ , HCl, CH ₃ Cl, C ₂ H ₃ Cl	<10	•		•				Chlorine poisoning mainly affects low-frequency impedance (<10 Hz). Temperature increase has a positive impact on the degradation rate for diatomic Cl compounds and negative impact for more complex compounds.
Li et al. [228]	Ni-YSZ	750, 850	CH ₃ Cl	10 to 30	•		•	•	•		A visible degradation occurs from 10 ppm at 850 °C, whereas the performances remained stable at 750 °C. The degradation is higher when using coal syngas rather than H ₂ .
Reeping and Walker [218]	Ni-YSZ + Ni-GDC	650	CH ₃ Cl	110	•	•				•	Presence of CH ₃ Cl eliminates carbon deposition. Degradation is observed only with pure CH ₄ but not with H ₂ .
Madi et al. [215]	Ni-YSZ	750	HCl	1 to 1000	•		•	•	•	•	A partial recovery is observed only below 200 ppm. Increasing the current density is detrimental. The TPBs and the fuel conversion are impacted, but only the latter recovers. The lower degradation observed in syngas is attributed to competitive adsorption of Cl and CO on Ni.
Kuramoto et al. [181]	Ni-YSZ	900	HCl	1 to 10		•	•	•			No apparent effect of HCl or current density is reported. A light sintering in the anode layer is observed.
Reeping [219]	Ni-YSZ + Ni-GDC	650, 700	HCl, CH ₃ Cl	110	•		•		•	•	The degradation rate is higher with synthetic biogas than with H ₂ or CH ₄ . Cl reduces catalytic activity.

to the cathodic polarization that reduces the partial pressure of steam in the vicinity of the TPB [226]. Replacing the glass sealing by a gold sealing effectively diminished the SiO_2 deposition [121]. Under high cathodic polarization, nano particles of SiO_2 have been found inside nickel particles, possibly due to a local reduction of SiO_2 to Si, which diffuses into Ni and is eventually re-oxidized to SiO_2 [227].

2.2.4 Tar

Tar is composed of long hydrocarbon chains or poly-aromatic hydrocarbons whose molecular weight is greater than benzene [182]. Tars are often produced during gasification and can thus be present in gasified coal or biomass. The composition of tars is complex and depends on the raw material and the method used for gasification. SOFC researchers have been focused on understanding whether tars present in bio-syngas or coal-syngas act as an additional fuel or as a contaminant; their main contributions and conclusions are presented in Table 2.7.

The principal threats for an SOFC operated with a tar-containing fuel is the possibility for carbon deposition that may clog fuel channels and H_2 -electrode pores, leading to the destruction of the SOFC due to fuel starvation [229, 230]. A secondary effect of carbon deposition is metal dusting, which eventually leads to a high level of erosion of the Ni present in the H_2 -electrode and current collector [231].

In some cases, small amounts of tar were found to improve the SOFC performance [232]. Baldinelli et al. [233] observed that the introduction of toluene in the simulated wood syngas used to feed an SOFC operated at 0.25 A cm^{-2} increased the SOC voltage, which returned to its original value when the toluene input was stopped. This reversible performance improvement was attributed to the increase of the fuel's LHV and thus the operating cell voltage. However, further increasing the toluene concentration can lead to carbon deposition and irreversible degradation. The presence of steam and/or carbon dioxide in the fuel improves the SOFC tolerance to toluene by enhancing the steam- and dry-reforming reactions, thus converting toluene into a useful fuel [201].

When heavier tars are used, the catalytic activity of the SOFC is affected [234]. Papurello et al. [232] observed little impact of naphthalene when the SOFC was fed with H_2 but the performances degraded when the fuel was switched to bio-syngas. As naphthalene is adsorbed on Ni and only slowly reformed, it blocks the Ni sites for the WGS reaction, thus limiting the supply of H_2 to the electrode.

Table 2.6 – Summarized literature review on silicon poisoning

Reference	HE	T °C	Impurity		Duration			Fuel mixture				Observations
				ppm	≤100 h	100-500 h	>500 h	H ₂	H ₂ O	CO _x	C _x H _y	
Hauch et al. [226]	Ni-YSZ	850 to 950	Si	?		•		•	•			Deposited silica was found close to the electrode–electrolyte interface. High steam content enhanced the formation of Si(OH) ₄ and volatilization of the Si contained in the glass sealing. Si redeposited where the steam partial pressure was lower, i.e., in the electrochemically active region.
Hauch et al. [121]	Ni-YSZ	850	Si	?		•		•	•			Evaporation of the Si contained in the glass sealing deposited in the H ₂ -electrode of a SOC operated in electrolysis mode. Using a Si-free sealing (gold) reduces the amount of deposited SiO ₂ but does not totally suppresses it.
Haga et al. [186]	Ni-ScSZ	800 to 1000	D5	10	•			•	•			Degradation due to SiO ₂ formation affects the TPB, thus increasing the ohmic and polarization resistance.
Madi et al. [225]	Ni-YSZ	750	D4	0.069 to 3		•		•	•	•	•	Degradation was attributed to the reduction of the gas–solid interaction at the TPB. D4-induced degradation was partially reversible. The degradation correlates with the D4 concentration but tends to an asymptote. SiO ₂ deposition increases from the fuel inlet to the outlet and from the electrode surface towards the electrolyte. Deposited SiO ₂ is revolatilized in the form of Si(OH) ₄ and transported in the electrode towards the electrolyte.
Papurello et al. [207]	Ni-YSZ	750	D4	0.111 to 1.92	•			•	•	•	•	D4 impacts the high-frequency region of the impedance spectra. Degradation was attributed to SiO ₂ deposition at the TPBs.
Tao et al. [227]	Ni-YSZ	875?	Si	?	•			•	•	•		Formation of nano-sized SiO ₂ particles inside Ni particles under high cathodic polarization (i.e., SOEC mode).
Kuramoto et al. [181]	Ni-YSZ	900	TEOS	0.14 to 0.24	•			•	•			The degradation is partially reversible and correlated to the TEOS content. SiO ₂ may be deposited first on the electrode surface, then is vaporized as SiO(g) and re-oxidized in the vicinity of the electrochemically active regions.

Table 2.7 – Summarized literature review on tar poisoning

Reference	HE	T °C	Impurity		Duration			Fuel mixture				Observations
				g/Nm ³ *ppm	≤ 100 h	100–500 h	> 500 h	H ₂	H ₂ O	CO _x	C _x H _y	
Mermelstein et al. [242]	Ni–YSZ	775	C ₆ H ₆ C ₇ H ₈ mix	15	•			•				Benzene easily forms carbon depositions. Naphthalene blocks the catalytic and electrochemical active sites.
Mermelstein et al. [243]	Ni–YSZ	765	C ₆ H ₆	0 to 0.35	•			•	•		•	Increased current density and addition of steam reduces carbon deposition.
Hauth et al. [234]	Ni–GDC	800 900	C ₁₀ H ₈	483 to 3606*	•			•	•	•	•	The current density has no impact on the degradation. Naphthalene inhibits CH ₄ reforming.
Mermelstein et al. [244]	Ni–GDC	765	C ₆ H ₆	0.5 to 16	•			•	•	•	•	Addition of CO and CH ₄ increases carbon deposition.
Liu et al. [245]	Ni–YSZ	800	C ₇ H ₈	6.3	•			•	•	•	•	Higher current density and steam content reduce carbon degradation. Carbon deposition occurred even when not thermodynamically favored.
Doyle et al. [246]	Ni–GDC	850	C ₇ H ₈	5 to 32	•			•	•	•	•	Toluene is never fully reformed. Simultaneous increase of toluene and fuel utilization lead to a large degradation due to carbon deposition.
Madi et al. [201]	Ni–YSZ	750	C ₇ H ₈	48 to 4350*	•			•	•	•		Switching the feed flow from H ₂ to biosyngas eliminates the degradation.
Papurello et al. [232]	Ni–YSZ	750	C ₇ H ₈ C ₁₀ H ₈	2 to 50*	•			•	•	•	•	Naphthalene limits methane reforming and the WGS reaction, virtually increasing the fuel utilization. A small amount of toluene in syngas improves the SOFC performances.
Baldinelli et al. [233]	Ni–YSZ	800	C ₇ H ₈	5 to 10	•			•		•	•	Operation in toluene-laden synthetic wood syngas led to stable performances and no carbon deposition.
Pumiglia et al. [229]	Ni–YSZ	650	C ₇ H ₈	255 to 537	•			•	•	•		Post-test analysis showed the presence of NiO, segregated ZrO ₂ , and carbon deposition when toluene was present. The proposed degradation mechanism includes pore clogging by carbon leading to local fuel starvation and Ni re-oxidation generating mechanical stresses that led to the formation of a monoclinic ZrO ₂ phase.
Geis et al. [247]	Ni–YSZ	700	C ₆ H ₆ O	1 to 8	•			•	•	•	•	Exposure to phenol led to carbon deposition and metal dusting from the SOFC's inlet to the outlet
Jeong et al. [231]	Ni–YSZ	715	mix	4.5 to 5	•			•	•	•	•	Operation under real wood syngas containing a mixture of tars (with sulfur and chlorine removal) led to significant changes in the microstructure (metal dusting) and carbon deposition deep in the electrode.
Fischer et al. [230]	Ni–YSZ	715	mix	3.5	•			•	•	•	•	Metal dusting affected both the SOFC's electrode and the Ni current collector. Under real bio-syngas, the carbon deposition was so intense that it led to a massive pressure drop increase and the failure of the test after only 5 h.

2.2.5 Miscellaneous

The presence of phosphine in the fuel can lead to substantial degradation of the SOC performances [213]. The driving degradation mechanism is the formation of a nickel-phosphorus secondary phase that enhances the mobility of Ni leading to nickel agglomeration [235]. The modification of the electrode's microstructure reduces the TPBs and limits the gas diffusion in the electrode, which in turn degrades the electrochemical performance of the SOC [236]. The interaction between Ni and P can be reduced by increasing the operating temperature, although this enhances phosphine diffusion in the electrode, thus making the TPBs more vulnerable and potentially reducing the SOC tolerance [216, 237]. However, the SOC tolerance to phosphine is not impacted by the fuel composition (H_2 or simulated coal syngas).

Mercury, zinc, and antimony are heavy metals regularly observed in coal syngas [238] that have no or little impact on a Ni-YSZ electrode up to a few ppm [213, 216]. However, arsenic, selenium, and cadmium can cause significant damage. Arsine (AsH_3) can lead to a complete failure of the SOC due to the formation of a brittle nickel-arsenide phase, which greatly deteriorates the electronic conductivity of the H_2 -electrode [213, 239]. The nickel-arsenide phase forms principally at the interface between the electrode and the gas channel but does not penetrate far enough to impact the electrochemically active region of an anode-supported cell (ASC) [240]. Electrolyte-supported cells (ESC) are more sensitive, as arsine penetrates the entire electrode, thus also affecting the electrochemical activity and leading to failure more quickly [239]. The behavior of a Ni-YSZ electrode exposed to hydrogen selenide (H_2Se) or hydrogen sulfide (H_2S) is similar and consists of a fast initial voltage drop followed by a lower degradation rate. As for sulfur poisoning, selenium is adsorbed on Ni, which reduces the electrocatalytic activity at the H_2 -electrode. The recovery potential of the SOC under clean gas is lower with H_2Se compared with H_2S [241]. Bao et al. [213] investigated the effects of cadmium and found that the effect of Cd are low at 800 °C but become major at 850 °C. The formation of a secondary phase between Ni and Cd has been proposed as a degradation mechanism, but has not been confirmed by post-test analysis.

Table 2.8 – Summarized literature review on heavy metals and phosphor poisoning

Reference	HE	T °C	Impurity		Duration			Fuel mixture				Observations
				ppm	≤ 100 h	100–500 h	> 500 h	H ₂	H ₂ O	CO _x	C _x H _y	
Zhi et al. [236]	Ni-YSZ	900	PH ₃	20	•			•	•	•		The increase of the diffusion and charge transfer resistance is attributed to the formation of Ni and Zr phosphate blocking the diffusion pathways and limit the electrochemical activity.
Xu et al. [235]	Ni-YSZ	800	PH ₃	10	•			•	•	•		The degradation is irreversible but stops when PH ₃ is stopped The important degradation observed is assigned to the relocation/agglomeration of nickel due to the interaction with phosphine possibly forming a liquid phase.
Xu et al. [237]	Ni-YSZ	750 850	PH ₃	10	•			•	•	•		Increasing the temperature reduces the interactions between P and Ni but improves the diffusion of PH ₃ in the electrode, which can then directly interact with the TPBs.
Li et al. [228]	Ni-YSZ	750 850	PH ₃	10 20	•			•	•	•		Increasing the temperature increases the impact of PH ₃ . The gas composition had no impact on the degradation.
Trembly et al. [240]	Ni-YSZ	750 and 800	AsH ₃	0.1 to 2		•		•	•	•		The formation of NiAs is time- rather than concentration- dependant. AsH ₃ is not as detrimental as HCl or H ₂ S as it interacts first with surface nickel and does not attack the electrochemically active sites directly.
Bao et al. [213]	Ni-YSZ	750 to 850	As, SbO, Zn, HgO, Cd	5 to 10	•			•	•	•		Exposure to As showed moderate impact at 750 °C but the SOFC failed rapidly when the temperature was raised to 800 °C. During exposure to Cd, increasing the temperature increases the degradation. SbO, Zn, HgO showed no to little impact.
Bao et al. [216]	Ni-YSZ	750 to 850	AsH ₃ ,Hg	0.18 to 1		•		•	•	•		Low levels of Hg showed no impact on the SOC performance. At 750 °C, the SOC started degrading when the AsH ₃ was greater than 0.5 ppm. At 750 °C, exposure to PH ₃ (even at sub-ppm level) leads to a significant irreversible degradation of the cell performance, which increases at higher temperature.
Coyle et al. [239]	Ni-YSZ	750 to 850	AsH ₃	1 to 10	•			•	•	•		The fuel utilization and current density have no impact on the tolerance to AsH ₃ . ESC are more sensitive than ASC due their thinner electrode, which allows for AsH ₃ to react directly in the electrochemically active region.
Marina et al. [241]	Ni-YSZ	700 to 800	AsH ₃ , H ₂ Se, Sb	0.1 to 10	•			•	•	•		Poisoning by H ₂ Se showed a similar behavior to H ₂ S exposure, i.e., a fast voltage drop followed by a stable voltage, but with a smaller recovery potential. Se is adsorbed on Ni and reduces the electrochemical activity. Sb forms Ni ₃ Sb, reducing the electrochemical activity. AsH ₃ forms a NiAs solid solution leading to a reduced electronic conduction.

2.3 Conclusions

Although the effects of impurities on Ni-containing H₂-electrodes have been intensively investigated in fuel cell mode, there is a clear lack of studies reporting on the effects of contaminants during electrolysis operation. A summary of identified impurities likely to be present in a CO₂ stream that can potentially be used for co-electrolysis applications and their effects on Ni-based H₂-electrode is presented in Table 2.9.

Sulfur compounds are present in most if not all captured CO₂ streams and can lead to major degradation of the catalytic and electrochemical reactions of an SOFC. The main sulfur compounds likely to be found in CO₂ are H₂S or SO₂, depending whether extraction occurs before or after a combustion, respectively. The majority of the emitted CO₂ originates from the combustion of carbon-containing fuel by the industrial and power sectors [248], suggesting that SO₂ is the most likely sulfur compound encountered. Although H₂S is the most commonly used compound for sulfur tolerance experiments on SOFCs, Jablonski et al. [192] observed a higher rate of deactivation when a nickel catalyst was exposed to SO₂ than when exposed to H₂S. Increasing the current density in fuel cell operation improves the SOC's tolerance to sulfur, possibly due to the oxidation of adsorbed S. Inverting the polarization could thus have the opposite effect and reduce the SOC tolerance. Residual traces of SO₂ are likely to be present in captured CO₂ and may be more critical in electrolysis than fuel cell operation on a Ni-YSZ H₂-electrode.

Chlorine compounds, mainly HCl, are present in various off-gases from combustion and industrial processes, as well as biogas. SOFCs generally tolerate a higher concentration of HCl than of H₂S. Exposure to chlorine leads to irreversible degradation of the TPB that could shorten the lifetime of the SOEC upon continuous exposure; however, extensive durability testing (>500 h) to clearly assess the long-term effect of chlorine has not yet been performed.

Si-induced degradation of an SOFC is due to the deposition of insulating SiO₂ particulate that is only partially reversible. The effect is even more important in electrolysis mode, as SiO₂ deposits preferentially at the TPB, thereby limiting the electrochemical activity. Except for biomass-derived CO₂-rich streams, silicon compounds have not been reported in off-gases from industrial processes or power plants. The risk of finding Si in captured CO₂ is thus relatively low.

Tars are present in a wide variety of combustion or gasification off-gases but in concentrations generally lower than chlorine or sulfur compounds [8]. Tar-induced degradation is due to carbon deposition and sluggish reforming. Tar concentration is expected to be lower than 1 ppmw in captured CO₂, which, together with the high steam content in electrolysis, makes carbon deposition unlikely. Tars are thus likely to be a lower threat than chlorine or sulfur compounds.

As, Se, and P can potentially be found in CO₂ captured from coal-fired power plants. The expected concentration of As and Se are below 1 ppmv but and likely below 0.1 ppmv [175], which is below the lowest concentration tested experimentally on an SOFC. The risk related to As and Se is likely minimal, even though As can lead to irreversible degradation due to the formation of a brittle Ni-As phase. P can be found in concentrations above 2 ppmv, which can be detrimental to an SOFC. The presence of P in off-gases is not widely spread but limited to coal-fired power plants and phosphate rock processing plants.

SO₂ and HCl represent two of the most likely threats to an SOEC performance and durability due to their likelihood of presence in CO₂ streams and potential impact on Ni-YSZ H₂-electrodes. They are thus considered for experimental investigation in this work.

Table 2.9 – Summary and effect of the principal impurities impacting Ni-based composites SOC H₂-electrode

Impurity	Chemical form	Concentration in ppm	Impact on tolerance			Reversibility	Observations	Presence
			$T \uparrow$	$j \uparrow$	H/C \downarrow			
S	H ₂ S, COS, C ₄ H ₄ S, CH ₃ SH	0.078 to 700	👍	👍	👎	partial to full	S adsorption on Ni Reduction of the catalytic activity Reduction of the electrochemical activity	C, Ce, B, CI
Cl	Cl ₂ , HCl, CH ₃ Cl, C ₂ H ₃ Cl, C ₂ Cl ₄	1 to 1000	👍	👎/👍	👍	partial to full	Cl adsorption on Ni Enhanced Ni redistribution Reduction of the catalytic activity	C, Ce, B, CI
Si	siloxane (D4,D5)	0.111 to 10	?	?	?	partial	SiO ₂ formation Reduction of the electrochemical activity Increase of the polarization and ohmic resistance	B
As	AsH ₃	0.5 to 10	👎/?	👍	?	none	Formation of brittle Ni-As phase Loss of electric conduction	C, Ce, CI
Se	H ₂ Se	0.5 to 5	?	👎	?	partial	Se adsorption on Ni Reduction of the electrocatalytic activity	C, Ce, CI
P	PH ₃	0.5 to 20	👎	👍/-	–	none	Formation of Ni-P secondary phase Nickel agglomeration	C, CI
Tars	C ₆ H ₆ , C ₆ H ₆ O, C ₇ H ₈ , C ₁₀ H ₈	48 to 4350	👍	?	?	none to full	Carbon deposition Metal dusting Reduction of the catalytic activity Presence of steam reduces carbon deposition	C, B, CI

^C : coal derived CO₂ stream (e.g., combustion or gasification)

^{Ce} : CO₂ stream from cement production

^B : biogenic CO₂ stream (e.g., gasification, combustion, or fermentation)

^{CI} : CO₂ stream from chemical industries (e.g., ammonia or ethylene oxide production)

CHAPTER 3

Experimental method

This chapter uses text and information published in Jeanmonod et al. [174]

3.1 Test rig

H₂-electrode supported ceramic cells from SOLIDpower originating from the same batch were used to evaluate the impact of HCl and SO₂ on a SOEC. The cells are composed of a cermet Ni-YSZ H₂-electrode, a YSZ electrolyte, a GDC barrier layer, and an LSCF O₂-electrode. The cells have a diameter of 60 mm with an active area of 12.56 cm² (40 mm diameter).

The cells were operated in a metallic test rig made of Inconel 601 that was heated to operating temperature in a Rohde furnace. The oxygen-side flange was coated with a MnCo₂O₄ spinel to mitigate Cr evaporation and the subsequent poisoning of the O₂-electrode whereas an enamel coating was deposited on the hydrogen side to limit the interaction between the reactant and the metallic flange. The reactant fed to the H₂-electrode was transported to the cell through a ceramic tube limiting the interactions of the feed flow with metallic compounds. On both electrodes, the gas flow was radially distributed from the center to the rim of the cell. The SOC was positioned on a Ni foam 0.6 mm thick and 60 mm in diameter that is used for both current collection and gas distribution. A glass sealant was deposited on the rim of the SOC and Ni foam assembly to avoid mixing of anode and cathode feeds. A gold mesh was used for current collection on the oxygen-side. In previous designs, the current and voltage at the H₂-electrode transit via the reactant inlet tube and a coaxial gold wire, as shown in Figure 3.1a. The mutual inductance between current lead wires was relatively important in this configuration as it is proportional to the area encompassed between them, which deteriorated the quality of the electrochemical impedance (EI) spectra at high frequencies. In a later design, twisted pair gold-wires were used from the current collectors to the furnace outlet for current and voltage probing, thereby limiting the inductive artifacts of the lead wires, as presented in Figure 3.1b.

The reduction of NiO to Ni was performed at 800 °C by slowly increasing the hydrogen content from 10 %vol H₂ and 90 %vol N₂ to 100 %vol H₂ with a flow rate of 200 Nmlmin⁻¹ on the hydrogen side and 500 Nmlmin⁻¹ of air on the oxygen side.

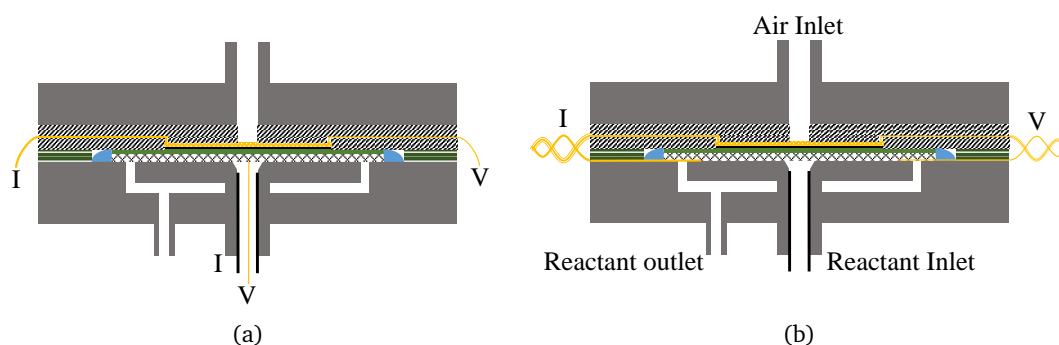


Figure 3.1 – Schematic representation of the SOC assembly with (a) central and (b) twisted lead wire configuration. The flange, the gold current lead wires, the glass sealant, and the SOC are colored in grey, yellow, blue, and green and black, respectively. The mica gasket, the alumina felt, and the Ni current collector are represented by green horizontal strips, black diagonal strips, and grey cross strips, respectively. The alumina tube in the gas inlet is represented in black.

3.2 Control, acquisition, and characterization

EL-FLOW[®] Select series mass flow meters from Bronkhorst[®] were used to regulate the flow rates of air, N₂, H₂, CO₂, Ar containing 1000 ppmv of SO₂, and H₂ containing 500 ppmv of HCl. High-purity gas bottles from Carbogas were used for all gases except the air (compressed ambient air was used). The ultra-pure water (Milli-Q[®]) flow used for steam generation was controlled by an Ismatec[®] Reglo ICC peristaltic pump. The SOC voltage and temperature were continuously monitored using an Agilent 34970A data logger coupled with an Agilent 34901A 20-channel multiplexer with a built-in thermocouple reference junction. A DC electronic load EA-EL 3160-60 from Elektro-Automatik connected in series with a DC power supply (6 V, 60 A) were used to modulate the applied current. The mass flow meters were controlled using a LabVIEW[™] interface developed in-house whereas proprietary software was used to control the other appliances.

EIS and j - V measurements were performed using a Zahner ZENNIUM Electrochemical Workstations coupled with an external potentiostat (PP201 from Zahner) allowing for current up to 20 A and frequency ranging from 10 μ Hz to 500 kHz.

3.3 Data analysis procedure

The SOEC voltage was constantly monitored and its evolution was used as a first evaluation of the effect of impurities on the SOEC performance. EIS measurements were then used to identify the mechanisms involved. EIS measurements were taken from 20 mHz to 200 kHz with a sinusoidal perturbation of ± 200 mA (corresponding to about ± 10 to ± 15 mV). The inductance of the lead wires was limited by the use of twisted pair wires and, if necessary, high-frequency points were manually removed. When twisted pairs were not used, the impedance spectra was corrected for a straight inductance, L , as described by Liu et al. [249]. The complex impedance of an inductance is purely imaginary and thus does not affect the real part (Z') of the Z ; only the imaginary component, Z'' , was corrected as follows:

$$L = \frac{Z''(f_{max})}{2\pi f_{max}}, \quad (3.1)$$

$$Z''_{cor}(f) = Z''(f) - 2\pi fL, \quad (3.2)$$

where f_{max} is the frequency at which the impedance spectra start deviating from a vertical asymptotic behavior (in a Nyquist representation), and Z''_{cor} is the corrected imaginary component of the impedance spectra. Data obtained at frequencies higher than f_{max} were then removed.

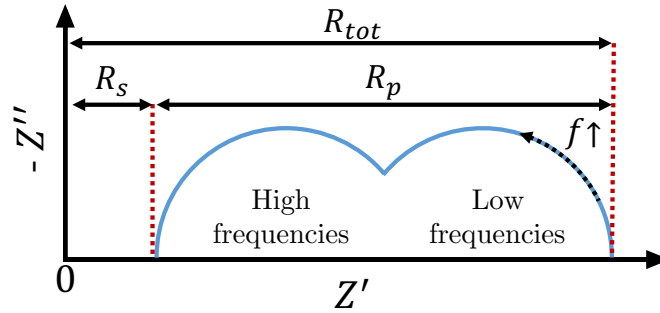


Figure 3.2 – Schematic Nyquist representation of the electrochemical impedance spectrum with the definition of the serial (R_s), polarization (R_p), and total cell resistance (R_{tot}). Z is the complex electrochemical impedance.

When represented in a Nyquist diagram, as in Figure 3.2, the low-frequency intercept (right-hand side) of the impedance spectra represents the total cell resistance (R_{tot}), and the high-frequency intercept (left-hand side) represents the serial (or ohmic) resistance (R_s). The difference between R_{tot} and R_s gives the polarization resistance (R_p). R_s and R_p were used as a first metric to identify and quantify the degradation processes.

To get a better insight into the degradation process, the DRT, $\gamma(\tau)$, of selected electrochemical impedance spectra was computed. The methodology described here is the one developed at GEM by Caliandro [120] in her thesis. Conceptually, the DRT computation consists of fitting an infinite number of $R//C$ elements in series [115] as illustrated in Figure 3.3. In mathematical terms, it involves solving equation (3.3) for $\gamma(\tau)$ knowing the impedance spectra $Z(\omega)$ where $\tau = 1/RC$ is the relaxation time of an $R//C$ element. The $\gamma(\tau)$ then represents the contribution of each $R//C$ elements contributes to the overall impedance $Z(\omega)$.

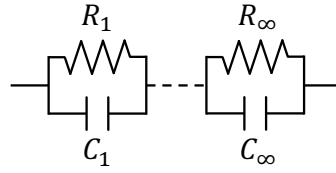


Figure 3.3 – A series connection of resistor (R) and capacitor (C) connected in parallel ($//$), representing the concept of DRT.

$$Z(\omega) = R_p \int_0^{\infty} \frac{\gamma(\tau)}{1 + j\omega\tau} d\tau \quad (3.3)$$

This ill-posed problem can be discretized and solved using Tikonov regularization [12, 116]. The DRT obtained is composed of multiple peaks, each corresponding to one or many elementary physical and/or chemical processes. DRT analysis is a powerful tool but it must be handled with great care as artifacts may appear if the quality of the recorded impedance spectra is not adequate [250]. The presence of an inductive behavior at high frequencies has been shown to temporally contract the DRT peaks and lead to erroneous estimation of the relaxation times. This effect may be limited by correcting the EI spectra using equation (3.2) prior to the DRT computation or by directly introducing an inductive term in the problem formulation [12].

Electrochemical devices generally present a capacitive impedance [251], which often enforces positive values for $\gamma(\tau)$, thereby limiting the solution space [115, 252]. A low frequency "pseudo-inductive" loop corresponding to a positive imaginary component Z has been observed with Li-ion batteries [253], PEM fuel cells [254], during O_2 reduction on Au-YSZ electrodes [255], and with SOECs [174, 256, 257]. The origin of this hook may be attributed to the presence of a two-step reaction including an intermediate species [255, 258, 259]. The complex impedance of a constant phase element, Z_Q , and zarc element (parallel connection of a resistor and Q element), Z_{zarc} , is defined by equations (3.4) and (3.5), respectively, where $0 \leq \alpha \leq 1$. The relaxation time of a zarc element, $\tau_0 = \sqrt[\alpha]{RQ}$, is equal to that of an $R//C$ element when $\alpha = 1$. An increase of R causes an increase of the τ_0 and thus a frequency shift of the DRT peak. Assuming that a zarc element is a good approximation of an elementary reaction, an increase of the resistance associated with that process also leads to a shift of the DRT peaks to a higher relaxation time (i.e., lower frequency). If R is set to a negative value, then Z_{zarc}'' is positive, leading

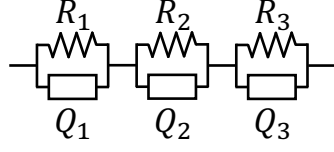


Figure 3.4 – Schematic representation of the electric circuit used for DRT comparison

Table 3.1 – Parameters of the electric circuit defined in Figure 3.4

	1	2	3
$R / \Omega\text{cm}^2$	0.05	0.1	-0.05
τ_0 / s	0.05	0.001	5
α	0.85	0.8	0.9

to a "pseudo-inductive" loop. Three zarc elements connected in series as shown in 3.4 with the parameters defined in Table 3.1 were used to simulate an impedance spectra with a low-frequency hook as shown in Figure 3.5a. The DRT of a series connection of zarc elements can then be analytically computed by summing the DRT of each zarc element whose analytical formulation is defined by equation (3.6) [260]. The DRT was then computed using Tikonov regularization with and without enforcing $\gamma > 0$. The Tikonov regularization method failed to reproduce the analytical DRT when γ was positively constrained as shown in Figure 3.5b. The peaks were compressed and shifted to higher frequencies, similarly to what was observed by Caliandro et al. [12] for EI spectra corrupted by lead wire inductance at high frequency. The analytical solution could, however, be approached using Tikonov regularization when the positivity constraint was removed at the small cost of wrinkles appearing as α approaches 1. In the presence of a low-frequency hook, the positivity constraint on γ should therefore be removed to obtain a meaningful DRT as suggested by [261] for PEM fuel cells. Furthermore, if the impedance should have to be extended to lower frequency, e.g., if the Fourier transform method proposed by [262] is used to solve equation (3.3), a solution could be to fit an R/Q element to the low-frequency hook.

$$Z_Q = \frac{1}{Q(j\omega)^\alpha} \quad (3.4)$$

$$Z_{zarc} = \frac{R}{1 + RQ(j\omega)^\alpha} \quad (3.5)$$

$$\gamma_{zarc} = \frac{R \cdot \sin((1-\alpha)\pi)}{2\pi \cdot [\cosh(\alpha \ln(\tau/\tau_0)) - \cos((1-\alpha)\pi)]} \quad (3.6)$$

The DRT corresponds to a superposition of elementary processes with distributed relaxation times and therefore the evolution of one DRT peak may also impact neighboring peaks. Klotz et al. [117] designed and fit an equivalent electric circuit based on the DRT results and the recorded EI to deconvolute the different contributions. The sum of the squared errors between the impedance spectra and the equivalent circuit for both imaginary and real components of the impedance, ϵ_Z , is defined in (3.8). The EEC used here was simply composed of six zarc elements, as proposed by Caliandro [120], which possess an analytical DRT formulation allowing to evaluate the sum of the error squared on the DRT, ϵ_{DRT} , as proposed by Klotz et al. [117] and defined by equation (3.9). A

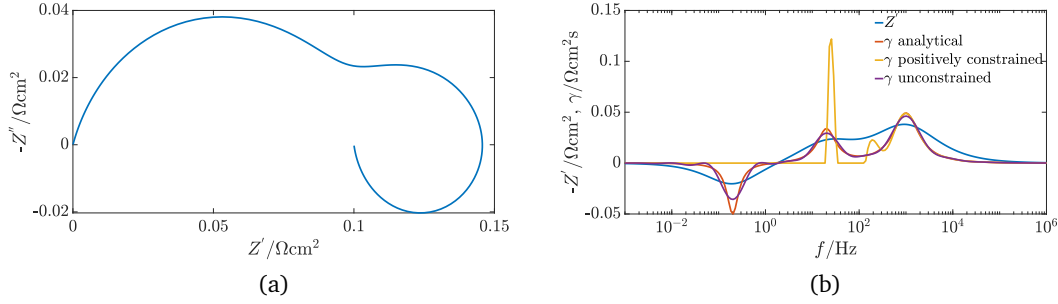


Figure 3.5 – Nyquist (a) and Bode (b) representation of the impedance spectra of the circuit defined in Table 3.1 showing a low frequency hook. The analytical and numerical DRT of the spectra is presented together with the Bode representation in (b).

complex non-linear least-square regression was performed to find the optimal set of parameters that minimizes ϵ defined by equations (3.7) to (3.11), where λ_i and κ_i are weighting factors, and N is the number of data points. The importance of the DRT in the fitting procedure can be adjusted by modifying β (typically around 1). The initial parameters for the CNLS regression were extracted from the DRT by fitting a Gaussian function to each peak. The associated resistance and relaxation were provided by the Gaussian curve summit and area, respectively, whereas a correlation function of the half height width (HHW) of the Gaussian function based on synthetic data was used to compute α [120].

$$\epsilon = \epsilon_Z + \beta \cdot \epsilon_{DRT} \quad (3.7)$$

$$\epsilon_Z = \sum_{i=1}^N \lambda_i \left[\left(Z'_i - Z'_{EEC,i} \right)^2 + \left(Z''_i - Z''_{EEC,i} \right)^2 \right] \quad (3.8)$$

$$\epsilon_{DRT} = \sum_{i=1}^N \kappa_i \left(\gamma_i - \gamma_{EEC,i} \right)^2 \quad (3.9)$$

$$\lambda_i = \left(Z'^2_i + Z''^2_i \right)^{-1} \quad (3.10)$$

$$\kappa_i = \left(\gamma^2_i + \gamma_{EEC,i}^2 \right)^{-0.5} \quad (3.11)$$

$$\alpha = -0.0032 \cdot HHW^3 + 0.0525 \cdot HHW^2 - 0.3209 \cdot HHW + 0.9847 \quad (3.12)$$

For consistency with the Nyquist representation of the impedance spectra used in this work, the DRT is represented in terms of frequency rather than time. The attribution of the DRT peaks to processes were made according to Caliendo et al. [12], who performed an extensive experimental sensitivity analysis combined with a dynamic numerical model

on SOCs originating from the same provider. Six DRT peaks were identified and are presented in Table 3.2.

Table 3.2 – Attribution of the DRT peaks to processes according to Caliendo et al. [12]

Name	Frequency	Attribution
P1	< 1 Hz	Conversion and diffusion at the O ₂ -electrode Transport in reforming mixture (H ₂ -electrode)
P2	1 to 10 Hz	Gas conversion (H ₂ -electrode)
P3	10 to 100 Hz	H ₂ -electrode diffusion O ₂ -electrode reaction and solid state diffusion
P4	100 to 500 Hz	Secondary peaks (H ₂ -electrode and O ₂ -electrode transport)
P5	0.5 to 1 kHz	H ₂ -electrode charge transfer
P6	5 to 200 kHz	Not attributed ^a

^a Possibly: solid–solid O₂-electrode transfer processes or electronic current losses between the O₂-electrode and the current collector

CHAPTER 4

Effect of HCl

The main objective of this chapter is to investigate the effect of HCl exposure at different concentration and duration on the Ni-YSZ H₂-electrode of an SOEC.

In section 4.1, the results obtained from an H₂-electrode-supported SOEC exposed to HCl concentrations ranging from 0 to 10 ppmv are presented and discussed. The SOC was exposed to HCl for short periods ranging from 18 to 55 h with a current bias ranging from 0 to 0.5 Acm⁻², corresponding to a maximal RU of 0.32. The SOC was assembled following a "central" lead wire connection scheme, as was described in Figure 3.1a.

A second SOEC was exposed to 1 and 2 ppmv of HCl over a longer period under galvanostatic operation (0.5 Acm⁻²) to assess the effect of HCl on the SOEC durability; these results are presented in section 4.2. After 763 h, of exposure the SOC was operated in an HCl-free atmosphere for 337 h before a final exposure to 2 ppmv of HCl. The SOC was assembled with twisted pair lead wires, as was described in Figure 3.1b.

After reduction, the gas composition on the H₂-electrode was changed to 65 vol% H₂O, 25 vol% CO₂, and 10 vol% H₂ and the flow rate was reduced to 150 Nmlmin⁻¹ on both the O₂-electrode and H₂-electrode. Hydrogen containing 500 ppmv of HCl was added using an additional mass flow controller to control the concentration in the reactant stream. As the added N₂ and HCl represented at most 2 % of the total reactant flow, the dilution effects were considered negligible.

Thermodynamic equilibrium calculations performed using HSC Chemistry 8.2.0 [263] predicted that the equilibrium reactant gas mixture was composed of 67.2 %vol H₂O, 22.9 %vol CO₂, 7.9 %vol H₂, and 2.1 %vol CO at 750 °C, which differed from the sent reactant gas mixture due to the RWGS reaction. HCl was the most stable chlorine species at 750 °C under 1 atm in this gas mixture.

Contributions to the Field

Evaluated the effect of HCl on the lifetime and performance of an SOC operated in co-electrolysis.

4.1 Effect of polarization and HCl concentration

4.1.1 Open circuit condition

Based on the thermodynamic equilibrium composition computation, the original OCV (0.868 V) was slightly greater than the theoretical Nernst potential (0.863 V), indicating a variation in the gas composition that likely originated from a small leakage, a lower temperature, or a lower steam content. The OCV recorded under pure hydrogen was 1.2 V at 750 °C and no signs of nickel re-oxidation were found after the SOC was cooled down (100 °C h⁻¹) in reducing atmosphere (H₂/N₂ 70 /30 vol%) and dismantled, indicating that an acceptable gas tightness was achieved. The difference between the measured voltage and theoretical Nernst potential was thus considered acceptable.

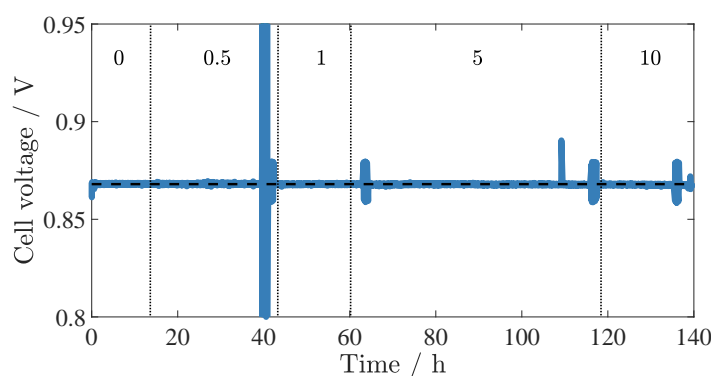


Figure 4.1 – Time evolution of the cell voltage when exposed to 0 to 10 ppmv of HCl in open-circuit conditions, the horizontal black dashed line is the initial cell voltage

The evolution of the cell voltage under open-circuit conditions (OCC) exposed to HCl concentrations ranging from 0.5 to 10 ppmv for 20 to 55 h, is shown in Figure 4.1. Only a slight decrease of the cell voltage was observed when the HCl concentration reached 10 ppmv. This suggests that the composition of the reactant on the hydrogen electrode remained somewhat constant and was independent of the HCl concentration. Hydrogen chloride thus had only a limited impact on the catalytic properties of the tested SOEC. Generally, <50 ppm of HCl can be tolerated in fuel cell operation before notable degradation [207, 211, 213]. The range of HCl concentration investigated may not have been high enough to sufficiently cover the Ni and reduce the catalytic reaction to cause a significant modification to the measured OCV.

The impact of HCl on the electrochemical performance of the SOEC was evaluated by performing EIS measurements before and after each contamination periods. As this test was performed without twisted lead wires, the impedance spectra were smoothed and inductance-corrected via equation (3.2). The ohmic and polarization resistances were only slightly impacted, as shown in Figure 4.2 (b) (a).

4.1. Effect of polarization and HCl concentration

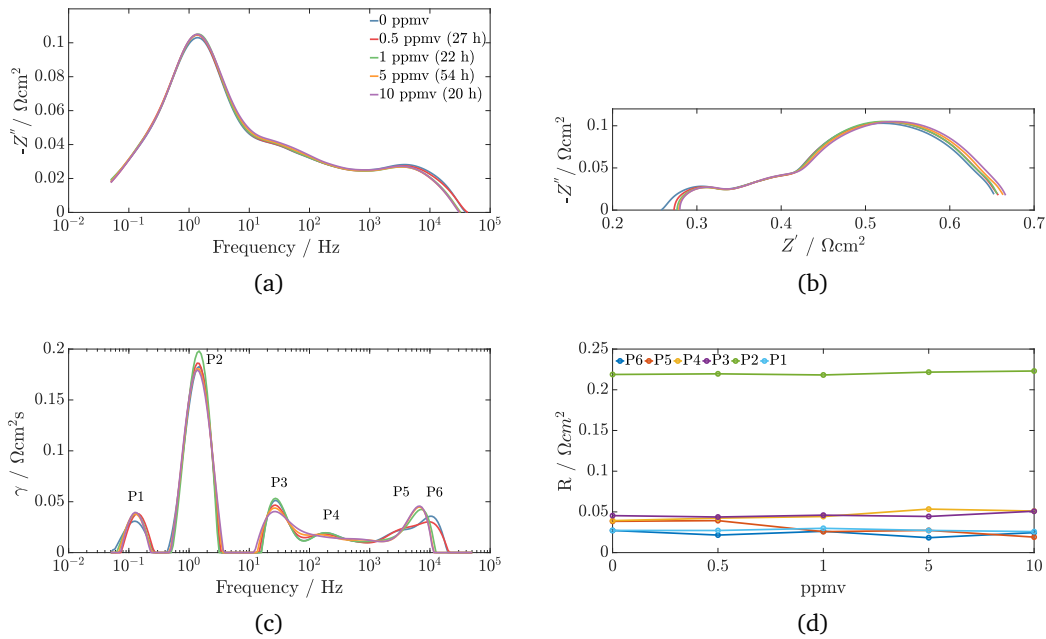


Figure 4.2 – (a) and (b) electrochemical impedance spectra taken at OCV after exposure to 0.5, 1, 5, and 10 ppmv of HCl, (c) corresponding distribution of relaxation time, and (d) resistance associated with peaks P1–P6 in function of the HCl concentration . The exposure durations are indicated in parentheses.

Analysis of the DRT showed a decrease and widening of the peaks P3 and P4 (at approximately 30 and 200 Hz respectively), when the HCl concentration was increased. These peaks are related to transport and diffusion at the H_2 -electrode and are particularly sensitive to the steam partial pressure [12]. The resistance associated with each peak was evaluated by fitting 6 RQ-elements in series while minimizing the error with the impedance and DRT spectra as defined in section 3.3. The resistance associated to these peaks remained nearly constant, as shown in Figure 4.2d. The widening of the peaks likely compensated for the amplitude decrease. As the width of DRT peaks can be linked to the spatial distribution of relaxation time related to a particular phenomenon [115]. The observed peak widening may thus be attributed to a spatial redistribution of the electrochemical activity due to the interaction between HCl and Ni.

The shape of the peaks located around 7 kHz, i.e., P5 and P6, evolved significantly during the test. The observed modifications were ambiguous as this part of the DRT was particularly affected by the lead wire inductance. The clear change in shape of the curves seen on the left side of Figure 4.2b (corresponding to the highest frequencies) was likely a consequence of the lead wire inductance and correction procedure.

4.1.2 Under polarization

The SOEC was then polarized at 0.25 A cm^{-2} and exposed to various concentrations of HCl from 0.5 to 10 ppmv for 18 to 26 h. The evolution of the cell voltage with respect to the relative time (i.e., the time since the EIS measurement taken prior to the first exposure to HCl under polarization) is presented in Figure 4.3. Unlike the OCV case in which a negligible degradation was observed, the presence of HCl clearly affected the SOEC performance under polarization. Under exposure to 0.5 ppmv, the SOC voltage decreased at a rate of approximately -20 mV kh^{-1} , suggesting an improvement of the SOC performance. When the SOC was exposed to a higher HCl concentration, the cell voltage increased steadily. The degradation rate increased with the HCl concentration from 30 to 50 mV kh^{-1} when the concentration was increased from 1 to 10 ppmv, respectively. When the HCl supply was cut, the cell continued degrading for approximately 20 h until the cell voltage stabilized. This behavior may have been related to the gradual release of non-permanently adsorbed HCl acting as a buffer and maintaining a certain HCl content in the reactant stream even though the HCl supply was shut off. The SOC voltage then remained stable for over 50 h in a HCl-free environment but did not show any signs of recovery, thus indicating that, under polarization, the SOC was irreversibly damaged by the presence of ≥ 1 ppmv of HCl.

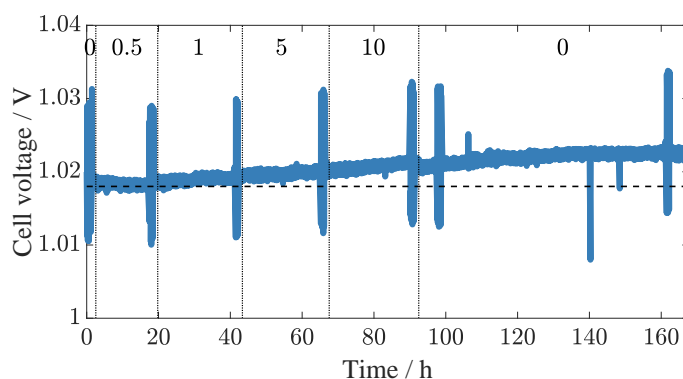


Figure 4.3 – Time evolution of the cell voltage when exposed to 0 to 10 ppmv of HCl polarized at 0.25 A cm^{-2} , the horizontal black dashed line is the initial cell voltage

The EIS measurements performed during the poisoning experiment are presented in Figure 4.2 (b) and (a). An increase of the high-frequency region of the impedance spectra was observed under HCl poisoning concentration of ≥ 1 ppmv but the ohmic resistance remained relatively constant. The total SOC resistance increased from 0.58 to $0.6 \Omega \text{ cm}^2$ between the first EIS measurement, taken before exposure to 0.5 ppmv HCl, and the last, taken after the recovery period. Analysis of the DRT, presented in Figure 4.4c, showed that the major changes occurred on the peaks P4, P5 and P6 (at approximately 200 Hz, 2 kHz, and 10 kHz). The resistance associated with each DRT peaks identified in Figure 4.4c is presented in Figure 4.4d. At concentrations lower than 5 ppmv, the

4.1. Effect of polarization and HCl concentration

overlap between P5 and P6 was large and the deconvolution was thus difficult, which could explain the mirroring evolution of P5 and P6 until 5 ppmv. It was, however, clear that the resistance associated with P5 significantly increased when the HCl concentration was increased to 10 ppmv and during the recovery in HCl-free atmosphere. Peak P5 is associated with the charge transfer processes at the H_2 -electrode, suggesting that HCl interacted irreversibly with the electrochemically active sites.

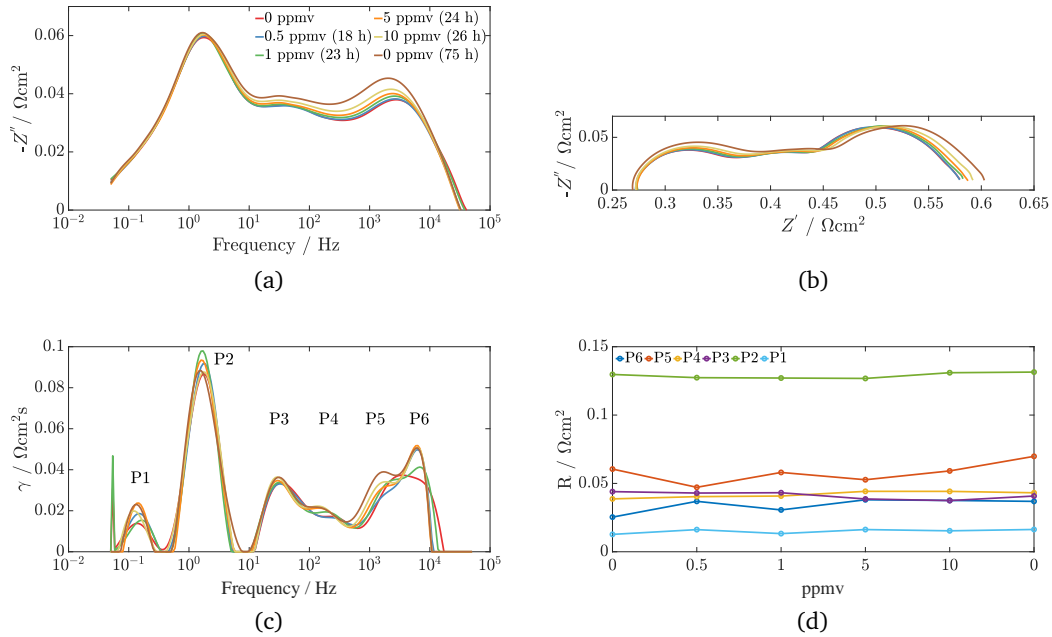


Figure 4.4 – (a) and (b) electrochemical impedance spectra taken at 0.25 Acm^{-2} after exposure to 0.5, 1, 5, and 10 ppmv of HCl, (c) corresponding distribution of relaxation time, and (d) resistances associated to peak P1–P6 as a function of the HCl concentration. The exposure durations are indicated in parentheses.

After the recovery period at 0.25 Acm^{-2} , the polarization was increased to 0.5 Acm^{-2} and the SOEC was exposed to HCl concentration ranging from 0.5 to 10 ppmv intercalated with recovery periods in HCl-free atmosphere. The evolution of the cell voltage with respect to the time since the exposure to HCl is presented in Figure 4.5. As when the cell was polarized at 0.25 Acm^{-2} , the effect of HCl remained relatively low below 5 ppmv of HCl; degradation rates of 30 and 20 mVkh^{-1} were recorded when the SOEC was exposed to 0.5 and 1 ppmv of HCl, respectively. These degradation rates were similar to that at the end of the last recovery period (20 mVkh^{-1} between 320 and 350 h).

The EIS measurements presented in Figures 4.4 (b) and (a) showed almost no modification to the serial resistance; however the high-frequency region of the polarization resistance, corresponding to charge transfer processes, increased, suggesting that the electrochemically active sites were mostly impacted. The total SOEC resistance increased from 0.57 (before exposure to HCl at 0.5 Acm^{-2}) to 0.66 and $0.67 \Omega\text{cm}^2$ after exposure

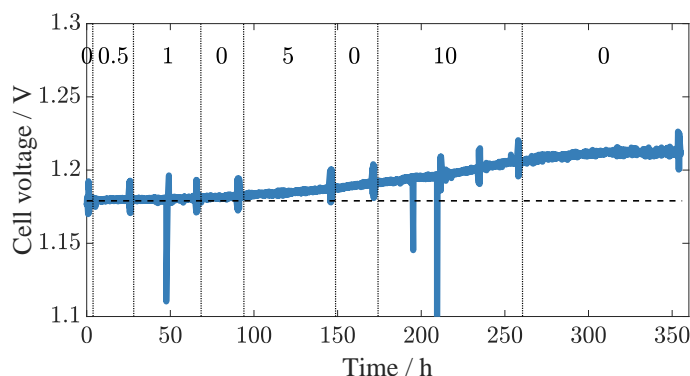


Figure 4.5 – Time evolution of the cell voltage when exposed to 0 to 10 ppmv of HCl polarized at 0.5 A cm^{-2} , the horizontal black dashed line is the initial cell voltage

to 0.5 and 1 ppmv of HCl, respectively. Analysis of the DRT showed a small increase of the peak located around 1 kHz (i.e., P5 in Figure 4.6), indicating an increase of the charge transfer resistance. When the contaminant was removed, the charge transfer peak continued increasing as was observed at 0.25 A cm^{-2} . After 58 h exposure to 5 ppmv HCl, the SOEC resistance increased from 0.68 to $0.69 \Omega \text{ cm}^2$, which corresponded to a degradation rate of 80 mV kh^{-1} . When the contamination was stopped, the degradation rose to 200 mV kh^{-1} , before continuously decreasing until the cell was exposed to 10 ppmv of HCl. The degradation was caused by the increase of the charge transfer resistance, i.e., P5, as shown in Figure 4.6. When the SOEC was exposed to 10 ppmv of HCl, the high-frequency region of the impedance spectra was affected and the SOEC resistance increased from 0.71 to $0.75 \Omega \text{ cm}^2$ in 71 h, corresponding to a degradation rate of 200 mV kh^{-1} . When the contamination was stopped, the degradation continued for approximately 60 h at a reduced rate of 100 mV kh^{-1} , and eventually dropped below 20 mV kh^{-1} by the end of the test. Similarly to what was observed at 0.25 A cm^{-2} , the increase of R_p in the HCl-free environment was caused by an increase of the charge transfer processes, as reflected by the evolution of peak P5 in Figure 4.6c. Additionally, the degradation became significant only at the highest current density investigated i.e., 0.5 A cm^{-2} . These results are coherent with those found by Madi et al. [215] in fuel cell operation, who also observed a negative impact of the current density and a continuous degradation of the high-frequency region of the impedance spectra but for a higher HCl concentration (100 ppmv), suggesting that electrolysis operation may reduce the tolerance to HCl.

Independently of the HCl concentration, the degradation was always irreversible. This may have originated from the presence of residual Cl, as observed by Madi et al. [215] and Marina et al. [208], who performed post-test composition analysis on SOCs exposed to HCl and found the presence of permanently adsorbed Cl in the SOC H_2 -electrode. However, the reaction of HCl with Ni to form NiCl_2 has been ruled out as thermodynamically unfavored [208, 209, 213, 214]. When exposed to HCl the SOC microstructure was found to be modified. Microscopic post-test analysis performed by Li et al. [206] and Kuramoto

et al. [181] showed a sintering of the Ni particle when the H_2 -electrode was exposed to chlorine, which reduced the catalytic activity. Xu et al. [209] observed a roughening of the Ni-particles exposed to HCl that was more important at the interface with the gas channel compared to the interface with the electrolyte, where the YSZ-particles were intact. They also observed a depletion of nickel during exposure to HCl. The evaporation of volatile nickel chloride particles could cause the reported depletion and sintering of Ni [153]. The presence of permanently adsorbed Cl and a modification of the nickel microstructure could have reduced the available TPB, which may explain the irreversible increase of the DRT peak P5, which is related to the charge-transfer processes at the H_2 -electrode. Additionally, nickel migration and depletion in the vicinity of the electrolyte is a well-known degradation mechanism observed in SOECs [80, 88, 89, 91, 264]. The presence of HCl may be critical for longer-term operation as it may accelerate the nickel redistribution and thus reduce the SOEC lifetime.

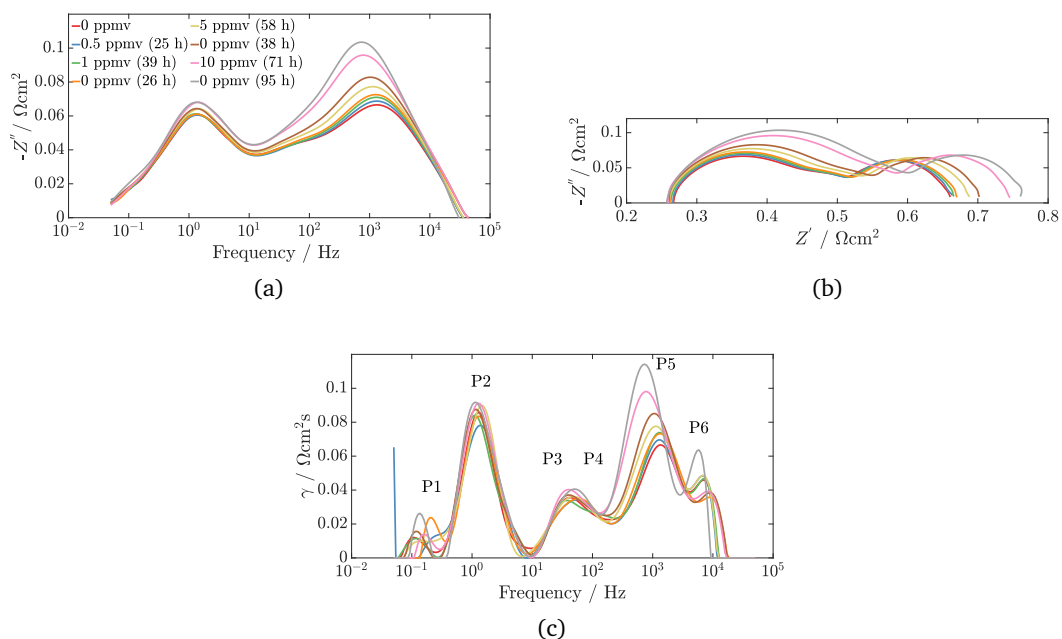


Figure 4.6 – (a) and (b) electrochemical impedance spectra taken at OCV after exposure to 0.5, 1, 5, and 10 ppmv of HCl and (c) corresponding spectra distribution of relaxation time. The exposure durations are indicated in parentheses.

4.2 Durability

Another SOC was operated for 1338 h at a constant current density of 0.5 Acm^{-2} and exposed to 1 ppmv of HCl for 763 h followed by a 337 h recovery period in an HCl-free atmosphere, before a final exposure to 2 ppmv of HCl for 238 h; the time evolution of the SOC voltage and the HCl concentration are reported in Figure 4.7a. During the first 450 h, the degradation was relatively mild and the voltage increased from 1.13 to

1.15 V corresponding to a degradation rate of 44 mVkh^{-1} , which is comparable to the 50 mVkh^{-1} recorded during the experiment presented in the section 4.1.2 for the same current density and HCl concentration. After 450 h, the SOC voltage began increasing drastically; the degradation rate reached 555 mVkh^{-1} between 525 h and 700 h and then slightly decreased before the HCl supply was cut. During the recovery in an HCl-free atmosphere, the cell voltage continued degrading for about 125 h and before showing a small improvement for the next 200 h. When 2 ppmv of HCl were added to the reactant feed, the cell voltage rose at a rate of 530 mVkh^{-1} and then began stabilizing after 150 h of exposure. Unfortunately, a water-pump dysfunction lead to a steam supply shortage that irreversibly damaged the SOC and ended the test prematurely.

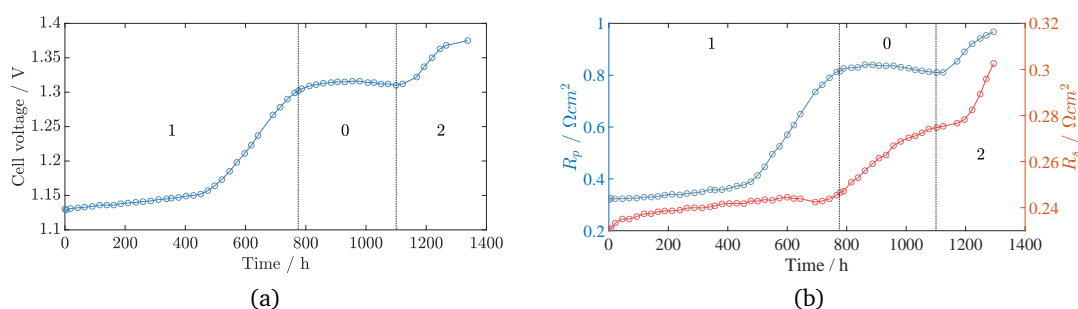


Figure 4.7 – Time evolution of (a) the cell voltage and (b) R_s and R_p during the durability test at a constant polarization of 0.5 Acm^{-2} , where the numbers in the plot area are the HCl content in ppmv

The observed voltage evolution was closely related to R_p , as shown in Figure 4.7b. Similarly to the cell voltage, R_p slowly increased during the first 450 h from 0.32 to $0.38 \Omega \text{cm}^2$ before it more than doubled over the next 325 h, reaching $0.82 \Omega \text{cm}^2$ before the HCl supply was shut off. R_s was much less impacted and only increased from 0.23 to $0.25 \Omega \text{cm}^2$ during the entire exposure to 1 ppmv of HCl. Interestingly, when the HCl supply was cut, R_p slowly stabilized and even decreased whereas R_s increased significantly but then stabilized towards the end of the recovery periods when R_p started decreasing. The increase of R_s was much larger during the recovery period than during the entire exposure to 1 ppmv of HCl. The behavior of R_s and R_p seemed to be highly correlated. When the 2 ppmv of HCl were added to the reactant stream, both R_p and R_s increased but with a slight time lag. R_p and R_s increased by approximately 19 % and 10 %, respectively, but only R_p showed signs of stabilization after 191 h of exposure.

During the first 450 h, the peak located between 3 and 10 kHz increased whereas the other peaks remained seemingly constant, corresponding to a mild voltage increase, as presented in Figure 4.8. After 450 h, the same peak began increasing rapidly and shifted towards lower frequencies, covering the peaks located between 100 Hz and 1 kHz, which made the deconvolution more difficult. The peak increase began slowing down after

715 h, which was reflected by an inflexion of the cell voltage. The peak located around 1 Hz, which is particularly sensitive to the reactant composition, also increased. Hagen et al. [265] observed a similar behavior during a sulphur poisoning experiment performed on the Ni–ScYSZ electrode of an SOFC fueled by methane, which they attributed to a S–Ni interaction affecting the catalytic and electrochemical properties of the electrode. It was thus assumed that the same processes were affected during the HCl contamination experiment. The increase of R_p around 1 Hz and 1 kHz was thus attributed to the deactivation of the catalytic activity and limitation of the charge transfer processes at the TPBs, respectively. Chlorine was also found to interact with Ni and reduce the catalytic activity of Ni-containing H_2 -electrode [153] and permanently deteriorate Ni-based catalysts [217]. The observed degradation thus was likely related to the interaction of Cl with Ni reducing the electrochemical and catalytic performance of the SOEC. Interestingly, unlike sulphur contamination where a fast degradation is observed initially due to the rapid adsorption of S on Ni, HCl appeared to be rather sluggish, suggesting that Cl adsorption on Ni was less favored. This may have been the result of a competitive adsorption between CO and Cl on Ni, as proposed by [215].

The trigger to the sudden voltage increase related to the degradation of the charge transfer processes may have been related to the time needed for the HCl to contaminate the entire Ni current-collector and SOC H_2 -electrode support, or the time related to a cumulative effect of HCl. After that time, HCl could interact significantly with the Ni electrochemically active sites and limit the processes at the TPBs. If this behavior is only related to an adsorption process then the sudden voltage increase should start when the concentration of HCl on the outlet gases is equal to that of the inlet gases. Therefore, the analysis of the outlet gas composition may provide a better insight on the degradation mechanism involved.

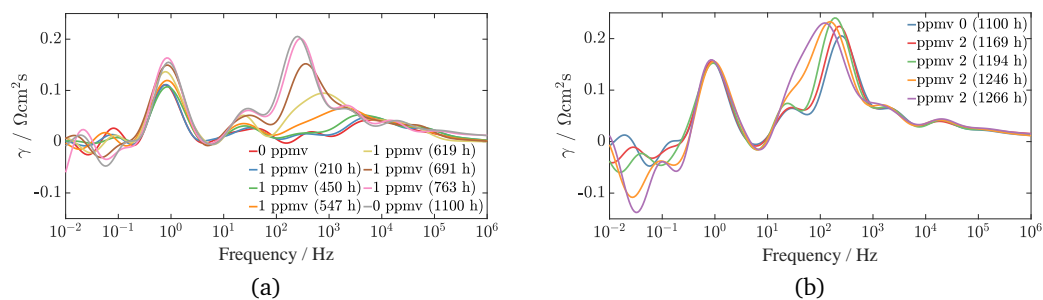


Figure 4.8 – Evolution of the DRT during a) exposure to 1 ppmv of HCl and recovery and b) exposure to 2 ppmv of HCl. The time at which the EIS were recorded are indicated in parentheses.

The DRT peak located between 3 and 10 kHz, which is related to the reactions at the TPBs in the H_2 -electrode, increased earlier and more than the conversion peak (around 1 Hz). This may be a result of the lower share of Ni electrochemical sites (vicinity of

the electrolyte) compared with the catalytic sites (entire electrode thickness and current collector) or may indicate that the HCl interacted preferentially with the electrochemically active Ni particles. The latter would be consistent with the results presented in section 4.1.2, where increasing the current density was found to increase the degradation of the DRT peak related to the reactions at the TPBs. During the recovery period in a HCl-free atmosphere, only a very small improvement of the peak located around 1 Hz was observed, which was similar to the results reported by Madi et al. [215] for an SOFC operated with H_2 and exposed to HCl. The TPBs were, however, irreversibly damaged by HCl and no recovery was observed. This may have originated from permanently adsorbed chlorine on Ni active sites, a modification of the microstructure potentially due to the reduced melting temperature of Ni in the presence of adsorbed chlorine [209], or a combination of both effects.

When the HCl concentration was increased to 2 ppmv, the peak related to the TPB's reaction started increasing again and also widened, leading to the formation of a single peak extending from 5 to 500 Hz. The peak located around 1 Hz did not increase any further, suggesting that the degradation related to the catalytic activity reached a saturation, and that HCl remained trapped in the H_2 -electrode and was not or only marginally removed during operation in a HCl-free atmosphere. As R_p , increased, so did R_s , likely caused by a cumulative effect of HCl blocking the electrochemically active sites in the vicinity of the electrolyte. The electrochemical reactions were then relocated further from the electrolyte virtually increasing the electrolyte thickness and consequently R_s . A similar behavior was observed during SO_2 poisoning and will be discussed in more detail in section 5.2.1.

After approximately 690 h, a low-frequency hook started appearing in the recorded electrochemical impedance spectra, as shown in Figure 4.9. This pseudo-inductive behavior stabilized when the HCl was stopped and increased again when the HCl supply was restarted, indicating a link with the HCl-induced degradation. The low-frequency hook corresponded to a negative relaxation time, as shown in Figure 4.8, at frequencies below 0.1 Hz. The growth of the low-frequency hook seemed to accompany the increase of the DRT peak related to charge transfer. Nechache et al. [257] observed a similar low-frequency hook on a highly degraded SOEC presenting deposits of Si-compounds. They attributed the presence of a low-frequency hook to either the electronic conductivity of the YSZ electrolyte [257] or a two-step reaction mechanism (Volmer–Heyrowsky-type reaction) involving adsorbed H_2O as an intermediate species [256]. A low-frequency hook was also observed during SO_2 poisoning, this will be discussed in more detail in section 5.2.2.

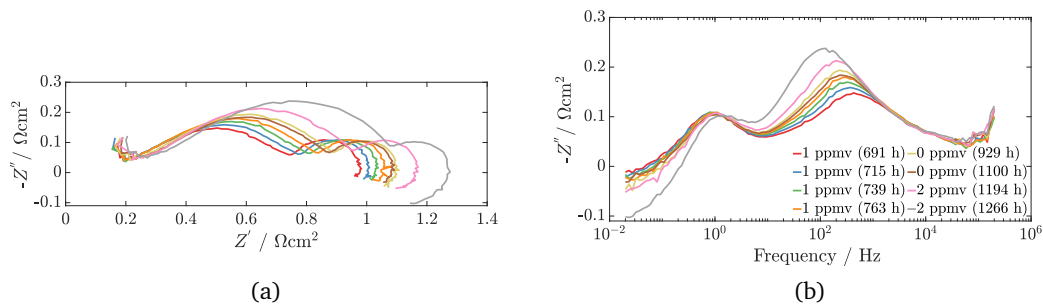


Figure 4.9 – Evolution of the EI taken at 0.5 Acm⁻² during exposure to HCl and recovery in HCl-free mixture. The time at which the EI were recorded are indicated in parentheses.

4.3 Conclusion

The impact of adding HCl to the reactant gas stream on the Ni-YSZ H₂-electrode of an SOC operated in co-electrolysis was investigated. When no current was applied, HCl concentration up to 10 ppmv did not significantly modify the SOC performances. The SOC was found to be more impacted under polarization with a significant degradation occurring with 5 ppmv of HCl. When the HCl was stopped and the SOC was operated in a HCl-free atmosphere, the SOC voltage increased further, possibly due to remaining HCl, before it eventually stabilized; but however the voltage never recovered. The correlation of the cell voltage evolution with the HCl content confirmed that the observed degradation was related to HCl poisoning.

Analysis of the DRT showed that the observed voltage increase originated mostly from an irreversible degradation of the charge transfer processes. Increasing the current density was found to be detrimental to the SOC tolerance towards HCl, as emphasized by the larger increase of the charge-transfer-related DRT peak at 0.5 than at 0.25 Acm⁻². This indicated that HCl preferentially interacted with the electrochemically active sites. The short-term test performed at 0.5 Acm⁻² was not done on a new SOC but on the same SOC that had already been exposed to HCl at 0 and 0.25 Acm⁻² which may have weakened the SOC. However, under the same operating conditions (0.5 Acm⁻², 1 ppmv of HCl), a similar degradation rate was observed on the fresh SOC used during the durability test, indicating that the history of the SOC used for short-term exposure did not influence its tolerance to HCl.

During the durability test performed at 0.5 Acm⁻² with 1 ppmv of HCl, the SOC voltage increased steadily at a rate of 44 mVkh⁻¹ for approximately 450 h before that the degradation rate increased drastically, reaching 555 mVkh⁻¹. When the HCl supply was shut off, the SOC voltage stabilized but did not significantly recover. HCl was found to principally impact the polarization resistance but, interestingly, the serial resistance

increased significantly during the recovery in a HCl-free atmosphere, suggesting that the HCl desorption was also detrimental. The exposure duration and history appeared to play key a role in the SOC degradation, thus emphasizing the necessity of performing longer term tests with contaminants and exposure-recovery cycling.

A low-frequency hook in the impedance spectra appeared when the SOC was degraded and was likely correlated with the increase of the charge-transfer processes' resistance at the H₂-electrode electrode. This phenomenon may have originated from the activation of an another electrochemical pathway including an intermediate species (Volmer–Heyrowsky-type reaction) or the enhancement of an electric current in the electrolyte.

The proposed degradation mechanism for chlorine poisoning involves the adsorption of a Cl species on Ni reducing principally the electrochemical activity and the catalytic reactions. The Cl adsorption is likely irreversible and may also accelerate the Ni depletion that is generally observed during longterm electrolysis [78, 88, 91, 92] by lowering the Ni melting point enhancing Ni mobility [209]. In this work, HCl was found to potentially interacts preferentially with the active Ni-site, i.e., close to the electrolyte, where Ni redistribution is the most important.

CHAPTER 5

Effect of SO₂

In section 5.1, the results obtained using a H₂-electrode-supported SOEC exposed to an SO₂ concentration ranging from 0 to 5 ppmv with a current bias ranging from 0 to 0.25 A cm⁻², corresponding to a maximal RU of 0.16 are presented and discussed. The SOC was exposed to SO₂ for short periods ranging from 19 to 70 h followed by a regeneration period in SO₂-free atmosphere for 20 to 120 h. The SOC was assembled with twisted pair lead wires, as described in Figure 3.1b.

In section 5.2, a second SOEC was exposed to 0.5 to 2 ppmv of SO₂ over a longer period in galvanostatic operation to assess the effect of SO₂ on the SOEC durability. The exposure duration varied from 50 to more than 500 h depending on the SOEC degradation behavior. After each exposure, the SOC was operated in an SO₂-free atmosphere. The SOC was assembled with twisted pair lead wires as described in Figure 3.1b.

After the reduction step, a mixture composed of 65 vol% H₂O, 25 vol% CO₂, and 10 vol% H₂ was used on the H₂-electrode side with a flow rate of 150 Nml min⁻¹. Addition of argon containing 1000 ppmv of SO₂ was used to control the concentration of SO₂ in the reactant stream. The added Ar and SO₂ always represented less than 1 % of the total reactant flow; the dilution effects were thus considered negligible. The O₂-electrode was swept by air with a flow rate of 150 Nml min⁻¹. The tests were performed at 750 °C.

Thermodynamic equilibrium calculations performed with HSC Chemistry 8.2.0 [263] showed that, with the reactant gas mixture used, SO₂ is not stable at 750 °C under 1 atm and tends to form H₂S. However, the kinetics of the decomposition reactions were not considered in this computation. The exact chemical form of the sulfur compound present at the hydrogen electrode is thus not exactly known. The thermodynamic equilibrium gas composition at 750 °C is 67.2 vol% H₂O, 22.9 vol% CO₂, 7.9 vol% H₂, and 2.1 vol% CO, which differs from the sent reactant gas mixture due to the RWGS reaction.

Contributions to the Field

Evaluated the effect of SO₂ on the lifetime and performance of an SOC operated in co-electrolysis. The results presented in this chapter have been published in [174].

5.1 The effect of polarization and SO₂ concentration

5.1.1 Open-circuit conditions

An SOEC under open-circuit conditions (OCC) was exposed to 0.5, 1, 2, and 5 ppmv of SO₂ during a period ranging from 19 to 24 h intercalated with a 20 h recovery period during which the cell was flushed with an SO₂-free reactant. Before the first exposure to SO₂, the measured cell voltage (V_0) was only 2 mV above the theoretical Nernst potential computed using the reactant composition at thermodynamic equilibrium, 0.865 and 0.863 V, respectively. This indicated that the reactant flow was close to the thermodynamic equilibrium and that the SOEC sealing was gas-tight.

For clarity, a schematic representation of the observed SOEC voltage time evolution during poisoning by SO₂ is presented in Figure 5.1; values reported in Table 5.1 are also represented.

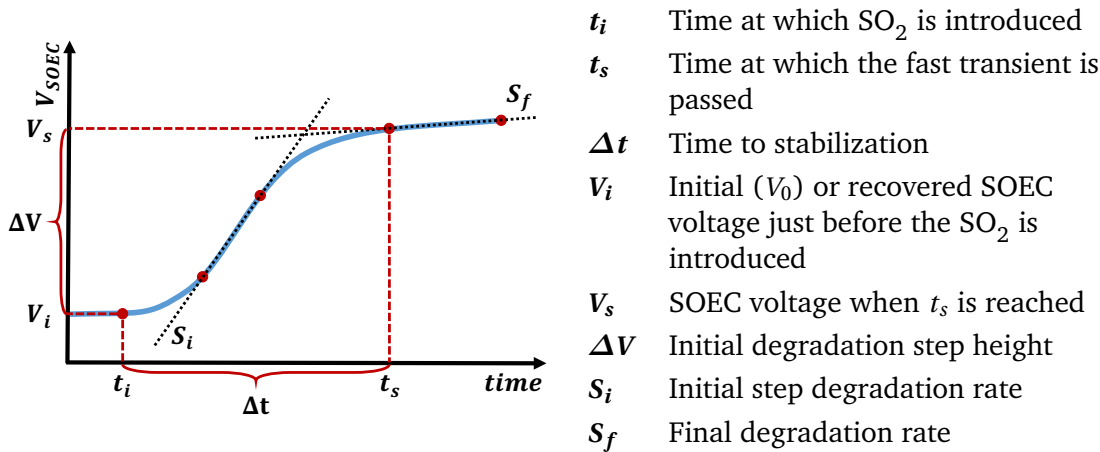


Figure 5.1 – Schematic representation of the SOEC voltage time evolution during poisoning by SO₂

When exposed to SO₂, the SOEC voltage showed a step-like increase pattern, as presented in Figure 5.2a. The height of the step, computed from V_0 , and the slope of the step appeared to be correlated with the SO₂ concentration, as presented in Table 5.1. After this initial step increase, the voltage steadily increased at a rate of approximately 20 to 30 mVkh⁻¹, without any apparent relation with the SO₂ concentration. When the exposure to SO₂ was stopped, the voltage almost instantaneously started decreasing. The recovery was much slower than the contamination and was never complete, suggesting an irreversible effect of sulfur even after exposure to only 0.5 ppmv of SO₂. The rapid initial degradation followed by a reduced and constant deactivation and a slower recovery process once the sulfur supply was stopped was in good agreement with observations reported for SOFCs exposed to sulfur compounds [183, 189, 193, 198, 199]. As the SOEC was not polarized, it was similar as testing an SOFC at high H₂O and CO₂ content.

5.1. The effect of polarization and SO₂ concentration

The initial voltage step was thus attributed to the same process that occurs in SOFC, i.e., adsorption of sulfur on nickel, which reduces both the catalytic and electrochemical performances of the SOEC. Analogously to (2.3), this adsorption reaction can be described as



or



depending on whether sulfur is present in the form of H₂S or SO₂, where S_{ad} represents the sulfur adsorbed on Ni.

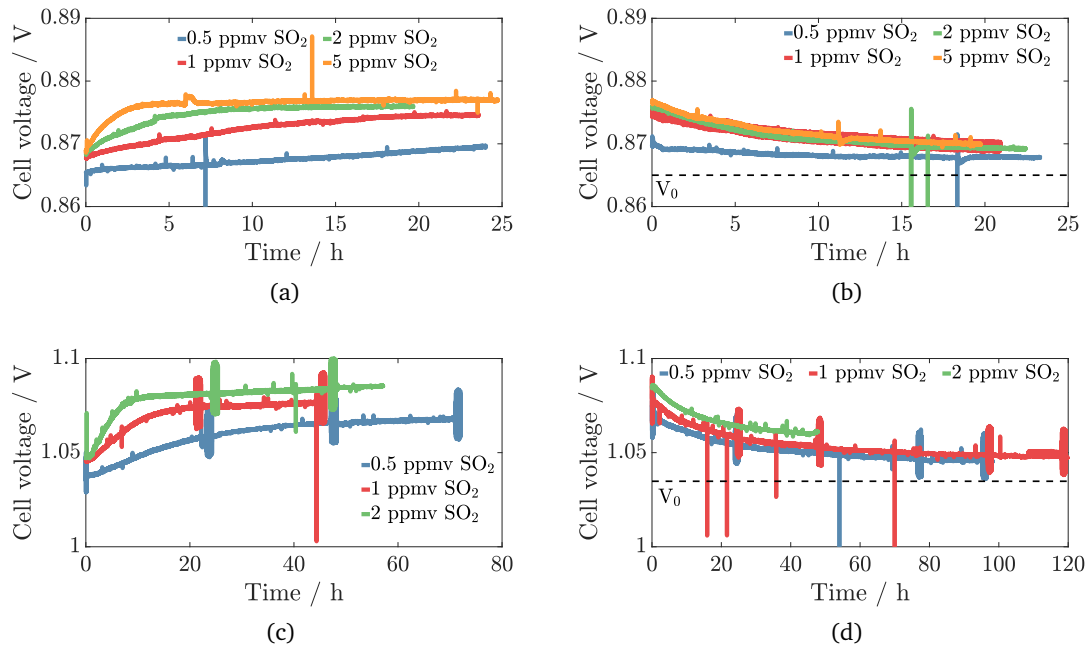


Figure 5.2 – Time evolution of the cell voltage when exposed to various concentrations of SO₂ and during recovery, respectively, at (a) and (b) OCV and (c) and (d) 0.25 A cm⁻², respectively.

As no bias current was applied, solely a modification of the gas composition at the hydrogen electrode could affect the measured cell voltage. It was thus assumed that the catalytic reactions (i.e., RWGS reaction) were limited due to the coverage of nickel by sulfur preventing the feed gas from reaching the thermodynamic equilibrium composition. This is in agreement with He et al. [266] and Hagen [199] who reported a deactivation of the RWGS reaction when the nickel-based anode of an SOFC operating on syngas was exposed to H₂S.

The deviation from thermodynamic equilibrium was then evaluated by assuming that the measured OCV corresponded to the Nernst potential of an effective gas composition between the inlet and thermodynamic equilibrium composition. Using HSC Chemistry 8.2.0 [263], thermodynamic equilibrium gas compositions were computed at varying effective temperatures until the corresponding Nernst potential matched the measured OCV. The difference between the effective and actual operating temperature represents the deviation of the composition from the thermodynamic equilibrium. The observed increase in OCV due to the presence of SO₂ thus corresponds to a thermodynamic equilibrium composition at an effective temperature lower than the actual operating temperature, indicating a reduction of the RWGS reaction. The increase of 12 mV observed after exposure to 5 ppmv of SO₂ seen in Figure 5.2a corresponded to a 25 °C decrease of the effective temperature. As the CO content of the equilibrium reactant composition originated only from the RWGS reaction, its variation relative to the composition before exposure to SO₂ was used as a quantitative indicator of the modification of the catalytic activity. In Figure 5.3, reduction of the CO content is compared with the surface coverage of Ni using correlation (5.3) proposed by Hansen [202] that was originally developed for H₂S and adapted here by simply replacing the partial pressure of H₂S by the partial pressure of SO₂. Further work is needed to assess the validity of this adaptation for SO₂.

$$\theta_s = 1.45 - 9.53 \cdot 10^{-5} \cdot T + 4.17 \cdot 10^{-5} \cdot T \cdot \ln \frac{p_{\text{SO}_2}}{p_{\text{H}_2}} \quad (5.3)$$

When the cell was exposed to 5 ppmv of SO₂, the surface coverage reached 0.93, whereas the CO content decreased by only 7.5 %. The reduction of the CO content seemed to stabilize below 10 %. The effect of SO₂ on the RWGS reaction was thus relatively small, thanks to the high nickel content present in the H₂-electrode (acting as a catalyst and electro-catalyst), and the nickel current collector (acting as a catalyst). However, the reduction of the catalytic activity in the vicinity of the TPB may still have a significant impact on the SOEC performance under polarization due to the limited RWGS reaction reducing the local steam content.

The modification of the electro-chemical performances of the SOEC was assessed by performing EIS measurements after each exposure to SO₂ and after each recovery period. The results, summarized in Figure 5.4, showed that most of the degradation occurred between 10 Hz and 10 kHz, whereas no increase of R_s was observed. The DRT results (Figure 5.4c) clearly demonstrated that the major contribution to the increase of R_p occurred on the peak located at approximately 1 kHz, which is associated with the charge transfer processes occurring at the H₂-electrode. The peak increased drastically and shifted towards a lower frequency, leading to the covering of the peak located around 100 Hz, which is related to the transport processes in the hydrogen and oxygen electrode, making the deconvolution impossible. Even though the measured cell potential mostly recovered from the exposure to SO₂, the impedance response did not completely recover,

5.1. The effect of polarization and SO₂ concentration

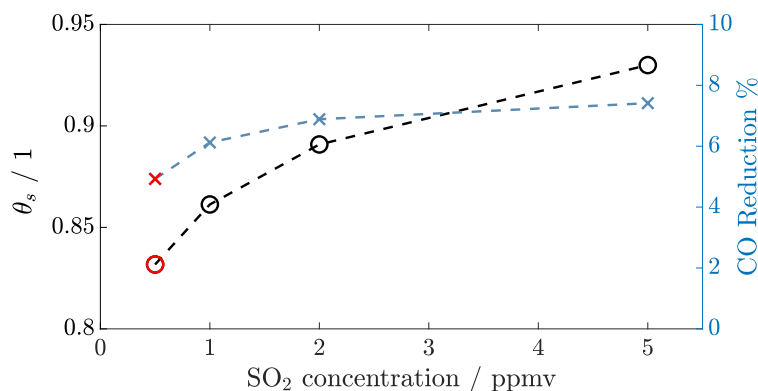


Figure 5.3 – Ni coverage and reduction of the CO content with respect to the SO₂ content. The reduction of the CO content was computed based on the equivalent composition corresponding to the initial OCV measured. The red data points were extrapolated.

suggesting that part of the Ni active sites remained covered. During the recovery following the exposure to 0.5 ppmv of SO₂, the DRT peak located around 1 kHz continued increasing, despite the decreasing (i.e., recovering) OCV. The current collector, being made of Ni, likely adsorbed sulfur during the exposure period and then slowly released it during the recovery period, thus acting as a sulfur buffer. This may have provided enough time and supply for sulfur to deposit on the active Ni, leading to the observed increase of impedance even after the SO₂ supply was shut off.

The increase in R_p after exposure to SO₂, presented in Figure 5.4d, showed a linear dependency with the Ni surface coverage, similarly to the results reported by Hansen [202] for H₂S poisoning. The polarization resistance obtained after exposure to 0.5 ppmv SO₂ was not considered here as it did not reach a stable state. The multiplicative coefficient of the linear interpolation was in good agreement with the results reported by Madi et al. [183] for an SOFC operated on synthetic bio-gas containing various amounts of thiophene. To a smaller extent, the increase in R_p after recovery was also found to be linearly dependent on θ_s , indicating that the retentive effect of SO₂ exposure was likely related to permanently adsorbed sulfur.

Table 5.1 – ΔV measured from the initial (recovered) voltage, S_i , S_f , and Δt as defined in Figure 5.1, when the SOECs were polarized at a current density j and exposed to various concentrations of SO₂.

j A cm ⁻²	SO ₂ ppmv	ΔV mV	S_i mVkh ⁻¹	S_f mVkh ⁻¹	Δt h
0	0.5	8 ^a	200	n.s. ^c	40 ^a
	1	9 (7)	400	20	20
	2	11 (7)	1100	30	10
	5	11 (8)	2500	20	4
0.25	0.5	28	1000	100	40
	1	36 (28)	2300	100	20
	2	42 (33)	4600	100	10
0.5 ^b	1	140	26'500	60	7.7
	1	230 (120)	29'500	40	5.3
	2	260 (150)	100'300	100	3.3
	0.5	260 (130)	11'400	30	20

^a linearly extrapolated based on the stabilization times obtained with other SO₂ concentrations and the initial degradation slope.

^b these results, obtained during the durability test, are discussed in section 5.2.

^c not stabilized

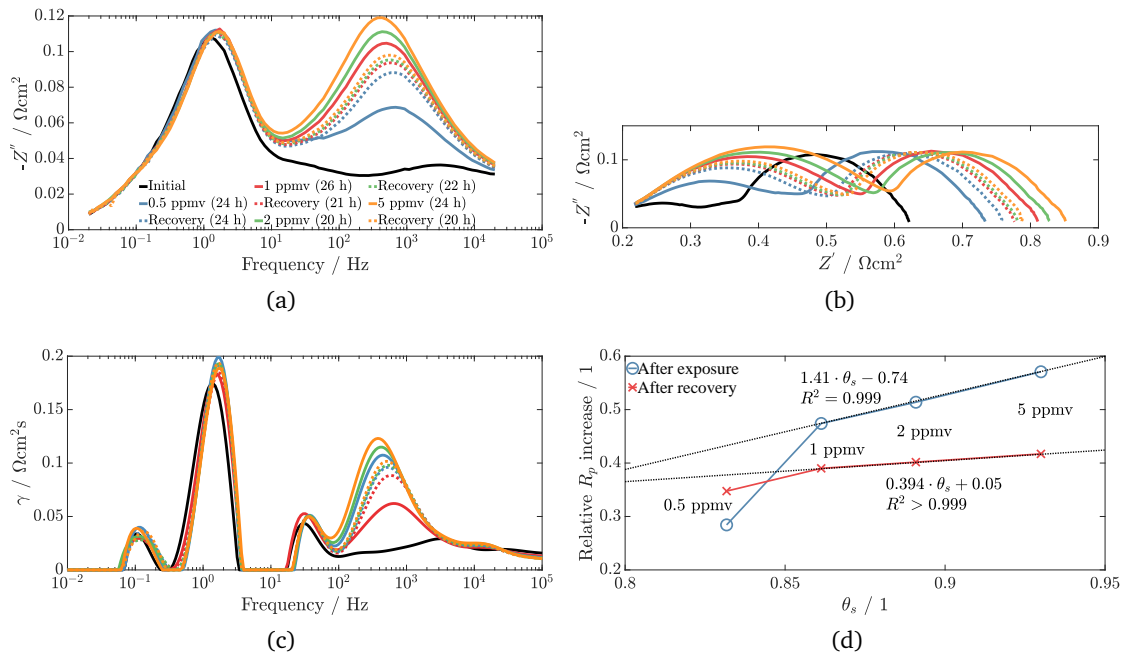


Figure 5.4 – (a) and (b) electrochemical impedance spectra taken at OCV after exposure to 0.5, 1, 2, and 5 ppmv of SO₂ followed by a recovery period without SO₂, (c) corresponding DRT, and (d) relative increase of R_p function of the surface coverage . The exposure/recovery durations are indicated in parentheses.

5.1.2 Under polarization (0.25 A cm⁻²)

A second SOEC was exposed to 1 ppmv of SO₂ for 25 h followed by a 40 h recovery period at OCC. The cell was, then, polarized at 0.25 A cm⁻² and successively exposed to 0.5, 1, and 2 ppmv of SO₂ during a period ranging from 45 to 70 h each time followed by a recovery period where the cell was flushed with an SO₂-free reactant.

Under polarization, the SOEC showed a step-like degradation when exposed to SO₂, as shown in Figure 5.2c, similarly to the OCV case. The initial degradation step height was about two to three times larger when the cell was polarized compared with the OCV case but the time needed to reach a stabilized state was similar regardless of whether a 0.25 A cm⁻² bias was applied or not, as seen in Table 5.1. However, the final degradation rate was about three to four times higher under polarization than at OCV. When the exposure to SO₂ was stopped, the SOEC's voltage decreased with an hyperbolic-like shape but the recovery was never complete, as presented in Figure 5.2d. During the recovery process, after exposure to 2 ppmv of SO₂, a technical issue with the galvanostat ended the test prematurely, thus only EIS data after exposure to 0.5 and 1 ppmv were available.

EIS measurements taken after 72 h of exposure to 0.5 ppmv of SO₂ showed that both the high- and low-frequency processes were affected, as shown in Figures 5.5b and 5.5a. Analysis of the DRT results of the impedance spectra showed that the peaks located around 1 Hz and between 100 Hz and 1 kHz increased, as presented in Figure 5.5c. The peak located around 1 Hz is sensitive to the reactant composition [12], which is coherent with a reduction of the catalytic reactions due to the coverage of nickel by sulfur [199]. This degradation should stabilize when the equilibrium between the surface coverage and the sulfur content in the reactant is reached. The increase of the peak located around 1 kHz was indicative of a deterioration of the charge-transfer processes and a modification of the gas composition. The behavior observed for an SOEC operated in co-electrolysis mode was found to be very similar to the one reported for an SOFC operated under reformat operation [194, 195], indicating an analogous contamination process independently of the current direction.

Increasing the SO₂ content to 1 ppmv led to an increase of the EI between 100 Hz and 1 kHz; no significant changes were observed around 1 Hz, suggesting that a saturation was reached (Figure 5.5). When the SO₂ content was raised to 2 ppmv, no further significant changes were observed when compared with 1 ppmv (Figure 5.5). After the recovery period, the peak located around 1 kHz shifted back to its original relaxation frequency but did not recover completely, whereas the peak located around 1 Hz almost completely recovered.

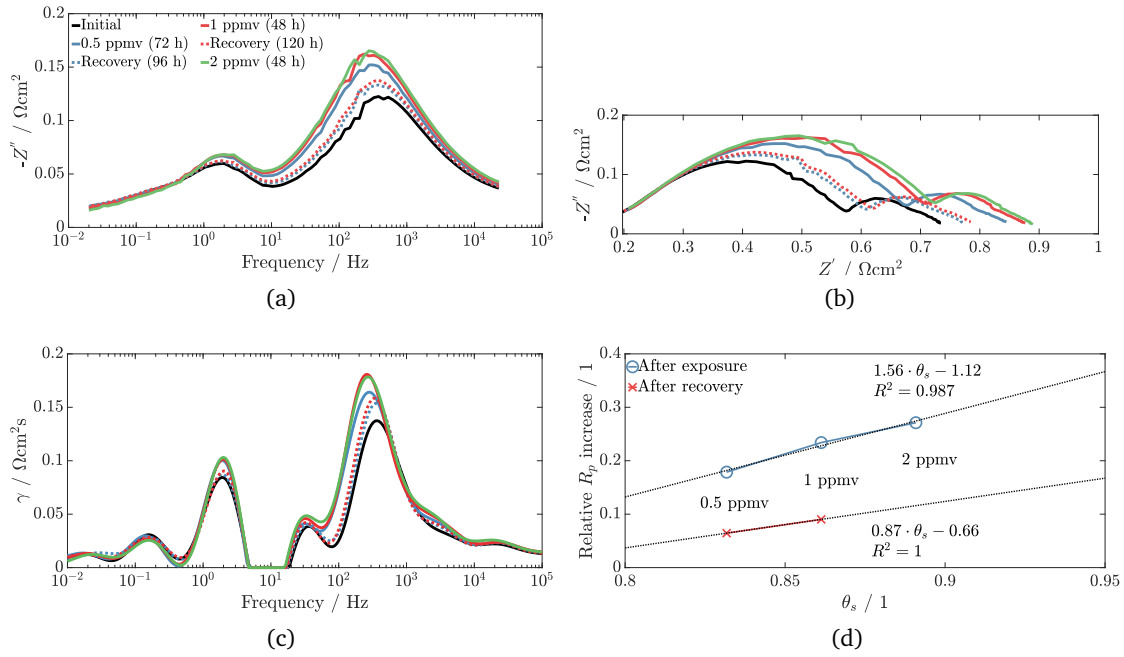


Figure 5.5 – (a) and (b) electrochemical impedance spectra taken at 0.25 Acm^{-2} after exposure to 0.5, 1, and 2 ppmv of SO₂ followed by a recovery period without SO₂ and (c) corresponding DRT and (d) relative increase of R_p as a function of the surface coverage. The exposure/recovery durations are indicated in parentheses.

Similarly to the OCV tests, the relative increase in R_p showed a linear behavior with respect to θ_s , as presented in Figure 5.5d. The relative increase in R_p was found to be smaller than at OCV but this was likely due to the test history. The initial impedance response at 0.25 Acm^{-2} (Figure 5.4d) was not measured on a "fresh" SOEC but after exposure at OCV to 1 ppmv of SO₂ and a recovery period. The relative increase of R_p was, thus, not computed on the same basis and can not be directly compared. The coefficients multiplying θ_s in Figure 5.4d and 5.5d represents the sensitivity of the relative increase in R_p towards θ_s . This coefficient was larger when the SOEC was polarized than in the OCC case, 1.56 and 1.41, respectively, indicating that the SOEC was more sensitive to an increase of the SO₂ content when polarized, and that the polarization had a negative impact on the SOEC tolerance to SO₂.

Under polarization, hydrogen was generated, which should reduce the surface coverage of nickel by sulfur, according to correlation (5.3). However, due to the logarithmic dependency on the hydrogen partial pressure and the low reactant utilization (0.15 at 0.25 Acm^{-2}), this effect was likely minor. In SOFC operation, the current density has been found to improve the sulfur tolerance [190, 221, 267]. A higher oxygen ion flux at the TPB has been suggested to help the desorption of the adsorbed sulfur by oxidation, which can be expressed as the reverse of equation (5.2). During operation as a SOEC, the opposite effect could be expected, as the polarity and thus oxygen ion flux is inverted.

However, prior researchers have shown no [265] or a negative impact [220, 268] of the current density on the sulfur tolerance of an SOFC. Future efforts should aim to clearly assess the effect of current density on the sulfur tolerance of an SOEC.

5.2 Effect on Durability

Another SOEC was operated during 2500 h at 0.5 A cm^{-2} with periodic exposure to SO_2 to assess the long-term stability; the time evolution of the cell voltage and SO_2 concentrations are presented in Figure 5.6a. In the first 200 h, the SOEC showed the same step-like degradation pattern as presented in sections 5.1.1 and 5.1.2, i.e., a fast degradation (0 to 15 h) followed by a reduced and constant degradation (15 to 200 h). When compared with exposure to 1 ppmv of SO_2 at lower current density, the initial degradation rate and the time to stabilization were strongly affected by the current density, whereas no apparent link was found with the height of the initial degradation step and the final degradation rate. At 0.5 A cm^{-2} , the kinetics of sulfur adsorption on nickel was likely promoted more than at a lower current density.

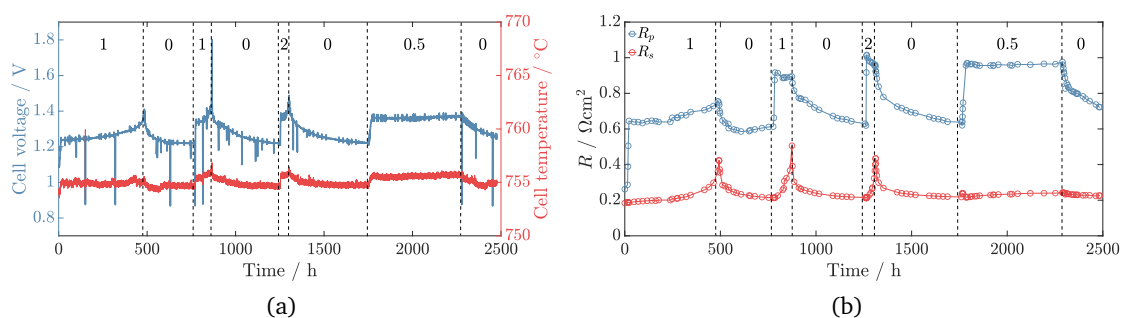


Figure 5.6 – Time evolution of (a) the cell voltage and temperature and (b) of R_s and R_p during the long-term stability test, where the numbers at the top of the graphic indicate the SO_2 concentration in ppmv.

For the first 11 h, the degradation was only caused by an increase of R_p , as shown in Figure 5.6b, where the time evolution of R_s and R_p is represented. According to the DRT of the EIS measurements taken during the rapid degradation, shown in Figure 5.7, the high-frequency impedance increased first, followed by an increase over the entire spectrum until a relative stabilization. The DRT peak located around 1 kHz increased massively and shifted towards a lower frequency, likely due to the adsorption of sulfur on the nickel active sites affecting the electrochemical conversion of $\text{H}_2\text{O}/\text{H}_2$ and CO_2/CO [194, 195]. The DRT peak located around 1 Hz first decreased and widened, and then increased while shifting towards a higher frequency. The width of a DRT peak can be related to the spatial distribution of the relaxation time associated with a particular phenomenon [115], e.g., due to inhomogeneities in the micro-structure [269]. During the initial fast degradation caused by sulfur, Rasmussen and Hagen [193], and Hagen

[199] observed a peak of the in-plane voltage that was attributed to a redistribution by the current due to the progressive adsorption of sulfur on nickel from the inlet to the outlet. The widening of the DRT peak located around 1 Hz was thus assumed to be the result of the progressive adsorption of sulfur on nickel, which locally reduced the catalytic and electrochemical reactions, thereby modifying the reactant composition until the nickel coverage was at equilibrium. The peak located around 25 Hz increased and shifted towards a higher frequency, suggesting that the diffusion processes at the H₂-electrode were impacted. As a consequence of the various peak shifting, the DRT between 10 Hz and about 30 kHz was compressed in a smaller frequency range after exposure to SO₂, making the deconvolution of the different processes involved more complicated.

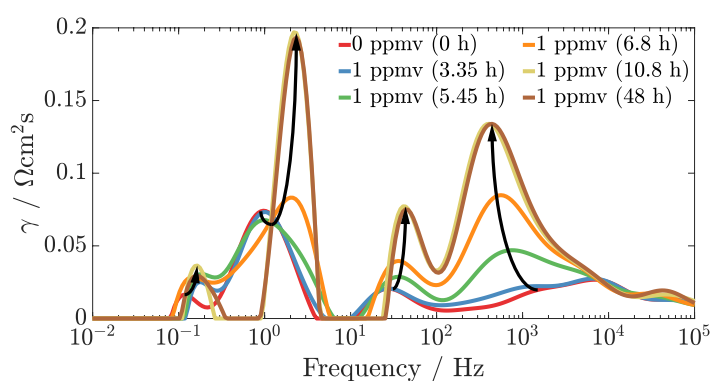


Figure 5.7 – Time evolution of the DRT during the long term stability test, where the arrows represent the observed trends.

After the initial fast voltage rise, the degradation rate remained at approximately 60 mVkh⁻¹ until 200 h, when both R_p and R_s began increasing, as shown in Figure 5.6b. The degradation rate then increased to 200 mVkh⁻¹. After approximately 400 h, the voltage began increasing exponentially due to an increase of the R_s , whereas the R_p remained nearly constant, thus suggesting the presence of a cumulative effect due to the exposure to SO₂. After 485 h, the exposure to SO₂ was stopped to limit the voltage increase. After less than 5 h, likely due to the presence of residual SO₂, the R_p and R_s began decreasing simultaneously. After about 280 h of recovery, only R_s and the low-frequency region of the EIS had partially recovered, whereas the high-frequency region of the EIS (charge transfer) remained almost unchanged, as shown in Figure 5.8 (b) and (a).

Analysis of the DRT of the impedance spectra, presented in Figure 5.8c, showed that when the SO₂ supply was shut off, the conversion peak (around 1 Hz) greatly recovered but remained shifted to a higher frequency, whereas the low-frequency peak (around 0.1 Hz) widened and shifted towards a higher frequency. The charge transfer peak (around 1 kHz) continued increasing while shifting towards higher frequency and getting sharper. The electrochemically active sites were seemingly affected more permanently by sulfur than the rest of the cell was, also suggesting a negative impact of the current density on the SOEC durability when exposed to SO₂. During the recovery process, the shape

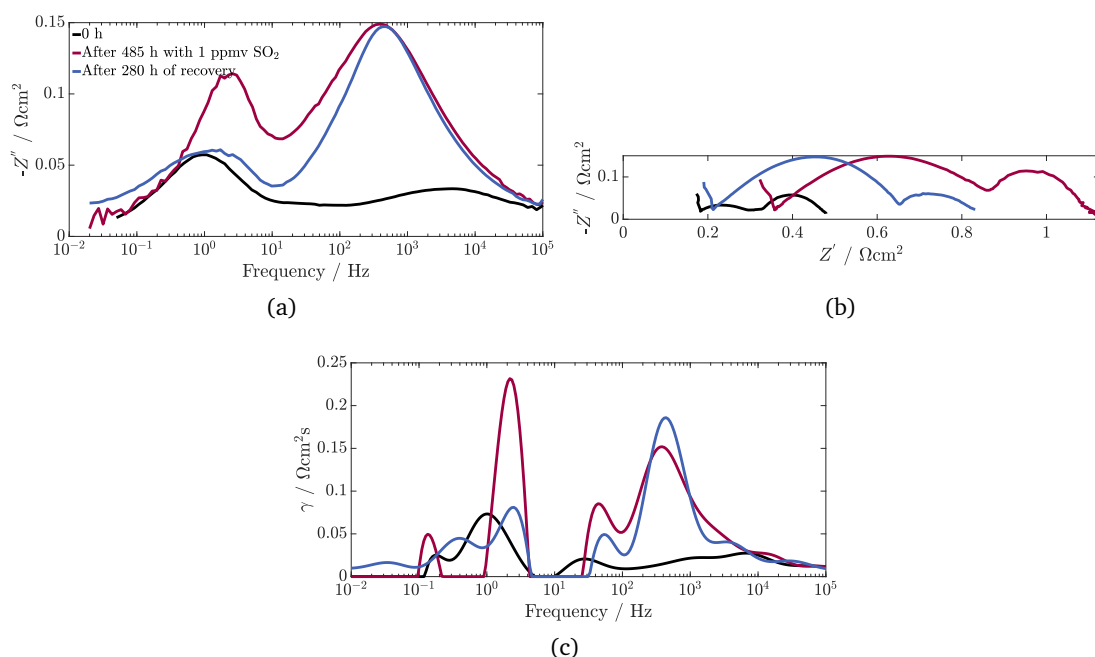


Figure 5.8 – (a) and (b) electrochemical impedance spectra taken at 0.5 Acm^{-2} during the first exposure to 1 ppmv of SO_2 followed by a recovery period without SO_2 and (c) corresponding DRT.

of the low-frequency region of the impedance spectra changed noticeably, especially below 0.1 Hz (Figure 5.8a), which resulted in the presence of a new peak at a very low frequency ($\approx 30 \text{ mHz}$), as shown in Figure 5.8c. The DRT fingerprints between 10 Hz and about 30 kHz remained compressed to a smaller frequency range.

The SOEC was then exposed to 1, 2, and 0.5 ppmv intercalated with a recovery period; the resulting SOEC voltage and cell temperature evolution are reported in Figure 5.6a. A similar behavior to the first exposure was observed: a fast initial increase of the cell voltage in the first hours after the introduction of SO_2 followed by a slower voltage increase, which eventually started to run away due to a drastic increase in R_s (only when exposed to 1 and 2 ppmv of SO_2), as shown in Figure 5.6b. The height of the initial step-like degradation was not found to be dependent on the SO_2 concentration, whereas the initial degradation rate and the time to stabilization appeared linked to the SO_2 concentration, as presented in Table 5.1.

5.2.1 Voltage "runaway"

The drastic increase of R_s occurred earlier when the SOEC was exposed to 1 ppmv of SO₂ for the second time and even earlier under 2 ppmv of SO₂. The polarization resistance between approximately 30 Hz and 1 kHz was the highest during the last exposure, even though the SO₂ concentration was the lowest (0.5 ppmv), thus indicating the presence of a cumulative effect caused by the successive exposure–recovery cycles.

The time needed to reach the voltage "runaway" regime was shorter during the second exposure to 1 ppmv of SO₂, suggesting a weakening of the SOEC after the first exposure. The voltage "runaway" regime was reached even more quickly during the exposure to 2 ppmv of SO₂. When the SO₂ supply was cut, R_s and R_p again decreased, confirming that the "runaway" behavior observed was linked to the presence of SO₂ in the reactant. When the SOEC was exposed to 0.5 ppmv of SO₂, however, the initial voltage increase was also present, but the voltage "runaway" was not observed even after more than 500 h of exposure. The "runaway" behavior thus appeared to be dependent on the history of exposure to SO₂ and only occurred above a certain SO₂ concentration.

When an increase in serial resistance was reported for an SOFC exposed to H₂S, it was found to be irreversible [222, 223], suggesting a different degradation and/or recovery mechanism for an SOEC exposed to SO₂. Two possible mechanisms, discussed in more detail in Appendix A, are proposed to explain the reversible increase of R_s :

- A progressive reduction of the active area due to the deactivation by sulfur of the electrochemically active Ni from the higher (inlet) to lower (outlet) current density regions. Assuming an analogous behavior to an electrode partial delamination, a comparable increase of R_s and R_p would be expected [270]. This is thus unlikely to be solely responsible for the observed behavior.
- A cumulative effect of sulfur blocking the electrochemically active regions located closest to the electrolyte, possibly from the higher (inlet) to lower (outlet) current density regions. The thickness of the electrolyte being on the order of 10 μm , the extent of the deactivated region would be on the order of 2 μm , considering that R_s increased by a factor of 2 to 3. This estimated thickness is in the order of the electrochemically active region in the vicinity of the electrolyte ($\approx 5 \mu\text{m}$) [88].

5.2.2 Low-frequency hook

During the second exposure to 1 ppmv of SO₂, a pseudo-inductive behavior began to appear at low frequencies when the SOEC was exposed to sulfur and during part of the recovery, as shown in Figure 5.9. This low-frequency pseudo-inductive behavior appeared to be more intense at the beginning of the exposures and then lowered in intensity, but did not completely disappear. It then slowly disappeared during the recovery period, as

shown in Figure 5.10a after exposure to 0.5 ppmv of SO₂. During the recovery, the low-frequency hook seemed to transition from an pseudo-inductive to a capacitive behavior only after the region around 2 Hz mostly recovered, as shown in Figure 5.10b.

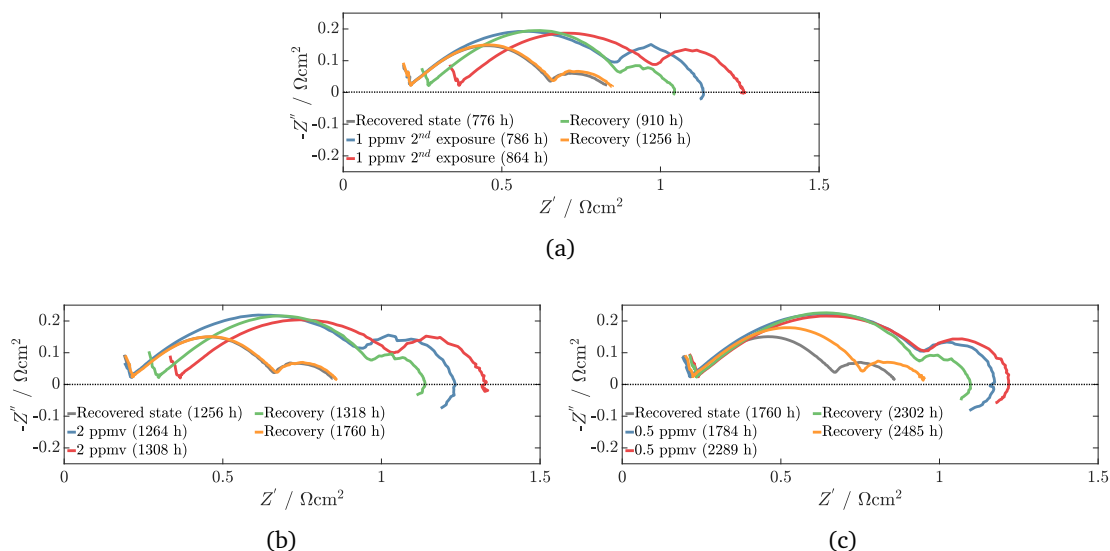


Figure 5.9 – Electrochemical impedance spectra taken at 0.5 Acm⁻² during the exposure to (a) 1 ppmv, (b) 2 ppmv, and (c) 0.5 ppmv of SO₂ followed by a recovery period without SO₂. The time from the beginning of the test at which the impedance spectra were measured is indicated in between parentheses.

Analysis of the DRT of the impedance measurements (Figure 5.10c) indicated that the peak located around 1 kHz first increased and then decreased while shifting towards a higher frequency during the entire recovery period, whereas the peak located around 100 Hz appeared to continuously improve and shift slightly towards a higher frequency. Due to the major overlapping of the DRT peaks between about 30 Hz and 1 kHz (Figure 5.10c), the observed peak transformation may have originated from the peak itself or the interaction with a neighbouring peak, making the physical interpretation complex. The other recovery periods showed a similar behavior except after the first exposure to SO₂. The low-frequency hook was not present during the first exposure period and was more intense when the cell was exposed to 2 ppmv of SO₂ than 1 ppmv (second exposure) but less than when exposed to 0.5 ppmv, as shown in Figure 5.9. This suggests that the inductive hook originated from the exposure–recovery cycling rather than from the concentration of SO₂ itself.

After the recovery period subsequent to the exposure to 0.5 ppmv of SO₂, EIS measurements were performed in co-electrolysis (65 %H₂O, 25 %CO₂, 10 %H₂) and steam-electrolysis (90 %H₂O, 10 %H₂) mode. Both showed an inductive hook at 0.75 Acm² but not at 0.5 Acm², indicating that the presence of CO₂ was not or only partially responsible for the low-frequency hook, whereas the current density or the overpotential plays a key role.

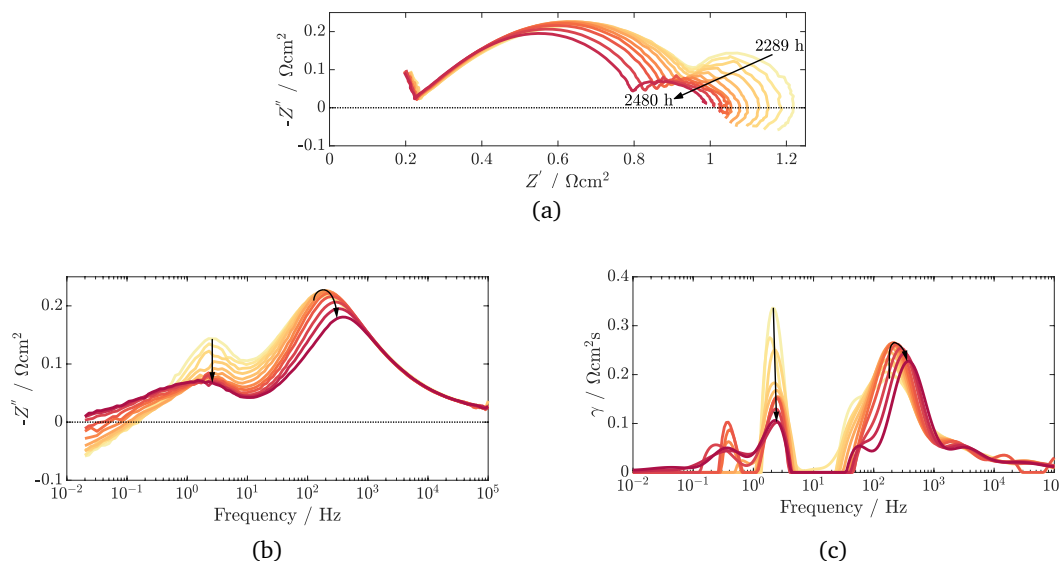


Figure 5.10 – (a) and (b) electrochemical impedance spectra at 0.5 Acm^{-2} taken during the recovery following the exposure to 0.5 ppmv of SO₂ and (c) the corresponding DRT. Black arrows represent the observed trends of the time-evolution from the last measurement taken with 0.5 ppmv of SO₂ (2289 h) until the end of the recovery period (2480 h) .

The low-frequency hook may be caused by a two-step reaction that involves an intermediate [254, 255, 271]. Nechache et al. [256] observed a low-frequency hook in the impedance spectra of an SOEC operated in steam-electrolysis and attributed it to the deposition of Si-containing impurities (originating from the glass gas sealing) in the H₂-electrode that limited the electrochemical reduction and transport of H₂O. They concluded that when a sufficiently high current density is applied, an additional reaction mechanism with a characteristic frequency between 1 and 10 mHz and involving adsorption of H₂O counterbalances the negative effects of Si-containing deposits. In electrolysis operation, the electronic conductivity of the YSZ electrolyte was also found to induce a low-frequency inductive arc [257]. Due to the clear correlation with the exposure to SO₂, the low-frequency hook was assumed to originate from the H₂-electrode but was not related to the deposition of Si-containing impurities. The low-frequency hook observed could then originate from either the activation of an additional reaction mechanism involving an intermediate [256] or the electronic conductivity of the YSZ [257], compensating for the deactivation of electrochemical active sites by sulfur. The presence of a low-frequency hook after recovery can be explained by the presence of residual sulfur on electrochemically active sites. A higher current was then necessary to activate the additional reaction mechanism. The oxidation of sulfur itself is rather unlikely to be responsible of this behavior as it would have thus only been visible when S was constantly supplied to the SOC.

5.3 Conclusion

The effect of SO_2 in the reactant gas stream of an SOE with an Ni-YSZ H_2 -electrode operated in co-electrolysis was investigated. Independently of the current density, exposure to as little as 0.5 ppmv of SO_2 showed irreversible effects on the SOEC performances, especially in the high-frequency domain of the impedance spectra, indicating a permanent damage done to the electrochemically active nickel. The general contamination process was found to be similar to an SOFC exposed to H_2S : a fast initial degradation followed by a steady degradation rate. A good correlation was found between the surface coverage of nickel by sulfur and the relative increase in polarization resistance. Analysis of the DRT of the impedance measurements showed that the charge transfer and gas conversion peaks were particularly affected by the exposure to SO_2 , thereby confirming that the interaction between sulfur and the nickel present in the electrode reduces the electrochemical and catalytic reactions.

The OCV values were used to estimate the variation of the reactant composition due to the deactivation of the catalytic activity. The estimated amount of CO, calculated via thermodynamic equilibrium, was used as an indicator, as CO originates only from the RWGS reaction. The estimated reduction of CO was only 7.5 % when the SOEC was exposed to 5 ppmv of SO_2 , corresponding to a nickel surface coverage of 0.93. This suggests a limited effect of the sulfur on the global catalytic activity under open-circuit conditions. The reduction of the CO seemed to stabilize below 10 %. In future works, gas chromatography, mass spectrometry, or other gas analysis methods should be used to assess the validity of these estimations.

The initial degradation rate was found to increase with the current density and the SO_2 concentration. Further, the time needed to reach stabilization was found dependent on the SO_2 concentration and potentially to the current density, whereas no clear correlations were found for the height of the initial step or the final degradation rate. At a higher current density, the relative increase of the polarization resistance relative to the SO_2 content was found to be greater. This indicates that the current density has a negative impact on the SOEC tolerance to SO_2 ; however, further investigation is necessary to completely assess the effect of the current density.

The durability test performed at 0.5 A cm^{-2} showed a drastic increase of the cell voltage tens of hours after the beginning of the exposure leading to a voltage "runaway" when the SOEC was exposed to 1 ppmv and 2 ppmv of SO_2 . This behavior was characterized by a large increase of the serial resistance. When the SO_2 supply was cut, the serial resistance recovered almost entirely. The origin of this behavior is not clear yet but may be related to a cumulative effect of SO_2 leading to the total deactivation of the TPB close to the electrolyte, thus shifting the electrochemically active area further and virtually increasing the electrolyte thickness. The extent of the affected region close to the electrolyte was estimated to about $2 \mu\text{m}$. This "runaway" behavior was not observed during the exposure

to 0.5 ppmv even after 500 h, suggesting that it is triggered by the SO₂ concentration and could be avoided by limiting the concentration to a sub-ppmv level at these operating conditions.

After successive exposure–recovery cycles, the SOEC's H₂-electrode seemed weakened and a low frequency pseudo-inductive hook was observed. This low-frequency hook expanded when the SOEC was exposed to SO₂, disappeared during the recovery period, and seemed to be dependant on the cell's exposure–recovery cycles rather than on the SO₂ concentration. The origin of this low–frequency hook is not clear yet but may be related to the activation of an additional electrochemical reaction involving an intermediate species or electronic conductivity of the YSZ phase.

Remarks

An informal discussion on YSZ electronic conductivity can be found in Appendix B.

PART

II

ACTIVE THERMOGRAPHY

CHAPTER 6

Introduction and basic principles

This chapter reviews the basics of thermal radiation, passive and active thermography, and the data analysis using Fourier transform. The theoretical introduction presented in this section is based on the work of Breitenstein et al. [272], Modest [273], Incropera and Incropera [274].

6.1 Thermal radiation

An object whose temperature is higher than 0 K emits electromagnetic radiation to its surroundings. The emitted radiation, which depends on the wavelength and the direction, is characterized by the spectral intensity I_λ . When dealing with radiative problems, it is often convenient to use spherical coordinates, where a direction is defined by a pair of angles θ and ϕ . I_λ was formally defined by Incropera and Incropera [274] in spherical coordinates as “the rate of radiant energy emitted at a specific wavelength λ in a direction (θ, ϕ) , per unit emitting surface normal to that direction, per solid angle about this direction, and per unit wavelength interval about λ ” and can be expressed as:

$$I_\lambda(\lambda, \theta, \phi) \equiv \frac{dq}{dA \cdot \cos(\theta) \cdot d\omega \cdot d\lambda}, \quad (6.1)$$

where dq is the rate at which radiation is emitted from the surface and propagates in a region defined by a solid angle $d\omega$, $d\lambda$ is a wavelength interval, and $dA \cos(\theta)$ is the projected area normal to the (θ, ϕ) direction. I_λ has the unit of $\text{W}^2 \text{m}^{-1} \text{sr}^{-1} \mu\text{m}^{-1}$ or $\text{Wm}^{-3} \text{sr}^{-1}$ depending on the unit used for the wavelength.

There are three possible interactions between thermal radiation and an object, i.e., radiation are absorbed, reflected, or pass through it. These can be represented by three coefficients: the absorbance α , the reflectance ρ , and the transmittance τ , respectively¹, which sums up to unity as expressed by (6.2). These coefficients are usually dependent

¹Although there is no real consensus, it is generally recommended to keep the “-ivity” ending, e.g., reflectivity, for “pure” surfaces whereas “-ance” ending, e.g., reflectance, should be used to refer to rough and contaminated surfaces [273].

Chapter 6. Introduction and basic principles

on the orientation and wavelength of the incoming radiations.

$$\alpha + \tau + \rho = 1 \quad (6.2)$$

A black-body is a theoretical object whose absorbance is equal to 1, thereby meaning that all the incoming radiation independently of the direction or the wavelength is absorbed. Additionally, a black body is a diffuse or Lambertian emitter, meaning that the radiation it emits does not depend on the direction. Practically, black-body behavior can be approached by building an isothermal cavity having a small aperture; the radiation exiting the cavity is then essentially the one of a black body [273]. The spectral intensity of a black body (*bb* subscript) is expressed as a function of the absolute temperature T in K by the Planck's law:

$$I_{bb}(\lambda, T) = \frac{2hc^2}{\lambda^5 \left(e^{\frac{hc}{\lambda k_B T}} - 1 \right)}, \quad (6.3)$$

where $h = 6.626 \times 10^{-34} \text{ Js}^{-1}$, $k = 1.381 \times 10^{-23} \text{ JK}^{-1}$, and $c = 2.99 \times 10^8 \text{ ms}^{-1}$ are the Planck constant, the Boltzmann constant, and the speed of light in a vacuum, respectively. The total hemispherical emissive power E can then be obtained by integrating the spectral intensity over the wavelength and a half sphere above the specimen surface:

$$E(T) = \int_0^\infty \int_0^{2\pi} \int_0^{\pi/2} I(\lambda, \theta, \phi) \cos(\theta) \sin(\theta) d\theta d\phi d\lambda \quad (6.4)$$

which for a black body whose spectral intensity is given by equation (6.3) can be shown to be :

$$E_{bb}(T) = \int_0^\infty \int_0^{2\pi} \int_0^{\pi/2} I_{bb}(\lambda, T) \cos(\theta) \sin(\theta) d\theta d\phi d\lambda \quad (6.5)$$

$$= \int_0^\infty \pi \cdot I_{bb}(\lambda, T) d\lambda \quad (6.6)$$

$$= \sigma T^4, \quad (6.7)$$

where $\sigma = 5.670 \times 10^{-8} \text{ Wm}^{-2} \text{ K}^{-4}$ is the Stefan-Boltzmann constant.

The behavior of real surfaces is characterized by the spectral directional emittance, which is the ratio between the spectral intensity of the surface divided by that of a black body:

$$\epsilon(\lambda, \theta, \phi, T) \equiv \frac{I(\lambda, \theta, \phi, T)}{I_{bb}(\lambda, T)} \quad (6.8)$$

which is thus equal to 1 for a black body. If the specimen is Lambertian and its emittance is independent of the wavelength, the specimen is referred to as a gray body (*gb*). The total hemispherical emittance of a grey body is only a function of the temperature and is expressed by equation (6.9).

$$\epsilon_{gb}(T) = \frac{E(T)}{E_{bb}(T)} \leq 1 \quad (6.9)$$

If the emittance and temperature of a specimen are known, then its total hemispherical emissive power can be computed as:

$$E_{gb}(T) = \epsilon_{gb}(T) \cdot \sigma T^4 \quad (6.10)$$

6.2 Thermography

Thermography is an optical method that uses the thermal radiations produced by an object to evaluate its temperature. Thermography is a non-contact method that offers two-dimensional temperature measurements in real-time allowing for fast-transient monitoring with a high spatial resolution [157]. The four infrared ranges generally used for thermal imaging as well as the dominant sensor technology and approximate price range for each category are shown in Table 6.1.

Table 6.1 – Summary of infrared imaging technologies

	Abreviation	Wavelength μm	Sensor type	Price range in kCHFrs
Near infrared	NIR	0.7 – 1	Si (CCD or CMOS)	0.5 – 5
Shortwave infrared	SWIR	1 – 1.7	InGaAs	10 – 30
Midwave infrared	MWIR	2 – 6	InSb	50 – 80
Longwave infrared	LWIR	7 – 14	Microbolometer	5 – 45

The I_{bb} computed for three temperatures in the range of an SOC operating temperature with the four wavelength ranges typically used for thermography is presented in Figure 6.1. Assuming that an SOC behaves as a black or grey body, thermal radiation is emitted at a significant level in the ranges from NIR to LWIR; thus, any infrared sensor technology could technically be used.

Obtaining precise quantitative temperature measurements is, however, not straight forward. Artefacts can arise from the reflection of surrounding elements onto the investigated surface or even from the camera lens itself. The latter artefact is also known as the narcissus effect. Infrared imagers are calibrated on a black-body whose emittance is well-known and close to 1 thus, if no correction is performed, the temperature indicated by the thermal camera is equivalent to the black-body temperature and not the specimen temperature. The real temperature of the object can be obtained if its emittance is known. The uncertainty regarding the specimen emittance may thus lead to an erroneous temperature estimation. Generally, using shorter wavelengths reduces these errors, as these wavelengths are always less sensitive to background reflection and emissivity missestimation [275].

Although they are less commonly used than MWIR sensors, NIR sensor are particularly adapted to high-temperature measurements and present similar or better performances with a reduced complexity, as the sensor does not need to be cooled. Using a commercial uncooled Si-based CCD camera, Orteu et al. [276] demonstrated that NIR imaging can be used at a temperature of 300 °C with an accuracy of ± 3 °C. Rotrou et al. [277] obtained a similar accuracy using a commercial uncooled NIR CCD camera, a cooled MWIR camera, and a cooled LWIR camera for temperature measurement between 300 °C and 600 °C. However, the CCD sensor was found to be far less sensitive to emittance non-uniformities [278]. A major drawback of the CCD sensor is the presence of smearing and blooming when the sensor is exposed to a high flux. For CCD sensors, smearing is characterized by strips that originate from the continuous reception of photons during the readout process when charges are transferred along a pixel array [277]. Blooming originates from the overexposure of a region leading to the leakage of charges to adjacent pixels, thus creating streaks on the images. As the analog-digital conversion is performed individually on each pixel, there is no transfer of charges between pixels in a CMOS sensor; they are thus less sensitive to blooming and smearing by design [277]. However, each individual analog-digital converter is slightly different and thus increases the non-uniformity of the photo-response when using a CMOS sensor [279].

InSb [2, 148, 280] and Si-CCD [132, 135, 147, 150] devices have been used successfully in SOFCs. Although intensity is higher in the MWIR range, the thermal radiation variation is more pronounced in the NIR region for a similar temperature modification than in the MWIR spectral range as shown in Figure 6.1. A small temperature variation may thus likely be more easily captured by an NIR sensor. Additionally, the limit of the spatial resolution δx is given by the diffraction limit:

$$\delta x = \frac{0.5\lambda}{n \cdot \sin \theta}, \quad (6.11)$$

where λ is the wave length, n the refraction index of the environment, and θ is the half angle of the light cone of the camera lens. Smaller features can thus theoretically be observed using NIR rather than MWIR.

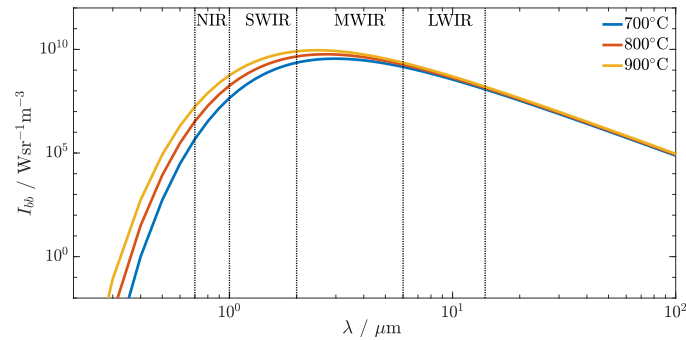


Figure 6.1 – Black body spectral radiance computed with equation (6.3) at varying temperatures and the four different spectral ranges used for thermal imaging.

6.3 Active thermography

Active thermography consists of identifying the local thermal response of a specimen subject to a thermal perturbation. It can be performed either in transmission (source and camera on opposite side of the sample) or reflective (camera and heat source on the same side of the sample) mode. The two main active thermography methods are pulse thermography (PT), where the sample is excited by a pulse signal, and lock-in thermography (LT), where the sample is excited by a periodic signal, typically a sine or a square wave. Active thermography measurements provide a three-dimensional (3-D) matrix of which two dimensions are used for the pixel position and the third represents the time.

A wide variety of data analysis procedures has been reported for PT measurements. Vavilov and Burleigh [281] reviewed 21 methods that have been used for PT analysis. The most basic methods are based on thermal contrast where a reference temperature is subtracted from each image. The images are then individually analyzed to find inhomogeneous areas. Despite their simplicity and overall good performances, these methods generally require the selection of a reference non-defective area and are affected by non-uniform heating [282]. More sophisticated methods have been developed in recent years that are less sensitive to non-homogeneous heating. A summary of the most widely used methods with principal references is presented in Table 6.2. Thermographic signal reconstruction (TSR), for example, consists of a polynomial fit of the temperature or of the temperature logarithm evolution. TSR intrinsically acts as a low-pass filter by reducing the noise and reduces the data storage needs; however, the number of coefficient used for the fitting is arbitrary and not well-detailed. Principal component thermography (PCT) and pulse phase thermography (PPT) both rely on the mathematical transformation of the original 3-D matrix into a different basis. The former is based on a principal component analysis (PCA) whereas the latter relies on the Fourier transform. The high-order statistical method (HOSM) treats the temporal evolution of each pixel as

a statistical distribution. The main disadvantage of PCA and HOSM is the loss of physical meaning.

The data treatment of lock-in thermography is generally straight forward and performed in a similar manner as EIS. Commonly, the phase and the amplitude of the thermal response are computed for each pixel using the Fourier transform. Two images can then be reconstructed: the amplitude and the phase image. These representation are usually less sensitive to emissivity differences, heating heterogeneities, reflections, and noise than classical passive thermographic measurements [157].

LT is particularly adapted for the identification of weak heat sources as it uses a periodic signal that can be averaged over multiple cycles reducing the effect of noise. Rakotoniaina et al. [166] managed to lower the noise level by a factor 100 to $44\mu\text{K}$ by taking a 1000 s measurements. Using microscopic LT on an integrated circuit, Breitenstein et al. [283] identified heat sources weaker than $5\mu\text{W}$ after a 30 min measurement at 13.5 Hz. Breitenstein et al. [272] demonstrated that the system-averaged amplitude noise level, $L_{noise,sys}$ decreases with the square roots of the total number of frames nN as expressed in equation (6.12), where n , N , and NETD represent the number of frames per cycle, the number of cycles, and the noise equivalent temperature difference, respectively. The NETD is a characteristic of the thermal camera and can be computed knowing the standard deviation σ_{cam} of the camera noise when exposed to a homogeneous temperature (or in the dark) and the transfer function $T = F(digits)$ to pass from digits to temperature, as expressed in equation (6.13).

$$L_{noise,sys} = \frac{2}{\sqrt{nN}} \cdot NETD \quad (6.12)$$

$$NETD = F(\sigma_{cam}) \quad (6.13)$$

Table 6.2 – Data processing for pulse thermography

Method	Description	Remarks	Ref.
PCA	Reduction of data space from 3-D matrix (t, x, y) to 2-D. Analysis based on eigenvectors and eigenvalues.	Good noise rejection and robustness in flaw depth estimation. Condensed information. Provides a high level of contrast for subsurface defects.	[157, 281, 284–287]
PPT	Frequency analysis of time data. Phase and amplitude diagrams are analyzed.	Relatively insensitive to heating and emissivity inhomogeneity. Faster than lock-in thermography, as many frequencies are recorded within a single experiment.	[281, 286, 288–291]
TSR	Polynomial time fitting of temperature evolution for each pixel, often with logarithmic polynomials. First and second derivative of the polynomial are studied.	Good compression of data as only polynomial coefficients need to be stored. A polynomial degree needs to be arbitrarily defined.	[157, 158, 281, 286]
HOSM	Temporal data are treated like statistical values. Third (skewness) and fourth (kurtosis) standardized statistical moment are computed.	Data are compressed into a single image. Kurtosis is affected by non-uniform heating but skewness is not. Kurtosis is related to the thermal diffusivity.	[157, 292, 293]

6.3.1 Fourier analysis

This section presents the basis of the Fourier transform and how it is applied to LT and PPT. The Fourier transform (\mathfrak{F}) of a continuous time function $x(t)$ is defined by equation (6.14), where ω is the pulsation and $i = \sqrt{-1}$. The Fourier transform can easily be expressed in terms of frequency f as $\omega = 2\pi f$. The time signal can then be retrieved using the inverse Fourier transform, as defined by equation (6.15).

$$\mathfrak{F}\{x(t)\} = \hat{X}(\omega) = \int_{-\infty}^{\infty} x(t) e^{-i\omega t} dt \quad (6.14)$$

$$\mathfrak{F}^{-1}\{\hat{X}(\omega)\} = x(t) = \frac{1}{2\pi} \int_{-\infty}^{\infty} \hat{X}(\omega) e^{i\omega t} d\omega \quad (6.15)$$

Chapter 6. Introduction and basic principles

The analytic solutions of the Fourier transform of a cosine, represented schematically in Figure 6.2a, and a sine function are given by equations (6.16) and (6.17), respectively, where $\delta(\omega)$ is the delta function whose properties are recalled in equation (6.18). The norm of the Fourier transform of a cosine/sine is presented in Figure 6.2b for positive decomposition frequency only. The entire power of a sine/cosine signal is thus concentrated at the excitation frequency, which makes it the best signal to identify a response at one particular frequency.

$$\mathfrak{F}\{A\cos(\omega_0 t)\} = A\pi [\delta(\omega + \omega_0) + \delta(\omega - \omega_0)] \quad (6.16)$$

$$\mathfrak{F}\{A\sin(\omega_0 t)\} = jA\pi [\delta(\omega + \omega_0) - \delta(\omega - \omega_0)] \quad (6.17)$$

$$\delta(\omega) = \begin{cases} 1 & \text{if } \omega = 0 \\ 0 & \text{if } \omega \neq 0 \end{cases} \quad (6.18)$$

A generic pulse signal, as represented in Figure 6.2c, starting at $t = t_1$ and ending at $t = t_2$ with an amplitude A is defined mathematically by equation (6.19). The analytic Fourier transform of this signal is then expressed by equation (6.20).

$$P_{sq}(t) = \begin{cases} A & \text{if } t_1 \leq t \leq t_2 \\ 0 & \text{otherwise} \end{cases} \quad (6.19)$$

$$\mathfrak{F}\{P_{sq}(t)\} = -A \frac{e^{-j\omega t_2} - e^{-j\omega t_1}}{j\omega} \quad (6.20)$$

The frequency spectrum of a pulse excitation is much broader than that of a sine/cosine signal, as presented in Figure 6.2d. Additionally, the frequency composition can be tuned by modifying the width of the pulse ($T = t_2 - t_1$). The maximum amplitude is reached at $\omega = 0$ and, using L'Hopital's rule, is equal to $A \cdot (t_2 - t_1) = AT$; the amplitudes of the secondary lobes then decrease quickly. Although the pulse excitation shows a wider bandwidth than the sinusoidal excitation, the measurement and sampling error can be greatly reduced and even eliminated when a sinusoidal excitation is used, which is particularly important when small signals need to be measured in a noisy environment.

The technical realization of LT and PPT implies the sampling of a continuous time signal which thus becomes discrete. As the data are then processed using a computer, the use of the discrete Fourier transform \mathfrak{F}_d (DFT), which provides a discrete frequency representation of a numerical signal, is more appropriate. The DFT provides a discrete frequential spectrum to a finite time measurement, which are normally two mutually exclusive conditions. To overcome this limitation, the signal is hypothetically considered periodic to generate a discrete frequency spectrum. The DFT and its synthesis are described in equations (6.21) and (6.22), respectively, where N is the number of sampled

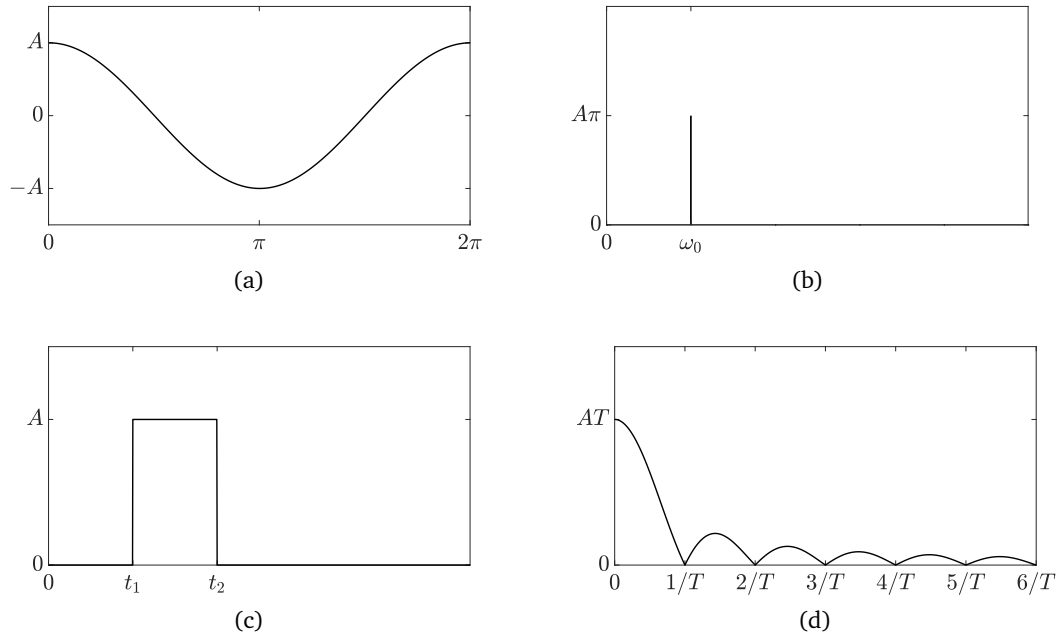


Figure 6.2 – (a) and (c) are the temporal representation of a cosine and pulse signal whereas (b) and (d) are the norm of their respective Fourier transform for positive frequency only. In both cases, the norm of the Fourier transform is symmetric with respect to $f = 0$ at negative frequencies.

data points and x_n is the n^{th} temperature sample of one pixel.

$$\mathfrak{F}_d \{x_n\} = \hat{X}_d(k) = \sum_{n=0}^{N-1} x_n e^{-i2\pi kn/N} \quad k = 0, 1, \dots, N-1 \quad (6.21)$$

$$\mathfrak{F}_d^{-1} \{\hat{X}_d(k)\} = x_n = \frac{1}{N} \sum_{k=0}^{N-1} \hat{X}_d(k) e^{i2\pi kn/N} \quad n = 0, 1, \dots, N-1 \quad (6.22)$$

The DFT can be efficiently computed using the fast Fourier transform (FFT) algorithm readily available in many software platforms. Improper measurements can lead to a deterioration of the DFT results. In the following, the three main sources of error that may affect the quality of the DFT are briefly discussed.

Truncation errors

The DFT assumes that the signal is periodic and thus that the first measurement comes immediately following the prior one, as if in a loop. When the signal is not periodic, e.g., a pulse, the last and first point may not be identical, especially if the measurement is stopped before the system returns to its original state, thereby generating a discontinuity. A truncation error is thus introduced due to the finite nature of the measurement. This error, also known as spectral leakage, can be mitigated by using an appropriate window,

e.g., a Hann or Hamming window, to force the signal to 0 at the beginning and end of the measurement period, thus allowing the signal to be hypothetically repeated periodically without discontinuities and satisfying the DFT periodicity hypothesis. Also, it is important to use the difference from the initial state to remove the constant component of the signal before windowing; otherwise, the signal would not naturally tend towards 0 and the corresponding DFT may reflect the frequency composition of the window rather than that of the signal. However, if the signal is periodic, e.g., a sine wave, and recorded over an exact integer number of cycles, then no error is introduced, which greatly facilitates the analysis of LT measurements if the data are acquired carefully.

Sampling error

Sampling errors arise from aliasing when the Shannon sampling is not respected, i.e., when the sampling frequency is lower than twice the highest frequency present in the measured signal. This can be limited by carefully selecting the sampling frequency.

Measurement error

Measurement errors affect the quality of the measurement and can originate from any type of unwanted perturbation, e.g., instrument noise or drift. When a periodic signal is used, this error can be reduced by increasing the number of cycles and averaging.

When the data are analyzed in the frequency domain, it is more convenient to normalize equation (6.21) rather than (6.22) by $1/N$. Otherwise, due to the summation over n , the amplitude obtained in the frequency domain will be n -times higher than that of the time domain signal. For physical signals, the DFT is a double-sided spectrum symmetrical around $f = 0$. The power contained in the time signal is thus split in half between positive and negative frequencies. A negative frequency has a mathematical but not a physical significance. A physical signal can thus be more conveniently represented by a single-sided spectrum (only positive frequencies) with double the amplitude of the original double-sided DFT. With these considerations, equation (6.21) can be rewritten as :

$$\hat{X}_d^{ss}(k) = \frac{2}{N} \sum_{n=0}^{N-1} x_n e^{-i2\pi kn/N} \quad k = 0, 1, \dots, (N-1)/2 \quad (6.23)$$

The DFT is generally computed off-line using an FFT algorithm once all the data have been recorded, which may often require a large data storage capacity. In their analysis of LT, Breitenstein et al. [272] focused only on the temperature response at the same frequency as that of the excitation (1^{st} harmonic). Therefore, only the DFT term for $k = 1$ was computed. For a periodic signal, the total number of sampled data points N_{tot} can be expressed as $N_{tot} = n \cdot N$ where N and n are the number of cycles and samples per cycle,

respectively. Equation (6.23) can then be rewritten for $k = 1$ as the double summation in equation (6.24), where $\hat{X}_d^{ss}(1)$ is the single-sided DFT evaluated at $k = 1$.

$$\hat{X}_d^{ss}(1) = \frac{2}{n \cdot N} \sum_{n_c=0}^{N-1} \sum_{n_s=0}^{n-1} x_{n_c, n_s} e^{-i2\pi k n_s / n} \quad (6.24)$$

Breitenstein et al. [272] defined two coefficients $K_{n_s}^0$ and $K_{n_s}^{90}$ by equations (6.25) and (6.26) respectively, which correspond to the real and imaginary part of $e^{-i2\pi k n_s / n}$ in trigonometrical form, respectively.

$$K_{n_s}^0 = 2 \sin(2\pi \cdot n_s / n) = -2 \operatorname{Im}(e^{-i2\pi k n_s / n}) \quad (6.25)$$

$$K_{n_s}^{90} = 2 \cos(2\pi \cdot n_s / n) = 2 \operatorname{Re}(e^{-i2\pi k n_s / n}) \quad (6.26)$$

Equation (6.24) can then be separated into two sums of real numbers S^0 and S^{90} defined by equations (6.27) and (6.28), respectively.

$$S^0 = \frac{1}{N_c \cdot N_s} \sum_{n_c=0}^{N_c-1} \sum_{n_s=0}^{N_s-1} x_{n_c, n_s} K_{n_s}^0 = \operatorname{Im}(\hat{X}_d^{ss}(1)) \quad (6.27)$$

$$S^{90} = \frac{1}{N_c \cdot N_s} \sum_{n_c=0}^{N_c-1} \sum_{n_s=0}^{N_s-1} x_{n_c, n_s} K_{n_s}^{90} = \operatorname{Re}(\hat{X}_d^{ss}(1)) \quad (6.28)$$

The two coefficients $K_{n_s}^0$ and $K_{n_s}^{90}$ can be computed beforehand allowing for the on-line computation of S^0 and S^{90} , thus reducing the amount of stored data to two images. If x is the temperature, then S^0 and S^{90} correspond to the imaginary and real components of the temperature modulation, respectively. The downside of this method is the loss of information on higher harmonics. In the present work, a thermal perturbation was generated by a sinusoidal current though Joule heating, which is proportional to the current squared, thereby including higher harmonics. Therefore, the FFT approach is preferred to be able to also analyze higher frequencies. The presented method for $k = 1$ can also be extended to any other k values. If only a few frequencies are of interest, the specific DFT terms can then be computed on-line, thereby greatly reducing the data storage need and post-processing time.

Instead of a Cartesian coordinate (expressing the real and imaginary part), $\hat{X}_d^{ss}(1)$ can also be expressed in polar coordinate with the amplitude $\|\hat{X}_d^{ss}(1)\|$ and phase ϕ defined by equations (6.29) and (6.30), respectively. As ϕ is independent of the amplitude of the signal, it is theoretically immune to non-uniform heating or emittance variation, facilitating the identification of thermal non-homogeneities.

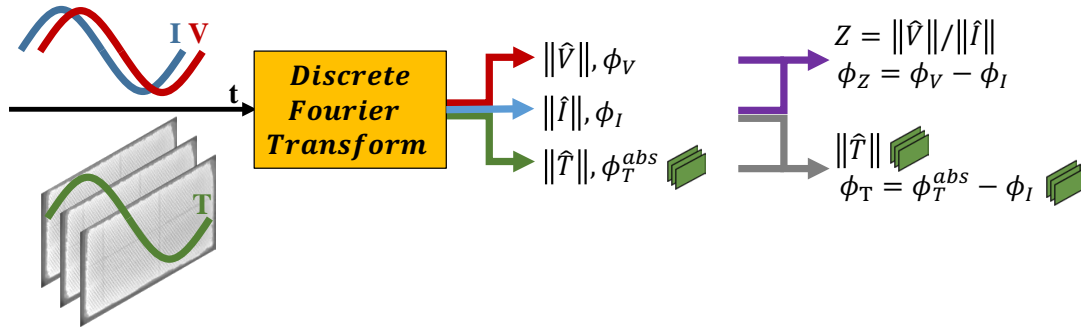


Figure 6.3 – Schematic representation of the LT and EI procedure.

$$\|\hat{X}_d^{ss}(1)\| = \sqrt{\text{Re}(\hat{X}_d^{ss}(1))^2 + \text{Im}(\hat{X}_d^{ss}(1))^2} \quad (6.29)$$

$$\phi = \arctan\left(\frac{\text{Im}(\hat{X}_d^{ss}(1))}{\text{Re}(\hat{X}_d^{ss}(1))}\right) \quad (6.30)$$

The phase obtained using equation (6.30) is referenced to a cosine signal with no phase lag. A coherent series of measurement requires, two conditions to be fulfilled:

- the excitation signal must be a cosine signal with no phase lag, and
- the temperature acquisition has to be synchronized and start at the beginning of an excitation cycle.

If these conditions are not satisfied, then the measured ϕ becomes meaningless and can not be compared between measurements. A more flexible method involves measuring both the excitation signal and thermal response and then correcting the phase of the temperature signal using the phase of the excitation signal. The phase thus represents the time shift between the excitation and the thermal response and can be compared. This method allows the excitation and acquisition to be decoupled. For LT, the excitation can thus be started before the acquisition to ensure that a periodic response is reached before beginning the acquisition.

As a summary, schematic representations of the LT and EIS procedures are presented in Figure 6.3. The two methods are similar except that LT considers 2-D rather than 1-D data.

6.4 Conclusion

In this chapter, the basics on thermal radiation, thermography, and Fourier transform analysis were presented. Due to their high operating temperature, SOCs emit infrared radiations over from the NIR to LWIR range, allowing any thermal radiation sensor.

Si-based NIR sensors offer good performances for temperature measurements above 300 °C and are less sensitive to emittance variations than the more-expensive InSb-based MWIR sensors. Si-CCD sensors have been successfully used for SOC temperature measurements in multiple works but can suffer from blooming and smearing contrary to Si-CMOS sensors which are immune to these by design. The use of Si-CMOS sensors thus is an affordable solution well adapted for SOCs.

PT and LT are the most widely used methods for active thermography measurements. LT measurements are typically analyzed using the DFT. The obtained phase image is particularly interesting as it is naturally immune to emittance and heating inhomogeneities. There is a wide variety of methods identified for PT data analysis, of which pulse phase thermography is particularly attractive because it also uses the DFT. A pulse excitation allows the thermal response to be monitored at various frequencies in one measurement however as the signal energy is spread over multiple frequencies the pulse amplitude necessary for the thermal response to overpass the noise level of the camera sensor may be so high that it could damage the sample. A sine excitation allows for averaging over multiple cycles reducing the impact of noise and allowing a smaller perturbation amplitude and/or smaller signal identification. LT is thus determined to be the most appropriate method if accuracy is preferred over measurement time.

CHAPTER 7

Numerical investigation

The numerical investigation presented in this chapter provides a support for the analysis of data acquired during the experimental campaign presented in Chapter 9.

Contributions to the Field

Identified heat sources and key parameters influencing an SOC's thermal response by performing a parametric analysis with a numerical model.

7.1 Model description

The model used in this work is a combination of the electrochemical model developed by Caliandro et al. [12] and the thermal model developed by Nakajo et al. [294] and adapted to more closely represent the test rig developed for active thermography that is presented in chapter 8. The model was implemented in gProms® [295] and a MATLAB® [296] routine was developed using the build-in FFT algorithm to analyze the results in the frequency domain.

The SOC model is a pseudo 2-D model discretized in the flow direction, x , and the thickness, z , as shown in Figure 7.1, where GDL and MIC represent the gas diffusion layer and metal interconnect, respectively. The red striped area on the wall represents one of the isothermal surfaces considered for the radiative exchange with each SOC area (e.g., red striped area in the x - y plane). The heat exchanged between the different constituents and the heat generated by the electrochemical reactions are treated as volumic terms; thus thermal gradients in the z -direction within the materials were disregarded. Thermal conduction through the GDL to the MIC was also modeled as a volumic term whereas no conduction was considered for the top GDL, as the MIC was removed to expose the O₂-electrode.

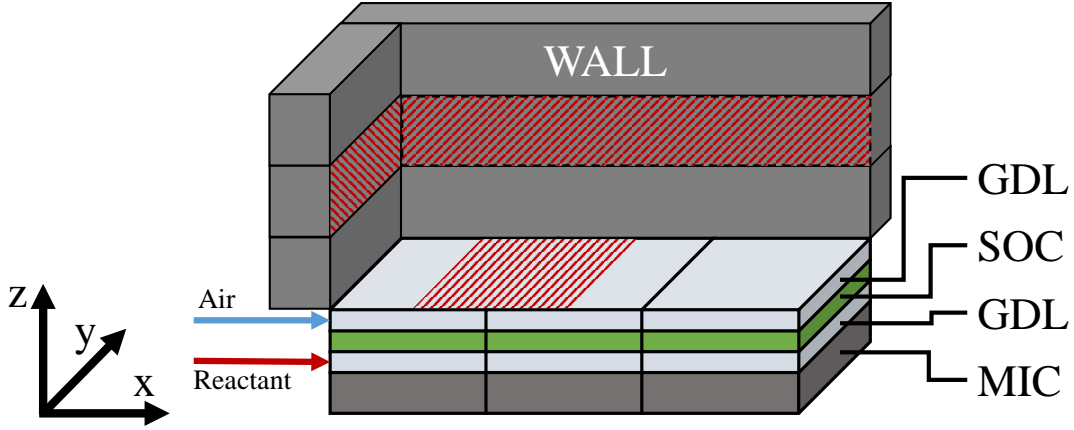


Figure 7.1 – Schematic representation of the discretization domain.

7.1.1 Thermal model

The main equations involving the SOC are presented here; a complete description of the thermal model can be found in [294]. The model enforces energy conservation for all of the phases, i.e., gas and solid, as well as mass conservation for the gas phases.

The energy conservation equation applied to the SOC gives:

$$\lambda_s \frac{\partial^2 T_{SOC}}{\partial x^2} + \dot{Q}_{rx} + \dot{Q}_{SOC_{cond}} + \dot{Q}_{SOC_{conv,R}} + \dot{Q}_{SOC_{conv,A}} + \dot{Q}_{SOC_{rad}} = \rho_{SOC} c_{h_{soc}} \frac{\partial T_{SOC}}{\partial t}, \quad (7.1)$$

where

$$\begin{aligned} \dot{Q}_{SOC_{cond}} &= \lambda_{GDL}(T_{MIC} - T_{SOC}) \\ \dot{Q}_{SOC_{conv}} &= h_R^c(T_R - T_{SOC}) \\ \dot{Q}_{SOC_{conv}} &= h_A^c(T_R - T_{SOC}) \\ \dot{Q}_{SOC_{rad}} &= -(\sigma T_{SOC}^4 - \dot{Q}_{rad}^{wall}) \\ \dot{Q}_{rx} &= \frac{j}{2F}(-\Delta_r h_{H_2O}^0 - \Delta_r g_{H_2O}) + j\eta_{tot} \end{aligned}$$

are detailed in the following sections.

Conduction

The heat conduction between the SOC and GDL occurs through the Ni foam used for current collection. For simplicity, the radiation and conduction in the porous media were

neglected and the effective thermal conductivity was estimated considering only the solid fraction as [297]:

$$\lambda_{GDL} = (1 - \chi)\lambda_{Ni} \quad (7.2)$$

where χ is the Ni foam porosity and $\lambda_{Ni} = 70 \text{ Wm}^{-1} \text{ K}^{-1}$ is the thermal conductivity of dense Ni. The porosity was assumed to be approximately 0.95 leading to an estimated $\lambda_{GDL} = 3.5 \text{ Wm}^{-1} \text{ K}^{-1}$.

Convection

The Reynolds number, $Re = \frac{\rho v D_h}{\mu}$, for the considered geometry and typical SOC operating conditions was approximately 1–5, which is well below 2300 that is considered as the critical Reynolds number for the onset of turbulence [274]. The flow regime was thus assumed to be laminar. The Nusselt number, Nu , was estimated using equation (7.3) which is an interpolation based on data from Incropera and Incropera [274] who reported a list of Nusselt numbers for fully developed laminar flow in pipes with a rectangular cross-section subjected to a uniform heat flux. The aspect ratio is the ratio between the gas channel width, W , and height, H , so that $AR \in [0, 1]$. The Nu is then related to the convective heat transfer coefficient, h^c , by equation (7.5), where D_h is the hydraulic diameter of the channel, as defined by equation (7.6), and λ_{gas} is the thermal conductivity of the gas mixture and is computed using the Mason-Saxena-Wassiljewa method [298].

$$Nu = 5.674e^{-3.158AR} + 2.575e^{0.2688AR} \quad (7.3)$$

$$AR = H/W \quad (7.4)$$

$$Nu = \frac{D_h h_{gas}^c}{\lambda_{gas}} \quad (7.5)$$

$$D_h = \frac{4WH}{2W + 2H} \quad (7.6)$$

Radiation

\dot{Q}_{rad}^{wall} is the radiative heat coming from the four walls enclosing the optical access. This term takes into account the view factor as well as the evolution of the wall temperature from the SOC to the top of the insulation. The wall was split into N isothermal layers for which a view factor was computed with each SOC discretization elements. The same area was attributed to each SOC discretization node with the center of the area located at the SOC discretization node as schematically represented by the red dashed area in Figure 7.1. Only half of the area was attributed to the end nodes, as one edge was located at the node position (i.e., the SOC edge). The view factors were computed as [4, 299]:

$$F_{1-2} = \frac{1}{(x_2 - x_1)(y_2 - y_1)} \sum_{l=1}^2 \sum_{k=1}^2 \sum_{j=1}^2 \sum_{i=1}^2 \left[(-1)^{(i+j+k+l)} G_{ijkl} \right] \quad (7.7)$$

$$G_{ijkl} = \frac{1}{2\pi} \left[(y_j - \eta)(x_i^2 + \xi_l^2)^{0.5} \tan^{-1}(K_{ijkl}) - \frac{1}{4} (x_i^2 + \xi_l^2) (1 - K_{ijkl}^2) \ln \left((x_i^2 + \xi_l^2) (1 + K_{ijkl}^2) \right) \right] \quad (7.8)$$

$$K_{ijkl} = \frac{y_j - \eta_k}{(x_i^2 + \xi_l^2)^{0.5}}, \quad (7.9)$$

where x_i, y_j, η_k and ξ_l are spatial coordinates that are defined in Figure 7.2. Assuming that the wall and the SOC O_2 -electrode behave as black bodies (i.e., $\epsilon = 1$), the heat flux exchanged between one wall and each SOC discretization element is given by [273]:

$$\dot{q}_i = E_{bb_i} - \sum_{j=1}^N E_{bb_j} F_{i-j} - H_{0_i}, \quad (7.10)$$

$$E_{bb_i} = n^2 \sigma T_i^4, \quad (7.11)$$

where E_{bb} is the emissive power, H_0 is the external irradiation contribution, n is the refractive index of the medium, and N the number of isothermal surfaces. The only external irradiation source is the thermal radiation from the environment entering through the optical access. As the optical access represents only a small fraction of the hemisphere above the SOC (i.e., corresponds to a small view factor) and that the atmospheric temperature, $T_{atm} \approx 300$ K, $T_{atm} \ll T_{SOC}^4$ ($T_{SOC} \approx 1023$ K), H_0 can thus be neglected. For each SOC discretization element, \dot{Q}_{rad}^{wall} is then calculated as the sum of each wall contribution, as expressed by equation (7.12).

$$\dot{Q}_{rad}^{wall} = \sum_{wall} \sum_{j=1}^N E_{bb_j} F_{i-j} \quad (7.12)$$

Formally \dot{Q}_{rad}^{wall} should be computed using an integral over infinitesimal isothermal surfaces. The discrete estimation of \dot{Q}_{rad}^{wall} , expressed by equation (7.12), however, converges for $N \geq 1000$ as shown in Figure 7.3 which represents \dot{Q}_{rad}^{wall} as function of the dimensionless position $x^* = x/L$ where L is the SOC length. Therefore, $N = 1000$ was selected in the present work.

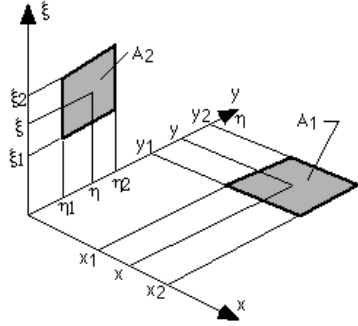


Figure 7.2 – Definition of the view factor parameters. Reproduced from [4].

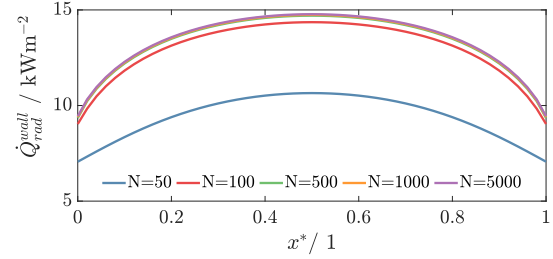


Figure 7.3 – Convergence of \dot{Q}_{rad}^{wall} with N .

Reaction

\dot{Q}_{rx} can be conveniently expressed in terms of voltages, as shown by equation (7.13), by using the definition of the V_{tn} and V_{soc} presented in equations (1.14) and (1.13), respectively. In fuel cell mode, $j > 0$ and $(V_{tn} - V_{SOC}) < 0$, thus, $\dot{Q}_{rx} > 0$. In electrolysis mode, however, $j < 0$, but $(V_{tn} - V_{SOC})$ is initially > 0 and becomes < 0 when $V_{SOC} > V_{tn}$, which corresponds to the transition from endothermic to exothermic operation.

$$\dot{Q}_{rx} = j(V_{tn} - V_{SOC}) \quad (7.13)$$

The frequency composition of \dot{Q}_{rx} during LT can be computed analytically by considering a sinusoidal modulation of the applied current density J , which can be expressed, in a generic form, as

$$J = J^0 + \|J\|^I \cdot \cos(\omega_0 t + \phi_J^I), \quad (7.14)$$

where $\omega_0 = 2\pi f_0$, and f_0 is the excitation frequency. The harmonic response of j , and V_{SOC} can then be expressed as:

$$V_{SOC}(t) = V^0 + \|V\|^I \cdot \cos(\omega_0 t + \phi_V^I) + \|V\|^{II} \cdot \cos(2\omega_0 t + \phi_V^{II}) \quad (7.15)$$

$$j(t) = j^0 + \|j\|^I \cdot \cos(\omega_0 t + \phi_j^I) + \|j\|^{II} \cdot \cos(2\omega_0 t + \phi_j^{II}) \quad (7.16)$$

where the superscript 0 refers to the (signed) steady-state value, ϕ is the phase, $\| \cdot \|$ is the amplitude (norm), and the superscripts I and II refer to the first, and second harmonic terms, respectively. It is often assumed that when the current perturbation is small, the SOC response is linear and only the first harmonic is kept. As this condition may not be satisfied during LT measurements, the second-order terms were also considered to obtain a more generic solution that also accounts for a moderate non-linearity of the SOC response.

Chapter 7. Numerical investigation

Equations (7.15) and (7.16) can be inserted in equation (7.13) and the analytical Fourier transform can then be computed with the help of equations (7.17), (7.18), and (7.19), where the $*$ operator is the convolution product.

$$\mathfrak{F}\{A \cos(\omega_0 t + \phi)\} = \frac{A}{2} \left[\delta(\omega - \omega_0) e^{-i\phi} + \delta(\omega + \omega_0) e^{i\phi} \right] \quad (7.17)$$

$$\mathfrak{F}\{j(t) \cdot V(t)\} = \hat{j}(\omega) * \hat{V}(\omega) \quad (7.18)$$

$$\delta(\omega - \omega_1) * \delta(\omega - \omega_2) = \delta(\omega - \omega_1 - \omega_2) \quad (7.19)$$

The analytic Fourier transform of equation (7.13) is composed of a constant term as well as 4 harmonic terms at 1, 2, 3, and 4 times the excitation angular frequency ω_0 . As the amplitude decreases quickly for higher harmonics, only the real and imaginary part of the first three terms are reported here. The complete development is presented in Appendix C.

Steady state ($\delta(\omega)$)

$$\hat{Q}_{rx}^I = j^0 (V_{tn} - V^0) - \left[\frac{\|V\|^I \|j\|^I}{2} \cos(\phi_V^I - \phi_j^I) + \frac{\|V\|^{II} \|j\|^{II}}{2} \cos(\phi_V^{II} - \phi_j^{II}) \right] \quad (7.20)$$

$$\hat{Q}_{rx}^{II} = 0 \quad (7.21)$$

1st harmonic ($\delta(\omega - \omega_0)$)

$$\begin{aligned} \hat{Q}_{rx}^I = & (V_{tn} - V^0) \|j\|^I \cos(\phi_j^I) - j^0 \|V\|^I \cos(\phi_V^I) \\ & - \frac{\|V\|^I \|j\|^{II}}{2} \cos(\phi_V^I - \phi_j^{II}) - \frac{\|j\|^I \|V\|^{II}}{2} \cos(\phi_V^{II} - \phi_j^I) \end{aligned} \quad (7.22)$$

$$\begin{aligned} \hat{Q}_{rx}^{II} = & - (V_{tn} - V^0) \|j\|^I \sin(\phi_j^I) + j^0 \|V\|^I \sin(\phi_V^I) \\ & + \frac{\|V\|^I \|j\|^{II}}{2} \sin(\phi_V^I - \phi_j^{II}) + \frac{\|j\|^I \|V\|^{II}}{2} \sin(\phi_V^{II} - \phi_j^I) \end{aligned} \quad (7.23)$$

2nd harmonic ($\delta(\omega - 2\omega_0)$)

$$\hat{Q}_{rx}^{'II} = (V_{tn} - V^0) \|j\|^{II} \cos(\phi_j^{II}) - \frac{\|V\|^I \|j\|^I}{2} \cos(\phi_V^I + \phi_j^I) - j^0 \|V\|^{II} \cos(\phi_V^{II}) \quad (7.24)$$

$$\hat{Q}_{rx}^{''II} = -(V_{tn} - V^0) \|j\|^{II} \sin(\phi_j^{II}) + \frac{\|V\|^I \|j\|^I}{2} \sin(\phi_V^I + \phi_j^I) + j^0 \|V\|^{II} \sin(\phi_V^{II}) \quad (7.25)$$

The steady-state heating contribution given by equation (7.20) causes an initial transient evolution of the SOC temperature towards a new equilibrium around which the SOC temperature oscillates. To avoid the deterioration of the quality of the LT measurement due to this temperature drift, it is necessary to start the current modulation well before the beginning of the temperature acquisition (typically 10–15 cycles).

Typically, $\|V\|^I$ and $\|j\|^I$ are on the order of 10^{-1} – 10^{-2} and $(V_{tn} - V^0)$ and j^0 are on the order of 10^{-1} – 10^{-2} ; therefore if $\|j\|^{II}$ and/or $\|V\|^{II}$ are on the order of 10^{-2} – 10^{-3} , the higher harmonics (here only the second harmonic was considered) present in j and V significantly contribute to \hat{Q}_{rx}^{II} and can not be neglected. The 1st harmonic is less impacted by non-linearities, so $\|j\|^{II}$ and/or $\|V\|^{II}$ would need to be one order of magnitude higher, i.e., 10^{-1} – 10^{-2} , to be significant.

As presented at the end of chapter 6, when the measurements and excitation signals are not synchronized, the measurements have to be referenced to the current excitation signal to be coherent. The phase ϕ_j^I in equation (7.14) can be used to correct the measurements. When performing the correction, there is a risk of double correction on terms such as $\cos(\phi_j^I - \phi_V^{II})$ where it is tempting to subtract ϕ_j^I on both ϕ_j^I and ϕ_V^{II} . As an example, the correction was applied to \hat{Q}_{rx}^I , as:

$$\begin{aligned} \hat{Q}_{rx}^{'I} = & (V_{tn} - V^0) \|j\|^I \cos(\phi_j^I - \phi_j^I) - j^0 \|V\|^I \cos(\phi_V^I - \phi_j^I) \\ & - \frac{\|V\|^I \|j\|^{II}}{2} \cos(\phi_V^I - \phi_j^{II} - \phi_j^I) - \frac{\|j\|^I \|V\|^{II}}{2} \cos(\phi_V^{II} - \phi_j^I - \phi_j^I) \end{aligned} \quad (7.26)$$

$$\begin{aligned} \hat{Q}_{rx}^{''I} = & -(V_{tn} - V^0) \|j\|^I \sin(\phi_j^I - \phi_j^I) + j^0 \|V\|^I \sin(\phi_V^I - \phi_j^I) \\ & + \frac{\|V\|^I \|j\|^{II}}{2} \sin(\phi_V^I - \phi_j^{II} - \phi_j^I) + \frac{\|j\|^I \|V\|^{II}}{2} \sin(\phi_V^{II} - \phi_j^I - \phi_j^I) \end{aligned} \quad (7.27)$$

At low frequencies, the SOC is always at equilibrium and $\phi_J^I = \phi_j^I$; when the frequency is increased the electrochemical and transport processes are not at equilibrium and spatially vary, and thus $\phi_J^I \neq \phi_j^I$. Therefore, these terms can not be simplified.

The results presented throughout this work always used the total current density as reference and are thus corrected by ϕ_J .

Boundaries

A simplified radiative heat transfer between the bottom and sides of the MIC and the furnace walls was considered. The desired SOC temperature was then obtained by modifying the furnace temperature iteratively. To obtain $T_{SOC} \approx 750^\circ\text{C}$, $T_{furnace}$ was set to 773°C . The reactant and air inlet temperature were assumed to be equal to the furnace temperature.

The optical access wall temperature was assumed to linearly decrease from $T_{furnace}$ at the SOC level to the value measured at the top of the wall in the test-rig, 200°C , described in chapter 8.

7.1.2 Electrochemical model

An overview of the equations comprising the electrochemical model are presented here; a complete description of the model can be found in [12, 120].

The gas transport in the porous electrodes was assumed to be uni-directional along the z-axis. It was resolved using a complete formulation of the dusty gas model (DGM), thereby also including transient terms. The DGM has been widely used for the modeling of SOCs [300] and accounts for both the Knudsen and binary pair diffusion process [294]. The overpotential related to the difference in concentrations between the gas channel and the electrode–electrolyte interface are then given by equations (7.28) and (7.29) for the O_2 -electrode and H_2 -electrode, respectively.

$$\eta_{conc}^{O_2} = \frac{RT}{2F} \ln \left(\frac{p_{O_2}^{channel}}{p_{O_2}^{interface}} \right) \quad (7.28)$$

$$\eta_{conc}^{H_2} = \frac{RT}{2F} \ln \left(\frac{p_{H_2}^{channel}}{p_{H_2}^{interface}} \frac{p_{H_2O}^{interface}}{p_{H_2O}^{channel}} \right) \quad (7.29)$$

In the H₂-electrode, the electrochemical reactions are assumed to only take place at the electrode–electrolyte interface. A concentration-dependent Butler-Volmer equation was then used to describe the electrochemical reactions:

$$i = i_0 \frac{\frac{c_{H_2}^{TPB}}{c_{H_2}^*} \left(\frac{c_{H_2O}^{TPB}}{c_{H_2}^*} \right)^{\alpha_a/2}}{1 + \left(\frac{c_{H_2}^{TPB}}{c_{H_2}^*} \right)^{0.5}} \left[\exp \left(\frac{\alpha_a F \eta_{act}^{H_2}}{RT} \right) - \exp \left(\frac{-\alpha_c F \eta_{act}^{H_2}}{RT} \right) \right], \quad (7.30)$$

where i is the local current, i_0 is the exchange current, $c_{H_2O}^{TPB}$ and $c_{H_2}^{TPB}$ are the H₂O and H₂ concentrations at the TPBs, respectively, α_a and α_c are the anodic and cathodic charge transfer coefficients, respectively, and $c_{H_2}^*$ is the equilibrium surface concentration for the $H_2(g) + 2\text{ads}_{Ni} \rightleftharpoons 2H_{Ni}$ reaction and follow an Arrhenius-type law [301]. The contribution of the charge transfer overpotential at the H₂-electrode, $\eta_{act}^{H_2}$, to the SOC impedance is purely resistive.

The considered electrochemical processes at the O₂-electrode involve the adsorption of oxygen on the MIEC, the bulk diffusion of vacancies, and the direct exchange of vacancies with the electrolyte, using the approach proposed by Adler et al. [302], and [303, 304], including diffusion transient terms. The model resolves the diffusion of vacancies caused by the chemical and electric potential gradients. The O₂-electrode was divided into three layers: 1) a contact layer at the interface with the gas channel where only gas transport was considered, 2) a pure LSCF layer where gas transport and electrochemical reactions are considered, and 3) a mixed LSCF-GDC layer at the electrolyte–O₂-electrode interface where gas transport and electrochemical reactions were considered. The overpotential related to the transport in layer 1 is accounted for in equation (7.28). The overpotential related to the electrochemical and transport processes taking place in layers 2 and 3 is then given by the deviation of the vacancy concentration from the equilibrium concentration (c_V^{eq}) as expressed by equation (7.31). Equation (7.31) was then applied individually to layers 2 and 3. The total overpotential for layers 2 and 3 was then $\eta_{cV}^{O_2} = \eta_{cV,2} + \eta_{cV,3}$.

$$\eta_{cV} = \frac{RT}{2F} \ln \left(\frac{c_V}{c_V^{eq}} \right) \quad (7.31)$$

In typical SOC operating conditions, the YSZ ionic transference number $t_{ion} = \frac{i_{ion}}{i_{tot}} \approx 1$. The electrolyte was thus considered to be a purely ionic conductor and was modeled as a resistor. The temperature dependence of the electrolyte ionic conductivity as well as the constriction effect due to the porosity of the electrodes were considered when computing the electrolyte ASR (ASR_{elyte}). Additional resistance contributions (e.g., contact with the current collectors) were considered using an additional $ASR_{add} = 0.1 \, \Omega \text{cm}^2$. Defective regions were simulated by adding a supplemental resistive term ASR_{def} to one or multiple

Chapter 7. Numerical investigation

SOC discretization elements. The overpotential related to these resistive contributions is then given by equation (7.32).

$$\eta_{ASR} = j \cdot (ASR_{elyte} + ASR_{add} + ASR_{def}) \quad (7.32)$$

The SOC voltage is then computed as:

$$V_{SOC} = E_N^{channel} + \eta_{cv}^{O_2} + \eta_{conc}^{O_2} + \eta_{conc}^{H_2} + \eta_{act}^{H_2} + \eta_{ASR} \quad (7.33)$$

where $E_N^{channel}$ is the Nernst potential computed with equation (1.12) using the local gas composition in the gas channel. An iso-potential operation was considered; thus even though the overpotentials and current density are locally different, V_{SOC} is the same for each SOC discretization element.

7.2 LT sensitivity analysis

In this section, the effects of various physical parameters on the dynamic thermal response of the SOC are investigated using the LT approach.

The Fourier transform outputs a series of complex numbers where each one corresponds to the contribution of an harmonic to the original signal. The analysis was limited to the 1st and 2nd harmonics which corresponded to the variable modulation at the excitation frequency and twice the excitation frequency, respectively. The complex representation of first harmonic of the Fourier transform of T_{SOC} , i.e., \hat{T}_{SOC}^I , is given by equation (7.34), where the superscripts ' and ' stand for the real and imaginary component of the Fourier transform, respectively. The superscript I was used to refer to the 1st harmonic; II was used instead when the 2nd harmonic was considered. In this section, the results of the Fourier transform were preferentially analyzed using an amplitude–phase representation, as defined for \hat{T}_{SOC}^I by equations (7.35)–(7.37). The same procedure and nomenclature were used for the other variables considered, e.g., \dot{Q}_{rx} .

$$\hat{T}_{SOC}^I = \hat{T}_{SOC}'^I + i \cdot \hat{T}_{SOC}''^I \quad (7.34)$$

$$\hat{T}_{SOC}^I = \|\hat{T}_{SOC}\|^I e^{i\phi_{SOC}^I} \quad (7.35)$$

$$\|\hat{T}_{SOC}\|^I = \sqrt{(\hat{T}_{SOC}'^I)^2 + (\hat{T}_{SOC}''^I)^2} \quad (7.36)$$

$$\phi_{SOC}^I = \tan\left(\frac{\hat{T}_{SOC}''^I}{\hat{T}_{SOC}'^I}\right) \quad (7.37)$$

The LT results were represented in the form of a 2-D image with the vertical and horizontal axis corresponding to the logarithm of the excitation frequency and the dimensionless position x^* , respectively, and a color scale was used to represent the variable of interest, as shown in Figure 7.4. Each "pixel" row thus corresponds to the spatial distribution of the SOC thermal response at a particular frequency. The SOC inlet and outlet corresponds to $x^* = 0$ and 1, respectively. The amplitude of the SOC thermal response, $\|\hat{T}_{SOC}\|^I$, depends on the excitation frequency and varies by multiple orders of magnitude within the frequency range investigated, which made it impractical to define an adequate color scale. The relative temperature amplitude, defined as the ratio between the local $\|\hat{T}_{SOC}\|^I$ and the maximal $\|\hat{T}_{SOC}\|^I$ at the considered frequency, which is mathematically formulated in equation (7.38), was preferred to represent the spatial distribution of $\|\hat{T}_{SOC}\|^I$ at various frequencies with a unique color scale.

$$\|T_{SOC}^{rel}\| = \frac{\|\hat{T}_{SOC}\|}{\max_{x^*} \|\hat{T}_{SOC}\|} \quad (7.38)$$

The interpretation of the phase image may not always be straight forward. To clarify, a generic representation of the phase difference between a sinusoidal excitation and the system response in terms of temporal shift as well as its impact on the real and imaginary part of the Fourier transform is presented in Figure 7.4. Typically, the phase shift is expected to be in Quadrant 4 due to the thermal inertia of the system.

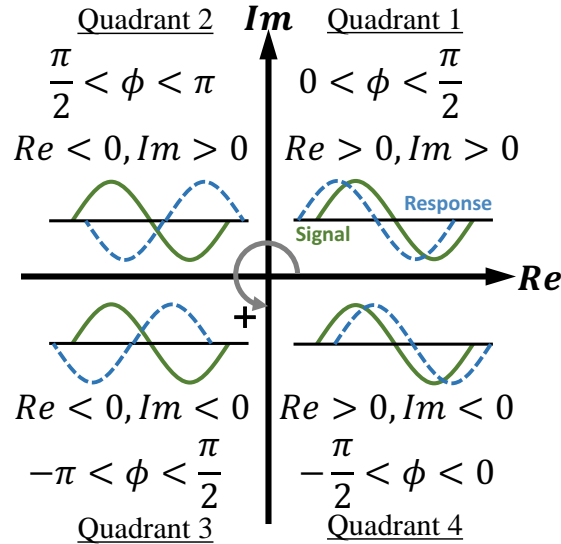
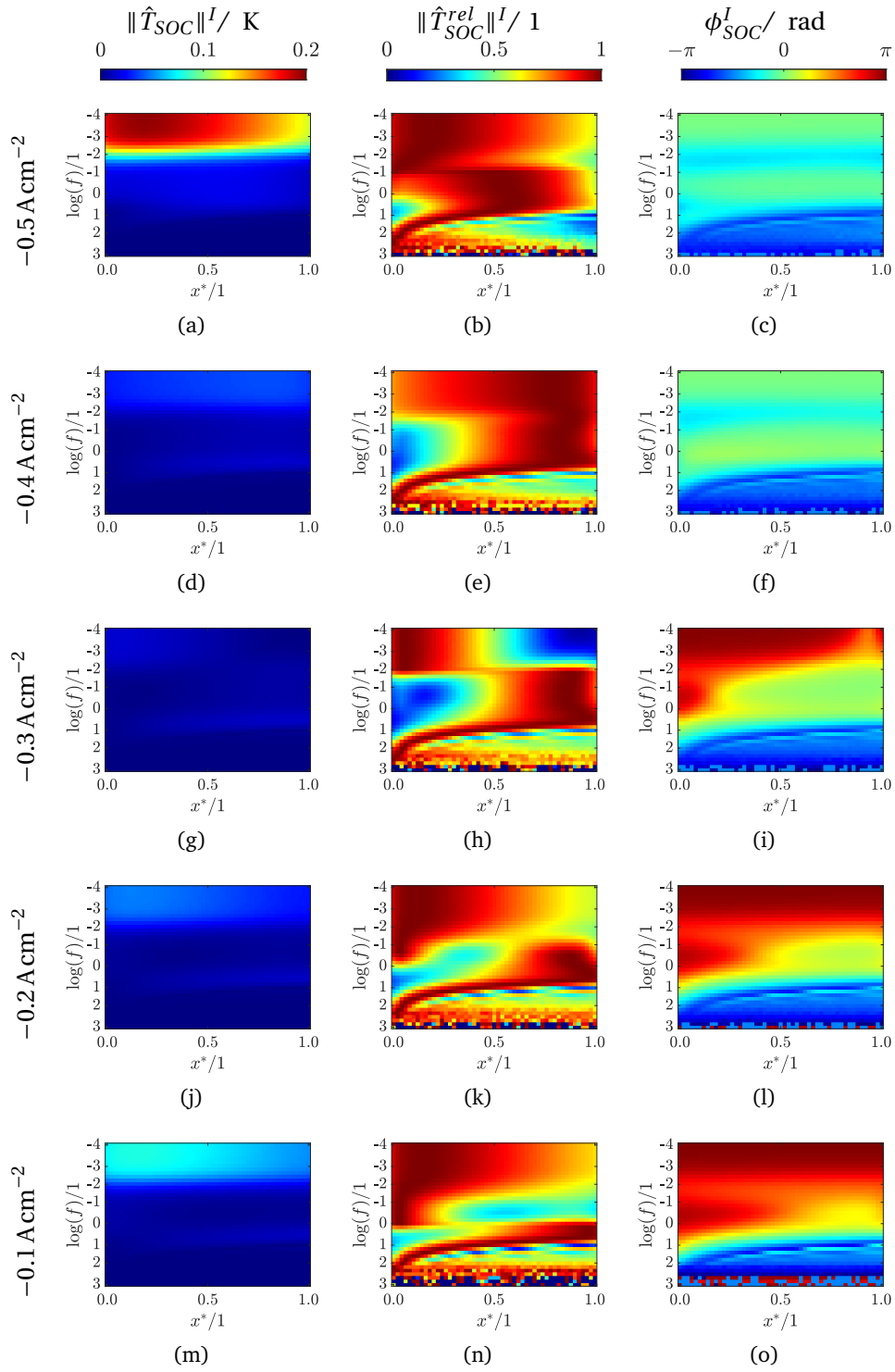


Figure 7.4 – Schematic representation of the phase shift between a sinusoidal signal and response, here, the current density and temperature, respectively. The resulting effect of the phase shift on the real and imaginary part of the response is also presented. The phase is positive in the counter-clockwise direction.

The reference case parameters used for the sensitivity analysis are presented in Table 7.1. The transient simulations were initialized using the steady-state values computed for each case investigated. Fifteen cycles were then simulated to allow the SOC to pass the initial transitory phase, owing to the additional terms in $\|Q_{rx}\|^0$ related to the current modulation, as shown in equation (7.20), and reach an harmonic oscillation around that new equilibrium. Only the last cycle was then used for the Fourier analysis.

Table 7.1 – Parameters used for the reference case

λ_{GDL} $\text{Wm}^{-1}\text{K}^{-1}$	λ_{MIC} $\text{Wm}^{-1}\text{K}^{-1}$	U_A $\text{Nm}^3\text{min}^{-1}$	c_{O_2} 1	c_{N_2} 1	U_R $\text{Nm}^3\text{min}^{-1}$	c_{H_2} 1	c_{H_2O} 1	ΔJ Acm^{-2}	f Hz
3.5	15	120	0.21	0.79	120	0.5	0.5	0.033	10^{-4} – 10^3



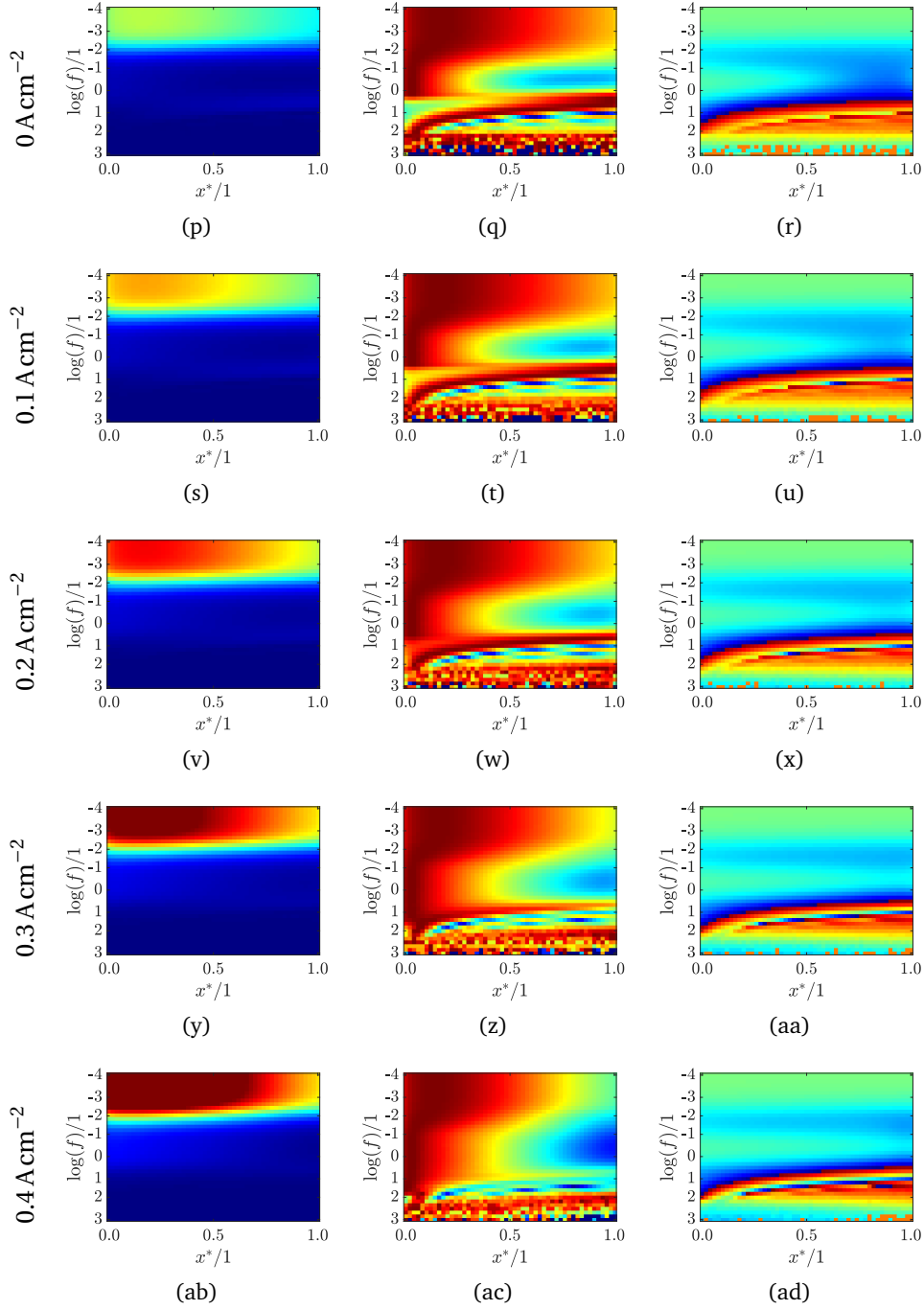


Figure 7.4 – Dependency of the SOC's thermal response on the steady-state current density. From the left to the right column : $\|\hat{T}_{SOC}\|^I$, $\|\hat{T}_{SOC}^{rel}\|^I$, and ϕ_{SOC}^I . Each line corresponds to a different current density.

7.2.1 Frequency dependency

The simulation performed at OCC was used as a base case to investigate the effect of the excitation frequency on the SOC thermal response. The corresponding $\|\hat{T}_{SOC}\|^I$, $\|\hat{T}_{SOC}^{rel}\|^I$, and ϕ_{SOC}^I images are reported in Figures 7.4 (p), (q), and (r), respectively. At frequencies below 0.1 Hz, the SOC's electrochemical impedance was almost constant, as shown in Figure 7.20 (b) indicating that below that frequency, the electrochemistry was at equilibrium and the electro-thermal behavior was thus only related to heat transfer mechanisms.

Between 0.1 and 1 mHz, $\|\hat{T}_{SOC}\|^I$ was highest and relatively independent of the excitation frequency. The amplitude was greater at the inlet than at the outlet, reflecting the modulation of \dot{Q}_{rx} and j , as shown in Figures 7.5 (d) and 7.6 (a), respectively. The phase difference between the current excitation and the SOC thermal response, ϕ_{SOC}^I , was close to 0 and constant from the inlet to the outlet. This indicated that the temperature changes were slow enough for the entire system to be constantly at "quasi-equilibrium". Here, "quasi-equilibrium" was used as the system is not strictly at equilibrium as it was still following the current modulation. Decreasing the excitation below 0.1 mHz would not increase the amplitude of the temperature modulation any further.

From 1 to 20 mHz, $\|\hat{T}_{SOC}\|^I$ constantly decreased but was still in phase with the MIC and reactant temperature modulation. ϕ_{SOC}^I became negative, indicating a capacitive behavior, and reached a minimum at a frequency of about 20 mHz. As the SOC electrochemical impedance was almost constant in that frequency range, this modification of the thermal response was related to the heat transfer processes. The heat transfer on the air side was relatively low owing to the absence of an MIC and the low heat capacity of air. As $\|\hat{T}_{SOC}\|^I$ was small and the environmental temperature considered constant, the radiative losses on the air side can be approximated by a first-order Taylor series:

$$\begin{aligned}\dot{Q}_{rad}(T_{soc}) &= \dot{Q}_{rad}(T_{ss}) + (T_{soc} - T_{ss}) \left. \frac{\partial \dot{Q}_{rad}(T)}{\partial T} \right|_{T=T_{ss}} \\ &= \dot{Q}_{rad}(T_{ss}) + (T_{soc} - T_{ss}) \cdot 4\epsilon\sigma T_{ss}^3,\end{aligned}\tag{7.39}$$

where T_{ss} is the steady-state temperature and $(T_{soc} - T_{ss})$ is the amplitude of the temperature modulation, i.e., $\|\hat{T}_{SOC}\|^I$. Within a small temperature variation, the radiative losses can be considered as a purely resistive process of resistance $(4\epsilon\sigma T_{ss}^3)^{-1}$. The observed capacitive behavior was thus related to the interaction between the SOC, the MIC, and the reactant gas stream.

Starting from about 1 mHz, ϕ_{SOC}^I decreased from the inlet to the outlet. As the frequency was increased, this difference also increased. Additionally, the relative amplitude between

the inlet and outlet also increased. Up to approximately 0.1 Hz, the SOC's electrochemical response could be considered spatially homogeneous and the observed thermal behavior was thus a consequence of a longitudinal modification of the heat transfer processes. Above 0.1 Hz, the electrochemical response of the SOC was no longer spatially uniform. When compared with the total applied current, the local current density at the inlet and outlet showed a negative and positive phase lag, respectively as shown in Figure 7.6 (b). This phase lag increased with the frequency up to about 3 Hz, which corresponded to the relaxation frequency of the conversion impedance. Above 1 Hz, $\|T_{MIC}\|^I$ was close to 0, suggesting that ϕ_{SOC}^I was still mostly influenced by the SOC's and reactant heat capacities. Around 3 Hz, \dot{Q}_{rx} became larger at the outlet than at the inlet and so did $\|\hat{T}_{SOC}\|^I$. Above 0.1 Hz, the SOC thermal response was thus a combination of heat transfer and electrochemical processes and exhibited a sharp transition around 1 Hz related to the transient local electrochemical behavior.

Above 100 Hz, the SOC temperature modulation was so small that it reached the limit of the numerical accuracy of gProms. $\|\hat{T}_{SOC}\|^I$ thus became extremely noisy, making these data meaningless.

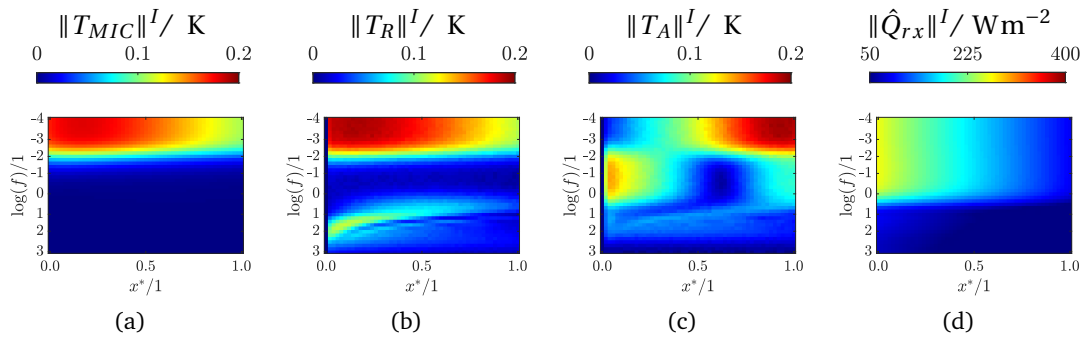


Figure 7.5 – Dependency of $\|T_{MIC}\|^I$, $\|T_R\|^I$, $\|T_A\|^I$, and \dot{Q}_{rx} on the excitation frequency at 0 Acm^{-2} .

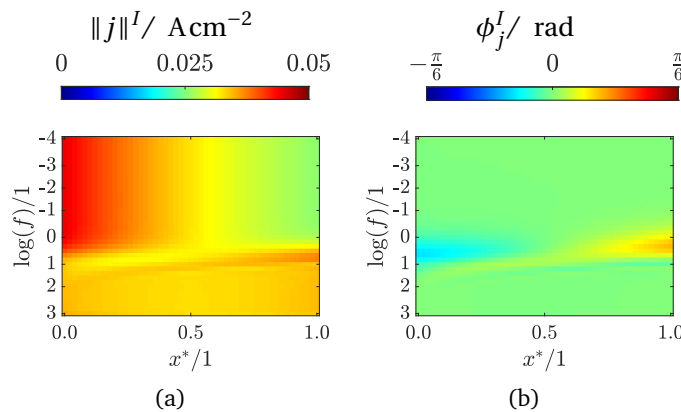


Figure 7.6 – Dependency of $\|j\|^I$ and ϕ_j^I on the excitation frequency at 0 Acm^{-2} .

7.2.2 Dependency on the MIC thermal conductivity

The effect of the conductivity of the SOC's support conductivity on the SOC thermal response was then investigated by changing λ_{MIC} by a factor of 0.5 and 2 compared to the base case.

Below 10 mHz, the amplitude of the thermal response became more homogeneous as λ_{MIC} was increased, as shown in Figure 7.7. When λ_{MIC} was increased, the heat was more easily transported from one end of the SOC to the other. The heat generated locally was thus more prone to diffusion and the $\|\hat{T}_{SOC}\|^I$ became "blurred". Above 10 mHz, the effect of the longitudinal conductivity appeared to be negligible; this was particularly clear in the resulting $\|\hat{T}_{SOC}^{rel}\|^I$, as presented in Figures 7.7 (b), (e) and (h). Interestingly, λ_{MIC} had only a limited impact on ϕ_{SOC}^I , as shown in Figures 7.7, (c), (f), and (i). Above 10 mHz, which also corresponded to a large drop of $\|T_{MIC}\|^I$ to near 0 K, the effect of lateral heat diffusion in the MIC was thus negligible.

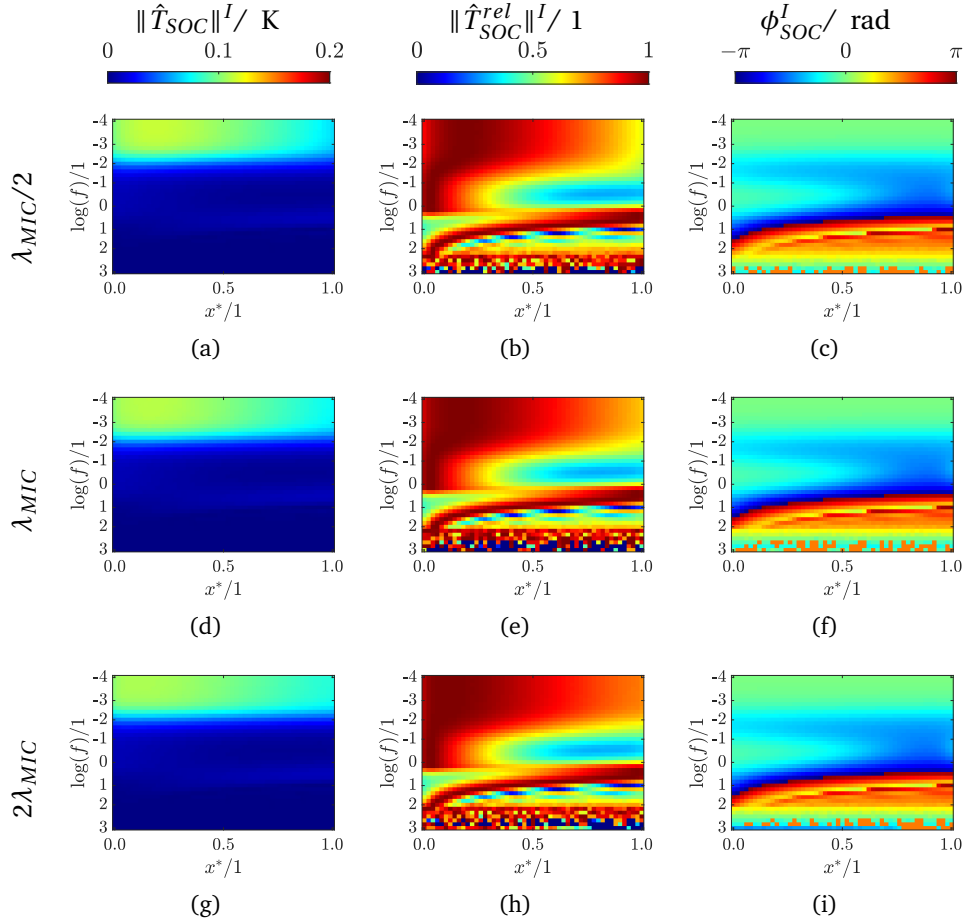


Figure 7.7 – Dependency of the SOC thermal response on λ_{MIC} at 0 Acm^{-2} . From the left to the right column : $\|\hat{T}_{SOC}\|^I$, $\|\hat{T}_{SOC}^{rel}\|^I$, and ϕ_{SOC}^I . Each line corresponds to a different value of λ_{MIC} .

7.2.3 SOFC operation

When the current was increased in fuel cell mode, both the $\|\hat{Q}_{rx}\|^I$ and $\|\hat{T}_{SOC}\|^I$ increased. The increase of $\|\hat{T}_{SOC}\|^I$ was greater at the SOC inlet, as illustrated by Figures 7.4 (s), (v), (y), and (ab). A similar behavior was observed for $\|\hat{Q}_{rx}\|^I$ as the current density principally increased near the SOC's inlet. The total current density was limited to 0.4 Acm^{-2} , which corresponds to the consumption of more than 80 % of the available oxygen, whereas only about 70 % of the hydrogen was converted.

Up to 0.3 Acm^{-2} , $\|\hat{Q}_{rx}\|^I$ increased over the entire SOC but principally at the inlet. Above 0.3 Acm^{-2} , $\|\hat{Q}_{rx}\|^I$ continued increasing at the SOC's inlet but began decreasing at the SOC's outlet. As the applied current was increased, more hydrogen was converted to H_2O and the H_2 content in the GDL decreased; this effect was particularly pronounced at the SOC outlet. Due to the limited amount of available H_2 , the local impedance at the outlet increased and the current was thus redistributed towards the inlet, where more H_2 was available and the local impedance was lower.

By increasing the current density, $\|\hat{T}_{SOC}\|^I$ principally increased near the inlet of the SOC but the high $\|\hat{T}_{SOC}\|^I$ region also spread towards the outlet especially below 10 mHz. For higher frequencies, i.e., up to about 2 Hz, $\|\hat{T}_{SOC}\|^I$ was less homogeneous presenting a larger intensity at the inlet compared to the outlet, as shown in Figures 7.4 (q), (t), (w), (z), and (ac). Above 2 Hz, $\|\hat{T}_{SOC}\|^I$ was lower at the inlet than at the outlet at low current densities and transitioned to a higher $\|\hat{T}_{SOC}\|^I$ at the inlet than at the outlet as the current density was increased. This behavior corresponded to a similar transition of $\|\hat{Q}_{rx}\|^I$, thereby indicating a similarity between $\|\hat{T}_{SOC}\|^I$ and the spatial distribution of the SOC's electrochemical activity.

Below 10 mHz, increasing the current density did not greatly impact ϕ_{SOC}^I , which remained spatially homogeneous and close to 0, as shown in Figures 7.4 (r), (u), (x), (aa), and (ad). The effects of the current density were more marked for frequencies of approximately 0.2 Hz. At 0 Acm^{-2} , ϕ_{SOC}^I at 0.25 Hz smoothly transitioned from -0.33 to -1.57 rad at the inlet and outlet, respectively. When the current density was increased, ϕ_{SOC}^I remained constant at the inlet of the SOC but gradually increased at the outlet to up to -0.76 rad at 0.4 Acm^{-2} . In fuel cell operation, the phase thus appeared to become more homogeneous when the current density was increased.

7.2.4 SOEC operation

The electrothermal behavior of the SOC was drastically different in electrolysis mode than in fuel cell mode. As the current density was increased (became more negative), $\|\hat{T}_{SOC}\|^I$ decreased to -0.3 Acm^{-2} , then increased, and was eventually higher than at 0 Acm^{-2} , when the current density reached -0.5 Acm^{-2} as shown in Figure 7.4. A similar behavior

was observed for $\|\hat{Q}_{rx}\|^I$ which decreased and reached a minimum at -0.3 Acm^{-2} before it quickly increased as the current density reached -0.5 Acm^{-2} .

For low current densities (up to -0.3 Acm^{-2}), ϕ_{SOC}^I was positive, indicating that a small current increase led to a reduction of the SOC's temperature. At higher current densities, the phase became negative, as was observed in fuel cell operation, indicating that the temperature of the SOC rose synchronously with the current density. This behavior was likely related to the transition from endothermic to exothermic operation as V_{SOC} passes from below to above V_{tn} , which is equal to 1.28 V for steam electrolysis at 750 °C. The evolution of \dot{Q}_{rx} as function of the SOC voltage is schematically represented in Figure 7.8. The transition of ϕ_{SOC}^I occurred when the current density was increased from -0.3 to -0.4 Acm^{-2} , which corresponded to a V_{SOC} increase from 1.09 to 1.14 V (represented by V1 and V2 in Figure 7.8, respectively), but did not occur across V_{tn} . Even though the SOC was globally endothermic, a small increase of voltage/current when $V_{SOC} = V_1$ led to a more negative \dot{Q}_{rx} , i.e., a temperature reduction, whereas a small increase of voltage/current when $V_{SOC} = V_2$ led to a less negative \dot{Q}_{rx} , i.e., a temperature increase. The phase image can thus be used to estimate V_{tr} , which corresponds to the voltage at which \dot{Q}_{rx} is the most negative. When the SOC was operated in electrolysis mode below V_{tr} , corresponding to a low current density, $\|\hat{T}_{SOC}\|^I$ was minimal, indicating that these are the least favorable operating conditions for performing active thermography.

In fuel cell operation, $\|\hat{T}_{SOC}\|^I$ was always larger at the SOC inlet than at the outlet; this was not the case during electrolysis mode, as shown in Figure 7.4. For excitation frequencies below 30 mHz, $\|\hat{T}_{SOC}\|^I$ was generally lower at the outlet than at the inlet for current densities ranging from 0 to -0.5 Acm^{-2} . Between 30 mHz and 1 Hz, a low $\|\hat{T}_{SOC}\|^I$ spot moved from the outlet of the SOC to the inlet of the SOC when the current was increased from 0 to -0.4 Acm^{-2} . It eventually led to an inverted behavior compared with that at lower frequency or in fuel cell operation where $\|\hat{T}_{SOC}\|^I$ was smaller at the inlet than at the outlet. In parallel, a reduced ϕ_{SOC}^I region spread from the SOC's outlet to its inlet following the low $\|\hat{T}_{SOC}\|^I$ spot motion as shown in Figure 7.4. When the current density was further increased, the spatial distribution of $\|\hat{T}_{SOC}\|^I$ and ϕ_{SOC}^I was similar to present in fuel cell operation. A deeper discussion on the origin of this behavior is presented in section 7.2.5.

7.2.5 Dependency on the convection coefficient

The effect of convective heat transfer on the LT results was investigated by artificially increasing and reducing the Nusselt number by a factor of 5 from the reference case ($Nu_R \approx 8.1$ for the reference case) while keeping all other parameters constant. The h_R^c is a function of the gas stream λ_R , which is dependent on the partial pressure of H_2O and H_2 . For the binary $\text{H}_2/\text{H}_2\text{O}$ reactant mixture considered, h_R^c can be expressed as a function of c_{H_2} , as shown graphically in Figure 7.9. The convective heat transfer

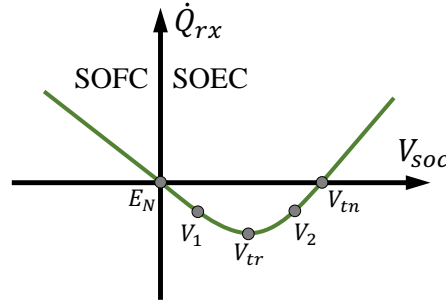


Figure 7.8 – Schematic representation of \dot{Q}_{rx} as function of the SOC's voltage.

coefficient increases with c_{H_2} with a quadratic-like behavior. In electrolysis operation, the convective heat transfer coefficient thus increased with an increased current density as H_2O was converted to H_2 . Additionally, c_{H_2} was always higher at the SOC outlet, this corresponds to the accumulation of the H_2 already produced upstream, thereby leading to a higher h_R^c near the outlet of the SOC. The opposite effect was seen in fuel cell operation, i.e., h_R^c decreased with the current density. The effect of the longitudinal variation of the convective heat transfer coefficient was further investigated by comparing the thermal behavior obtained with the concentration-dependent h_R^c against a constant value based on the inlet gas composition ($h_R^c = 3330 \text{ W m}^{-2} \text{ K}^{-1}$).

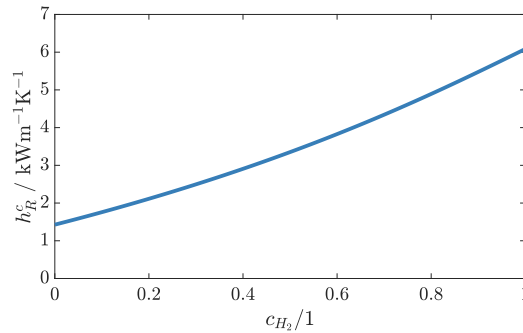


Figure 7.9 – Dependency of h_R^c on c_{H_2} for a H_2O / H_2 mixture at 750°C .

The current density distribution and $\|\hat{Q}_{rx}\|^I$ were fairly independent of h_R^c , indicating that the variation in the SOC thermal behavior was mainly related to the modification of the heat transfer processes. As the reactant exchanged heat with both the SOC and the MIC, it was also an indirect pathway for heat exchange between the MIC and the SOC. An increase of h_R^c thus also reduced the overall heat transfer resistance between the SOC and MIC. The temperature modulation of the MIC was, however, only slightly impacted by the modification of Nu_R .

The modification of Nu_R mainly affected the thermal response of the SOC between approximately 10 mHz and 2 Hz, whereas it had a limited impact on the thermal response of the SOC below 10 mHz, as shown by the evolution of $\|\hat{T}_{SOC}^{rel}\|^I$ in Figure 7.13. Between

approximately 10 mHz and 2 Hz, a low $\|\hat{T}_{SOC}\|^I$ region became more important and shifted from the outlet of the SOC towards its inlet as h_R^c was increased; this effect was particularly evident when $\|\hat{T}_{SOC}^{rel}\|^I$ was considered.

At frequencies <10 mHz, the $\|\hat{T}_{SOC}\|^I$ was lower at higher Nusselt numbers as illustrated in Figure 7.10. When operated in electrolysis mode, the $\|\hat{T}_{SOC}\|^I$ increased near the SOC outlet for frequencies >10 mHz when Nu_R was increased, as shown in Figure 7.10. The current density and therefore \dot{Q}_{rx} were small at the SOC outlet and were independent on the convective heat transfer coefficient. Therefore, the modification of the SOC outlet thermal behavior was essentially related to the transport and exchange of heat rather than to the local heat generation.

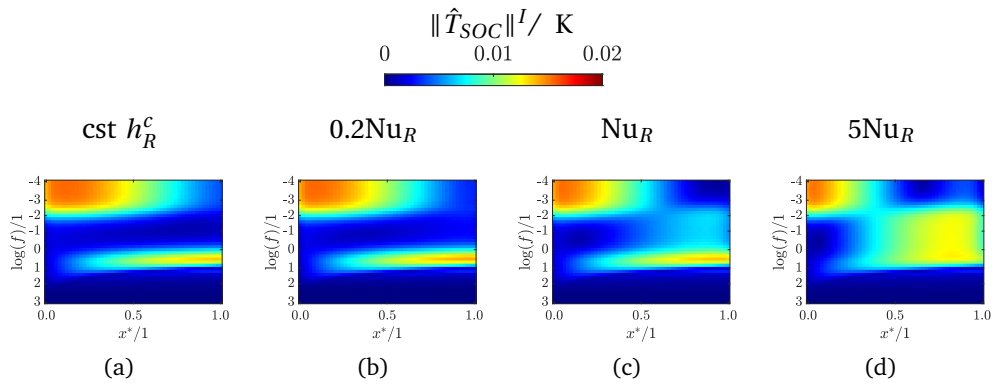


Figure 7.10 – Dependency of $\|\hat{T}_{SOC}\|^I$ on h_R^c at -0.3 Acm^{-2} . The first column corresponds to a spatially constant h_R^c computed based on the inlet composition ($3330 \text{ Wm}^{-2} \text{ K}^{-1}$) and the three other columns correspond to a different values of Nu_R and thus h_R^c .

A modification of ϕ_{SOC}^I was also observed particularly between 30 mHz and 3 Hz, as shown in Figure 7.12. As the Nu_R increased, a sharp phase transition formed near the SOC's outlet and propagated towards its inlet. This sharp transition corresponded to the observed minimum $\|\hat{T}_{SOC}\|^I$. At the inlet, ϕ_{SOC}^I was within quadrant 2 and 3 but moved to quadrant 1 and 4 at the outlet of the SOC, as defined in Figure 7.4, indicating a transition from a negative to a positive \hat{T}_{SOC}^I . As $\|\hat{T}_{SOC}\|^I$ can only be positive by definition, the continuous transition from a positive to a negative \hat{T}_{SOC}^I thus leads to the observed low $\|\hat{T}_{SOC}\|^I$ in the vicinity of the transition. The temperature field modulation can thus be imagined as an oscillating beam with the pivot located at the low $\|\hat{T}_{SOC}\|^I$ region.

The thermal response of the SOC can be influenced by both the steady-state and dynamic distribution of h_R^c . The latter originates from the local c_{H_2} modulation induced by the current perturbation. The spatial distribution of the steady-state local h_R^c at current densities other than the reference case showed that h_R^c can significantly vary between the inlet and outlet of the SOC as presented in Figure 7.11 (a). An increase of more than 50 % was observed between the inlet and outlet of the SOC at -0.5 Acm^{-2} . The applied 0.033 Acm^{-2} current density modulation led to a $\pm 5.8 \%$ variation of the global

reactant utilization, which caused a significant modulation of h_R^c in electrolysis mode, as shown in Figure 7.11 (b). As the H_2 concentration increased, h_R^c became more sensitive to modifications to c_{H_2} owing to the quadratic-like relationship between c_{H_2} and h_R^c as shown in Figure 7.9.

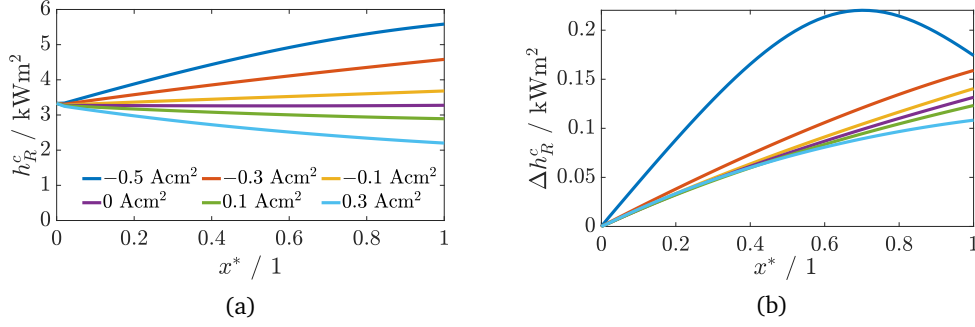


Figure 7.11 – Spatial distribution of a) the steady-state value and b) modulation amplitude (Δh_R^c) of h_R^c .

The SOC thermal response obtained with a constant convective heat transfer coefficient led to similar results than those obtained when employing the lowest Nu_R considering a concentration-dependent h_R^c , as shown in Figures 7.12 and 7.13. At 0 Acm^{-2} , the H_2 concentration gradient from the inlet to the outlet of the SOC is null; the steady-state distribution of the convective heat transfer coefficient is thus a constant. Therefore, only the spatial distribution of h_R^c resulting from the current perturbation influenced the SOC's thermal response. The major difference occurred between 10 mHz and 2 Hz, where a sharp phase transition was observed, particularly at higher values of Nu_R , as presented in Figure 7.12. This demonstrated that in this frequency range, the variation of h_R^c due to the modification of the local composition caused by the current perturbation was sufficient to affect $\|\hat{T}_{SOC}\|^I$ and ϕ_{SOC}^I .

When the SOC was polarized in fuel cell mode, the difference between a constant and concentration-dependent h_R^c diminished with an increased current density, as shown in Figures 7.12 and 7.13. This change likely originated from the reduction of c_{H_2} , which reduced both the steady-state and modulated h_R^c due to the quadratic-like relationship between c_{H_2} and h_R^c . During electrolysis, the ϕ_{SOC}^I difference between the constant and concentration-dependent h_R^c , increased until -0.3 Acm^{-2} and then became smaller at -0.5 Acm^{-2} , which also corresponded to the transition from below to above the V_{tr} .

At a frequency greater than approximately 1 Hz, the $\|\hat{T}_{SOC}\|^I$ was generally lower at the inlet than at the outlet, as illustrated by the $\|\hat{T}_{SOC}^{rel}\|^I$ in Figure 7.13, which was also valid for other current densities. This was likely related to the electrochemical behavior of the SOC as it was within the same frequency range as the conversion impedance. At higher Nu_R in electrolysis mode, the $\|\hat{T}_{SOC}\|^I$ was also lower at the inlet than at the

outlet between about 30 mHz and 1 Hz, as illustrated by the evolution of the $\|\hat{T}_{SOC}^{rel}\|^I$ in Figure 7.13. During half of the modulation period, the current density was higher than at steady state and c_{H_2} increased, increasing the h_R^c . As the reactant exchanged heat with both the SOC and the MIC, it was also an indirect pathway for heat exchange between the MIC and the SOC. An increase of h_R^c thus reduced the overall heat transfer resistance between the SOC, the reactant, and the MIC. The reduction of the heat transfer resistance thus lead to a reduction of the temperature difference between the SOC, the reactant, and the MIC. In that frequency range, the thermal inertia of the MIC was sufficient to keep the T_{MIC} constant and higher than the T_{SOC} , thus leading to an increase of the T_{SOC} as the thermal resistance decreased. During the second half of the modulation period, the current was lower than at steady state, thereby reducing c_{H_2} . Consequently, h_R^c decreased, the SOC cooled down as the heat transferred from the MIC, and the reactant were no longer sufficient to compensate for the local heat losses. The observed higher intensity at the outlet of the SOC was, thus, the result of a local modification of h_R^c , which then modified the heat transfer between the SOC, the reactant, and the MIC.

At the inlet of the SOC, the modification of h_R^c during the current modulation was significantly smaller than at the outlet and the temperature modulation was thus dominated by \dot{Q}_{rx} , which counter balanced the effect of the increased h_R^c until the V_{tr} was passed. Therefore, the low $\|\hat{T}_{SOC}\|^I$ region observed between 10 mHz and 0.25 Hz, corresponding to the transition from a positive to a negative real component of the SOC temperature modulation, indicated the transition from a \dot{Q}_{rx} - to a h_R^c -driven temperature modulation. This transition disappeared when V_{SOC} was higher than V_{tr} , as here a current modulation had the same impact on \dot{Q}_{rx} and h_R^c and the c_{H_2} was throughout the SOC, leading to a relatively homogeneous ϕ_{SOC}^I , as shown in Figures 7.12 (b), (c) and, (d).

In fuel cell operation, the effect of h_R^c diminished when the current density was increased, as more H_2 was converted to H_2O , thereby decreasing the amplitude of the h_R^c modulation. When the current density was increased, the h_R^c -dominated region shifted towards the outlet of the SOC where the c_{H_2} modulation was the most important due to the accumulation effect.

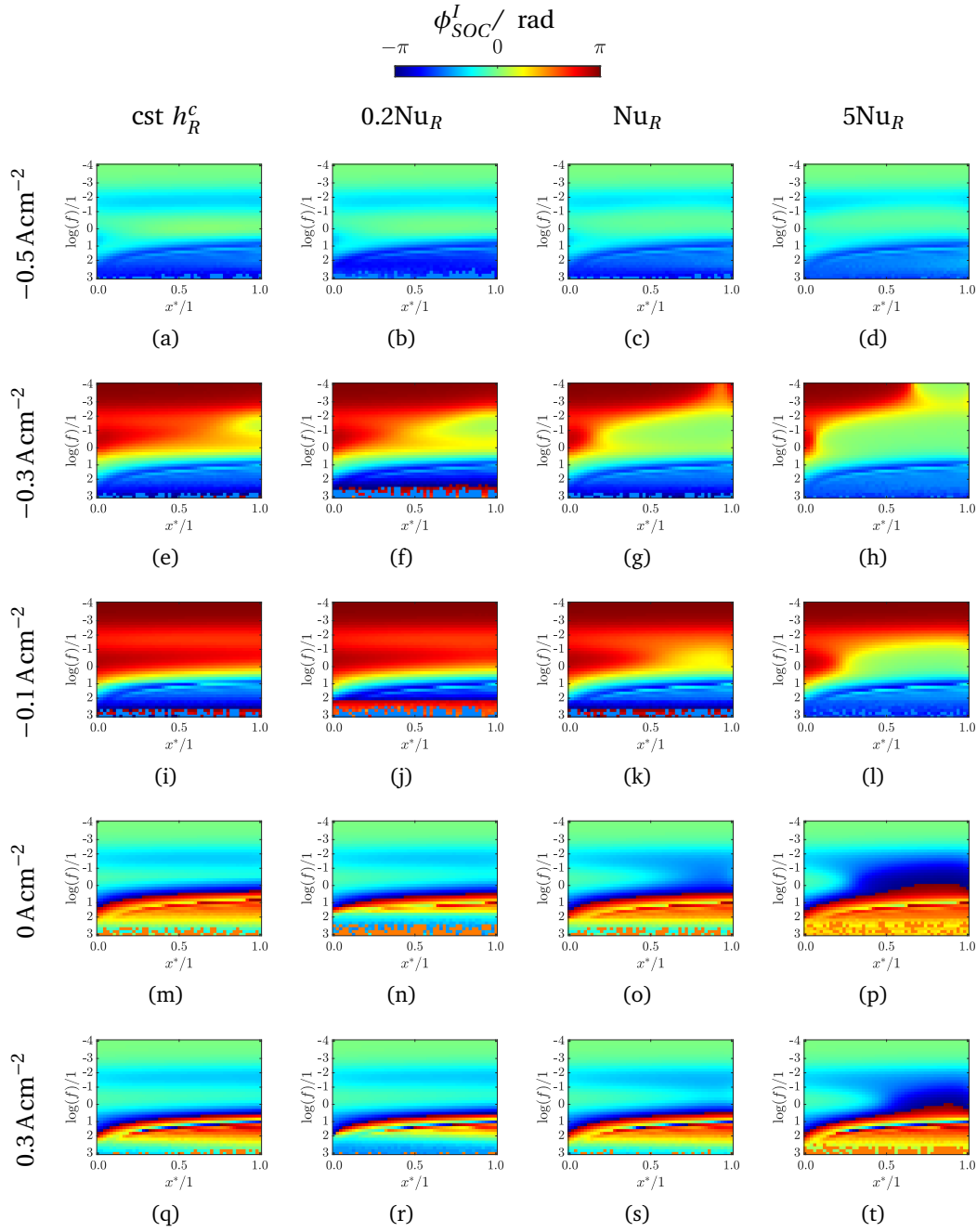


Figure 7.12 – Dependency of ϕ_{SOC}^I on h_R^c at various current densities. The first column corresponds to a spatially constant h_R^c computed based on the inlet composition ($3330 \text{ W m}^{-2} \text{ K}^{-1}$) and the three other columns correspond to different values of Nu_R and thus h_R^c .

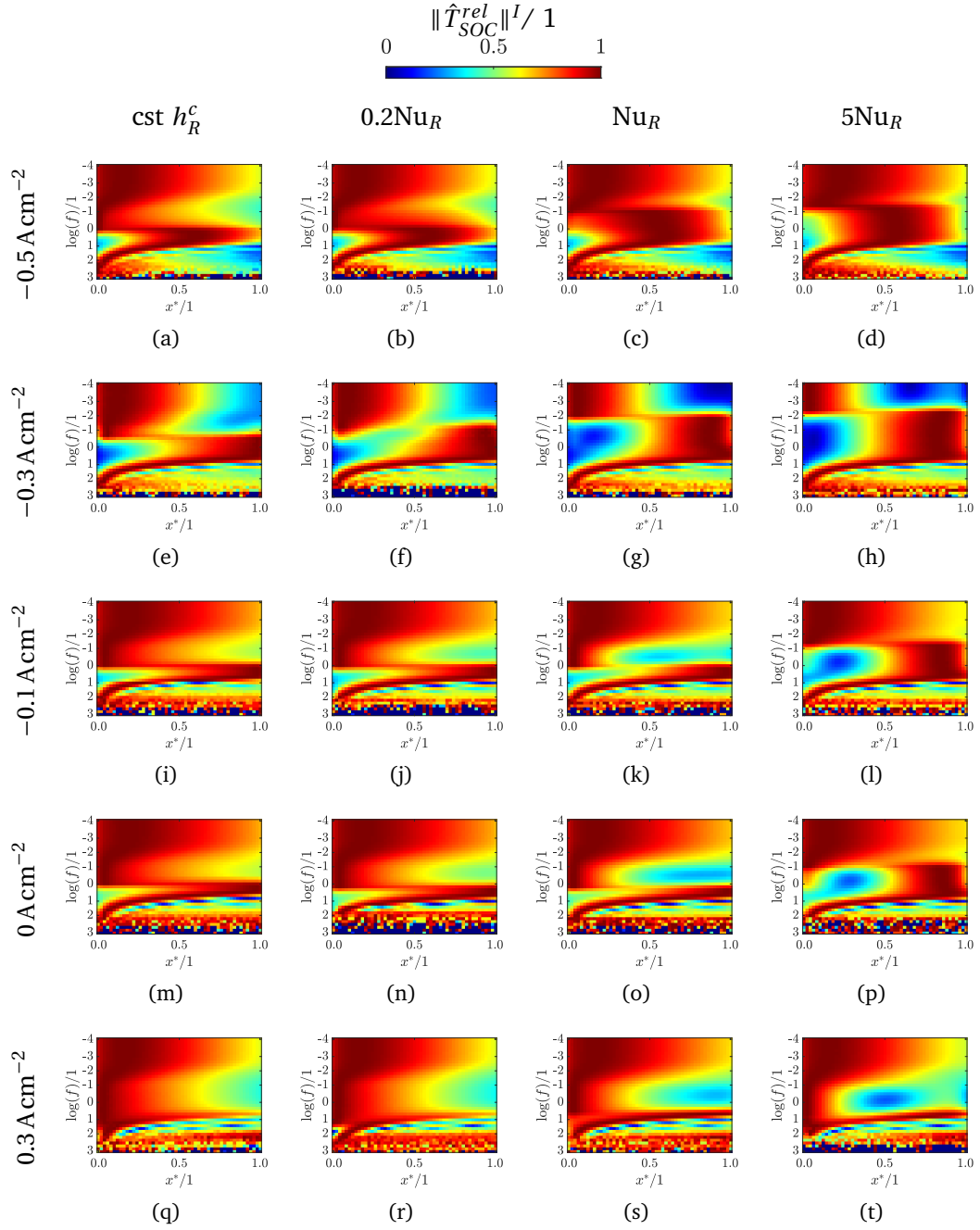


Figure 7.13 – Dependency of $\|\hat{T}_{SOC}^{rel}\|^I$ on h_R^c at various current densities. The first column corresponds to a spatially constant h_R^c computed based on the inlet composition ($3330 \text{ W m}^{-2} \text{ K}^{-1}$) and the three other columns correspond to different values of Nu_R and thus h_R^c .

7.2.6 Dependency on flow rate and reactant utilization

The sensitivity of the thermal response on the gas flow rate was investigated by increasing and decreasing each stream individually by a factor of 1.5 and 2, respectively, while keeping the others at the reference condition. A set of simulations was performed at 0 Acm^{-2} to compare the effect of the air and reactant flow rate on the same basis. Additional simulations were performed at higher current densities to distinguish between the effects of the reactant utilization and current density.

The modification of the air flow (U_A) showed only a negligible impact on the thermal response of the SOC at 0 Acm^{-2} , whereas a modification of the reactant flow rate (U_R) led to significant changes, as shown by the trends of the $\|\hat{T}_{SOC}^{rel}\|^I$ and ϕ_{SOC}^I in Figure 7.14. This indicates that, for the considered model, the convective heat transfer on the air side had no significant impact on the thermal response of the SOC.

Reducing the reactant flow rate led to a similar behavior as increasing the Nu_R or the polarization in electrolysis mode, whereas an increase of the reactant flow rate led to a similar response as a lower Nu_R or polarization in fuel cell mode. A lower reactant flow rate led to a higher variation of the reactant composition during the current modulation than with a higher reactant flow rate. Therefore, the modification of the thermal behavior was attributed to the modification of h_R^c , as described in section 7.2.5.

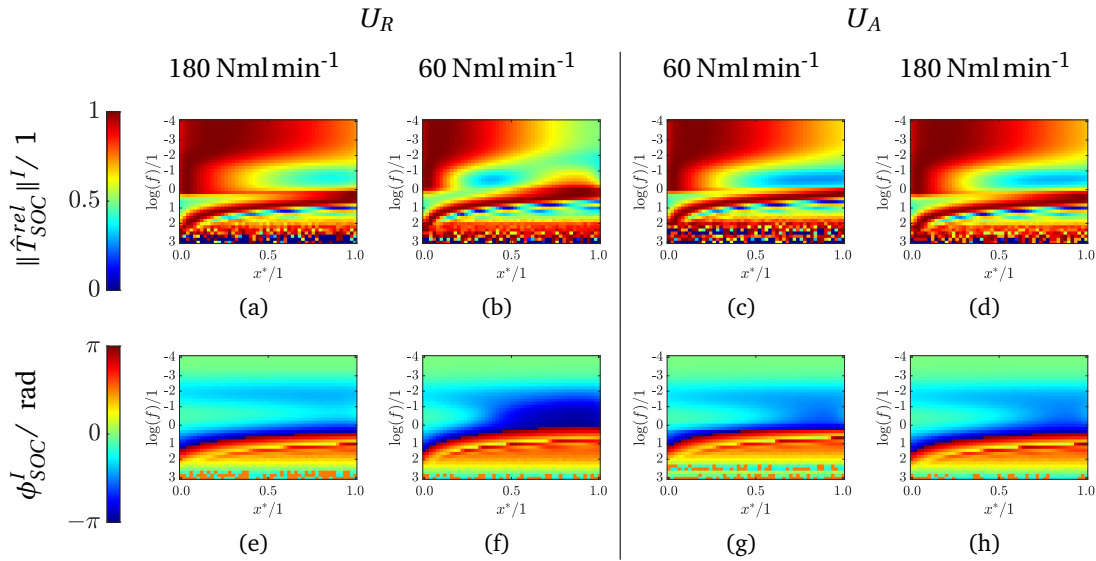


Figure 7.14 – Dependency of the $\|\hat{T}_{SOC}^{rel}\|^I$ and ϕ_{SOC}^I on the reactant (U_R) and air (U_A) flow rate at 0 Acm^{-2} .

During electrolysis operation, the ϕ_{SOC}^I responded similarly the same RU but not for the same current density as presented in Figure 7.15. The phase dependency on the RU was particularly visible around 0.25 Hz. The thermal response of the SOC in this frequency range depended on the the local modification of h_R^c , which is a function of

c_{H_2} . The phase was also impacted by varying the U_R ; as the same current perturbation used independently of the flow rate it led to a larger modulation of the c_{H_2} for lower than higher U_R . The lowest U_R led to a similar spatial distribution of ϕ_{SOC}^I , but the values showed significant deviation when compared with the higher U_R investigated. The relative amplitude of the thermal response of the SOC was dependent on the RU at frequencies around 0.25 Hz and on the current density at frequencies above about 2 Hz, as shown in Figure 7.15. The $\|\hat{T}_{SOC}\|^I$ was dependent on the current density and the U_R but not on the RU. In electrolysis mode, increasing the current density and thus the cell voltage led to a decrease of the $\|\hat{T}_{SOC}\|^I$ until V_{tr} was reached. When $RU = 0.35$, the $V_{SOC} = 1.01, 1.04, \text{ and } 1.08 \text{ V}$ from the lowest to the highest flow rate, respectively, but ϕ_{SOC}^I remained positive indicating that V_{tr} was not reached. When the reactant flow rate was increased, the SOC was operated closer to V_{tr} to achieve the same RU of 0.35

In fuel cell operation, a $RU = 0.35$ was reached at a cell voltage of 0.91, 0.87, and 0.84 V and a current density of 0.1, 0.2, and 0.3 A cm^{-2} for the lowest to highest U_R , respectively. Consequently, the power dissipated to achieve the same RU was higher for the higher flow rate, which was reflected by a higher $\|\hat{T}_{SOC}\|^I$, as shown in Figure 7.16. The spatial distribution of the $\|\hat{T}_{SOC}\|^I$ was similar to $\|\hat{Q}_{rx}\|^I$. At a constant current density and varying reactant flow rate, the $\|\hat{T}_{SOC}\|^I$ behaved similarly, as presented in Figures 7.16 (a), (j), and (p) for 0.1 A cm^{-2} and Figures 7.16 (d) and (m) for 0.2 A cm^{-2} , indicating that the $\|\hat{T}_{SOC}\|^I$ was current-dependent than RU-dependent. For the lowest U_R , the $\|\hat{T}_{SOC}\|^I$ was higher than for higher U_R because for the same current modulation, the reactant concentration modulation was higher, which led to a significantly larger voltage amplitude and thus a larger heat modulation. The $\|\hat{T}_{SOC}^{rel}\|^I$ was dependent on the current density for frequencies above 1 Hz, as shown by the central column in Figure 7.16. Below 1 Hz, the $\|\hat{T}_{SOC}^{rel}\|^I$ was dependent on both the current density and U_R but not on the RU. The ϕ_{SOC}^I was not directly dependent on the RU, as shown in the third column of Figure 7.16. However, modifying the flow rate and the current density led to a significant modification of the ϕ_{SOC}^I between 30 mHz and 2 Hz. The phase difference between the inlet and outlet of the SOC was more significant for lower values of U_R and current density. In these conditions, the effect of the current modulation on h_R^c was more pronounced for lower U_R and higher c_{H_2} due to the larger induced RU modulation and to the quadratic-like relationship between h_R^c and c_{H_2} , as was presented in section 7.2.5. The spatial distribution of the ϕ_{SOC}^I in that frequency range reflected the impact of a current perturbation on the local h_R^c and thus the local gas composition.

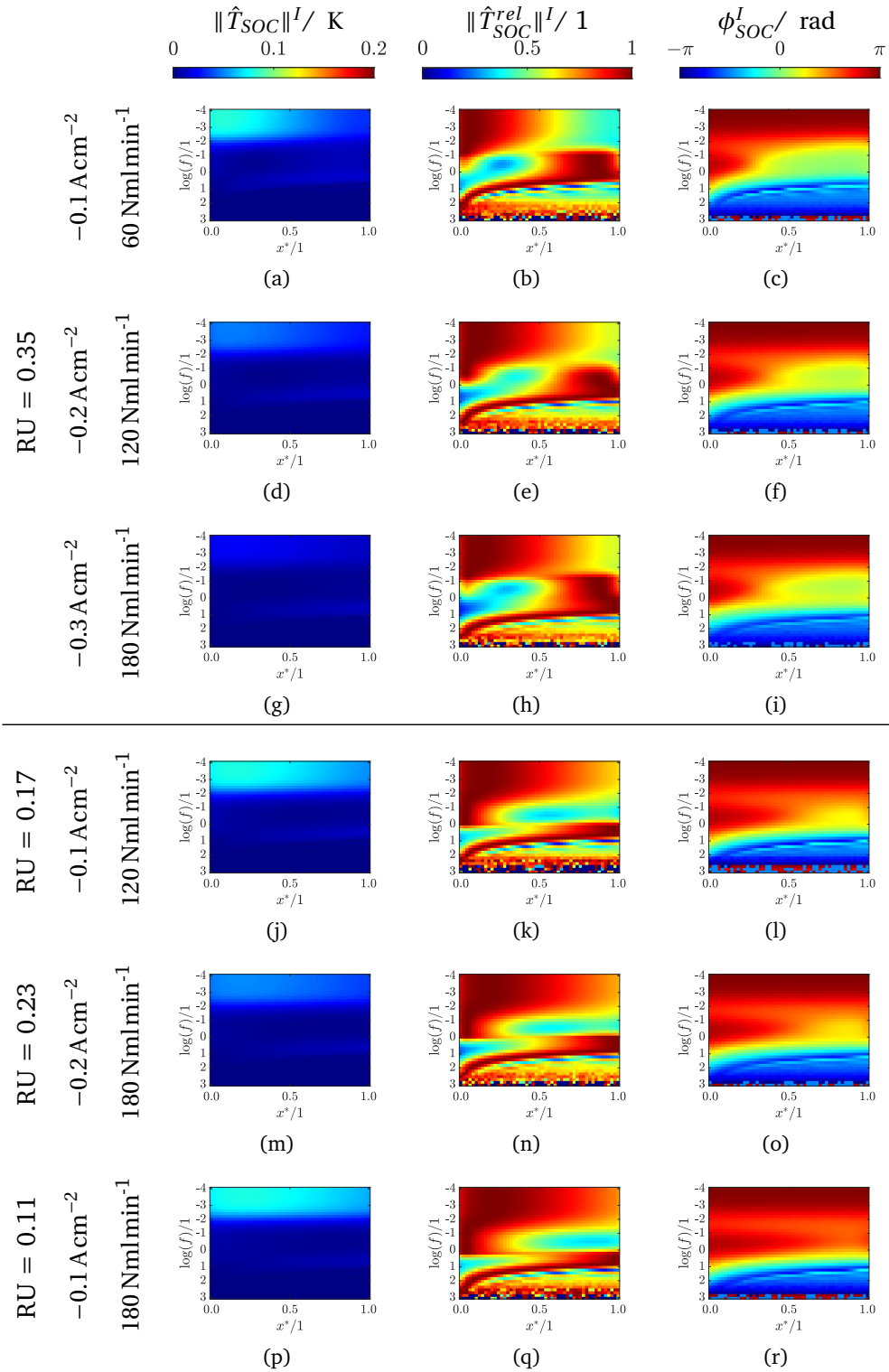


Figure 7.15 – Dependency of the thermal response of the SOC on the U_R and RU in electrolysis operation.

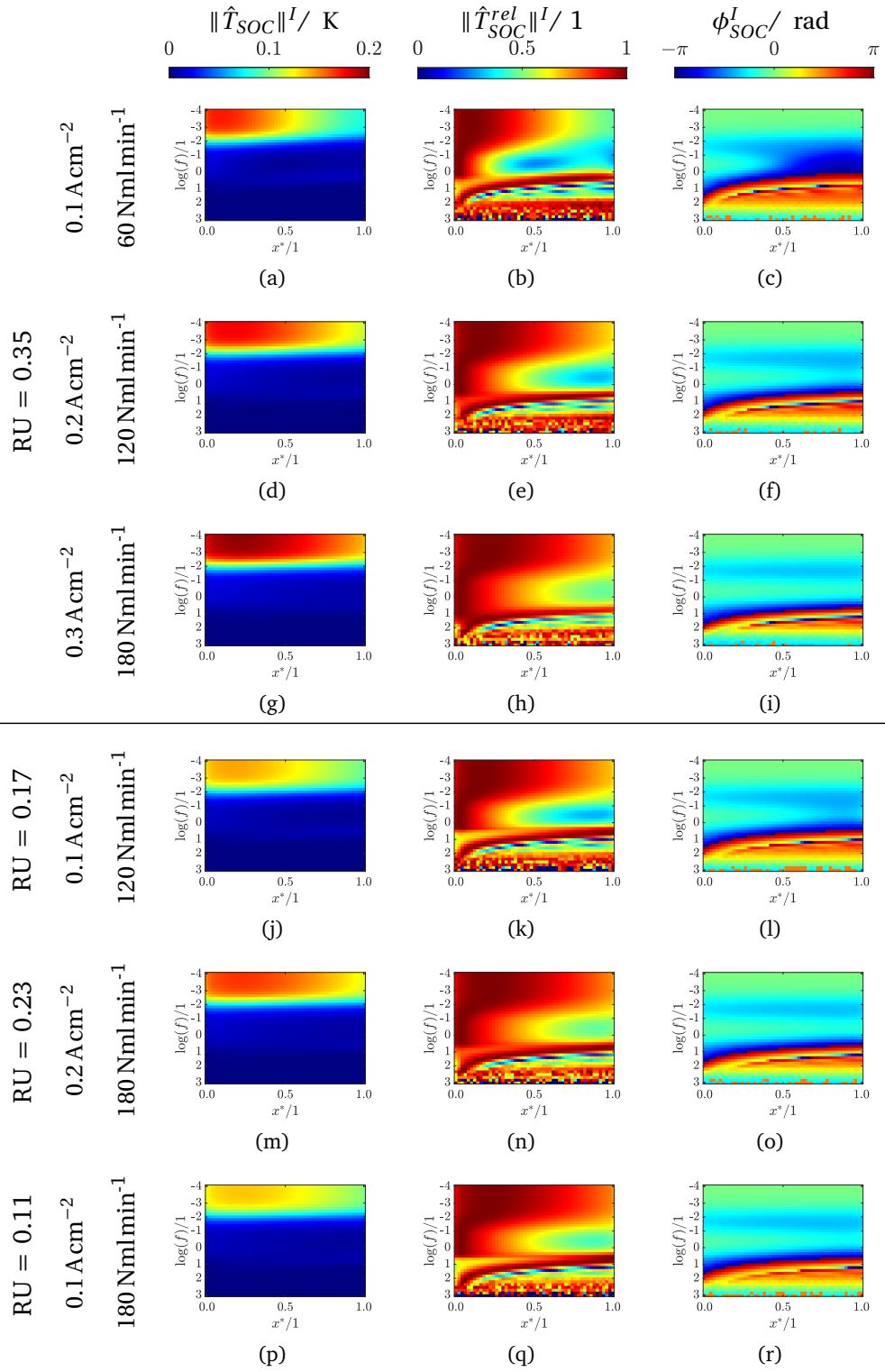


Figure 7.16 – Dependency of the SOC thermal response on U_R and RU in fuel cell operation.

High reactant utilization

When equal flow rates are present at the H_2 -electrode and O_2 -electrode, the supplied O_2 is below the stoichiometric amount, thereby limiting the maximal RU in fuel cell mode to approximately 0.8 for the 50/50 vol% H_2/H_2O reactant mixture considered. To investigate the effect of $RU > 0.8$, the air flow rate was increased from 120 to 180 Nmlmin⁻¹ to avoid O_2 limitation and allow RU to become the limiting factor. As varying the air flow rate only marginally affected the thermal response of the SOC, the obtained results were compared directly with those presented in Figure 7.4.

At an $RU = 0.87$ in fuel cell mode, corresponding to a current density of 0.5 Acm^{-2} , below 10 mHz, the $\|\hat{T}_{SOC}\|^I$ was higher at the inlet than at 0.4 Acm^{-2} but lower at the outlet of the SOC as shown in Figures 7.17 (a) and (ab), respectively. Between 30 mHz and 2 Hz, the $\|\hat{T}_{SOC}^{rel}\|^I$ showed a shift of the low $\|\hat{T}_{SOC}\|^I$ region from the inlet toward the outlet of the SOC at 0.5 Acm^{-2} compared with 0.4 Acm^{-2} , as shown in Figures 7.17 (b) and 7.4 (ac), respectively. In parallel, ϕ_{SOC}^I changed drastically at the outlet of the SOC compared to a lower current density as shown in Figure 7.17c and 7.4ad, respectively. The phase transitioned from about -0.8 rad at 0.4 Acm^{-2} to almost 3 rad at 2 Acm^{-2} , corresponding to a switch of the complex thermal response from quadrant 4 to 1 as defined in Figure 7.4. The T_{SOC} from the position at $x^* = 0.84$ to 1 oscillated almost in counter phase with the applied current modulation, whereas the rest was lagging behind the current modulation. The phase of the local current density presented a similar behavior, as shown in Figure 7.18. The local current density was thus oscillating in counter phase near the outlet of the SOC and in phase near the inlet of the SOC, as shown by the temporal evolution of the local and total current density around the steady-state value at 0.25 Hz reported in Figure 7.18 (b). Although the applied total current density was sinusoidal, the local current density showed a non-symmetric oscillation between the first and second half of the oscillation period. This induced a second harmonic to V_{SOC} , which indicates a non-linear behavior of the SOC current-voltage response. The counter-intuitive evolution of the local current density near the outlet of the SOC resulted from the high reactant utilization. While the current was increasing during sinusoidal excitation, the RU increased from 0.81 to 0.93, thereby limiting the H_2 availability near the outlet of the SOC. The local impedance increased and led to a redistribution of the current density towards the inlet, where more reactant was available and the impedance was lower. The situation was reversed during the second half of the cycle; as the total applied current decreased, more reactant became available and the local current density was redistributed towards the outlet.

This behavior was present at the lowest frequency for the current density, but only appeared for excitation frequencies above 30 mHz in the thermal response, likely owing to the limited effect of conduction in the MIC with increasing frequency. The SOC thermal response above 30 mHz thus appeared to be representative of the spatial and temporal evolution of the local current density modulation.

In electrolysis mode at $RU = 0.87$, a similar local current density behavior was observed. However, this was not visible in the $\|\hat{T}_{SOC}\|^I$, $\|\hat{T}_{SOC}^{rel}\|^I$, or ϕ_{SOC}^I images, as shown in Figures 7.17 (d), (e), and (f), respectively. If the second order terms are neglected from equations (7.22) and (7.23), $\|\hat{Q}_{rx}\|^I = \|j\|^I \cdot (\|V_{tn} - V_{SOC}\|^0) + \|V_{SOC}\|^I \cdot \|j\|^0$. At -0.5 A cm^{-2} , the SOC voltage was 1.21 V which is close to the $V_{tn} = 1.28 \text{ V}$ for steam electrolysis at 750°C . Consequently, the term $\|j\|^I \cdot (\|V_{tn} - V_{SOC}\|^0) \approx 0$ and only $\|V_{SOC}\|^I \cdot \|j\|^0$ contributed to the temperature modulation of the SOC. The voltage modulation $\|V_{SOC}\|^I$ was by definition spatially uniform and as $\|j\|^0$ is the steady-state current density distribution, which is time invariant, the local heat generation was thus independent of the local current density modulation $\|j\|^I$. The contribution of the local current modulation was thus negligible to the ϕ_{SOC}^I or $\|\hat{T}_{SOC}\|^I$ when the V_{SOC} was $\approx V_{tn}$.

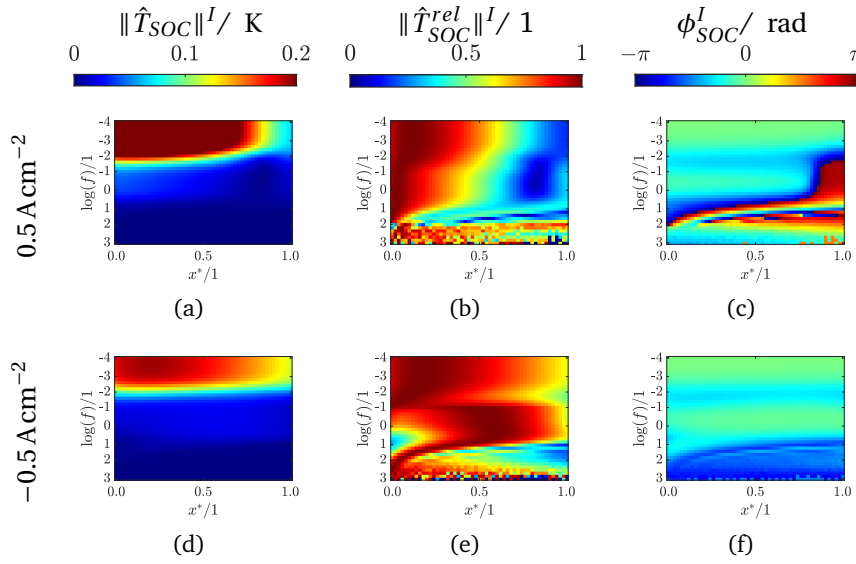


Figure 7.17 – Thermal response of the SOC at $RU = 0.87$ in (a)–(c) fuel cell and (d)–(f) in electrolysis operation.

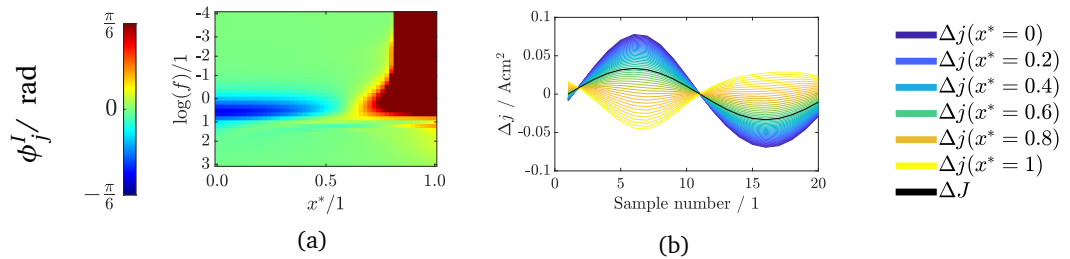


Figure 7.18 – Effect of high RU on the local current density, (a) phase shift between the local and applied current density modulation in fuel cell operation at $RU = 0.87$ and (b) local and total current density modulation from the steady state-value.

7.2.7 Dependency on the thermal conductivity of the GDL

The effect of the thermal conductivity of the GDL (λ_{GDL}) on the local thermal behavior of the SOC was investigated by varying the λ_{GDL} by a factor of 10 from the reference case while keeping all other parameters constant. An increase of the thermal conductivity corresponds to a decrease of the thermal resistance and thus an improvement of the heat transfer.

Increasing λ_{GDL} from 3.5 to 35 Wm⁻¹K⁻¹ led to a negligible modification of the $\|\hat{T}_{SOC}\|^I$ between 0.1 and 10 mHz, as shown in Figures 7.19 (d) and (a), respectively. Although barely visible due to the scaling, a significant modification of the $\|\hat{T}_{SOC}\|^I$ was observed between 30 mHz and 2 Hz, i.e., it decreased by a factor 10 at the inlet of the SOC when λ_{GDL} was increased from 3.5 to 35 Wm⁻¹K⁻¹. Reducing λ_{GDL} to 0.35 Wm⁻¹K⁻¹ led to a significant modification of the behavior of the $\|\hat{T}_{SOC}\|^I$ from the lowest frequency to 2 Hz, as shown in Figure 7.19 (g). Below 10 mHz, the maximal value of the $\|\hat{T}_{SOC}\|^I$ was lower for a λ_{GDL} of 3.5 than 0.35 Wm⁻¹K⁻¹ and the spatial distribution showed a less extended high $\|\hat{T}_{SOC}\|^I$ region for the lowest λ_{GDL} , as shown in Figure 7.19. Reducing λ_{GDL} also likely reduced the impact of the lateral heat diffusion by limiting the direct exchange with the MIC and the indirect exchange with the reactant. Between 30 mHz and 2 Hz, the lowest λ_{GDL} case presented a high $\|\hat{T}_{SOC}\|^I$ region at the inlet of the SOC and another near the outlet, whereas only one high $\|\hat{T}_{SOC}\|^I$ region was visible near the inlet with an intensity about 5 and 10 times lower for a λ_{GDL} of 3.5 and 35 Wm⁻¹K⁻¹, respectively.

Reducing the λ_{GDL} increased the steady-state temperature difference between the MIC and the SOC. For the same modification of h_R^c caused by the current modulation, the SOC temperature modulation was enhanced compared with a higher λ_{GDL} and led to a high $\|\hat{T}_{SOC}\|^I$ region at the outlet of the SOC, as visible in Figure 7.19 7.19g. Between 30 mHz and 2 Hz, reducing λ_{GDL} had a similar effect on the $\|\hat{T}_{SOC}\|^I$ as an increase of the Nusselt number. Reducing the λ_{GDL} thus increased the importance of the reactant–SOC heat transfer. Below 10 mHz, modifying the λ_{GDL} seemed to have a larger impact on the spatial distribution of $\|\hat{T}_{SOC}\|^I$ than a modifying h_R^c , thus suggesting that the heat transfer with the MIC was dominant in that frequency range.

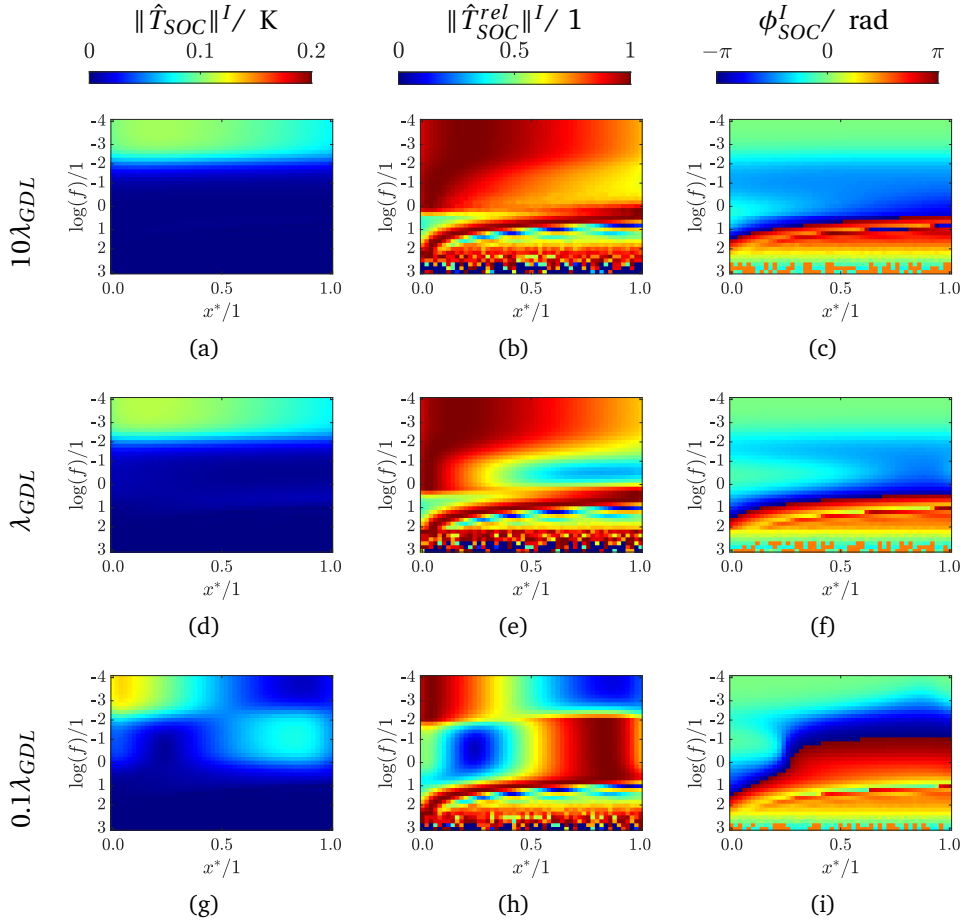
Modifying the λ_{GDL} had a major impact on the ϕ_{SOC}^I , as shown in Figures 7.19 (c), (f), and (i). Below 10 mHz, ϕ_{SOC}^I was only marginally impacted by an increase of the λ_{GDL} but when λ_{GDL} was decreased, a small region where ϕ_{SOC}^I was lower than $-\pi/2$ rad appeared near the SOC outlet at frequency closed to 10 mHz. It corresponded to an oscillation almost in counter-phase with the current excitation. This behavior indicated that the effect of h_R^c modulation could already be observed below 10 mHz for the lowest λ_{GDL} .

A modification of λ_{GDL} led to a significant variation of the spatial and frequency distribution of ϕ_{SOC}^I between about 10 mHz and 4 Hz. When λ_{GDL} was set to 35 Wm⁻¹K⁻¹, the

ϕ_{SOC}^I became more negative between 10 mHz and 0.25 Hz than it was below 10 mHz, as shown by the blue region extending from the inlet to outlet of the SOC in Figure 7.19 (c). In that frequency range, the ϕ_{SOC}^I near the inlet of the SOC reached a minimum of -1.34 rad at 50 mHz, whereas ϕ_{SOC}^I at the outlet was continuously decreasing as the frequency was increased. When the λ_{GDL} was reduced, the minimum ϕ_{SOC}^I increased and moved towards lower frequencies, reaching -0.95 rad at 20 mHz and -0.55 rad at 10 mHz for a λ_{GDL} of 3.5 and $0.35 \text{ Wm}^{-1} \text{ K}^{-1}$, respectively as shown in Figures 7.19 (f) and (i), respectively. The frequency range associated with the low ϕ_{SOC}^I region also shrunk as the λ_{GDL} increased and almost vanished for a λ_{GDL} of $0.35 \text{ Wm}^{-1} \text{ K}^{-1}$. Additionally, the ϕ_{SOC}^I at the inlet of the SOC reached a maximum at 0.4 Hz for a λ_{GDL} of $3.5 \text{ Wm}^{-1} \text{ K}^{-1}$. This maximum was shifted to a lower or higher frequency when λ_{GDL} was reduced to $0.35 \text{ Wm}^{-1} \text{ K}^{-1}$ or increased to $35 \text{ Wm}^{-1} \text{ K}^{-1}$, respectively.

A generic heat transfer process can be represented using an electrical analogy where the current, the voltage, the electrical conductivity, and the electrical capacity are used to represent the heat flux, the temperature difference, the thermal conductivity, and the heat capacity multiplied by the mass, respectively [305, 306]. The relaxation time associated with the impedance of a simple $R//C$ circuit is given by $\tau = RC$. If R is increased, τ is also increased, which corresponds to a reduction of the characteristic frequency. This frequency corresponds to a minimum of the imaginary part of the complex impedance for a $R//C$. The observed frequency shift of the ϕ_{SOC}^I especially at the inlet of the SOC was thus in agreement with the modification of the heat transfer resistance and was associated with a modification of the time constant related to the conductive heat transfer between the MIC and the SOC.

When the λ_{GDL} was set to $0.35 \text{ Wm}^{-1} \text{ K}^{-1}$, the ϕ_{SOC}^I was within quadrant 1 up to $x^* = 0.34$ before switching to the quadrant 2 or 3 as defined in Figure 7.4. This behavior reflected the transition from an SOC temperature modulation dominated by \dot{Q}_{rx} (near the inlet) or by an h_R^c modulation (toward the outlet of the SOC). The thermal behavior for a reduced λ_{GDL} was similar to that of an increased h_R^c suggesting that rather than their absolute values, the ratio between λ_{GDL} and h_R^c may be more appropriate to describe the thermal behavior of the SOC.


 Figure 7.19 – Dependency of the thermal response of the SOC to the λ_{GDL} at 0 Acm^{-2} .

7.2.8 Local defect identification

An additional resistive term $ASR_{def} = 1000 \Omega \text{ cm}^2$ was added on two adjacent nodes to simulate the effect of a local complete deactivation of the SOC (i.e., $j \approx 0 \text{ Acm}^{-2}$ on these elements), which could be associated with a local delamination of the air electrode. Three sets of simulations were performed for six current densities with the defect located near the inlet of the SOC ($x^* = 0.1$ to 0.12), near the center of the SOC ($x^* = 0.5$ to 0.52), and near the outlet of the SOC ($x^* = 0.9$ to 0.92). Only a subset of the simulation results, representative of the thermal response of the SOC, are presented in this section; the entirety of the results can be found in appendix D.

The presence of the ASR_{def} affected the global performance of the SOC leading to an increase of the EI, as shown in Figure 7.20. The defect location, however, had almost no impact on the EI, emphasizing the limits of EIS in assessing the distribution of the local electrochemical performances.

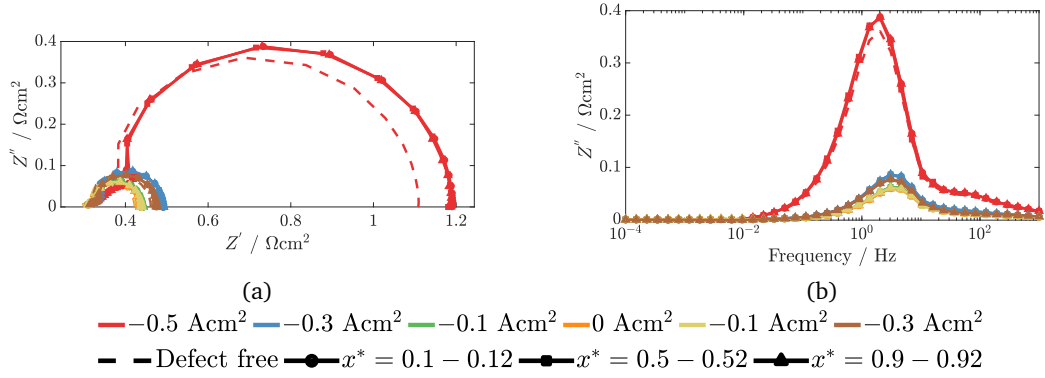


Figure 7.20 – Simulated EI spectra for the three different defect location at various current densities in a) Nyquist and b) Bode representation

The effect of the ASR_{def} on the $\|\hat{T}_{SOC}\|^I$ was rather small and more distinguishable when the ASR_{def} was added near the outlet of the SOC as shown in Figures 7.21 (a), (d), and (g). However, when the $\|\hat{T}_{SOC}^{rel}\|^I$ or ϕ_{SOC}^I were considered, the location of the ASR_{def} was easily identified, as shown in Figure 7.21. The defect was particularly well contrasted for excitation frequencies above approximately 30 mHz for $\|\hat{T}_{SOC}^{rel}\|^I$ and 10 mHz for ϕ_{SOC}^I . This frequency threshold was likely related to the reduced effect of the MIC thermal conductivity above 10 mHz. The location of the ASR_{def} seemed to have a significant impact on the contrast when the $\|\hat{T}_{SOC}\|^I$ or $\|\hat{T}_{SOC}^{rel}\|^I$ were considered but when the ϕ_{SOC}^I contrast was considered, it appeared to be relatively independent of the defect's location. Below 10 mHz, no ASR_{def} were visible in the phase image. In that frequency range, the lateral heat conduction was important and led to a quasi-synchronous thermal oscillation of the defective region with the neighboring elements. If the defect was spread over a larger part of the SOC, it could already be seen at a lower frequency.

In fuel cell operation at 0.1 and 0.3 Acm⁻², the effect of the ASR_{def} remained relatively similar and was always detectable, especially on ϕ_{SOC}^I . These results are thus not presented here. In electrolysis mode, however, the defect became less visible on the ϕ_{SOC}^I when the polarization was increased, as shown in Figure 7.22 for an ASR_{def} located at the center of the SOC. The defect was still visible on the $\|\hat{T}_{SOC}^{rel}\|^I$ but became much less visible on the $\|\hat{T}_{SOC}\|^I$ as the heat generated for the same current density modulation decreased when V_{SOC} approached V_{tr} . As discussed in section 7.2.5, h_R^c increased with c_{H_2} . The lateral heat transfer via convection thus increased with the current density during electrolysis and particularly near the outlet of the SOC as H₂ accumulated from the inlet to the outlet. Similarly to frequencies below 10 mHz, where heat for neighboring elements was transferred via conduction, the defective elements were heated/cooled by convection with a low latency thanks to the high local h_R^c . The defect was always visible in the ϕ_{SOC}^I image when the ASR_{def} was added near the SOC's inlet where the h_R^c

was lower, which supports the assumption that lateral heat transfer by convection is the dominating mechanism reducing the defect visibility in the ϕ_{SOC}^I .

As shown by equations (7.24) and (7.25), heat was also generated at the 2nd harmonic during the sinusoidal current perturbation. The temperature evolution of the SOC was thus expected to also possess a 2nd harmonic term. The amplitude of the 2nd harmonic of the temperature response, $\|\hat{T}_{SOC}\|^{II}$, was generally approximately one order of magnitude lower than the $\|\hat{T}_{SOC}\|^I$ but continuously increased with the current density and did not show a minimum when the V_{SOC} was close to the V_{tr} as shown in Figure 7.23. Using the 2nd harmonic allowed defects to be identified independently of the current density. The ϕ_{SOC}^{II} and $\|\hat{T}_{SOC}^{rel}\|^{II}$ were found to be particularly sensitive compared with ϕ_{SOC}^I and $\|\hat{T}_{SOC}^{rel}\|^I$, as shown in Figures 7.23 and 7.22 respectively. If the temperature modulation is sufficient for the thermal imaging system, using both the 1st and 2nd harmonic thus may be a promising solution for local defect detection.

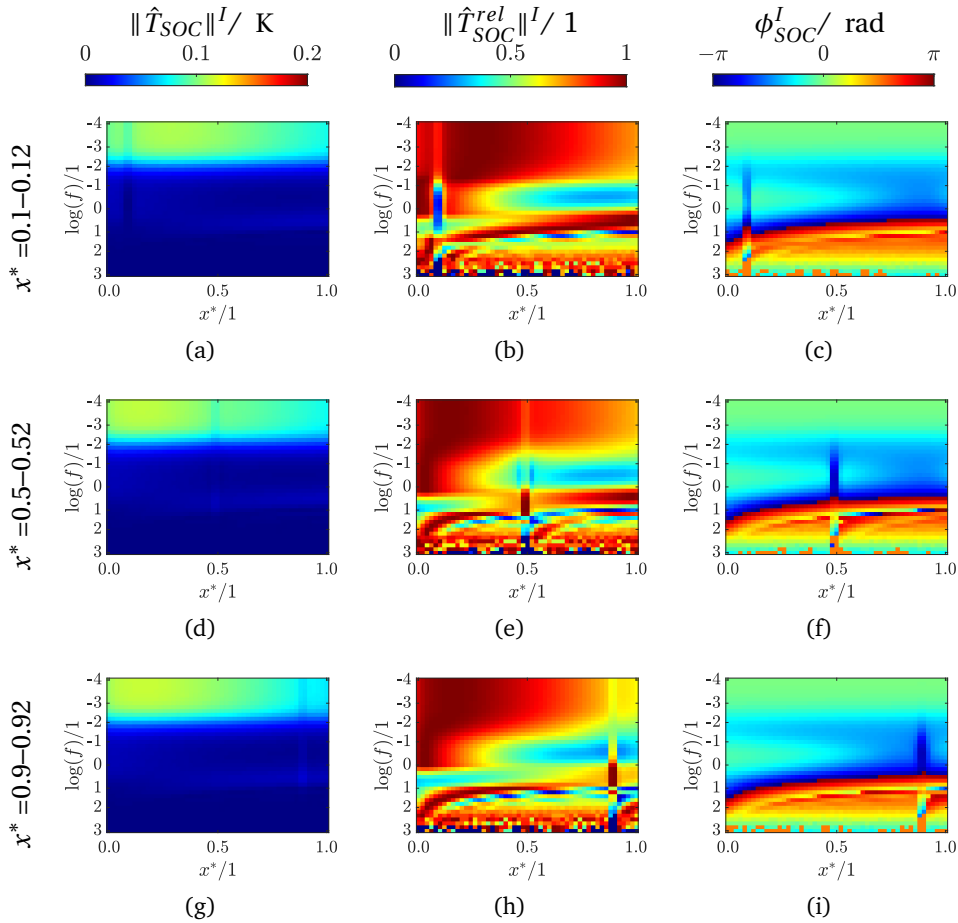


Figure 7.21 – Thermal response of an SOC at 0 A cm^{-2} containing a defective area defined by a supplementary local resistance ASR_{def} . From the left to right column: $\|\hat{T}_{SOC}\|^I$, $\|\hat{T}_{SOC}^{rel}\|^I$, and ϕ_{SOC}^I . Each line corresponds to the ASR_{def} being added at different values of x^* .

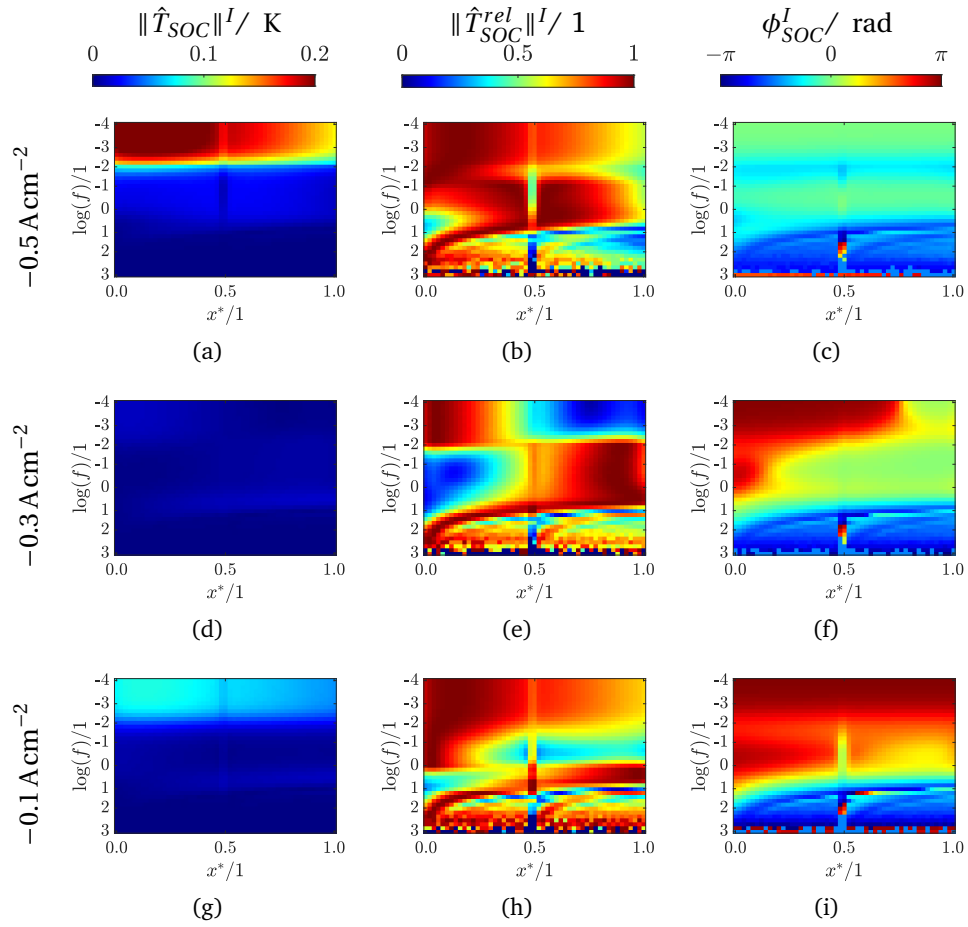


Figure 7.22 – The thermal response of the SOC containing a defective area defined by a supplementary local resistance ASR_{def} . From left to right columns: $\|\hat{T}_{SOC}\|^I$, $\|\hat{T}_{SOC}^{rel}\|^I$, and ϕ_{SOC}^I . Each line corresponds to different applied current density.

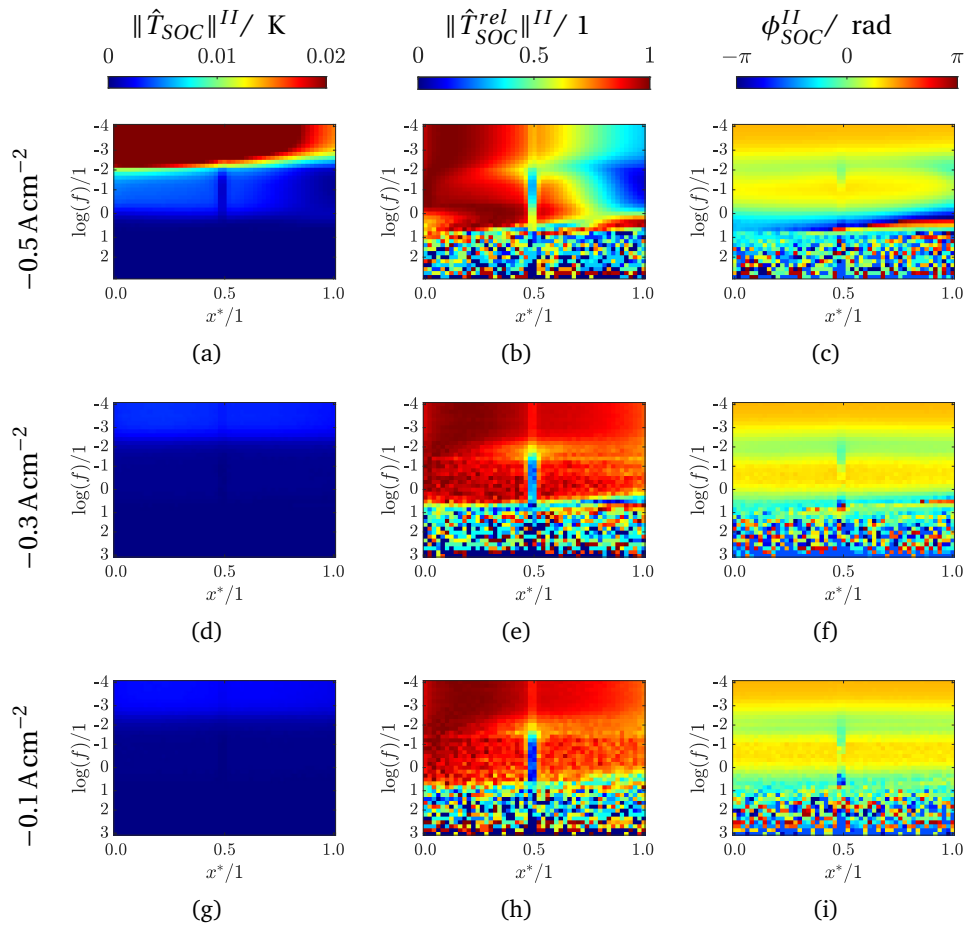


Figure 7.23 – Thermal response of an SOC containing a defective area defined by a supplementary local resistance ASR_{def} . From left to right columns: $\|\hat{T}_{SOC}\|^I$, $\|\hat{T}_{SOC}^{rel}\|^I$, and ϕ_{SOC}^I . Each line corresponds to different applied current density.

7.2.9 Local power density estimation

The method described here corresponds to the image integration method proposed by Breitenstein et al. [272], who used it on photovoltaic cells to evaluate the local current density.

The rate of change of a body's volumetric internal energy density ($\dot{Q}(t)$ in Wm^{-3}) is related to its temperature variation rate by equation (7.40). Equation (7.41) is the Fourier transform of equation (7.40) which shows that, in the frequency domain, the $\hat{T}(\omega)$ and $\hat{Q}(\omega)$ are phased out by $\pi/2$.

$$\dot{Q}(t) = \rho C_p \frac{\partial T(t)}{\partial t} \quad (7.40)$$

$$\mathfrak{F}\{\dot{Q}(t)\} = \hat{Q}(\omega) = \rho C_p i\omega \hat{T}(\omega) \quad (7.41)$$

If a specimen discretized into n elements with homogeneous physical properties is considered, equation (7.40) can then be applied on each discretization element individually and the $\dot{Q}(t)$ for the entire object becomes:

$$v\dot{Q}(t) = \sum_{k=1}^n v_k \dot{q}_k(t) = \rho C_p \sum_{k=1}^n v_k \frac{\partial T_k(t)}{\partial t} \quad (7.42)$$

where v, v_k , and $\dot{q}_k(t)$ are the volume of the total specimen, the volume of element k such as $v = \sum_{k=1}^n v_k$, and the $\dot{q}_k(t)$ of element k . If the ρ and C_p are not homogeneous, they must be kept within the summation. The Fourier transform can then be applied to equation (7.42):

$$\mathfrak{F}\{v\dot{Q}(t)\} = \mathfrak{F}\left\{\sum_{k=1}^n v_k \dot{q}_k(t)\right\} = \mathfrak{F}\left\{\rho C_p \sum_{k=1}^n v_k \frac{\partial T_k(t)}{\partial t}\right\}, \quad (7.43)$$

which can be rewritten as equation (7.44) by using the linearity property of the Fourier transform.

$$v\hat{Q}(\omega) = \sum_{k=1}^n v_k \hat{q}_k(\omega) = \rho C_p \sum_{k=1}^n i\omega v_k \hat{T}_k(\omega) \quad (7.44)$$

Here, $\hat{T}(\omega)$, $\hat{Q}(\omega)$, and $\hat{q}_k(\omega)$ are complex numbers which can be written in the form: $\hat{x} = x' + ix''$. The real and imaginary component of equation (7.44) can then be considered independently as equations (7.45) and (7.46), respectively.

$$Re: \quad v\hat{Q}'(\omega) = \sum_{k=1}^n v_k \hat{q}'_k(\omega) = -\rho C_p \sum_{k=1}^n \omega v_k \hat{T}_k''(\omega) \quad (7.45)$$

$$Im: \quad v\hat{Q}''(\omega) = \sum_{k=1}^n v_k \hat{q}''_k(\omega) = \rho C_p \sum_{k=1}^n \omega v_k \hat{T}_k'(\omega) \quad (7.46)$$

Chapter 7. Numerical investigation

Considering first only the real component, equation (7.45) can be simplified if each of the n elements have the same volume $v_k = v/n$, leading to

$$v\hat{Q}' = \sum_{k=1}^n \frac{v}{n} \hat{q}'_k(\omega) = \frac{v}{n} \sum_{k=1}^n \hat{q}'_k(\omega) \quad (7.47)$$

$$= -\rho C_p \sum_{k=1}^n \frac{v}{n} \omega \hat{T}_k''(\omega) = -\rho C_p \frac{v}{n} \omega \sum_{k=1}^n \hat{T}_k''(\omega) \quad (7.48)$$

which, divided by v , leads to equation (7.49).

$$\hat{Q}' = \frac{1}{n} \sum_{k=1}^n \hat{q}'_k(\omega) = -\rho C_p \omega \frac{1}{n} \sum_{k=1}^n \hat{T}_k''(\omega) \quad (7.49)$$

The ratio between the real component of the local and total power is then:

$$\frac{v_k \hat{q}'_k(\omega)}{v \hat{Q}'(\omega)} = \frac{-\rho C_p \omega v_k \hat{T}_k''(\omega)}{-\rho C_p \omega \frac{v}{n} \sum_{k=1}^n \hat{T}_k''(\omega)}. \quad (7.50)$$

Using equation (7.49), equation (7.50) can be simplified to the more compact equation (7.51). The same procedure can be followed starting this time with equation (7.46) and ending with equation (7.52).

$$Re: \quad \frac{\hat{q}'_k(\omega)}{\hat{Q}'(\omega)} = n \frac{\hat{q}'_k(\omega)}{\sum_{k=1}^n \hat{q}'_k(\omega)} = n \frac{\hat{T}_k''(\omega)}{\sum_{k=1}^n \hat{T}_k''(\omega)} \quad (7.51)$$

$$Im: \quad \frac{\hat{q}''_k(\omega)}{\hat{Q}''(\omega)} = n \frac{\hat{q}''_k(\omega)}{\sum_{k=1}^n \hat{q}''_k(\omega)} = n \frac{\hat{T}'_k(\omega)}{\sum_{k=1}^n \hat{T}'_k(\omega)} \quad (7.52)$$

Assuming that during an LT measurement the \hat{q}_k is equal to the heating power introduced by the local current modulation, equations (7.51) and (7.52) can then be used to relate the measured temperature modulation to the local \hat{Q}_{rx} and thus the electrochemical performances without prior knowledge of the material properties as long as they are spatially homogeneous.

When the corrected phase, $(\phi^* = \phi - \phi_J)$, is used to compute the imaginary and real components, then \hat{Q}_{rx}^I has essentially a real component ($\hat{Q}_{rx}^{II} \approx 0$) as long as the values of

ϕ_j^I and ϕ_V^I are close to $\phi_j + k\pi$, as seen from equation (7.26) and (7.27), where k is an integer. Therefore, only equation 7.51 was required to estimate the power distribution. The error of the power distribution estimation was then defined by equation (7.53).

$$\epsilon_Q = \left| 1 - \frac{\hat{T}_k''(\omega)}{\sum_{k=1}^n \hat{T}_k''(\omega)} \middle/ \frac{\hat{q}_k'(\omega)}{\sum_{k=1}^n \hat{q}_k'(\omega)} \right| \quad (7.53)$$

The contour plot of ϵ_Q for the 1st harmonic, i.e., $\omega = \omega_0$ where ω_0 represents the excitation pulsation, showed that equation (7.51) provided a good estimate of the power distribution up to approximately 1 Hz with a larger deviation near the SOC extremities. The ϵ_Q was minimal between 10 mHz and 0.25 Hz, i.e., above the frequency where the lateral conduction in the MIC dominated until the SOC's impedance was not purely resistive and began to show a capacitive behavior. During electrolysis, the ϵ_Q was significantly higher at a current density of -0.3 and -0.4 A cm^{-2} but improved again at higher current densities as shown in Figures 7.24 (a) to (c). This transition also occurred near V_{tr} , where the heat modulation was minimal.

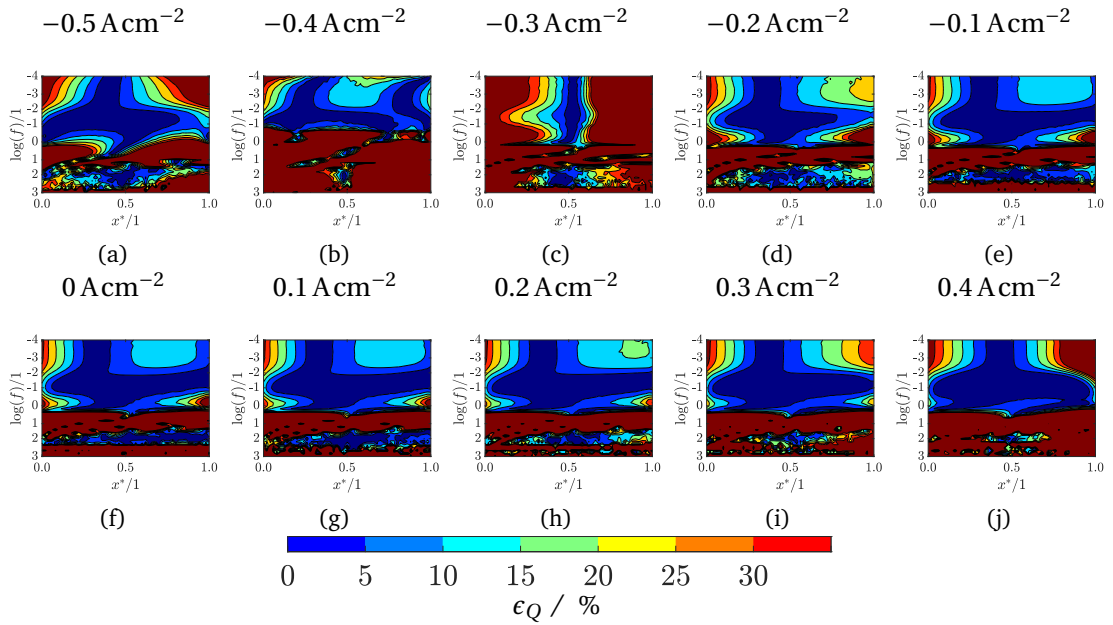


Figure 7.24 – ϵ_Q for various current densities under reference conditions.

A decrease of the λ_{GDL} was highly detrimental to the power distribution estimation as the ϵ_Q increased massively especially for frequencies between approximately 50 mHz and 1 Hz. In this frequency range, the thermal behavior was significantly modified by a reduction of the λ_{GDL} as the effect of the h_R^c modulation became more important, as was discussed in section 7.2.7. The assumption that the \dot{Q}_{rx} was driving the temperature modulation of the SOC did not hold, leading to the observed erroneous power distribution

estimation. Modifying the Nu_R had a smaller impact than modifying the λ_{GDL} on the thermal response of the SOC, thus, the power distribution estimation was relatively independent of the Nu_R , as shown in Figures 7.25 (c) and (d).

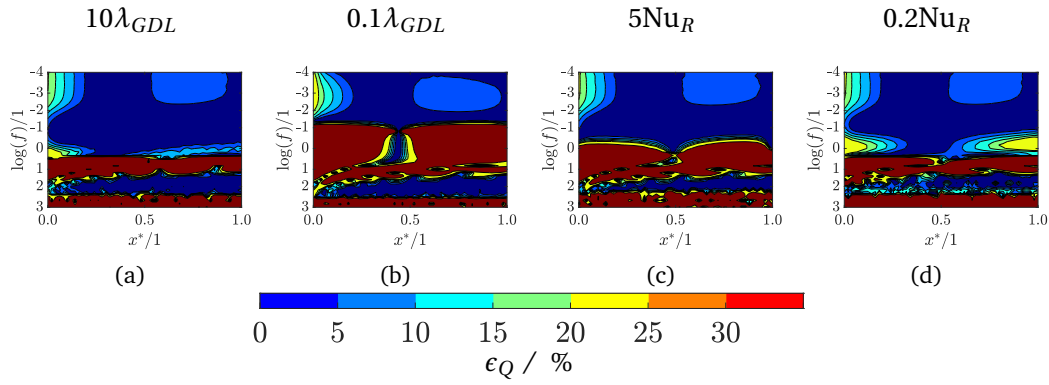


Figure 7.25 – ϵ_Q for various current densities under reference conditions.

7.3 Conclusion

LT numerical simulations with a pseudo 2-D model were performed under a wide variety of conditions to investigate the dynamic thermal behavior of an SOC and identify the parameters critical for LT measurements.

The general thermal response as a function of the excitation frequency, f_0 , can be summarized as:

$f_0 < 10\text{mHz}$ The SOC was in a "quasi-equilibrium" state for both the thermal and electrochemical response. The temperature of the reactant, air, SOC, and MIC oscillated synchronously. The lateral heat transfer in the MIC was significant.

$10\text{ mHz} < f_0 < 0.3\text{ Hz}$ The electrochemical response was still close to that at equilibrium. The temperature of the MIC was marginally affected by the current modulation. The effect of the heat capacity of the SOC began to appear.

$0.3\text{ Hz} < f_0$ The thermal response of the SOC was a complex combination of the transient electrochemical and thermal processes.

During fuel cell operation, the amplitude of the SOC's thermal response was constantly increased with the current density. During electrolysis, the thermal response of the SOC was initially in phase opposition with the current modulation, i.e., the temperature decreased as the current increased, and the amplitude decreased with an increase of the current density until $V_{tr} \approx 1.1\text{ V}$ was reached. Above the V_{tr} , the SOC's thermal response was in phase with the current modulation and increased with the current density. This transition voltage corresponded to the voltage at which the \dot{Q}_{rx} was minimal. The electro-thermal response of the SOC during electrolysis was highly dependent on the V_{SOC} , V_{tm} , and V_{tr} and generally had a lower amplitude than during fuel cell operation.

The temperature modulation of the SOC resulted from the heat modulation related to the electrochemical reaction and the modulation of h_R^c . The former was more important near the inlet of the SOC whereas the latter was dominant near the outlet. The effect of the h_R^c was more significant in electrolysis operation due to the higher h_R^c modulation when H_2 rather than H_2O was produced. During electrolysis, these two contributions could be discriminated below V_{tr} , as they were in opposition of phase; however above V_{tr} , they could not, which provided a method to estimate V_{tr} .

The interaction of the SOC with the reactant dominated over the interactions with air flow which could generally be neglected. The contribution of the h_R^c on the thermal behavior of the SOC was found to be dependent on the thermal conductivity of the GDL. Reducing the λ_{GDL} increased the amplitude of the temperature modulation of the SOC and enhanced the influence of the h_R^c .

When operated outside of ideal conditions, the electro-thermal behavior of the SOC was modified, which was accurately captured by LT. At $RU > 0.8$, the reactant availability became a limiting factor of the SOC's performance especially near the outlet. Due to the reactant concentration modulation induced by the current perturbation, the local current density near the inlet and outlet of the SOC modulated in phase opposition, which also affected the temperature modulation of the SOC and could thus be captured using LT. When $V_{SOC} \approx V_{tn}$, the contribution of the local current density modulation to the electrochemical heat modulation was small and the effects of the reactant limitation were not visible using LT.

The local deactivation of the electrochemical process was simulated by adding an additional resistance to specific SOC elements. The position of the defect could easily be identified when the ϕ_{SOC}^I was considered and particularly between approximately 10 mHz and 1 Hz, whereas analysis using EI could not be used to determine the location of the defect. During electrolysis, the defect was hardly visible when $V_{SOC} \approx V_{tr}$ owing to the reduced heat modulation and increased lateral heat transfer by convection. This issue can be overcome by analyzing the 2nd harmonic of the thermal response of the SOC which had a lower amplitude but appeared to be less dependent on heat diffusion.

A method based on LT measurements to estimate the distribution of the electrochemical power modulation was presented. The proposed method was particularly accurate ($\pm 5\%$) between 10 mHz and 0.25 Hz and especially in fuel cell mode. The estimation greatly deteriorated when the SOC was operated in electrolysis mode near V_{tr} , where the heat modulation was minimal. A reduction of the thermal conductivity of the GDL also deteriorated the estimate, as the effect of the h_R^c was enhanced and the electrochemical power modulation was not the dominant contributor to the temperature modulation of the SOC.

Generally, electrolysis operation was less favorable than fuel cell operation for analysis via LT due to the reduced temperature modulation and electro-thermal behavior modification related to V_{tr} and V_{tn} . The optimal frequency range for analysis via LT measurements appeared to be ≈ 10 mHz–1 Hz, as the lateral conduction in the MIC is negligible, the electrochemical modulation is significant, and the effect of the SOC's thermal capacity is limited.

CHAPTER 8

Test bench description

This chapter presents the test bench developed during this thesis to perform active thermography on SOC_s.

Contributions to the Field

Developed a test-bench to perform active thermography on 15 cm² SOC_s that is more representative of standard-sized SOC (≈ 80 cm²) than typically used for passive thermography measurements (i.e., ≈ 2 cm²).

8.1 Test bench

A photograph and a schematic of the test bench are presented in Figure 8.1, whereas a detailed CAD representation of the SOC test-rig with the furnace assembly is shown in Figure 8.2. The 500 W in-house designed furnace was composed of a single heating element made out of 15 m of 0.5 mm diameter Kanthal D wire that was coiled with an internal diameter of 4 mm. The furnace walls were made out of five magnesium oxide plates in which serpentine grooves were machined to hold the heating coil. The furnace was then placed vertically with the quartz window facing down to limit convective effects and thus heat losses. The furnace was thermally insulated by porous refractory bricks. A photograph of the SOC assembly in the homemade furnace is presented in Figure 8.3 (a), where the optical opening and the O₂-electrode are visible.

The camera was placed below the furnace and air-cooled with an external fan to prevent overheating and limit the thermal noise of the sensor, as shown in Figure 8.3 (b). The SOC can be placed with either the H₂-electrode or the O₂-electrode facing towards the camera technically allowing the observation of both electrodes (not simultaneously). Also, the air and reactant flow can either be in co-flow or counter-flow configuration, i.e., reactant and air inlet on the same end or opposite ends, respectively.

To fully benefit from the high resolution of the NIR camera selected in section 8.2, a rectangular cell 60 mm \times 40 mm with an active area of 50 mm \times 30 mm, similar to the

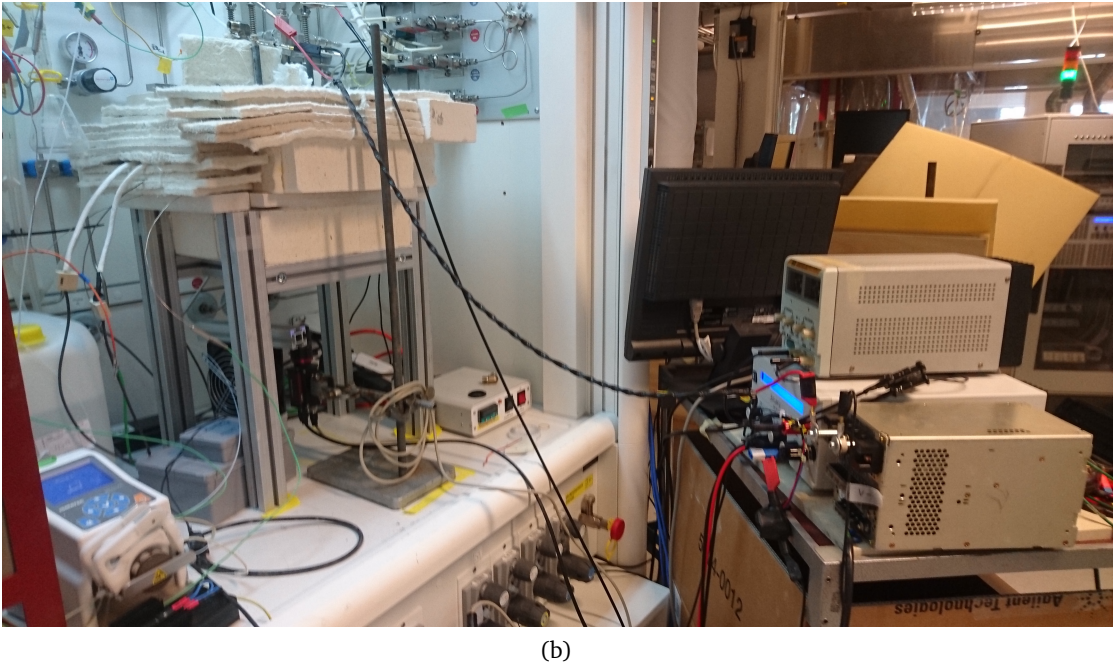
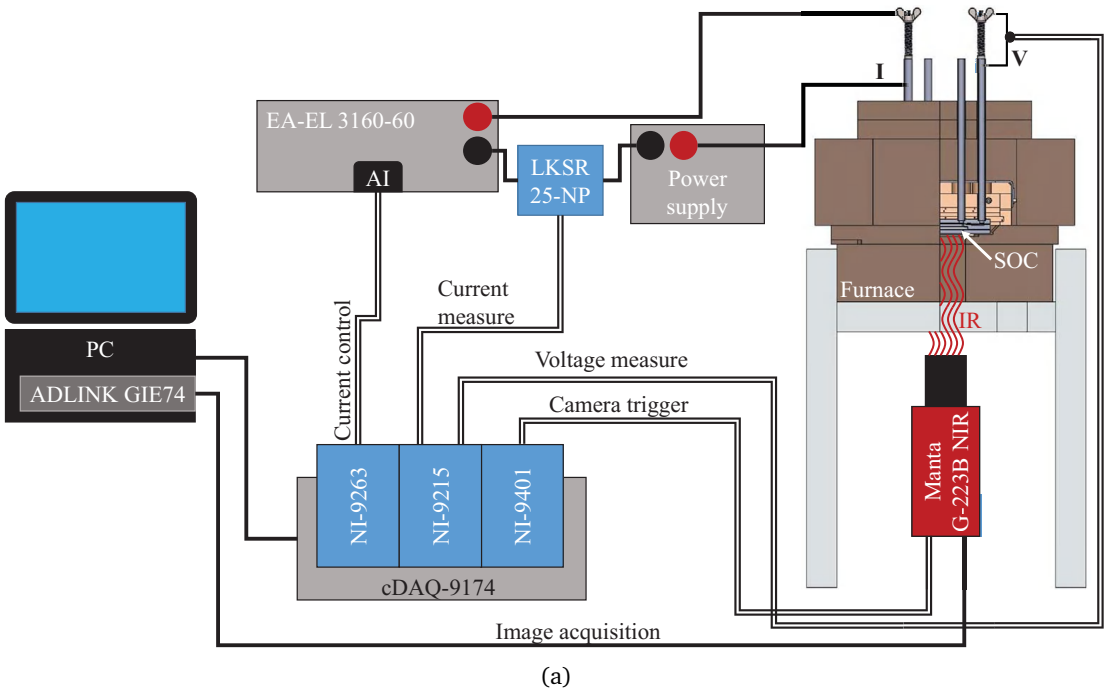


Figure 8.1 – (a) schematic and (b) photograph of the test bench dedicated to active thermography experiments.

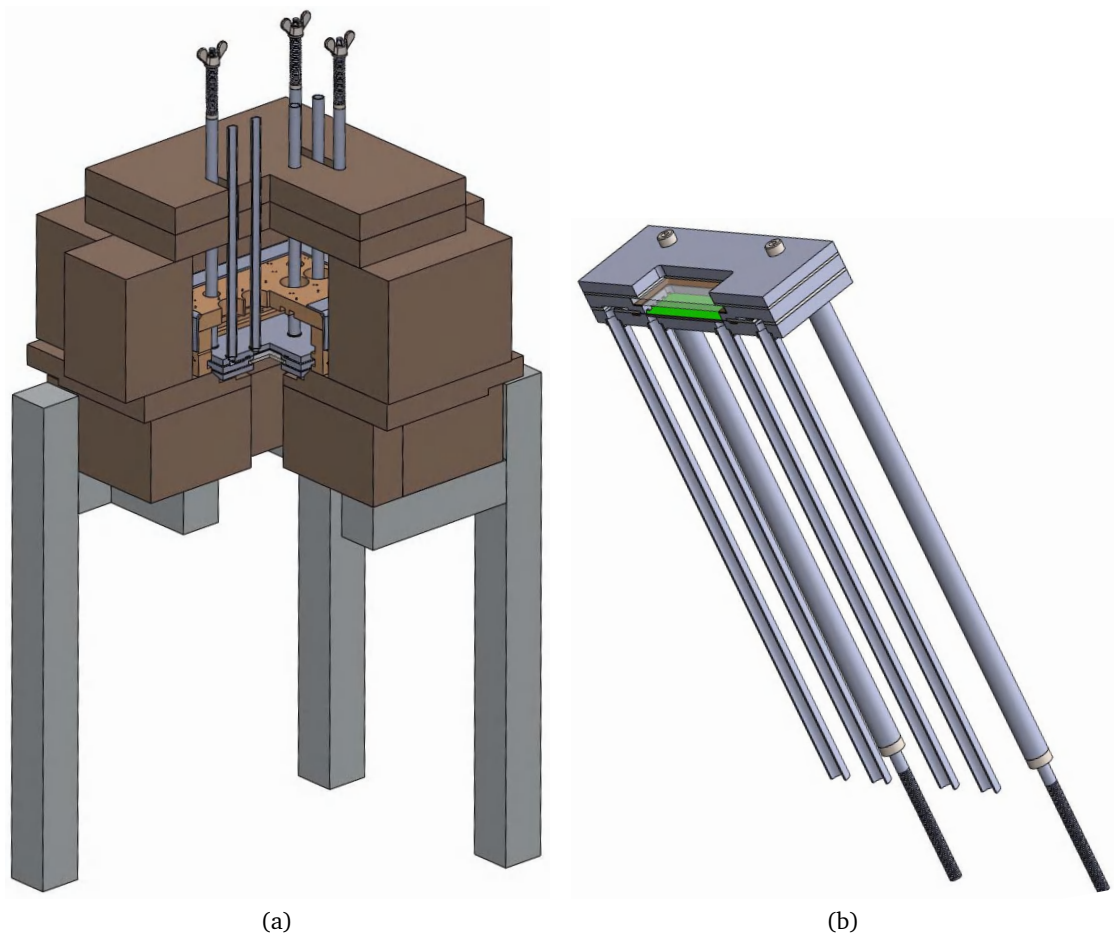


Figure 8.2 – CAD of the test bench showing a cut through the set-up (a) and a close-up view of the SOC frame (b).

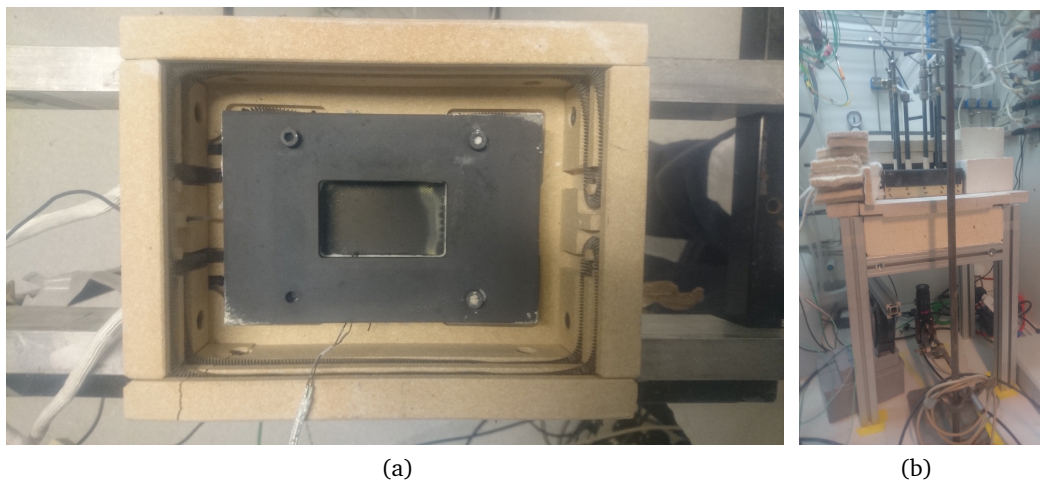


Figure 8.3 – Photograph of (a) the SOC assembly in the homemade furnace and (b) SOC assembly positioned above the camera with part of the insulation removed.

length-to-width ratio of the camera sensor, was selected. Using cells larger than most of the SoA presented in section 1.5.3 was expected to promote the emergence of inhomogeneities and facilitate their monitoring. The SOC test rig assembly was made of Inconel 600. Ceramic tubes were inserted in the gases inlet and outlet tubes to limit gas-metal interactions (e.g., chromium evaporation). The SOC loading was controlled using four springs compressed with wing nuts to generate a simultaneous pull on the threaded rod connected to the top plate and push on the tubes connected to the bottom plate to compress the SOC, as shown in Figure 8.2. This rod-tube assembly also provides a co-axial configuration for the current limiting mutual inductance and parasitic disturbances. The inward current travels in the rod and the return current in the tube (or vice-versa depending on the operating mode). The inductance of a co-axial conductor configuration is given by [307]:

$$L = \frac{\mu_0 l}{2\pi} \ln\left(\frac{r_2}{r_1}\right), \quad (8.1)$$

where $\mu_0 = 4\pi \cdot 10^{-7} \text{kgmA}^{-2}\text{s}^{-2}$ is the vacuum permittivity, and r_1 , r_2 , and l are the external radius of the internal conductor, the internal radius of the external conductor, and the length of the co-axial conductors, respectively. The inductance of a co-axial configuration thus reduces with the length of the conductor and the ratio r_2/r_1 .

EIS measurements with the same instruments under similar operating conditions (0 A cm^{-2} , $50/50 \text{ vol\% H}_2/\text{H}_2\text{O}$ mixture at $12 \text{ Nml min}^{-1} \text{ cm}^{-2}$) with the untwisted, twisted, and co-axial conductor configurations as described in Figures 3.1 (a), (b), and 8.2 (b), respectively, are presented in Figure 8.4. The inductance of the untwisted configuration was estimated using equation (3.2) to be approximately $9 \times 10^{-8} \text{ H}$. The theoretical inductance of the designed co-axial configuration ($r_1 = 4 \text{ mm}$, $r_2 = 6 \text{ mm}$, $l = 210 \text{ mm}$) was approximately $1.7 \times 10^{-8} \text{ H}$, which is more than 5 times lower as the untwisted configuration. The co-axial configuration showed similar results than the twisted configuration at high frequencies but without the hurdle of having to carefully twist the cables for each experiment.

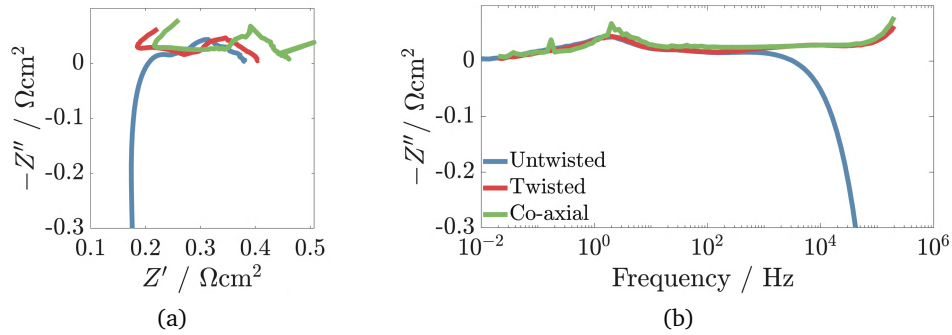


Figure 8.4 – EIS measurements at 0 A cm^{-2} in a 50/50 vol% $\text{H}_2/\text{H}_2\text{O}$ at $12 \text{ Nml min}^{-1} \text{ cm}^{-2}$ with different current and voltage measurements configuration. The untwisted, twisted, and co-axial configuration are defined in Figures 3.1 (a), (b), and 8.2 (b), respectively.

8.2 Control and data acquisition

A schematic of the different components comprising the test bench is presented in Figure 8.1. A DC electronic load EA-EL 3160-60 from Elektro-Automatik connected in series with a DC power supply (6 V, 60 A) were used to modulate the applied current. The electronic load was controlled externally using a 0–10 V analogue signal provided by a NI-9263 four-channel analog output module. The cell voltage and the applied current were measured by a NI-9215 four-channel analog input module. A LEM LKSR 25-NP current transducer was used to convert the current into a 0–5 V analog voltage. The current transducer was encased in a tin-plated steel sheet to shield it from external magnetic fields. The image acquisition was triggered by a NI-9401 eight-channel TTL digital input/output module. The three NI modules were inserted in a cDAQ-9174 data acquisition module which was controlled by a dedicated Labview VI developed in-house.

An Allied Vision Manta G-223B NIR camera was used to monitor the SOC infrared emissions. The camera has a global shutter which allows to simultaneously readout all the pixel's value, thereby avoiding any additional phase lag that could be introduced by a rolling shutter (line-by-line reading). The sensor possesses 2048×1088 pixels with a maximum depth of 12 bits and an improved quantum efficiency ¹, QE , in the NIR than the standard Manta G-223B, as shown in Figure 8.5. The QE approaches 0 for wavelengths $>1000 \text{ nm}$ as Si transmittance ≈ 1 , i.e., Si is transparent and photons pass through the sensor without generating charges. The active area of the SOC was $50 \text{ mm} \times 30 \text{ mm}$, corresponding to a resolution of $24 \mu\text{m} \times 28 \mu\text{m}$ when the entire active area was pictured. The resolution can be improved using a higher-magnification lens, an extension tube, or a close-up lens. The effect of ambient light was minimized by adding an ultra-violet

¹The quantum efficiency, $QE \in [0, 1]$, is the ratio between the incoming photons and the electrons generated in the sensor. It depends on the wave length of the incoming light and sensor technology/material.

and visible light filter to the objective (50 mm C-Series lens from Edmund Optics Ltd), limiting the spectral range from approximately 720 to 1100 nm.

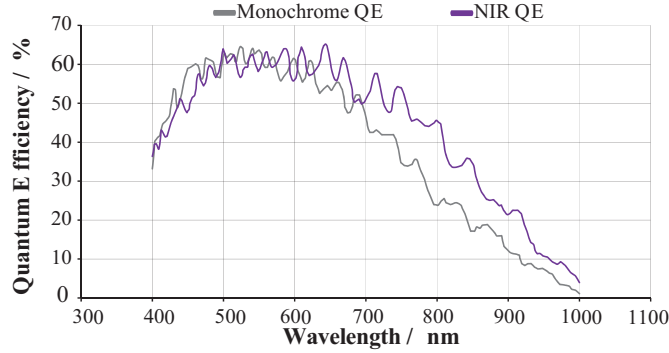


Figure 8.5 – Quantum efficiency of the Allied Vision Manta G-223B (grey) and G-223B NIR (purple). Adapted from [5]

The acquisition was managed by the cDAQ-9174 hardware, which synchronizes the clock of the trigger to the camera and the analog input module leading to the simultaneous acquisition of the cell voltage, applied current, and NIR image. The NIR images were acquired by an ADLINK GIE74 frame grabber and stored as TIFF files. The measured current and cell voltage were saved using LabView's proprietary TDMS file format.

8.3 Camera calibration

For each pixel, the camera outputs a number ranging from 0 to 4095 (12 bits) which can then be converted to a temperature using a radiometric model. The parameters of the radiometric model, however, must be calibrated for each device. Additionally, the camera and sensor imperfections should be considered to obtain the best results.

The sensor of a camera can be regarded as a collection of smaller sensors i.e., the pixels. Due to imperfections caused by the electronic and manufacturing process, each pixel may behave differently. Under no illumination, the camera sensor generally outputs a non-zero grey-level, known as the "dark signal", I_{DS} . The I_{DS} is expressed by equation (8.2), where $I_{DS}^0(T_{sen})$, and $I_{DS}^t(T_{sen})$ are two constant which increase with the sensor temperature, T_{sen} , and t_i is the integration time. This signal is mainly caused by charges generated by thermal- rather than photon-excitation [308]. As this signal varies from one pixel to another, it is generally referred to as the dark signal non-uniformity (DSNU). When the sensor is illuminated, each pixel may output a different grey value even when the illumination is homogeneous. This photo-response non-uniformity (PRNU) originates from manufacturing homogeneities (e.g., thickness variations) and can depend on the wavelength of the incoming illumination [277].

$$I_{DS} = I_{DS}^0(T_{sen}) + t_i \cdot I_{DS}^t(T_{sen}) \quad (8.2)$$

To correct for the DSNU, the $I_{DS}^0(T_{sen})$ and $I_{DS}^t(T_{sen})$ were identified by taking series of images with the lens cap on, i.e., no illumination, for fifteen $t_i \in [25, 1250] \mu\text{s}$ at $T_{sen} = 30^\circ\text{C}$ and 37°C . To limit the effect of random noise, each measurement was averaged over 100 images. For the considered range (i.e., short t_i), t_i was found to have negligible impact on I_{DS} and was thus not considered for the DSNU correction. Increasing T_{sen} by 7°C had a perceptible impact on the I_{DS} . The camera was thus cooled with fan allowing the experiment to keep $T_{sen} \approx 30^\circ\text{C}$ and a low dark signal. The DSNU correction consisted thus in subtracting $I_{DS}^0(30^\circ\text{C})$ from every frame.

Correcting the PRNU is a more complex process and requires a homogeneous illumination over the entire sensor. Additionally, the PRNU in CMOS sensors has been found to depend on the wavelength of the incoming light [277]. During the correction procedure, the sensor must thus be illuminated with a light source containing a similar wavelength composition to that used during thermographic measurements. One solution would involve using a high-temperature black body with a sufficiently large area to homogeneously illuminate the entire sensor at once. High-temperature black bodies generally rely on a cavity design. As the emittance of these geometries depends on the ratio between the aperture and cavity surface area [309], the aperture is usually small to achieve a high emittance for a reasonable size. Consequently, the entire sensor could not be illuminated and the PRNU was thus not corrected. In this work, the camera is used for a very specific application within a small temperature range where the exact absolute temperature is not crucial for determining the capability of active thermography. If highly precise quantitative measurements were desired and the adequate equipment was available, then the PRNU could be corrected following the methodology proposed by Rotrou [310] or Ferrero et al. [311].

A simple radiometric model based on an effective wavelength was used to convert the grey-level pixel values to temperatures [278]:

$$I = A \cdot t_i \exp(-B/T), \quad (8.3)$$

where $I = I_{sen} - I_{DS}$ is the grey value output of the camera (I_{sen}) corrected for DSNU, t_i is the integration time in μs (i.e., the exposure time of one frame), T the sample temperature in K, and A and B are fitting parameters. A and B were estimated using a non-linear least-squares regression on 20 data points: four temperatures ranging from 710°C to 770°C and five integration times ranging from $100\mu\text{s}$ to $300\mu\text{s}$. This combination of temperature and t_i ensured a linear response of the camera with t_i . However, in the vicinity of the pixel saturation or detection limit, i.e., a too high or too low illumination, respectively, the response was not linear, which could greatly deteriorate the quality of the temperature estimation. The calibration was performed in-situ by modifying the furnace temperature and recording the SOC surface temperature using a K-type thermocouple touching the O_2 -electrode. As the calibration was performed directly on the sample,

the effects of the sample emittance were directly included in the fitting parameters. If another specimen, i.e., a different material or configuration, was imaged, the obtained temperature would need to be corrected for the new specimen's emittance. To mitigate the effect of the PRNU, the grey values were averaged in a small homogeneous area near the thermocouple as shown in Figure 8.6 and a single set of parameters A and B was obtained. Ideally, the calibration should be performed individually on each pixel, i.e., on the set of parameters A and B per pixel, to obtain the best results. Deducting $7\mu\text{s}$ from t_i led to an improved fitting. This phenomenon was assumed to originate from smearing [310]. Smearing is independent of t_i and corresponds to a photon-induced charge generation process taking place after the end of the integration time, which thus corresponds into an increased t_i . Further on, these $7\mu\text{s}$ were thus always deducted from the set t_i as proposed by [310].

The regression results and $\pm 5\%$ prediction bounds, i.e., 95 % confidence level, are presented in Figure 8.6. The temperature uncertainty with the regression parameters defined in Table 8.1 was within $\pm 0.5\text{ K}$ over the entire fitting range.

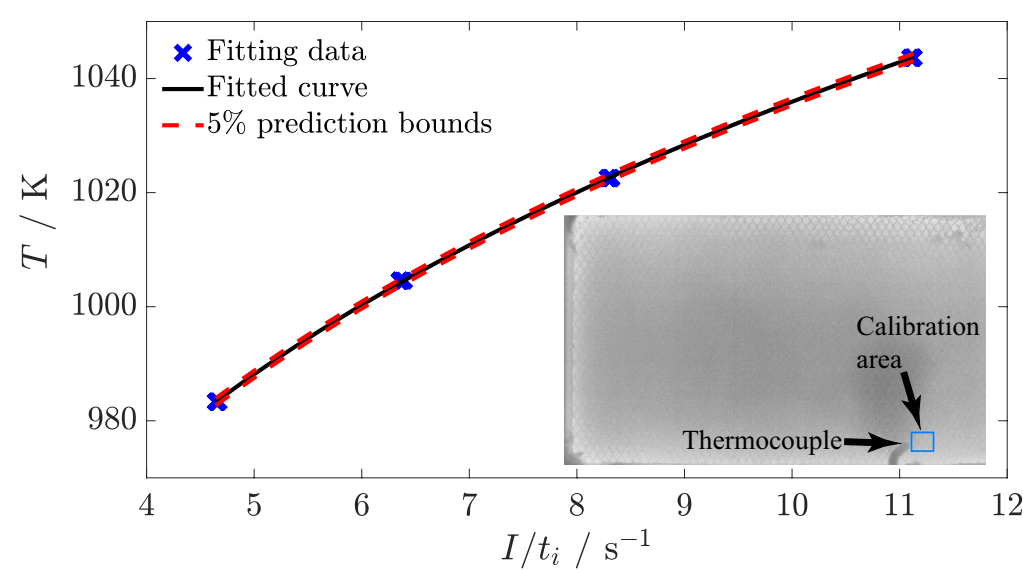


Figure 8.6 – Results of the least-squares fitting used for the camera calibration including the upper and lower prediction bounds.

Table 8.1 – Values of the fitting parameters obtained by regression

A	B
$1.682\,663\,846 \times 10^7$	$1.485\,109\,014 \times 10^4$

8.4 SOC preparation and assembly

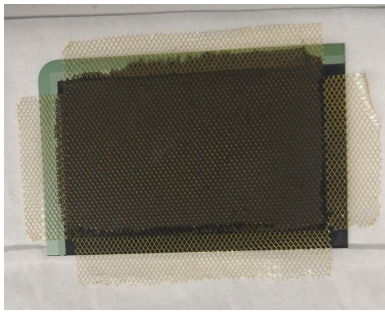
The SOC of 40 mm × 60 mm was obtained by laser cutting a standard size (80 mm × 120 mm) SOC from SOLIDpower. A 5 mm width on the border of the SOC was used for sealing and loading, leading to an SOC active area 30 mm × 50 mm. As the compression was only applied on the SOC rim, ensuring a good lateral current distribution while applying a reasonable pressure without breaking the SOC was challenging.

A layer of LSC paste was screen-printed on the O₂-electrode; while still wet, a gold mesh was then positioned atop and covered by another layer of LSC paste (also screen-printed). The assembly was then dried using a heat gun. The gold mesh was approximately 2 cm larger and longer than the O₂-electrode, as shown in Figure 8.7 (a). Beforehand, the gold mesh was heated to 800 °C–900 °C to soften it and facilitate its positioning. The SOC–gold-mesh assembly was sintered at 870 °C (oven-controlled temperature) for 15 h. The heating ramp was set to 60 °C h⁻¹. When the gold mesh was still visible after sintering, an additional LSC layer was screen-printed atop it to ensure a good lateral electronic conductivity and obtain the most homogeneous emittance possible. An additional sintering was then performed.

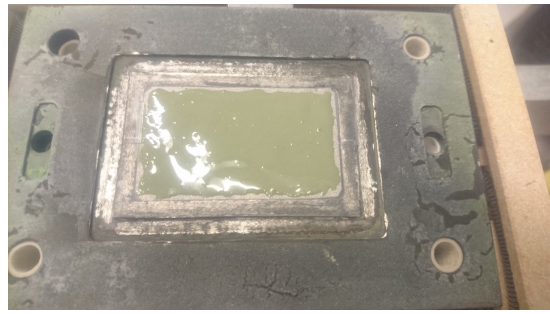
On the H₂-electrode side, a 0.3 mm-thick Ni foam was used for current collection and gas diffusion. To improve the electronic conduction, an NiO paste was deposited on top of the Ni foam as shown in Figure 8.7b. Plastic tape was added on top of the Ni foam before the NiO paste to avoid the NiO paste entering in the Ni foam during the assembly. When placed in the insulation, thanks to gravity, the NiO paste stayed in position after the tape burned out as the SOC was heated up. The NiO-paste was composed of 66 w% NiO powder diluted in a 4 w% ethylcellulose terpeneole solution. The dilution of ethylcellulose in terpeneole was facilitated by adding a few drops of isopropanol and heating the mixture to 60 °C while constantly stirring.

The SOC–gold-mesh assembly was then placed on top of the NiO paste and a weight was added on top to keep it in position, as shown in Figure 8.7 (c). The glass sealant was then added around the SOC and the groove was filled with a rectangular frame made out of alumina felt. Finally, a mica sheet was added on top to provide additional gas tightness, electric insulation, and improve the load distribution, as shown in Figure 8.7 (d). The gold mesh was folded on top of the mica to be in contact with the top flange. Additionally, LSC was used to improve the electronic connection between the gold-mesh and the flange.

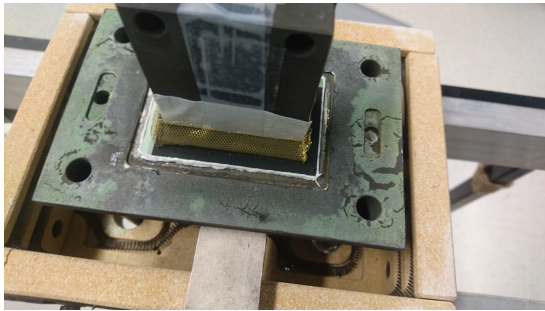
To avoid any short-circuit between the top and bottom flange, ceramic guiding tubes were added at each end of the outer tubes, as shown in Figure 8.7 (b). The top flange was then added and the springs were carefully compressed by ≈4 mm, corresponding to a force of 36 N per spring, using four spring nuts.



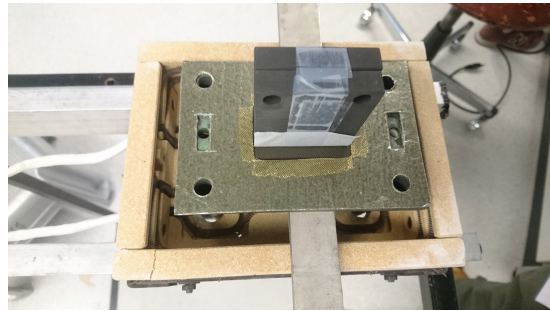
(a)



(b)



(c)



(d)

Figure 8.7 – Photographs of (a) the SOC-gold-mesh assembly, (b) of the Ni-foam with the NiO paste deposited, (c) the glass sealing positioning, (d) the mica gasket.

CHAPTER 9

Experimental results

The LT measurements were performed over 10 cycles with an acquisition frequency 10 times higher than the excitation frequency, corresponding to 100 images per measurement. The image data set was then reduced by averaging the 10 cycles, leaving 10 images to be analyzed by FFT. As the current excitation was not synchronized with the acquisition, the phase of the current excitation was always subtracted from the phase obtained for the temperature signal after FFT to keep the same reference for all measurements, as expressed by equation (9.1). A coherent imaginary and real representation of the temperature response of the SOC can then be obtained with equations (9.2) and (9.3).

$$\phi_{SOC}^I = \phi_{SOC,fft}^I - \phi_J^I \quad (9.1)$$

$$\hat{T}_{SOC}^{I'} = \|\hat{T}_{SOC}\|^I \cdot \cos(\phi_{SOC}^I) \quad (9.2)$$

$$\hat{T}_{SOC}^{I''} = \|\hat{T}_{SOC}\|^I \cdot \sin(\phi_{SOC}^I) \quad (9.3)$$

Based on the methodology described in 6, a MATLAB® [296] routine was developed using the built-in FFT algorithm to analyze the series of data acquired during an active thermography measurement. The desired measurements can then be saved in one pdf containing the identification number of each measurement as well as the key operating parameters and if requested a Bode or Nyquist representation of the impedance corresponding to each measurements selected. An example of the routine output is presented in Appendix E.

Contributions to the Field

Demonstrated that active thermography can be applied to an operating SOC in both fuel cell and electrolysis operation. Compared the performance of PT and LT for the characterization of an SOC. Demonstrated the ability of LT to characterize the local behavior of an SOC and monitor the propagation of a degradation. Demonstrated that LT and DRT analysis can be combined to provide a better understanding of the degradation mechanisms.

9.1 Model-based interpretation of experimental LT

To assess the validity of the model and the capability of the designed test bench to perform active thermography, experimental and numerical results were compared using the same operating conditions. The model was then used to interpret the experimental results.

A colorized temperature field of an operating SOC is shown in Figure 9.1, where the reactant and air flow direction and the position of the thermocouple are indicated. The grid on the picture corresponds to the gold mesh (0.2 mm diameter wires) used for current collection on the O₂-electrode, which provides a visual indication of the spatial resolution of the camera.

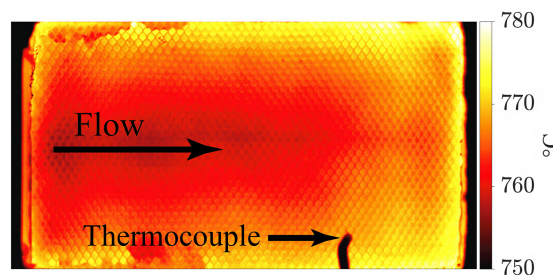


Figure 9.1 – Colorized temperature field of the SOC.

9.1.1 Electrolysis

The temperature was set to 750 °C, the H₂-electrode was fed with 180 Nmlmin⁻¹ of a 50/50 vol% H₂O/H₂ mixture, and the O₂-electrode was swept by 200 Nmlmin⁻¹ of air. The O₂-electrode was not closed by the quartz window during this experiment and thus the O₂-electrode was open to the furnace atmosphere and the air flow was not channelled. LT measurements were then performed in electrolysis mode at -0.2 and -0.4 Acm⁻² at frequencies ranging from 0.01 to 1 Hz with a perturbation amplitude of 1 A.

LT measurements obtained experimentally showed a larger $\|\hat{T}_{SOC}\|^I$ at the outlet of the SOC than the inlet, as illustrated by the LT measurement taken at 0.01 Hz and reported in Figure 9.2 (i). When the frequency was increased, the $\|\hat{T}_{SOC}\|^I$ at the outlet of the SOC increased to 0.05 Hz and then sharply decreased as the frequency was increased and eventually faded away at frequencies above 0.3 Hz, as shown by the first column of Figure 9.2 starting and ending with (i) and (ag), respectively.

At the inlet of the SOC, ϕ_{SOC}^I was positive from 0.01 to 0.5 Hz whereas it shifted from approximately zero to a negative value at the outlet of the SOC as shown by the second column of Figure 9.2 starting and ending with (j) and (ah), respectively. At 1 Hz, ϕ_{SOC}^I was negative but relatively homogeneous over the entire SOC. The temperature at the inlet of the SOC oscillated in counter phase with the current modulation, which was expected, as

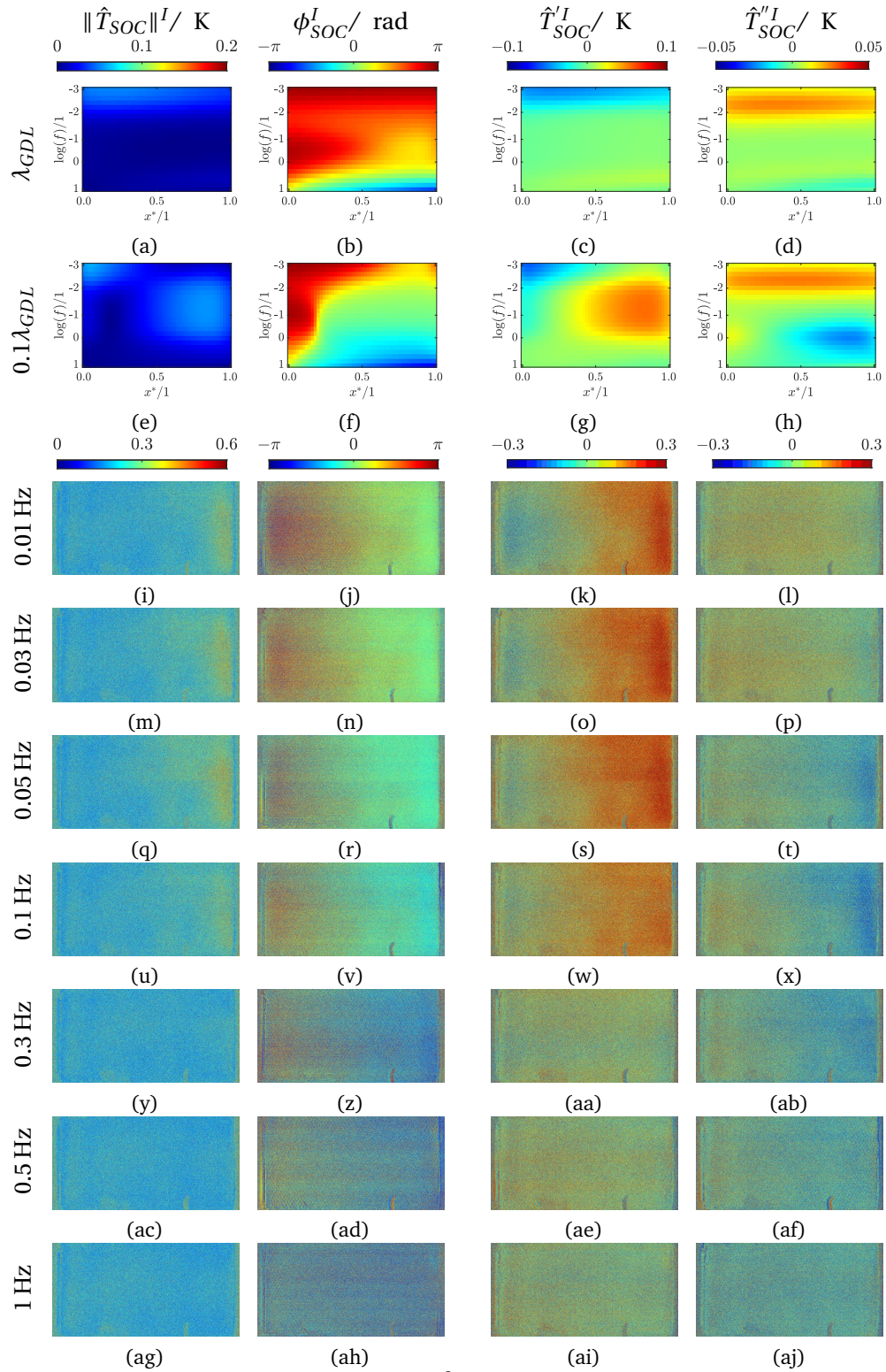


Figure 9.2 – Thermal response at -0.2 A cm^{-2} to a 1 A perturbation at various frequencies. The reactant and air flow from left to right. Images (a)–(d) and (e)–(f) are simulation results obtained with λ_{GDL} set to 3.5 and $0.35 \text{ W m}^{-1} \text{ K}^{-1}$, respectively, whereas images (i)–(j) are experimental data.

the SOC was operated in electrolysis mode below V_{tr} whereas the temperature modulation at the outlet of the SOC was in phase with the current modulation at low frequencies and eventually showed a phase delay as the excitation frequency was increased.

The decomposition of the thermal response in terms of the real and imaginary components, i.e., \hat{T}_{SOC}^I and \hat{T}_{SOC}^{II} , respectively, are presented in the columns of Figure 9.2 defined by (k) to (ai) and (a) to (d), respectively. At low frequencies, \hat{T}_{SOC}^I was negative near the inlet of the SOC and positive towards the outlet, thereby reflecting the evolution of ϕ_{SOC}^I . A negative and a positive high-amplitude rectangular areas were distinguishable at the inlet and outlet of the SOC as shown in Figure 9.2 (k). These regions corresponded to the position of two pockets machined in the H_2 -electrode metallic flange to improve lateral reactant diffusion. Above these pockets, the Ni-foam used for current collection was not in contact with the flange, which reduced the thermal conductivity thus increasing the temperature modulation. These regions were practically not visible in the ϕ_{SOC}^I images and only the effect of the outlet pocket could be distinguished in the $\|\hat{T}_{SOC}\|^I$ image, as shown in Figures 9.2 (i) and (j), respectively. Using \hat{T}_{SOC}^I thus offered a better contrast than the $\|\hat{T}_{SOC}\|^I$ for a similar scaling and also provided information on whether the temperature of the SOC increased ($\hat{T}_{SOC}^I > 0$) or decreased ($\hat{T}_{SOC}^I < 0$) with the current modulation.

At 0.01 and 0.03 Hz, the \hat{T}_{SOC}^{II} was relatively homogeneous and positive with a lower amplitude than the \hat{T}_{SOC}^I . When the frequency was increased, a negative \hat{T}_{SOC}^{II} region developed at the SOC's outlet, which peaked in intensity at approximately 0.1 Hz, and then decreased together with the spatial homogenization of \hat{T}_{SOC}^{II} to a negative value.

Numerical results obtained with a $\lambda_{GDL} = 3.5 \text{ W m}^{-1} \text{ K}^{-1}$, which are presented in Figures 9.2 (a) to (d), showed a large discrepancy with the experimental data presented in Figure 9.2 (i) to (aj). As the modelled SOC was only discretized in the flow direction, each experimental LT are represented as a single line in the numerical results images. None of the $\|\hat{T}_{SOC}\|^I$, ϕ_{SOC}^I , \hat{T}_{SOC}^I , and \hat{T}_{SOC}^{II} images obtained numerically represented the experimental data. However, numerical simulation performed with a λ_{GDL} reduced to $0.35 \text{ W m}^{-1} \text{ K}^{-1}$, presented in Figures 9.2 (e) to (h), were in better agreement with the experimental data, especially in term of the spatial and frequency distribution, thus suggesting that λ_{GDL} was initially over-estimated. The magnitude of the $\|\hat{T}_{SOC}\|^I$ was lower for the numerical model but both the numerical and experimental results showed a larger $\|\hat{T}_{SOC}\|^I$ at the outlet which peaked at a frequency of approximately 0.05 and 0.07 Hz in the experimental and numerical results, respectively. Part of the difference in magnitude originated from the amplitude of the current perturbation used which was set to 0.5 and 1 A for the numerical and experimental case, respectively. Additionally, the presence of the gas diffusion pocket limiting heat conduction also played a role.

The spatial distribution of ϕ_{SOC}^I obtained experimentally at 0.01 Hz, consisting of a transition from a positive to near-zero value between the inlet and outlet, was found

to be in good agreement with the numerical results, as shown in Figure 9.2 (j) and (f), respectively. When the frequency was increased, the ϕ_{SOC}^I at the outlet of the SOC transitioned from a near-zero to a negative value similarly for both the numerical and experimental results, as shown in the column of Figure 9.2 delimited by (j) to (ah).

The numerical results showed a large positive $\hat{T}_{SOC}^{I'}$ value at the outlet from approximately 0.01 to 1 Hz that then decreased as the frequency was increased, as shown in Figure 9.2 (g). The $\hat{T}_{SOC}^{I''}$ was positive over the entire SOC at low frequencies, then decreased as the frequency was increased, and then became negative near the outlet at approximately 1 Hz as shown in Figure 9.2 (h). The experimental results presented a similar behavior but were shifted to a slightly lower frequency. This frequency shift may have originated from an over-simplification of the model, e.g., the negligible thermal gradients within the materials thicknesses. A more complex model would likely lead to better agreement; here, only a reproduction of the trends were necessary, as only a qualitative analysis was performed.

At higher current densities, the numerical and experimental data also agreed well. When the current density was increased, the high intensity $\hat{T}_{SOC}^{I'}$ at the outlet expended to lower frequencies and also towards the SOC's inlet as shown by the experimental and numerical LT results in Figure 9.3. The negative $\hat{T}_{SOC}^{I'}$ at the inlet disappeared for both the experimental and numerical results. When the current density was increased from -0.2 to -0.4 Acm^{-2} , V_{SOC} passed from 1.04 to 1.16 V, respectively, and, the ϕ_{SOC}^I became spatially more homogeneous with a near-zero. This thus indicated that the V_{SOC} had transitioned from below to above the V_{tr} as was demonstrated in section 7.2. These results are also coherent with the numerical simulation, which experienced a similar ϕ_{SOC}^I evolution, as shown in Figures 9.2 and 9.3, respectively, when the current density increased from -0.2 to -0.4 Acm^{-2} and the measured V_{SOC} increased from 1.04 to 1.12 V, respectively. At low frequencies, the $\hat{T}_{SOC}^{I'}$ decreased homogeneously from a positive to a near-zero value. The negative $\hat{T}_{SOC}^{I''}$ region near the outlet observed at 0.1 Hz increased in magnitude and spread towards the SOC inlet. This behavior was in good agreement with the numerical results obtained at -0.2 and -0.4 Acm^{-2} , as shown in Figure 9.2 (h) and 9.3 (d), respectively.

9.1.2 Fuel cell

LT measurements were performed in fuel cell mode at 0.1 Acm^{-2} with a current modulation amplitude of 0.5 A corresponding to a 33 mV cell voltage modulation. The H_2 -electrode was fed with 120 Nml min^{-1} of a 50/50 $\text{H}_2\text{O}/\text{H}_2$ mixture whereas no air was fed to the O_2 -electrode which was thus only exposed to hot ambient air.

As observed in chapter 7, polarization in fuel cell mode was expected to lead to a different local thermal response than in electrolysis operation. At 0.01 Hz, the ϕ_{SOC}^I at the SOC

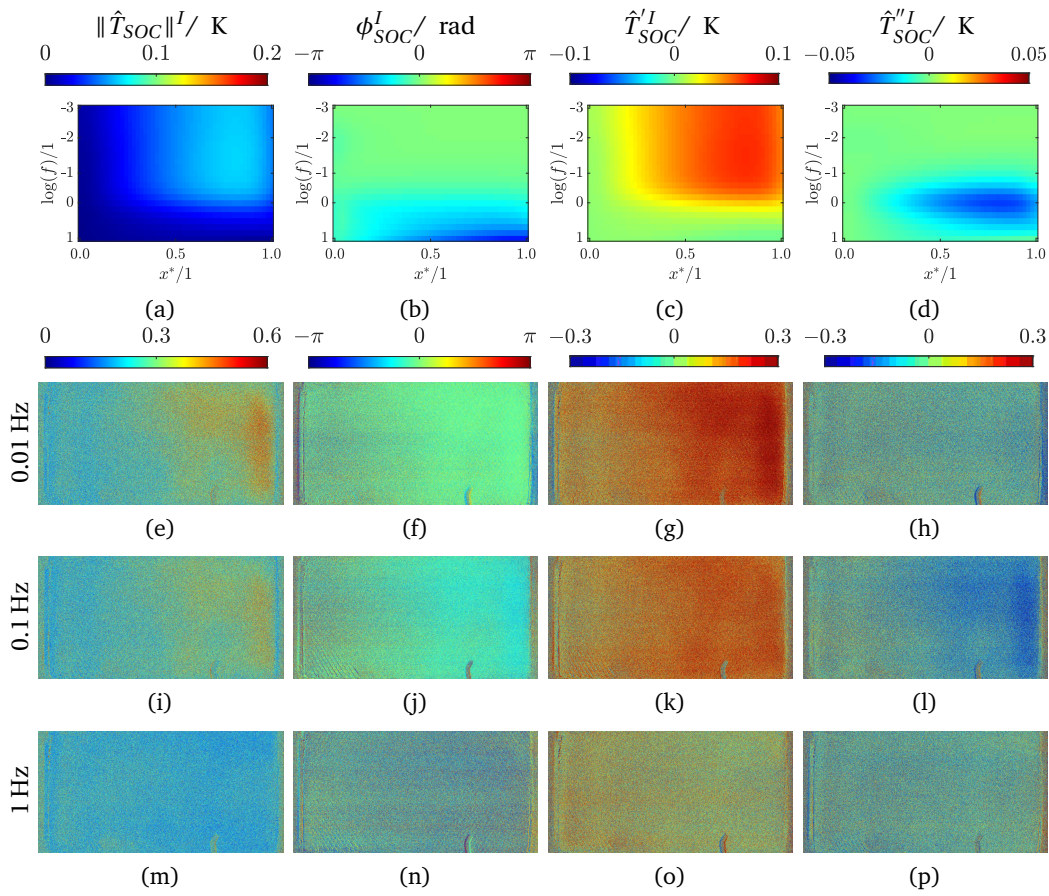


Figure 9.3 – Thermal response of the SOC at -0.4 A cm^{-2} to a 1 A perturbation at various frequencies. The reactant and air flow from left to right. Images (a)–(d) are simulation results obtained with λ_{GDL} set to $0.35 \text{ W m}^{-1} \text{ K}^{-1}$ whereas images (e)–(p) are experimental data.

inlet was shifted by approximately π when compared with electrolysis operation; thus, the SOC temperature evolved, here, almost in phase with the current modulation. This corresponded to the expected behavior during fuel cell operation i.e., exothermic, thus, increasing the current always led to a temperature increase.

Although the current modulation amplitude was, in this case, the same for the simulated and experimental LT, the $\|\hat{T}_{SOC}\|^I$ obtained experimentally was still larger than the one obtained numerically, suggesting that the heat transfer losses were over-estimated by the numerical model. The higher $\|\hat{T}_{SOC}\|^I$ at the inlet and outlet given by the numerical model were barely visible in the $\|\hat{T}_{SOC}\|^I$ image obtained experimentally. However, they were clearly visible in the $\hat{T}_{SOC}'^I$ image due the higher contrast caused by the difference of ϕ_{SOC}^I in these two regions. The $\|\hat{T}_{SOC}\|^I$ image thus appeared to be the less appropriate to identify local thermal behavior as it presented the lowest contrast.

9.1. Model-based interpretation of experimental LT

The thermal response of the SOC was not laterally homogeneous and showed a triangle-like shape near the inlet which was similar to the steady-state temperature field presented in 9.1 but with a lower extent. The response was generally more intense along the center line of the SOC and extended further away from the inlet than near the edges, which was particularly visible in the ϕ_{SOC}^I and \hat{T}_{SOC}^I image in Figure 9.4. The region where $\phi_{SOC}^I \approx 0$ near the inlet spread toward the outlet when the flow rate of reactant was increased as described, in Figure 7.14. As the reactant flow inlet of the set-up was located at the SOC center, a non ideal distribution of the reactant was coherent with a larger extent of the $\phi_{SOC}^I \approx 0$ region along the center line of the SOC.

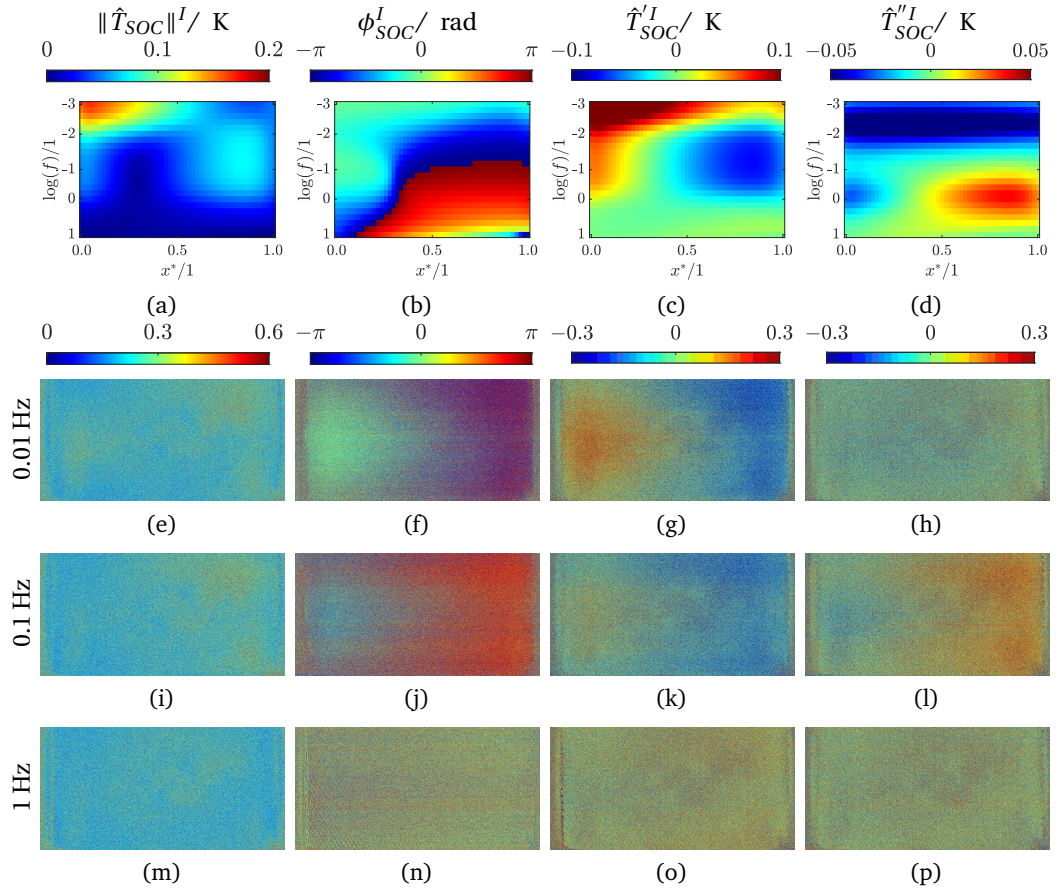


Figure 9.4 – Thermal response of the SOC at 0.1 A cm^{-2} to a 0.5 A perturbation at various frequencies. The reactant and air flow from left to right. Images (a)–(b) are simulation results obtained with λ_{GDL} set to $0.35 \text{ W m}^{-1} \text{ K}^{-1}$ whereas images (e)–(p) are experimental data.

9.1.3 Intermediate discussion

The numerical simulation and experimental measurements showed good agreement in terms of thermal response in both electrolysis and fuel cell operation. Therefore, other variables of interest (e.g., local current density, heat generation) computed by the model were assumed to be well represented (at least qualitatively) by the experimental data. The model and the results obtained in chapter 7 were thus used for the analysis and understanding of experimental measurements.

In section 7.2.5, it was shown that the large $\|\hat{T}_{SOC}\|^I$ regions near the inlet and outlet of the SOC were due to the local electrochemical reactions (i.e., \dot{Q}_{rx}) and modification of h_R^c , respectively. The regions could be differentiated by analyzing the ϕ_{SOC}^I , which was close to 0 and near $-\pi$ in fuel cell mode when the \dot{Q}_{rx} and h_R^c modulation dominated, respectively. The situation was inverted in electrolysis operation below V_{tr} , as the modulation of \dot{Q}_{rx} led to $\phi_{SOC}^I \approx \phi$ whereas the modulation of h_R^c lead to $\phi_{SOC}^I \approx 0$. Above V_{tr} , however, this transition vanished, as the temperature modulation induced by \dot{Q}_{rx} and h_R^c were both in-phase with the current modulation. The same behavior was observed in the experimental data, as presented in Figures 9.2, 9.3, and 9.4, and can thus be attributed to the same mechanisms, demonstrating the ability of LT to characterize the local thermal response of an SOC.

When the thermal response was represented using a real–imaginary instead of an amplitude–phase coordinate system, the effect of \dot{Q}_{rx} and h_R^c modulation could be directly identified from the \hat{T}_{SOC}^I , which were positive and negative in fuel cell mode when \dot{Q}_{rx} and h_R^c modulation dominated, respectively, as shown in Figure 9.4 (c). The opposite behavior was observed in electrolysis below V_{tr} , whereas, similarly to ϕ_{SOC}^I , both phenomena could not be distinguished above V_{tr} , as shown in Figures 9.2 (g) and 9.3 (c), respectively.

Above 0.1 Hz, the \hat{T}_{SOC}^I showed a spatially non-uniform behavior. In fuel cell operation, the ϕ_{SOC}^I was negative near the inlet and positive near the outlet, as shown in Figure 9.4 (d). The opposite behavior was found during electrolysis operation, as shown in Figure 9.2 (h), where the positive region at the inlet of the SOC vanished when the current density was increased, as shown in Figure 9.3 (d). In that frequency range, the thermal response of the SOC was a complex combination of \dot{Q}_{rx} , the thermal inertia of the SOC, and the reactant transport in the gas channel. The latter effect was related to the propagation of a "composition wave" in the reactant channel, which led to a phase shift between the current density modulation at the inlet and outlet of the SOC, as shown in Figure 7.6 (a). This also corresponded to the propagation of a wave-like modification of the h_R^c due to the dependency of h_R^c on the reactant composition. Additionally, the SOC's heat capacity also influenced the dynamic thermal response of the SOC above 0.1 Hz, thus leading to an extra phase lag.

9.2 Pulse thermography

A PT measurement was performed on a SOC from open circuit conditions in a 50/50 vol% $\text{H}_2/\text{H}_2\text{O}$ mixture. The pulse amplitude was 1.5 A and lasted 5 s. The frequency composition of the pulse excitation up to 4 Hz is represented by the black curve in Figure 9.5. Prior to the beginning of the pulse, eight images were averaged to serve as a reference. This reference image was then subtracted from the images taken during PT to obtain differential variables so that the signal began and ended at ≈ 0 , thereby mitigating the truncation error. The acquisition frequency was set to 4 Hz and 400 images were recorded leading to an available frequency range $\in [0, 2]$ Hz with a resolution of 0.01 Hz, as shown by the red dots in Figure 9.5.

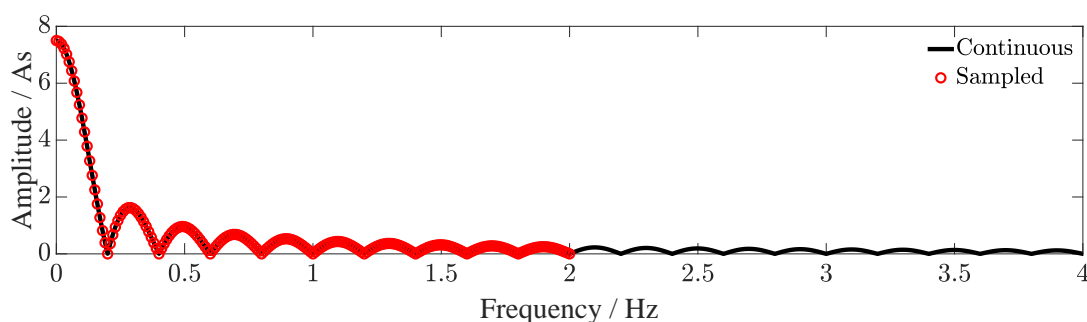


Figure 9.5 – Frequency content of the pulse excitation signal sent (continuous) and recorded (sampled).

The thermal response of the SOC at five frequencies are presented in Figure 9.6. A crack that formed at the top-right corner of the SOC before the PT measurement was visible in both ϕ_{SOC}^I and $\|\hat{T}_{SOC}\|^I$. With the used pulse parameters, only the results obtained for frequencies approximately ≤ 0.1 Hz were sufficiently above the noise level to be usable, which was approximately one third down the main lobe, as shown in Figure 9.5.

Compared with LT measurements taken in similar conditions, i.e., 1.5 A current bias and the same reactant composition as presented in Figure 9.4, the $\|\hat{T}_{SOC}\|^I$ was much smaller for PT than LT, as the excitation signal power was distributed over a much wider frequency range for PT than LT. A higher pulse amplitude or duration would be necessary to obtain a similar amplitude as in LT; however this may damage the SOC or impact the available frequency distribution of the pulse, respectively. Additionally, the electrochemical response of the SOC may then be nonlinear, thereby making the data interpretation more complex.

PT and LT measurements showed a similar spatial distribution of ϕ_{SOC}^I at 0.01 Hz, as shown in Figures 9.6 (a) and 9.4 (f), respectively. Although the PT signal faded rapidly at higher frequencies, similarities in ϕ_{SOC}^I were distinguishable at 0.1 Hz as shown in Figures 9.6 (d) and 9.4 (j).

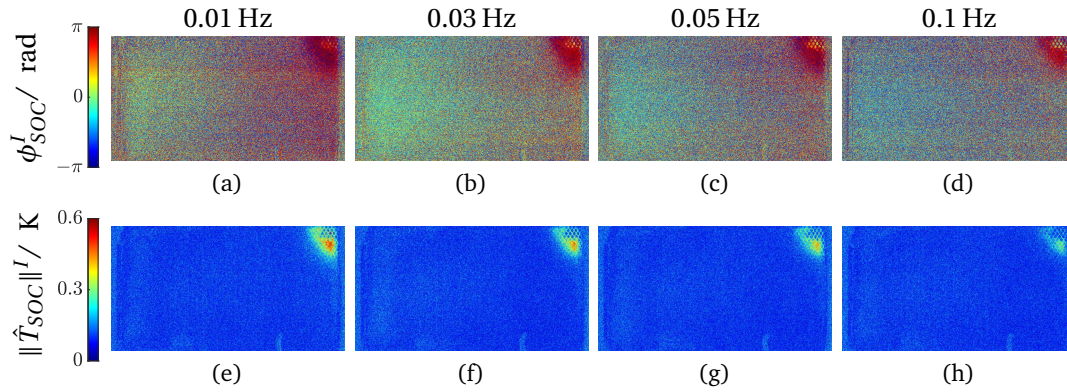


Figure 9.6 – SOC thermal response to a 1.5 A current pulse perturbation in fuel cell operation. The reactant and air flow from left to right.

It was demonstrated in section 7.1.1 that for a sinusoidal current modulation, $\|\hat{Q}_{rx}\|^I$ had a non-zero component at the excitation frequency and at higher harmonics. The PT results may thus be harder to analyze as the amplitude obtained at each frequency is a composition of the 1st harmonic and the higher harmonics of lower frequencies. Unlike EIS measurements where any signal can theoretically be used, LT and PT may not always be used interchangeably, especially when higher harmonics become significant. Here PT and LT showed similar results because the 1st harmonic likely dominated the thermal response of the SOC.

9.3 Electrolysis and Co-electrolysis

The effect of the reactant mixture composition on the SOC's electro-thermal response was investigated by operating the SOC in electrolysis and co-electrolysis mode using the reactant mixtures defined in Table 9.1. The SOC's performance was similar for each of the three reactant mixtures, as shown in Figure 9.7. The V_{SOC} was lowest in electrolysis operation and increased with the CO_2 content; this effect was more pronounced at higher current densities.

The SOC's thermal response during co-electrolysis differed from that during electrolysis as shown by the \hat{T}_{SOC}^I and \hat{T}_{SOC}^{II} taken at -0.1 A cm^{-2} and presented in Figures 9.10 and 9.11, respectively. The difference was particularly visible near the outlet, where the intensity decreased as the CO_2 content was increased. The opposite behavior was observed near the SOC's inlet, where \hat{T}_{SOC}^I and \hat{T}_{SOC}^{II} were larger for CE30 than CE15 or SE80.

As discussed in section 9.1, the higher \hat{T}_{SOC}^I near the outlet of the SOC during steam electrolysis was the result of an h_R^c modification due to the current-induced c_{H_2} modulation. For an H_2O/H_2 mixture, the h_R^c increased by a factor of more than 3 when the c_{H_2} increased from 0 to 1, as shown in Figure 7.9. For a CO/CO_2 mixture, however, the h_R^c

Table 9.1 – Reactant composition in electrolysis (SE80) and co-electrolysis (CE15 and CE30) operation. The air flow was always 200 Nmlmin⁻¹.

	U_F Nml/ min	H ₂ O vol%	CO ₂ vol%	H ₂ vol%
SE80	120	80	0.0	20
CE15	120	65	15	20
CE30	120	50	30	20

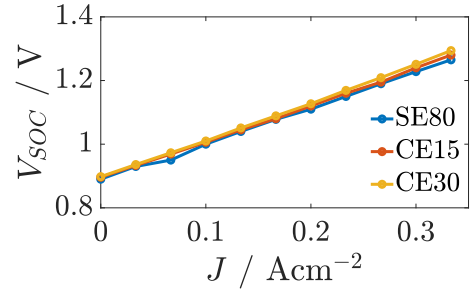


Figure 9.7 – SOC's current voltage-characterization for the reactant compositions defined in Table 9.1

was nearly independent of the composition, as shown in Figure 9.8. Additionally, the h_R^c was always smaller for a CO/CO₂ mixture ($\approx 1 \text{ kWm}^{-1} \text{ K}^{-1}$) than for a H₂/H₂O mixture (from ≈ 1.5 to $6.5 \text{ kWm}^{-1} \text{ K}^{-1}$). During co-electrolysis, the h_R^c thus was in between the h_R^c of an H₂/H₂O and CO/CO₂ mixture, as all four chemical species were present. For the same c_{H_2} modulation, the variation of h_R^c was thus smaller during co-electrolysis than electrolysis, and became less and less sensitive to a c_{H_2} modulation as the CO₂ share was increased. Additionally, during co-electrolysis, CO₂ is also reduced to CO either electrochemically or via the RWGS reaction, thus leading to a lower c_{H_2} modulation for the same current disturbance than in electrolysis mode, which further reduced the h_R^c modulation. The lower \hat{T}_{SOC}^I observed in co-electrolysis operation near the SOC outlet was thus likely the result of a reduced h_R^c modulation due to the presence of CO₂ and CO, which reduced the c_{H_2} modulation and the dependency of h_R^c on c_{H_2} .

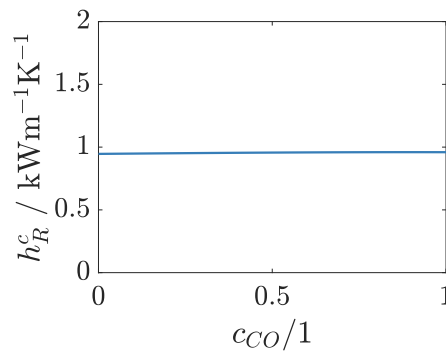


Figure 9.8 – Dependency of the h_R^c on c_{CO} for a CO₂ / CO mixture at 750 °C.

During steam electrolysis, the region surrounding the inlet of the SOC was dominated by electrochemical processes and was only marginally impacted by a modification of h_R^c , as demonstrated in chapter 7. The larger temperature modulation observed near the inlet of the SOC may thus have originated from the reduction of CO₂ to CO, which is more endothermic than the reduction of H₂O. As the reaction enthalpy is independent of the reaction steps, there is no difference whether CO₂ is converted to CO electrochemically

or via electrochemical H_2 generation combined with the RWGS reaction. As such, the two reaction pathways can not be discriminated but it can be assumed that near the inlet H_2O and CO_2 were reduced to H_2 and CO , respectively.

The positive $\hat{T}_{SOC}''^I$ region near the inlet of the SOC increased with the reactant's CO_2 content, which was particularly visible between 0.05 and 0.3 Hz in Figure 9.11. In that frequency range, the SOC's thermal response was a combination of the local heat modulation, the SOC's thermal inertia, and reactant transport in the gas channel, as demonstrated in section 9.1. During co-electrolysis, the $\hat{T}_{SOC}''^I$ showed a maximum at 0.05 Hz near the inlet and a minimum at 0.1 Hz near the outlet of the SOC, as shown in Figure 9.9 (a). During steam electrolysis, the $\hat{T}_{SOC}''^I$ near the inlet showed a similar behavior with a larger amplitude, whereas near the inlet, the $\hat{T}_{SOC}''^I$ decreased with the frequency without passing by a maximum at an intermediate frequency, as shown in Figure 9.9 (b). This may indicate a different heat modulation process related to the presence of CO_2 , e.g., RWGS.

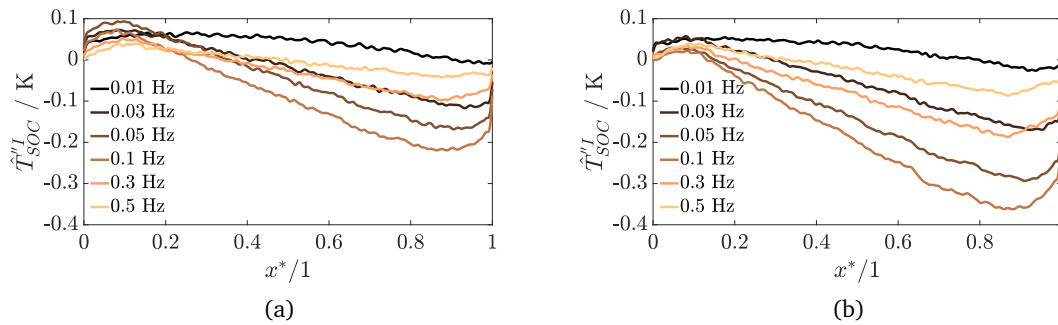


Figure 9.9 – $\hat{T}_{SOC}''^I$ averaged perpendicularly to the flow for (a) CE30 and (b) SE80 reactant mixtures.

When the current was increased to -0.3 A cm^{-2} , the V_{SOC} increased to 1.23, 1.24, and 1.25 V when using the SE80, CE15, and CE30 mixtures, respectively. The SOC responded similarly to an increase of the current density for the three gas mixtures, as shown in Figures 9.12 and 9.13. For the three reactant mixtures investigated, both the $\hat{T}_{SOC}''^I$ and $\hat{T}_{SOC}''^I$ were different but the variations were significantly less marked than at a lower current density.

Near the outlet of the SOC, the $\hat{T}_{SOC}''^I$ was higher than at -0.1 A cm^{-2} for the three reactant mixtures investigated. The increase was particularly visible with the SE80 reactant mixture due to the greater c_{H_2} and h_R^c modulations than for the CE15 and CE30 mixture. Near the inlet of the SOC, the $\hat{T}_{SOC}''^I$ and $\hat{T}_{SOC}''^I$ were similar for the three compositions; this suggests that as the current density was increased, the local heat modulation became similar for the SE80, CE15, and CE30 mixtures.

At -0.3 A cm^{-2} , the \hat{T}_{SOC}^I was positive over the entire SOC area for the three compositions, thereby indicating that the SOC was operated above V_{tr} . As the V_{SOC} was between the V_{tr} and V_{tn} (1.28 V for SE80), the electrochemical heat modulation was dominated by the steady-state local current density and voltage modulation, as demonstrated in chapter 7. As the V_{SOC} modulation was similar for the considered frequencies (within 5 mV), the temperature modulation can thus be assumed to be representative of the local current density, thereby suggesting that the local current density distribution near the inlet of the SOC was similar, regardless of the composition.

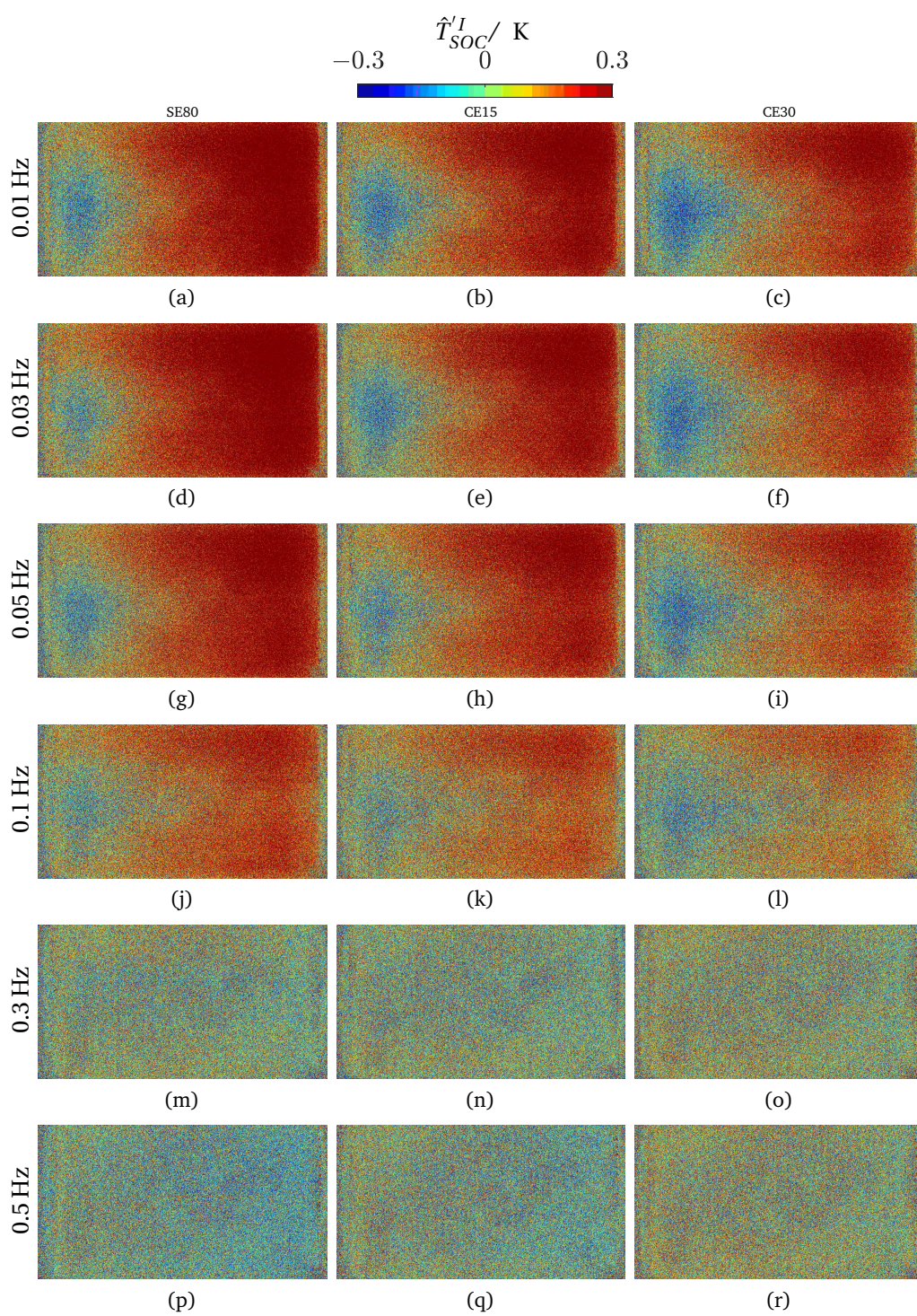


Figure 9.10 – \hat{T}_{SOC}^I at -0.1 A cm^{-2} and 1 A perturbation for the reactant mixture defined in Table 9.1

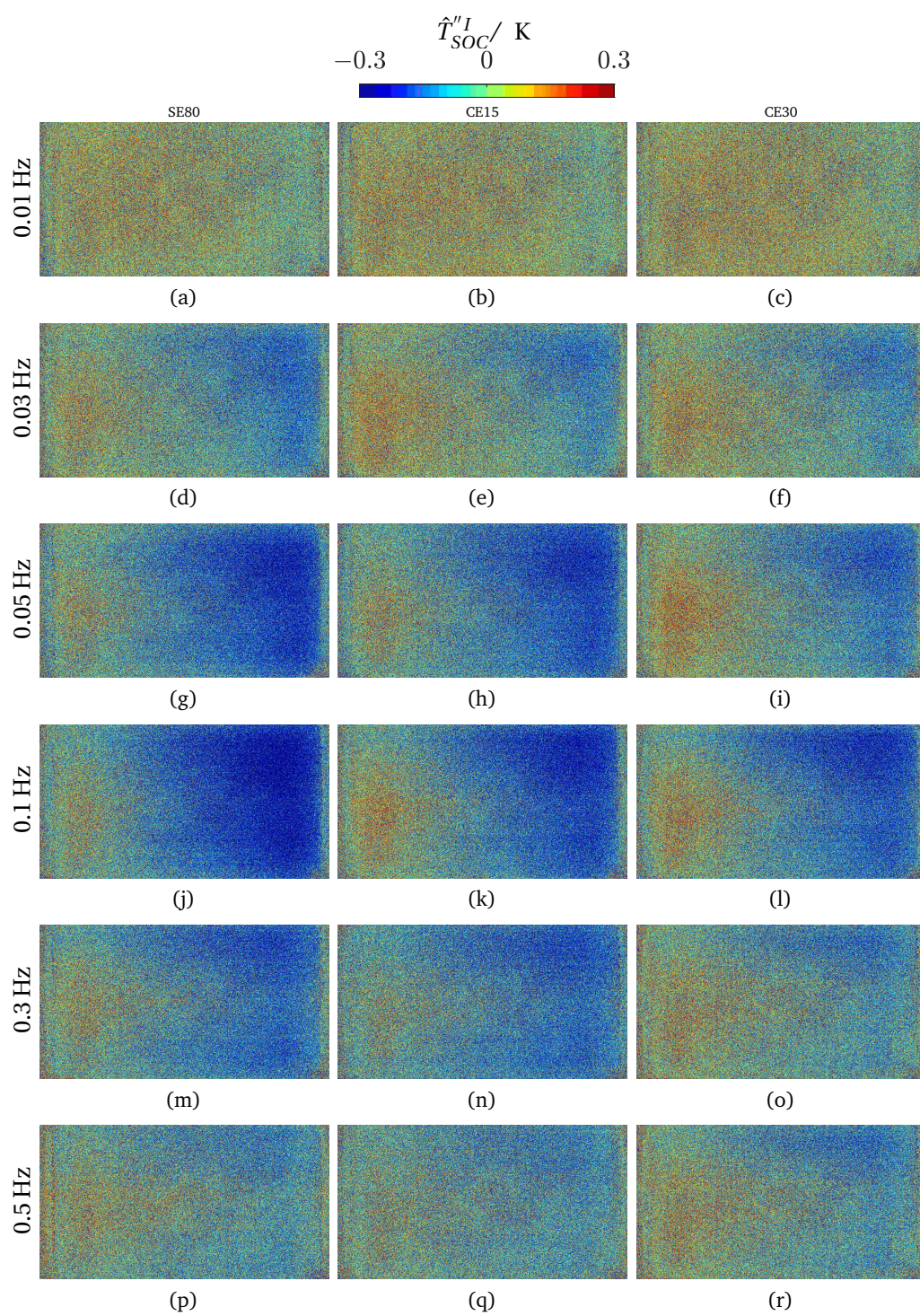


Figure 9.11 – $\hat{T}_{SOC}^{''I}$ at -0.1 A cm^{-2} and 1 A perturbation for the reactant mixture defined in Table 9.1

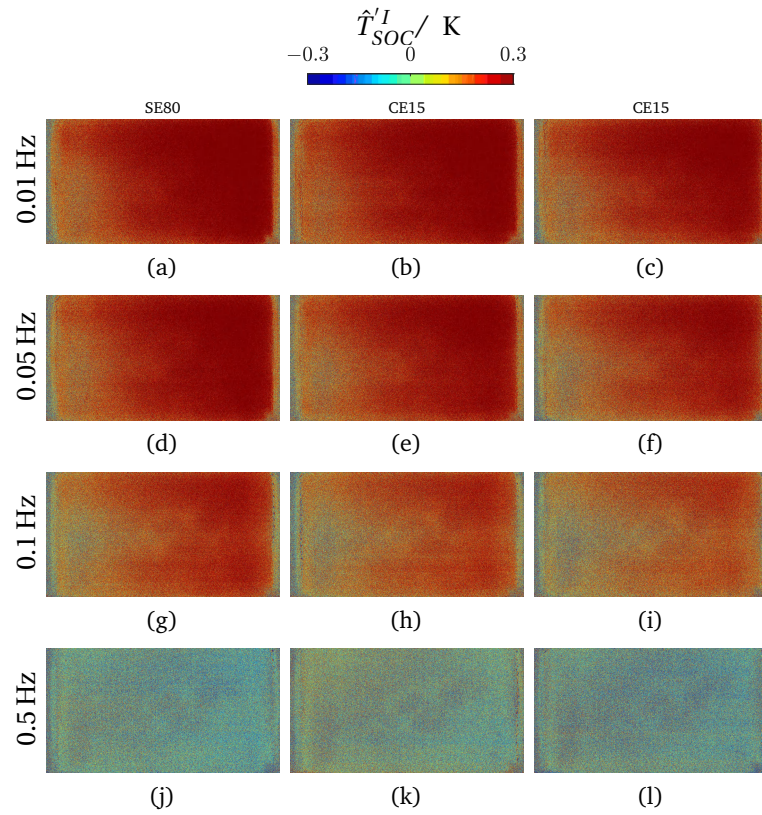


Figure 9.12 – \hat{T}_{SOC}^I at -0.3 A cm^{-2} and 1 A perturbation for the reactant mixture defined in Table 9.1

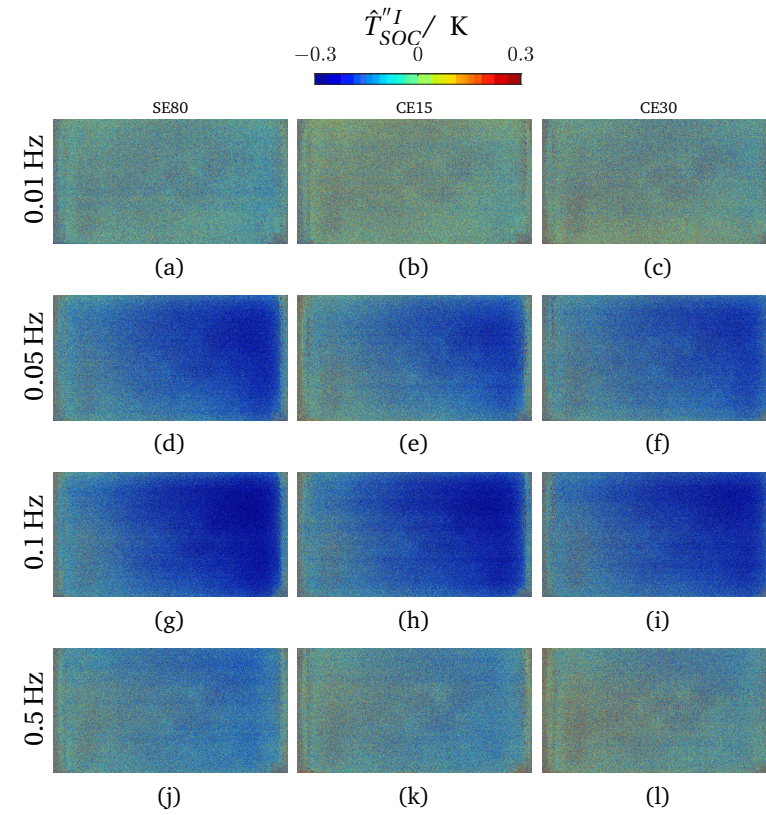


Figure 9.13 – \hat{T}_{SOC}^{II} at -0.3 A cm^{-2} and 1 A perturbation for the reactant mixture defined in Table 9.1

9.4 SO₂ poisoning

The reactant flow rate was set to 180 Nmlmin⁻¹ and was composed of 65/25/10 vol% of H₂O/CO₂/H₂ to reproduce the operating conditions used in chapter 5. The SOC was then operated at a constant current density of -0.2 Acm^{-2} .

When SO₂ was added to the reactant stream, the V_{SOC} increased in a step-like manner, as shown in Figure 9.14. The initial fast degradation step lasted approximately 18 h, which was similar to that reported in chapter 5 for a similar reactant flow, SO₂ content, and current density, as shown in Figure 5.2 (c). After approximately 20 h, the SO₂ supply was stopped and the V_{SOC} slowly recovered but only partially, similarly to what was reported in chapter 5.

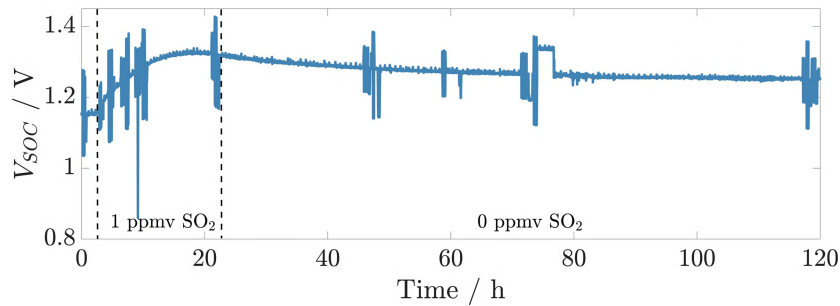


Figure 9.14 – Time evolution of the V_{SOC} operated at -0.2 Acm^{-2} in a 65/25/10 H₂O/CO₂/H₂ vol% mixture with the addition of 1 ppmv of SO₂ and during the recovery period in an SO₂-free atmosphere

The first set of LT measurements were taken at 0.01 and 0.1 Hz before exposure to SO₂ and are presented in Figures 9.16 (a) to (d). Here, the \hat{T}_{SOC}^I was positive over the entire SOC indicating that $V_{\text{SOC}} = 1.15 \text{ V}$ was larger than V_{tr} . The \hat{T}_{SOC}^I and \hat{T}_{SOC}^I showed a higher intensity near the SOC's outlet due to the h_R^c modulation. A small crack was present near the top-right corner, which took the form of a higher intensity region on both \hat{T}_{SOC}^I and \hat{T}_{SOC}^I , as shown in Figure 9.16. The $\hat{T}_{\text{SOC}}^{II}$ at 0.01 Hz was close to 0 as there was almost no phase lag between the thermal response and the current modulation at that frequency.

Two hours after the beginning of the exposure to SO₂, the $\hat{T}_{\text{SOC}}^{II}$ and \hat{T}_{SOC}^I showed a distinctive increase on the right half of the SOC, which was particularly evident at 0.1 Hz, as shown in Figures 9.16 (e) to (f). After 6 h of exposure, the \hat{T}_{SOC}^I and \hat{T}_{SOC}^I seemed similar to those taken after 2 h. The high-intensity region had slightly retreated towards the outlet and thus represented a smaller area of the SOC. Meanwhile, the \hat{T}_{SOC}^I and \hat{T}_{SOC}^I slightly increased on the left half of the SOC. After 9 h of exposure, the distribution of the \hat{T}_{SOC}^I and \hat{T}_{SOC}^I was more homogeneous as the intensity near the inlet also increased. The V_{SOC} degradation also began to decrease. After 20 h of exposure, the fast initial voltage degradation step characteristic of sulfur poisoning had passed and the \hat{T}_{SOC}^I and \hat{T}_{SOC}^I resembled the results of the initial LT measurement but with a higher amplitude. As the

same \hat{T}_{SOC}^I behavior was observed at two different frequencies, i.e., two independent measurements, and was correlated with V_{SOC} evolution, the observed modifications of the SOC electro-thermal behavior were determined to be caused by the interaction of the SOC with SO_2 .

A simpler representation the thermal response profile in the flow direction was obtained by averaging the \hat{T}_{SOC}^I signal perpendicularly to the flow within three regions of interest as defined in Figure 9.17 (a). Areas A1–A3 started at the inlet of the SOC and stopped at the limit of the crack, thereby avoiding interference. A low-pass filter was applied on the averaged data to further reduce the noise and make them more easily readable. The profile obtained before exposure to SO_2 , \hat{T}_{SOC}^I (0 h), was then subtracted from the following LT measurements to emphasize the variation of the \hat{T}_{SOC}^I in the flow direction when exposed to SO_2 . A similar evolution was found in the three regions investigated but the intensity of the \hat{T}_{SOC}^I was generally higher in the region A2; this could indicate a non-homogeneous reactant distribution, as shown in Figure 9.17 (b)–(d). Two hours after SO_2 was introduced, $\hat{T}_{SOC}^I - \hat{T}_{SOC}^I$ (0 h) was close to or slightly below zero until $x^* \approx 0.2$, gradually increased until $x^* \approx 0.4$ – 0.5 , where it even reached a peak for area A2, and then remained constant or slightly decreased until to $x^* = 1$. After 6 h, $\hat{T}_{SOC}^I - \hat{T}_{SOC}^I$ (0 h) continued increasing near the SOC's outlet and also began increasing near the inlet. The peak present in area A2 shifted towards the outlet whereas the region where $\hat{T}_{SOC}^I - \hat{T}_{SOC}^I$ (0 h) was gradually increasing covered a larger part of the SOC but with a more moderate slope that extended from $x^* \approx 0.2$ – 0.3 to ≈ 0.6 – 0.7 . After 9 h of exposure, $\hat{T}_{SOC}^I - \hat{T}_{SOC}^I$ (0 h) was U-shaped with a minimum at $x^* \approx 0.2$ – 0.4 . Additionally, for $x^* > 0.5$, $\hat{T}_{SOC}^I - \hat{T}_{SOC}^I$ (0 h) increased in area A3, where it had remained constant since the beginning of the exposure to SO_2 , to A1. After 20 h of exposure to SO_2 , $\hat{T}_{SOC}^I - \hat{T}_{SOC}^I$ (0 h) was almost constant from $x^* = 0$ – 1 and higher than after 9 h of exposure to SO_2 .

During the recovery period in an SO_2 -free atmosphere, the \hat{T}_{SOC}^I and \hat{T}_{SOC}^{II} decreased over the entire area of the SOC as shown in Figure 9.16 (u) to (af). The recovery was relatively homogeneous although the decrease of \hat{T}_{SOC}^I near the outlet of the SOC was slightly larger, as shown by the value of $\hat{T}_{SOC}^I - \hat{T}_{SOC}^I$ (0 h) in Figure 9.17 (e)–(f). Similarly to the V_{SOC} , the thermal response of the SOC did not completely recover. After 25 h in an SO_2 -free atmosphere (i.e., >45 h after the beginning of the SO_2 exposure), the thermal response of the SOC did not show a significant evolution, which was in agreement with the moderate V_{SOC} reduction that was observed during the same period shown in Figure 9.14. The first LT measurement taken during operation in a SO_2 -free atmosphere was performed after 25 h of recovery, which may have hindered the monitoring of a spatially non-homogeneous recovery process occurring earlier.

When SO_2 was introduced into the reactant stream, it reduced the catalytic (i.e., RWGS reaction) and electrochemical performances of the SOC, as demonstrated in chapter 5. The composition of the reactant mixture sent to the SOC (65/25/10 vol% $H_2O/CO_2/H_2$) was

not that of the thermodynamic equilibrium at 750 °C (67.5/22.9/7.9/2.1 vol% H₂O/CO₂/H₂/CO). As the catalytic activity was reduced, less CO₂ was converted to CO via the RWGS reaction, thereby increasing the c_{H_2} . Additionally, a smaller share of the electrochemically produced H₂ was consumed by the RWGS reaction further increasing c_{H_2} . In section 9.3, it was demonstrated that in the presence of CO₂, the \hat{T}_{SOC}^I and \hat{T}_{SOC}^{II} had a lower intensity near the SOC's outlet than during steam electrolysis owing to the reduced modulation of the c_{H_2} and h_R^c . The former was caused by the RWGS reaction, which converted part of the H₂ to H₂O, whereas the latter was related to the insensitivity of the h_R^c on the CO₂ and CO content. As the catalytic activity was limited by the exposure to SO₂, the c_{H_2} increased, thereby increasing the h_R^c and its sensitivity to a modulation of the H₂ concentration. Additionally, the current-induced c_{H_2} modulation that takes place during LT measurements was also increased by the reduction of the RWGS reaction. Therefore, the observed increase of \hat{T}_{SOC}^I near the outlet of the SOC during SO₂ poisoning was likely due to the reduction of the catalytic activity of the SOC (i.e., RWGS) due to the poisoning of the Ni by sulfur.

These results also suggest that after 2 h, the RWGS was limited over the entire area of the SOC; otherwise \hat{T}_{SOC}^I near the outlet of the SOC would have been closer the initial state as the gas composition and modulation would be similar due to the RWGS taking place in not-poisoned area. The propagation of the higher-intensity peak toward the outlet and the delayed increase of the \hat{T}_{SOC}^I near the inlet of the SOC suggested a spatially non-homogeneous propagation of the degradation. At least two processes were thus likely involved during the fast initial degradation step characteristic to sulfur poisoning.

9.4.1 Proposed SO₂ degradation mechanism

A degradation mechanism is proposed based on the results obtained in this section from LT measurements and the time evolution of the DRT during the fast initial degradation reported in chapter 5. For ease of reading, the latter, originally reported in Figure 5.7, is reproduced in Figure 9.15 (a).

As RU was low (≈ 0.13), most of the reactant sent to the H₂-electrode was only flushed through the Ni current collector before exiting the SOC. When SO₂ was introduced in the reactant, it thus likely deposited first on the Ni current collector and possibly superficially on the H₂-electrode, limiting the RWGS reaction along the gas channel, and thereby modifying the reactant composition. This may correspond to the 3.35 h DRT results reported in Figure 9.15 (a), where a small increase of the peak related to the charge-transfer processes (≈ 1 kHz), which is sensitive to the reactant composition, was observed. The S¹ then diffused into the H₂-electrode and reached the electrochemically

¹As stated in chapter 5, the chemical form of the S compound interacting with the H₂-electrode is not known, as H₂S is thermodynamically more stable than SO₂ but the kinetics are unknown. S was thus used to refer to sulfur in any chemical form.

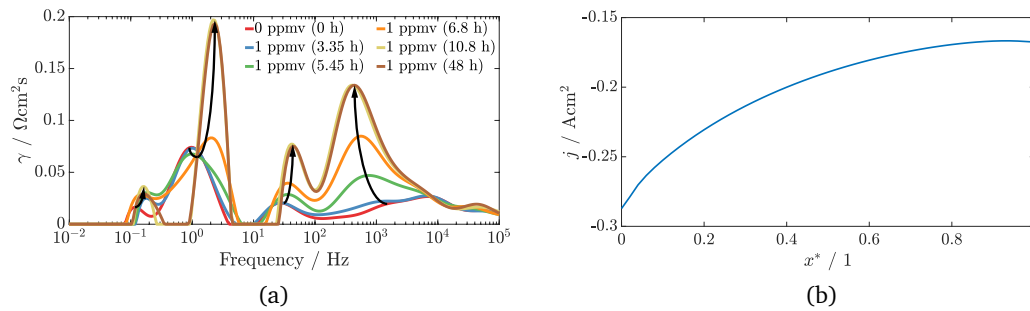


Figure 9.15 – (a) The time evolution of the DRT during the initial degradation step (reproduction of Figure 5.7 and (b) current density distribution computed with the model described in Chapter 7 for a 90/10 vol% $\text{H}_2\text{O}/\text{H}_2$ mixture at -0.2 A cm^{-2} and a $\text{RU} = 0.13$

active zone in the vicinity of the electrolyte. Ebbesen et al. [73] suggested that, during electrolysis, the volume flow rate leaving the TPB is lower than that reaching the TPB as smaller molecules are produced, i.e., H_2 and CO , thereby inducing a flow bias towards the TPB. The transport of S towards the TPB may therefore have been promoted in regions of the SOC where the current density, and thus the flow bias, was larger. Assuming that the current density distribution in co-electrolysis followed that of steam electrolysis, the current density near the inlet would be >1.5 times greater than at the outlet, as shown by the simulation results presented in Figure 9.15 (b). Near the inlet of the SOC, the flow bias towards the TPB was thus greater, which may have enhanced the transport of S towards the TPB in this region.

As the S was transported towards the TPB, it reduced the catalytic activity locally, which limited the RWGS reaction in the H_2 -electrode. When S reached and interacted with the electrochemically active Ni, it deteriorated the charge-transfer processes, thereby increasing the local impedance. Consequently, the current was partially redistributed downstream where the impedance was lower. As the RWGS reaction was limited in the gas channel and in the H_2 -electrode near the SOC's inlet, a smaller share of the H_2 produced in this region was converted back to H_2O . Additionally, as the current distribution was different from the initial state, the gas composition distribution was further modified. Both of these effects would affect the conversion impedance, and could thus be at the origin of the widening and shifting of the peak located at $\approx 1 \text{ Hz}$ that was observed after 5.45 and 6.8 h, as shown in Figure 9.15 (a). This inference was also supported by the evolution of the peak located around 1 kHz, which was coherent with a partial degradation of the charge-transfer processes and a modification of the reactant composition. In terms of thermal response, this situation would correspond to the measurement taken after 2 h of exposure, where the peak of the $\hat{T}_{\text{SOC}}' - \hat{T}_{\text{SOC}}^I(0 \text{ h})$ observed in Figure 9.17 (c) would then have been caused by the local current density increase.

As the current density increased downstream from the SOC inlet and S was made more available in the reactant due to the saturation of the H₂-electrode by S near the inlet, the effect of S was enhanced downstream. The S poisoning thus propagated downstream together with the local current increase, corresponding to the $\hat{T}'^I_{SOC} - \hat{T}'^I_{SOC}(0\text{ h})$ peak shift towards the outlet visible in the LT measurements taken after 2–9 h in Figure 9.17 (c). As the S poisoning propagated towards the outlet, at some point, the current could not be redistributed further downstream and thus increased near the SOC's inlet where the impedance was comparatively lower. This then corresponded with the increase of the \hat{T}'^I_{SOC} observed near the inlet after 6–9 h in Figure 9.17 (c). After ≈ 20 h of exposure, the S–Ni interactions were at equilibrium, i.e., equilibrium surface coverage, the \hat{T}'^I_{SOC} had a similar spatial distribution but with larger amplitude, and the current was likely distributed similarly or more homogeneously than before the exposure. An SOC can be treated in an analogous manner as a parallel connection of local impedances in which a current proportional to $Z_{loc}/(\sum 1/Z_{loc})^{-1}$ flows. If each local impedance increased by the same amount, then the current distribution would be more homogeneous; if the increase was proportional to the initial value, then the current distribution would be unchanged.

In summary, the proposed mechanism involved the fast deactivation of the catalytic properties of the current collector followed by a gradual reduction of the catalytic and electrochemical activity from the inlet to the outlet of the SOC, thereby inducing a redistribution of the current until the entire SOC was saturated.

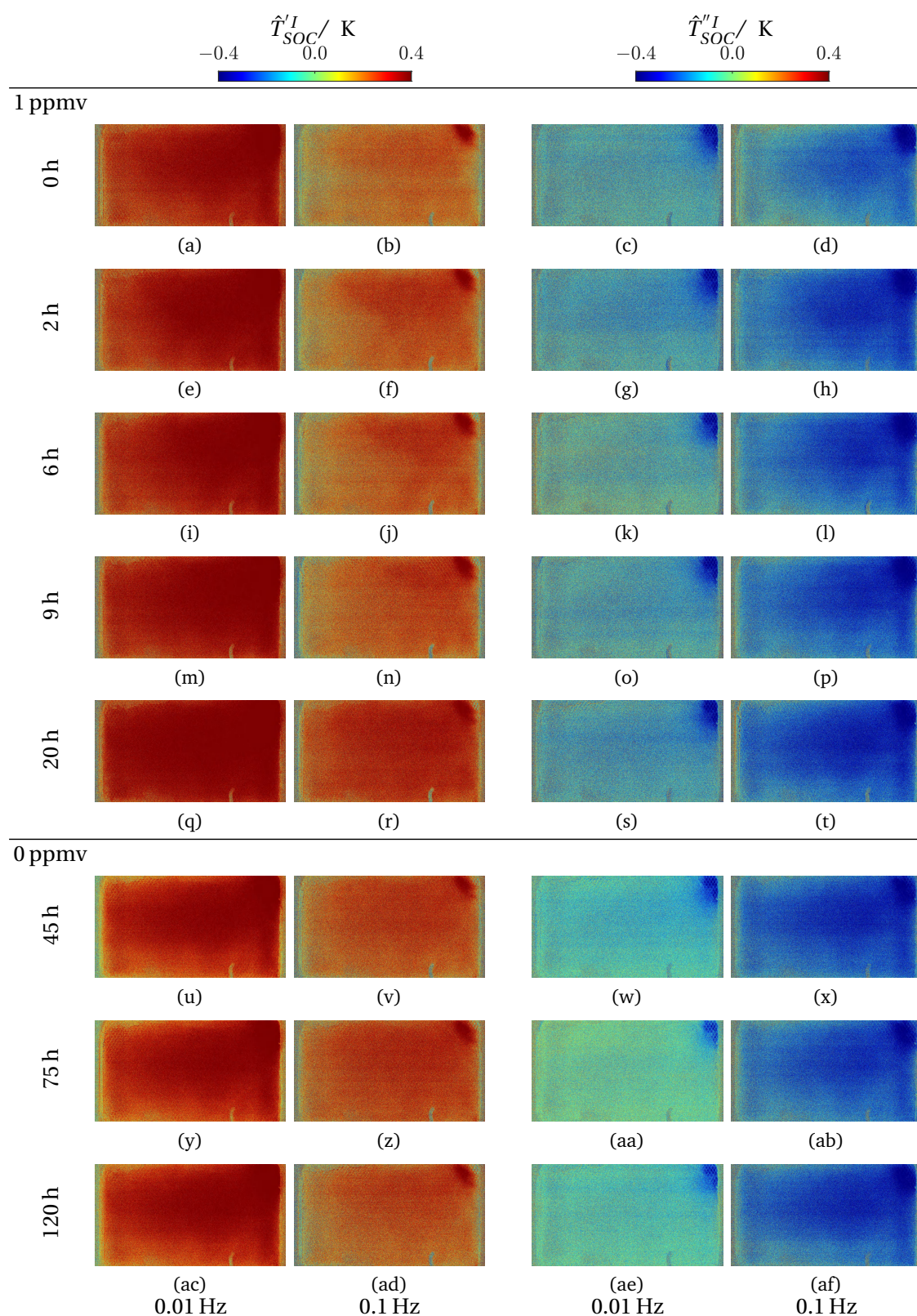


Figure 9.16 – Thermal response of the SOC at -0.2 A cm^{-2} to a 1 A perturbation at various frequencies when exposed to 1 ppmv of SO_2 and during recovery. The reactant and air flow from left to right.

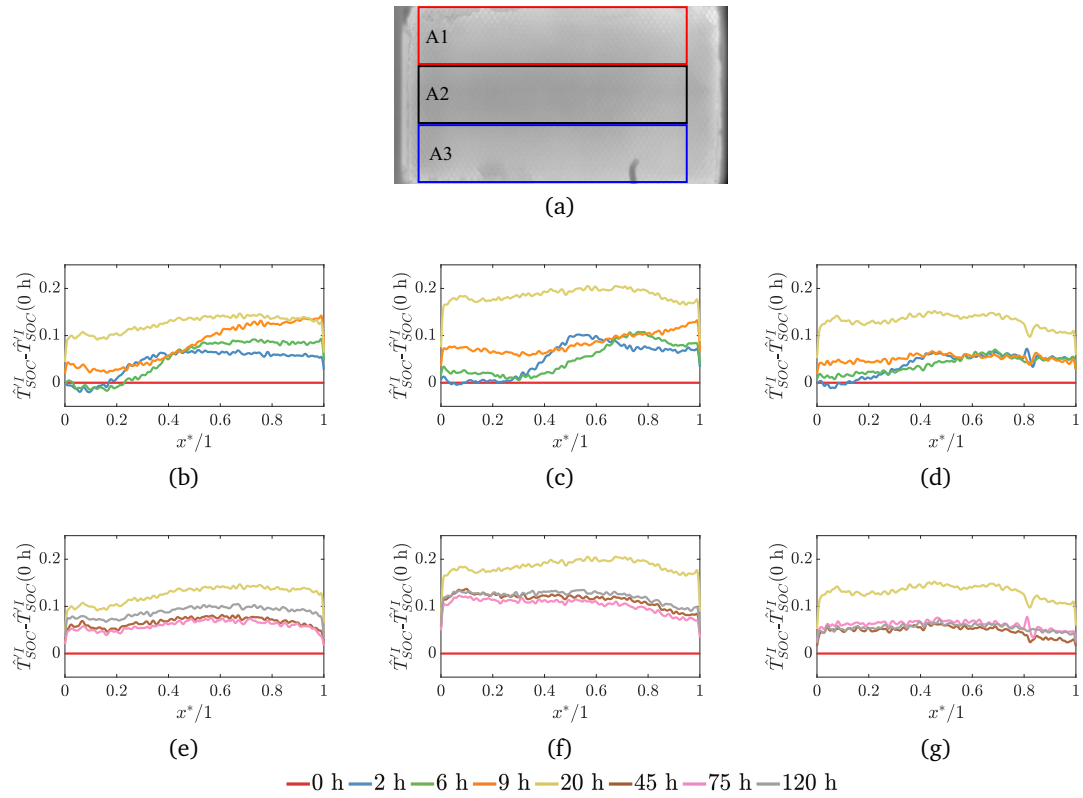


Figure 9.17 – Difference between the value of \hat{T}'_{SOC} measured at 0.01 Hz before and (a)–(d) during SO₂ poisoning (2 h–20 h) and during (e)–(f) recovery (20 h–120 h). \hat{T}'_{SOC} was averaged perpendicularly to the flow in three regions of interest (b) and (e) A1, (c) and (f) A2, and (d) and (g) A3 as defined in (a). The reactant and air flow from left to right.

9.5 Conclusion

LT measurements were performed on a SOC operated in fuel cell and electrolysis mode. The results were in good agreement with the numerical results, thus confirming simultaneously the validity of the model and the experimental measurements. The SOC's thermal response was spatially non-homogeneous and reflected the local operating conditions. The amplitude of the thermal response was found to be the least contrasted image and thus less adapted for analysis of LT measurements than the phase, real, or imaginary component.

Electrolysis and co-electrolysis operation were compared at various current densities using three different mixtures. Changing the gas composition led to a modification of the SOC thermal response. A different frequency-dependent behavior near the SOC's inlet was evidenced in the presence of CO_2 , which could have been caused by the RWGS reaction. The thermal response of the SOC became less dependent on the reactant composition when the current density was increased. The current densities investigated were moderate; a different behavior at higher current density (or reactant utilization) is likely.

PT and LT measurements led to similar phase images for similar decomposition frequencies. The amplitude image was, however, far smaller for the PT than LT results. Due to the nature of the signal, higher harmonics are more present in PT results, which makes their interpretation more complex. PT and LT can thus not be used interchangeably. Additionally, if a higher pulse amplitude is used to increase the SOC's thermal response, it may damage the SOC. LT appeared was thus deemed better suited to SOC applications.

An SOC operated in co-electrolysis was exposed to 1 ppmv of SO_2 for 20 h during which LT measurements were taken. The results provided evidence of an increase of the H_2 concentration in the reactant, which indicated a reduction of the catalytic activity caused by S. A modification of the local electro-thermal behavior of the SOC during exposure to SO_2 was identified using LT. The thermal response showed clear indication of a non-homogeneous propagation of the S-induced degradation. A mechanism describing the initial fast degradation observed during S poisoning, which was corroborated by the DRT analysis performed in chapter 5, was proposed. The degradation steps involved the fast deactivation of the catalytic properties of the current collector followed by a gradual reduction of the catalytic and electrochemical activity from the inlet to the outlet of the SOC, which then induced a redistribution of the current until the entire SOC was saturated. When the SO_2 supply was shut off, the SOC voltage partially recovered which led to a modification of the LT measurements, thereby confirming that the local electro-thermal behavior an SOC can be effectively characterized using LT.

Overall, the use of active thermography to study SOCs which offers the unique possibility of characterizing and monitoring in-situ the local behavior of normal-sized SOCs at a global scale with a high resolution.

CHAPTER 10

Concluding remarks & outlook

10.1 Concluding remarks

The work presented in this dissertation was motivated by two observations made on the available literature.

Observation 1 *The effect of impurities in the reactant stream is very well documented in fuel cell mode but it is rather sparse for electrolysis operation despite evidence of a potentially higher sensitivity.*

Observation 2 *The degradation/performance of an SOC is not spatially homogeneous but "classical" in-situ characterization methods (i.e., EIS and J–V) do not address it properly.*

These two observations were then addressed in parts I and II, respectively.

10.1.1 Part I

In chapter 2, potential CO₂ streams suitable for co-electrolysis were reviewed, demonstrating that an extremely vast variety of impurities may be present in captured CO₂. The impact of reactant feed impurities on the Ni–YSZ H₂-electrode of an SOFC has been extensively investigated, but a clear lack of literature on the effect of impurities during electrolysis operation was identified. To narrow down the potential threats to an SOEC's durability and performances, the impurities impacting Ni–YSZ electrodes in fuel cell operation were assumed to also be detrimental in co-electrolysis. By comparing the impurities potentially present in the CO₂ streams with the major threats to SOFC performance, SO₂ and HCl were identified as the two most likely to poison SOECs. Silicon compounds were also identified as a potential damage-causing impurities and should be considered in future research.

The impact of HCl concentrations ranging from 0.5 to 10 ppmv at a current density ranging from 0 to 0.5 A cm⁻² was investigated in chapter 4; similarly the impact of exposure to 0.5 to 5 ppmv of SO₂ at current densities ranging from 0 to 0.5 A cm⁻² is reported in chapter

5. Generally, operation in electrolysis mode was found to reduce the tolerance of an SOC towards impurities, as 1 ppmv of HCl or SO₂ already caused significant degradation. The electrochemically active sites were deteriorated relatively equally by SO₂ and HCl, whereas the catalytic reactions were principally impacted by SO₂. The degradation of the TPBs led to an increase and a shift to lower frequency of the DRT peak related to the charge-transfer processes (P5). Another peak was then revealed in the DRT spectrum, suggesting that P5 comprised two overlapping processes. Exposure to SO₂ led to a partially reversible reaction, whereas HCl poisoning was completely irreversible.

During both durability tests performed with 1 ppmv of HCl or SO₂, a low-frequency hook appeared in the impedance spectra when the SOC was degraded. As detailed in chapter 3, a meaningful DRT can only be obtained if γ is not positively constrained. The characteristic frequency of the inductive hook was thus estimated to be in between 10 and 100 mHz. The presence of the inductive hook was correlated with a large increase of the resistance associated with the charge-transfer processes at the H₂-electrode. Two physical processes were identified as possible causes of the observed inductive hook: 1) a two-step reaction mechanism involving an intermediate species (Volmer–Heyrovský mechanism) or 2) the development of an electronic conductivity in the electrolyte. As the SOC was operated in steady-state condition with a low reactant utilization (0.34), it is rather unlikely that the oxygen partial pressure dropped sufficiently to significantly increase the electronic conductivity of the YSZ. The two-step reaction mechanism is thus the most likely explanation.

Both durability tests showed a relatively stable and steady degradation rate around approximately 50 mVkh⁻¹ for at least 200 h before the voltage began rapidly increasing, increasing the degradation rate by a factor of at least 4. During SO₂ poisoning, the SOC's voltage rose from 1.4 to 1.8 V in a matter of hours. In both cases, this accelerating degradation could be stopped by stopping the supply of the contaminant. This behavior was observed multiple times during the SO₂ poisoning, confirming that it is related to the presence of contaminants in the reactant stream. Poisoning experiments shorter than 200–500 h may thus lead to an underestimation of the impact of impurities, which is a critical parameter for the design of the gas-cleaning units. The proposed mechanism for this behavior involves the accumulation of impurities blocking the electrochemically active sites in the vicinity of the electrolyte, thereby relocating the charge-transfer reactions away from the electrolyte and virtually increasing the electrolyte's thickness, leading to the observed increase in serial resistance.

The results obtained in Part I are expected to provide guidelines for future investigations on the interaction between impurities and an SOEC's Ni–YSZ electrode. Furthermore, the presented results will help decision makers to define a threshold for future power-to-X applications, especially regarding the required CO₂ quality.

Contributions to the field

- Determined the main chemical species that can affect a Ni-containing H_2 -electrode and thus threaten the lifetime and performance of SOC's operated in co-electrolysis.
- Evaluated the effect of SO_2 and HCl on SOC's performance and lifetime in co-electrolysis operation.
- Confirmed that SOC's operated in co-electrolysis are more sensitive to impurities than in fuel cell operation.
- Observed a voltage runaway behavior which evidenced the necessity to perform long-term testing with impurities.

10.1.2 Part II

The second part of this thesis was dedicated to the development and application of active thermography as a novel method to characterize the local behavior of operating SOC.

In chapter 7, existing electrochemical and thermal models were combined into a single model to allow the simulation of the transient electrochemical and thermal response of an SOC. The model was used to simulate LT measurements in different operating conditions and identify the critical parameters. The analysis essentially relied on the 1st harmonic, which possessed the largest amplitude.

Aside from the heat generated by the electrochemical reactions and the Joule effect, the modulation of the local convective heat transfer coefficient of the reactant stream greatly participated in the thermal response of the SOC. The latter effect became preponderant when the thermal conductivity between the SOC and the interconnect was reduced, thus providing guidelines for designing the appropriate test bench whether the effect of the reactant composition or of the electrochemical reaction are of interest. Additionally, increasing the H_2 content in the reactant increased the effect of the convective heat transfer modulation, which was thus more pronounced in electrolysis operation especially near the outlet of the SOC where H_2 accumulated. The air flow, however, had almost no impact on the thermal response of the SOC for the considered geometry.

The transient thermal response was more complex in electrolysis operation than in fuel cell operation and had a strong dependence on the operating voltage. The SOC's temperature modulation was in counter phase or in phase with the current oscillation depending whether the SOC voltage was below or above $V_{tr} \approx 1.1$ V, respectively, which corresponded to the voltage at which the SOC is the most endothermic and SOC's thermal response to a current modulation is the lowest and thus the most critical for active thermography. When the SOC was operated near the thermoneutral voltage, the electrochemical heat generation was independent of the local current and was only a

function of the steady-state current density and voltage modulation, thereby making certain features invisible. Some of these shortcomings were overcome by also analyzing the 2nd harmonic of the SOC's thermal response.

A method to estimate the local power modulation from a LT measurement was then proposed, which showed an accuracy of approximately $\pm 5\%$. The method quality of the estimate was, however, greatly deteriorated when the thermal conductivity between the SOC and the MIC was decreased as the effect of the convective heat transfer coefficient became dominant.

In chapter 9, PT and LT measurements were performed using the test bench developed in chapter 8. LT measurements performed in electrolysis and fuel cell mode were in good agreement with the model used in chapter 7, which was used as a support for the interpretation of the active thermography measurements. Although the electrochemical performances were similar, the SOC's thermal response was different when operated in electrolysis or co-electrolysis mode, which demonstrated the high sensitivity of active thermography to the reactant composition. Although PT and LT results were consistent, LT was more adapted to SOC applications, as a lower noise level can be achieved while keeping the current modulation reasonably low by averaging the SOC thermal response over multiple cycles. LT is thus more appropriate for identifying small signals in a noisy environment.

The capability of LT to monitor *operando* the local evolution of an SOC was demonstrated by poisoning the SOC with SO₂. A modification of the local thermal behavior of the SOC was clearly observed despite the use of operating conditions poorly suited for active thermography measurements i.e., the SOC voltage was between V_{tr} and V_{tn} . By combining these results with those obtained during the SO₂ poisoning experiments of part I, a detailed degradation mechanism involving a fast and slower deactivation, was proposed. The results demonstrated that the combination of LT measurements with DRT could become a powerful tool for the analysis of SOCs in operation.

The results obtained in part II are expected to open the door to a new approach to study the local catalytic and electrochemical behavior of SOCs as well as flow patterns. This work also provides an additional criterion to validate multi-dimensional models that are generally only validated with spatially averaged measurements (i.e., J - V and/or EIS). Furthermore, it will contribute to the expansion of active thermography to other electrochemical devices such as other types of fuel cell and electrolyzer or thermo-electric materials.

Contributions to the field

- Developed a dedicated test bench allowing to perform active thermography measurements.
- Developed codes for the analysis of PT and LT measurements.
- Identified key parameters influencing an SOC's thermal response by performing a parametric analysis with a numerical model.
- Evidenced that the SOC's temperature modulation is not only influenced by the electrochemical reactions or Joule-type heating but also by a modification of the convective heat transfer coefficient.
- Applied active thermography to an operating SOC in both fuel cell and electrolysis operation.
- Compared the performance of PT and LT for the characterization of an SOC.
- Demonstrated the ability of LT to characterize the local behavior of an SOC and monitor degradation propagated.
- Demonstrated that LT and DRT analysis can be combined to provide a better understanding of the degradation mechanisms.

10.2 Outlook

Gas analysis on the SOC's gas product should be performed to validate the observed reduction of the catalytic activity, i.e., RWGS, especially during the fast initial degradation step. This could also help to clarify the exact nature of the sulfur compound that interacted with the SOC and provide information on the kinetics of SO_2 decomposition to H_2S and on the validity of the equation used to evaluate the surface coverage of Ni by sulfur that was originally developed for H_2S . Post-mortem analysis should be performed, especially on the sample exposed to impurities for an extended period, to investigate the impact on the Ni microstructure particularly near the electrolyte and when exposed to HCl, which may have enhanced Ni migration and led to the observed irreversible degradation of the charge-transfer processes. To clarify the origin of the voltage runaway behavior observed, a new set of longterm experiments with impurities could be performed with a very fast cooling of the SOC when the voltage increases rapidly, which may allow to "freeze" the state of the SOC for post-mortem analysis. Using LT may also provide more information on the propagation of this degradation phenomenon and possibly allow specific regions to be targeted for post-mortem analysis. Additionally, modeling a two-step reaction scheme and the electronic conductivity of the electrolyte could provide a better insight on which mechanism is most likely to be responsible for the observed low-frequency hook. The formation of the low-frequency hook can then be triggered by

adding impurities in the reactant and specific measurements performed to corroborate the modeling results. As Ni-YSZ electrodes were found to be particularly sensitive to impurities when the SOC was operated in electrolysis mode, recovery strategies should be deeply investigated. In real applications, multiple impurities can be present at once in the reactant. The combined effect of multiple contaminants should thus also be assessed.

Above all else, the second part of this work aimed to investigate whether active thermography could be used for the local characterization of an SOC in operation. An accurate calibration of the infrared camera was thus not essential to this work. However, proper calibration would allow quantitative rather than qualitative results to be generated. Online FFT would allow longer LT measurements to be performed and thus could improve the signal-to-noise ratio while limiting the amount of data to be stored. This may also allow the thermal behavior of an SOC at higher frequencies to be observed. Performing LT measurements and full EIS measurements simultaneously, i.e., not limited to the LT frequencies, would allow a more comprehensive characterization of the SOC to be obtained. The experimental sensitivity analysis presented in this work was focused on electrolysis and co-electrolysis operation. Similarly to what has been done with EIS and DRT, LT measurements should be performed on a wider range of parameters, such as different SOC technologies (e.g., different cell support or electrode materials), flow pattern, temperatures, and reactant compositions to obtain a better overview on the limits and capabilities of active thermography. The 2nd harmonic should also be investigated in more detail, as it may not be subject to the same intrinsic limitations as the 1st harmonic. In the developed test bench, the O₂-electrode was not in contact with a MIC, which was not representative of an SOC operated in conventional conditions. Theoretically, LT measurements can also be performed if an MIC is added, although the temperature modulation and the spatial resolution would likely be affected. This should nevertheless be investigated in future work as the SOC would be operated closer to a "real" system.

CHAPTER A

Reversible R_s increase

A deeper discussion on the proposed mechanism explaining the reversible increase of R_s is presented in this appendix.

Hypothesis 1 *A progressive reduction of the active area due to the deactivation by sulphur of the electrochemically active Ni from the higher (inlet) to lower (outlet) current density regions.*

As discussed in section 5.1, a higher current density may have a negative impact on the SOEC tolerance towards SO_2 . Regions with a high current density could thus be deactivated first, leading to a reduction of the active area and a concomitant apparent increase of the area specific serial resistance. The current originally flowing through the now deactivated area would then be redistributed towards the cell outlet, locally increasing the current density. This increase in current density would trigger the deactivation process, gradually expanding the inactive regions from the SOEC inlet toward the outlet and leading to the observed voltage "runaway" behavior. Assuming that a partial deactivation of the active area is analogous to an electrode partial delamination, a concurrent and comparable increase of R_s and R_p is expected [270]. During the first voltage "runaway" (from about 230 to 500 h on Figure 5.6b), R_s and R_p increased by a factor of 2.1 and 1.1, respectively. A progressive deactivation of the active area is thus unlikely to be solely responsible for the observed behavior.

Hypothesis 2 *A cumulative effect of sulphur blocking the electrochemical active regions located closest to the electrolyte, possibly from the higher (inlet) to lower (outlet) current density regions.*

The electrochemically active region would be relocated away from the electrolyte, virtually increasing the electrolyte thickness. The serial resistance would automatically rise due to the increased distance that the oxygen ions have to travel to reach the OE and due to the constriction effect caused by the porosity of the HE compared with the dense electrolyte. The polarization resistance would not be greatly impacted, as the

Appendix A. Reversible R_s increase

electrochemical reactions would not be affected, but only displaced. Once the SO_2 supply was cut, the blocked electrochemically active regions would be recovered, reducing the R_s . The virtual increase of the electrolyte thickness was evaluated considering the ratio (M) between the effective ionic conductivity of the YSZ phase present in the HE (σ_{eff}) and the bulk conductivity of YSZ (σ_0), which was estimated to about 0.15 from [312] assuming a volume fraction of YSZ $\epsilon \approx 0.4$ [82]. The effective ionic conductivity of the porous electrode is [312]:

$$\sigma_{eff} = \sigma_0 \cdot M. \quad (\text{A.1})$$

The area specific resistance related to the virtual increase of the electrolyte thickness, L , becomes:

$$R_s^{virtual} = L \cdot \sigma_{eff}^{-1}, \quad (\text{A.2})$$

and the serial resistance:

$$R_s = R_s^{el} + R_s^{virtual} \quad (\text{A.3})$$

where $R_s^{el} = L^{el} \cdot \sigma_0^{-1}$ is the area specific resistance of the electrolyte, and L^{el} the electrolyte thickness. The contact resistance and electronic resistance in the electrodes are neglected. The thickness of the electrolyte being on the order of $10 \mu\text{m}$, the extent of the deactivated region would be in the order of $2 \mu\text{m}$, considering that R_s increased by a factor 2 to 3.

CHAPTER B

Electronic conductivity of YSZ

This appendix provide a short and informal discussion on the electronic conductivity of YSZ.

The electronic and ionic conductivity of the electrolyte can be estimated using the empirical equations derived by Park and Blumenthal [313] zirconia stabilized with 8 mol% of yttria ($Y_{0.148}Z_{0.852}O_{1.9259}$):

$$\sigma_{ion} = 163 \cdot \exp(0.79/kT) \quad (B.1)$$

$$\sigma_e = 1.31 \cdot 10^7 \exp(-3.88/kT) \cdot p_{O_2}^{-0.25} \quad (B.2)$$

$$\sigma_h = 235 \cdot \exp(-1.67/kT) \cdot p_{O_2}^{0.25} \quad (B.3)$$

where σ_{ion} , σ_e , σ_h are the ion, electron, and hole conductivity in $\Omega^{-1}cm^{-1}$, respectively, k is the Boltzmann constant ($8.614 \times 10^{-5} eVK^{-1}$), T the temperature in K. Assuming that these relation remain valid for any value of p_{O_2} , the electron and ion conductivity are equal for a p_{O_2} of 5.47×10^{-42} atm at 750 °C. The oxygen partial pressure in the YSZ corresponds to the "degree of filling" of the oxygen vacancy by oxygen atoms. When one oxygen is incorporated in a YSZ oxygen vacancy, a surplus of electron is generated and the YSZ becomes "N-doped" and inversely when one oxygen is removed and an oxygen vacancy created YSZ becomes "P-doped". In SOEC operation, it can thus be expected that the H_2 -electrode-interface is P-doped and the O_2 -electrode-interface N-doped (i.e., there is a P-N junction within the YSZ electrolyte where electrons and holes recombine).

The electronic and ionic conductivity of YSZ at 800 °C as a function of the oxygen partial pressure at which the YSZ is at equilibrium with is presented in Figure B.1. The typical p_{O_2} on the H_2 -electrode for operating conditions considered in this thesis, i.e., 150 Nm/min of $H_2O/CO_2/H_2$ 65 /25 /10 vol% and a maximal RU = 0.32 at $0.5 Acm^{-2}$ at 750 °C, is represented by a red rectangle. The conductivity reported in Figure B.1 have been computed at 800 °C but they should not be drastically different at 750 °C, in the sense that $\sigma_{ion} \gg \sigma_e$.

Appendix B. Electronic conductivity of YSZ

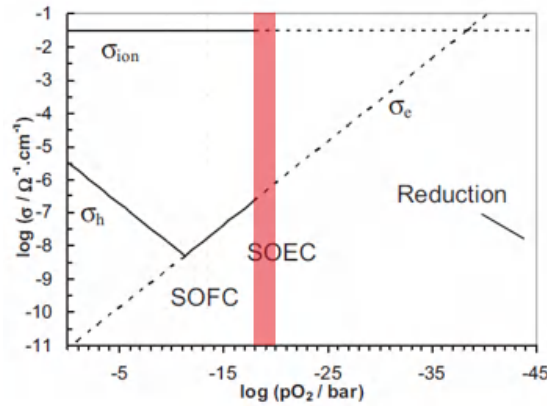


Figure B.1 – YSZ ionic, electron, and hole conductivity at 800 °C function of the oxygen partial pressure at which the YSZ is at equilibrium with. The red rectangle correspond the typical range of oxygen partial pressure experienced during the poisoning experiments performed in this thesis. Reproduced from Schefold et al. [6].

The dynamic behavior of the mix-electronic ionic the YSZ electrode could then be modeled following a similar approach than that proposed by Kee et al. [314] for a proton conducting membrane (see also Zhu et al. [315]). The presence of a low frequency hook in the impedance spectra could then be related to the time needed to the establishment of an electronic current in the YSZ, i.e., the time needed for a concentration wave to propagate from the H₂-electrode to the O₂-electrode thus "emptying" the oxygen vacancies. It is worth mentioning that the YSZ is not reduced (keep its structural integrity) as the electronic current develops only due to the increase of unoccupied oxygen vacancy. Schefold et al. [67] demonstrated that a significant electronic current is formed before that the reduction of YSZ occurs which actually protects the electrolyte.

As a boundary condition, it is generally assumed that YSZ is at equilibrium with the gas phase (in term of p_{O_2}). The σ_e is thus only dependent on the local reactant mixture. It is therefore difficult to explain how the addition of an impurity or the degradation of the charge transfer processes could lead to an electronic current in the YSZ. Chen et al. [316] have suggested that the overpotential at the Ni–YSZ interface (i.e., associated with the charge transfer resistance) can be related to the ratio of oxygen partial pressure in the gas phase and the partial pressure at the Ni–YSZ interface:

$$\eta_{ct} = R \cdot T \cdot \ln \left(\frac{p_{O_2}^{gas}}{p_{O_2}^{Ni-YSZ}} \right) \quad (B.4)$$

where η_{ct} is the overpotential related to charge transfer [124], $p_{O_2}^{gas}$, and $p_{O_2}^{Ni-YSZ}$ are the partial pressure of oxygen in the gas phase at the TPB and at the Ni–YSZ interface, respectively. This definition would then allow for a lower p_{O_2} in the YSZ induced solely by an increase of the charge transfer resistance without having to modify the local gas

composition. This behavior is thus consistent with the observed increase of the charge transfer resistance together with the appearance of the low frequency hook (this relation was particularly visible during the durability experiment with HCl). However, the validity of this relation is still prone to controversy as it does not (but theoretically should) formally involve a charge transfer process.

CHAPTER C

Analytical Fourier Transform

The detailed development of the Fourier transform of \dot{Q}_{rx} is presented in this Appendix.

The Fourier transform of $\dot{Q}_{rx} = j(V_{tn} - V_{SOC})$ is:

$$\mathfrak{F}\{\dot{Q}_{rx}\} = \mathfrak{F}\{j(V_{tn} - V_{SOC})\} = \mathfrak{F}\{jV_{tn}\} - \mathfrak{F}\{jV_{SOC}\},$$

which can thus be computed separately for $\mathfrak{F}\{jV_{tn}\}$ and $\mathfrak{F}\{jV_{SOC}\}$. Considering moderated non-linearities, form for V_{SOC} and j can be written as:

$$\begin{aligned} V_{SOC}(t) &= V^0 + \|V\|^I \cdot \cos(\omega_0 t + \phi_V^I) + \|V\|^{II} \cdot \cos(2\omega_0 t + \phi_V^{II}), \\ j(t) &= j^0 + \|j\|^I \cdot \cos(\omega_0 t + \phi_j^I) + \|j\|^{II} \cdot \cos(2\omega_0 t + \phi_j^{II}). \end{aligned}$$

Three useful mathematical properties are recalled:

$$\begin{aligned} \mathfrak{F}\{A\} &= A\delta(\omega), \\ \mathfrak{F}\{A\cos(\omega_0 t + \phi)\} &= \frac{A}{2} \left[\delta(\omega - \omega_0)e^{-i\phi} + \delta(\omega + \omega_0)e^{i\phi} \right], \\ \mathfrak{F}\{j(t) \cdot V(t)\} &= \hat{j}(\omega) * \hat{V}(\omega), \\ \delta(\omega - \omega_1) * \delta(\omega - \omega_2) &= \delta(\omega - \omega_1 - \omega_2). \end{aligned}$$

Appendix C. Analytical Fourier Transform

The Fourier transform of V_{SOC} and j can then be expressed as:

$$\begin{aligned}\hat{V}_{SOC}(\omega) &= V^0 \delta(\omega) + \frac{\|V\|^I}{2} \left[\delta(\omega - \omega_0) e^{-i\phi_V^I} + \delta(\omega + \omega_0) e^{i\phi_V^I} \right] + \frac{\|V\|^{II}}{2} \cdot \left[\delta(\omega - 2\omega_0) e^{-i\phi_V^{II}} + \delta(\omega + 2\omega_0) e^{i\phi_V^{II}} \right], \\ \hat{j}(\omega) &= j^0 \delta(\omega) + \frac{\|j\|^I}{2} \left[\delta(\omega - \omega_0) e^{-i\phi_j^I} + \delta(\omega + \omega_0) e^{i\phi_j^I} \right] + \frac{\|j\|^{II}}{2} \cdot \left[\delta(\omega - 2\omega_0) e^{-i\phi_j^{II}} + \delta(\omega + 2\omega_0) e^{i\phi_j^{II}} \right].\end{aligned}$$

Considering the single sided Fourier transform, i.e., keeping positive pulsation and multiplying by 2, $\mathfrak{F}\{jV_{tn}\}$ becomes:

$$\mathfrak{F}\{jV_{tn}\} = j^0 V_{tn} + \|j\|^I e^{-i\phi_j^I} V_{tn} + \|j\|^{II} e^{-i\phi_j^{II}} V_{tn}. \quad (C.1)$$

$\mathfrak{F}\{jV_{SOC}\}$ can be computed with the convolution product and its distribution property:

$$\begin{aligned}\mathfrak{F}\{j(t) \cdot V(t)\} &= \hat{j}(\omega) * \hat{V}(\omega) \\ &= V^0 j^0 \delta(\omega) * \delta(\omega) \\ &+ \frac{V^0 \|j\|^I}{2} \delta(\omega) * \left[\delta(\omega - \omega_0) e^{-i\phi_j^I} + \delta(\omega + \omega_0) e^{i\phi_j^I} \right] \\ &+ \frac{V^0 \|j\|^{II}}{2} \delta(\omega) * \left[\delta(\omega - 2\omega_0) e^{-i\phi_j^{II}} + \delta(\omega + 2\omega_0) e^{i\phi_j^{II}} \right] \\ &+ \frac{\|V\|^I j^0}{2} \delta(\omega) * \left[\delta(\omega - \omega_0) e^{-i\phi_V^I} + \delta(\omega + \omega_0) e^{i\phi_V^I} \right] \\ &+ \frac{\|V\|^I \|j\|^I}{4} \left[\delta(\omega - \omega_0) e^{-i\phi_V^I} + \delta(\omega + \omega_0) e^{i\phi_V^I} \right] * \left[\delta(\omega - \omega_0) e^{-i\phi_j^I} + \delta(\omega + \omega_0) e^{i\phi_j^I} \right] \\ &+ \frac{\|V\|^I \|j\|^{II}}{4} \left[\delta(\omega - \omega_0) e^{-i\phi_V^I} + \delta(\omega + \omega_0) e^{i\phi_V^I} \right] * \left[\delta(\omega - 2\omega_0) e^{-i\phi_j^{II}} + \delta(\omega + 2\omega_0) e^{i\phi_j^{II}} \right] \\ &+ \frac{\|V\|^{II} j^0}{2} \delta(\omega) * \left[\delta(\omega - 2\omega_0) e^{-i\phi_V^{II}} + \delta(\omega + 2\omega_0) e^{i\phi_V^{II}} \right] \\ &+ \frac{\|V\|^{II} \|j\|^I}{4} \left[\delta(\omega - 2\omega_0) e^{-i\phi_V^{II}} + \delta(\omega + 2\omega_0) e^{i\phi_V^{II}} \right] * \left[\delta(\omega - \omega_0) e^{-i\phi_j^I} + \delta(\omega + \omega_0) e^{i\phi_j^I} \right] \\ &+ \frac{\|V\|^{II} \|j\|^{II}}{4} \left[\delta(\omega - 2\omega_0) e^{-i\phi_V^{II}} + \delta(\omega + 2\omega_0) e^{i\phi_V^{II}} \right] * \left[\delta(\omega - 2\omega_0) e^{-i\phi_j^{II}} + \delta(\omega + 2\omega_0) e^{i\phi_j^{II}} \right].\end{aligned}$$

Using the distribution property of the convolution product it leads to:

$$\begin{aligned}
\mathfrak{F}\{j(t) \cdot V(t)\} &= \hat{j}(\omega) * \hat{V}(\omega) \\
&= V^0 j^0 \delta(\omega) \\
&+ \frac{V^0 \|j\|^I}{2} \left[\delta(\omega - \omega_0) e^{-i\phi_j^I} + \delta(\omega + \omega_0) e^{i\phi_j^I} \right] \\
&+ \frac{V^0 \|j\|^{II}}{2} \left[\delta(\omega - 2\omega_0) e^{-i\phi_j^{II}} + \delta(\omega + 2\omega_0) e^{i\phi_j^{II}} \right] \\
&+ \frac{\|V\|^I j^0}{2} \left[\delta(\omega - \omega_0) e^{-i\phi_V^I} + \delta(\omega + \omega_0) e^{i\phi_V^I} \right] \\
&+ \frac{\|V\|^I \|j\|^I}{4} \left[\delta(\omega - 2\omega_0) e^{-i(\phi_V^I + \phi_j^I)} + \delta(\omega) e^{-i(\phi_V^I - \phi_j^I)} + \delta(\omega) e^{i(\phi_V^I - \phi_j^I)} + \delta(\omega + 2\omega_0) e^{i(\phi_V^I + \phi_j^I)} \right] \\
&+ \frac{\|V\|^I \|j\|^{II}}{4} \left[\delta(\omega - 3\omega_0) e^{-i(\phi_V^I + \phi_j^{II})} + \delta(\omega - \omega_0) e^{-i(\phi_V^I - \phi_j^{II})} + \delta(\omega + \omega_0) e^{i(\phi_V^I - \phi_j^{II})} + \delta(\omega + 3\omega_0) e^{i(\phi_V^I + \phi_j^{II})} \right] \\
&+ \frac{\|V\|^{II} j^0}{2} \left[\delta(\omega - 2\omega_0) e^{-i\phi_V^{II}} + \delta(\omega + 2\omega_0) e^{i\phi_V^{II}} \right] \\
&+ \frac{\|V\|^{II} \|j\|^I}{4} \left[\delta(\omega - 3\omega_0) e^{-i(\phi_V^{II} + \phi_j^I)} + \delta(\omega - \omega_0) e^{-i(\phi_V^{II} - \phi_j^I)} + \delta(\omega + \omega_0) e^{i(\phi_V^{II} - \phi_j^I)} + \delta(\omega + 3\omega_0) e^{i(\phi_V^{II} + \phi_j^I)} \right] \\
&+ \frac{\|V\|^{II} \|j\|^{II}}{4} \left[\delta(\omega - 4\omega_0) e^{-i(\phi_V^{II} + \phi_j^{II})} + \delta(\omega) e^{-i(\phi_V^{II} - \phi_j^{II})} + \delta(\omega) e^{i(\phi_V^{II} - \phi_j^{II})} + \delta(\omega + 4\omega_0) e^{i(\phi_V^{II} + \phi_j^{II})} \right]
\end{aligned}$$

The terms at the pulsation of interest, i.e., 0, ω_0 , and $2\omega_0$, can then be extracted and multiplied by 2 (excepted the steady state term) as single sided spectra are desired.

Steady state $\delta(\omega)$

$$V^0 j^0 + \frac{\|V\|^I \|j\|^I}{4} e^{-i(\phi_V^I - \phi_j^I)} + \frac{\|V\|^I \|j\|^I}{4} e^{i(\phi_V^I - \phi_j^I)} + \frac{\|V\|^{II} \|j\|^{II}}{4} e^{-i(\phi_V^{II} - \phi_j^{II})} + \frac{\|V\|^{II} \|j\|^{II}}{4} e^{i(\phi_V^{II} - \phi_j^{II})}$$

1st harmonic $\delta(\omega - \omega_0)$

$$V^0 \|j\|^I e^{-i\phi_j^I} + \|V\|^I j^0 e^{-i\phi_V^I} + \frac{\|V\|^I \|j\|^{II}}{2} e^{-i(\phi_V^I - \phi_j^{II})} + \frac{\|V\|^{II} \|j\|^I}{2} e^{-i(\phi_V^{II} - \phi_j^I)}$$

2nd harmonic $\delta(\omega - 2\omega_0)$

$$V^0 \|j\|^{II} e^{-i\phi_j^{II}} + \frac{\|V\|^I \|j\|^I}{2} e^{-i(\phi_V^I + \phi_j^I)} + \|V\|^{II} j^0 e^{-i\phi_V^{II}}$$

Now that the Fourier transforms of $\mathfrak{F}\{j V_{tn}\} - \mathfrak{F}\{j V_{SOC}\}$ are known, the first three terms of $\mathfrak{F}\{\dot{Q}_{rx}\}$ can be computed term by term as:

Appendix C. Analytical Fourier Transform

Steady state $\delta(\omega)$

$$j^0 V_{tn} - \left[V^0 j^0 + \frac{\|V\|^I \|j\|^I}{4} e^{-i(\phi_V^I - \phi_j^I)} + \frac{\|V\|^I \|j\|^I}{4} e^{i(\phi_V^I - \phi_j^I)} + \frac{\|V\|^{II} \|j\|^{II}}{4} e^{-i(\phi_V^{II} - \phi_j^{II})} + \frac{\|V\|^{II} \|j\|^{II}}{4} e^{i(\phi_V^{II} - \phi_j^{II})} \right]$$

1st harmonic $\delta(\omega - \omega_0)$

$$\|j\|^I e^{-i\phi_j^I} V_{tn} - \left[V^0 \|j\|^I e^{-i\phi_j^I} + \|V\|^I j^0 e^{-i\phi_V^I} + \frac{\|V\|^I \|j\|^{II}}{2} e^{-i(\phi_V^I - \phi_j^{II})} + \frac{\|V\|^{II} \|j\|^I}{2} e^{-i(\phi_V^{II} - \phi_j^I)} \right]$$

2nd harmonic $\delta(\omega - 2\omega_0)$

$$\|j\|^{II} e^{-i\phi_j^{II}} V_{tn} - \left[V^0 \|j\|^{II} e^{-i\phi_j^{II}} + \frac{\|V\|^I \|j\|^I}{2} e^{-i(\phi_V^I + \phi_j^I)} + \|V\|^{II} j^0 e^{-i\phi_V^{II}} \right]$$

The real and imaginary component of each harmonic can be computed using $e^{i\phi} = \cos(\phi) + i \sin(\phi)$, $\cos(\phi) = \cos(-\phi)$, and $\sin(\phi) = -\sin(-\phi)$:

Steady state $\delta(\omega)$

Real:

$$j^0 V_{tn} - \left[V^0 j^0 + \frac{\|V\|^I \|j\|^I}{2} \cos(\phi_V^I - \phi_j^I) + \frac{\|V\|^{II} \|j\|^{II}}{2} \cos(\phi_V^{II} - \phi_j^{II}) \right]$$

Imaginary:

$$0$$

1st harmonic $\delta(\omega - \omega_0)$

Real:

$$\|j\|^I \cos(\phi_j^I) V_{tn} - \left[V^0 \|j\|^I \cos(\phi_j^I) + \|V\|^I j^0 \cos(\phi_V^I) + \frac{\|V\|^I \|j\|^{II}}{2} \cos(\phi_V^I - \phi_j^{II}) + \frac{\|V\|^{II} \|j\|^I}{2} \cos(\phi_V^{II} - \phi_j^I) \right]$$

Imaginary:

$$-\|j\|^I \sin(\phi_j^I) V_{tn} + \left[V^0 \|j\|^I \sin(\phi_j^I) + \|V\|^I j^0 \sin(\phi_V^I) + \frac{\|V\|^I \|j\|^{II}}{2} \sin(\phi_V^I - \phi_j^{II}) + \frac{\|V\|^{II} \|j\|^I}{2} \sin(\phi_V^{II} - \phi_j^I) \right]$$

2nd **harmonic** $\delta(\omega - 2\omega_0)$

Real:

$$\|j\|^I \cos(\phi_j^I) V_{tn} - \left[V^0 \|j\|^I \cos(\phi_j^I) + \frac{\|V\|^I \|j\|^I}{2} \cos(\phi_V^I + \phi_j^I) + \|V\|^I j^0 \cos(\phi_V^I) \right]$$

Imaginary:

$$-\|j\|^I \sin(\phi_j^I) V_{tn} + \left[V^0 \|j\|^I \sin(\phi_j^I) + \frac{\|V\|^I \|j\|^I}{2} \sin(\phi_V^I + \phi_j^I) + \|V\|^I j^0 \sin(\phi_V^I) \right]$$

CHAPTER D

LT defect

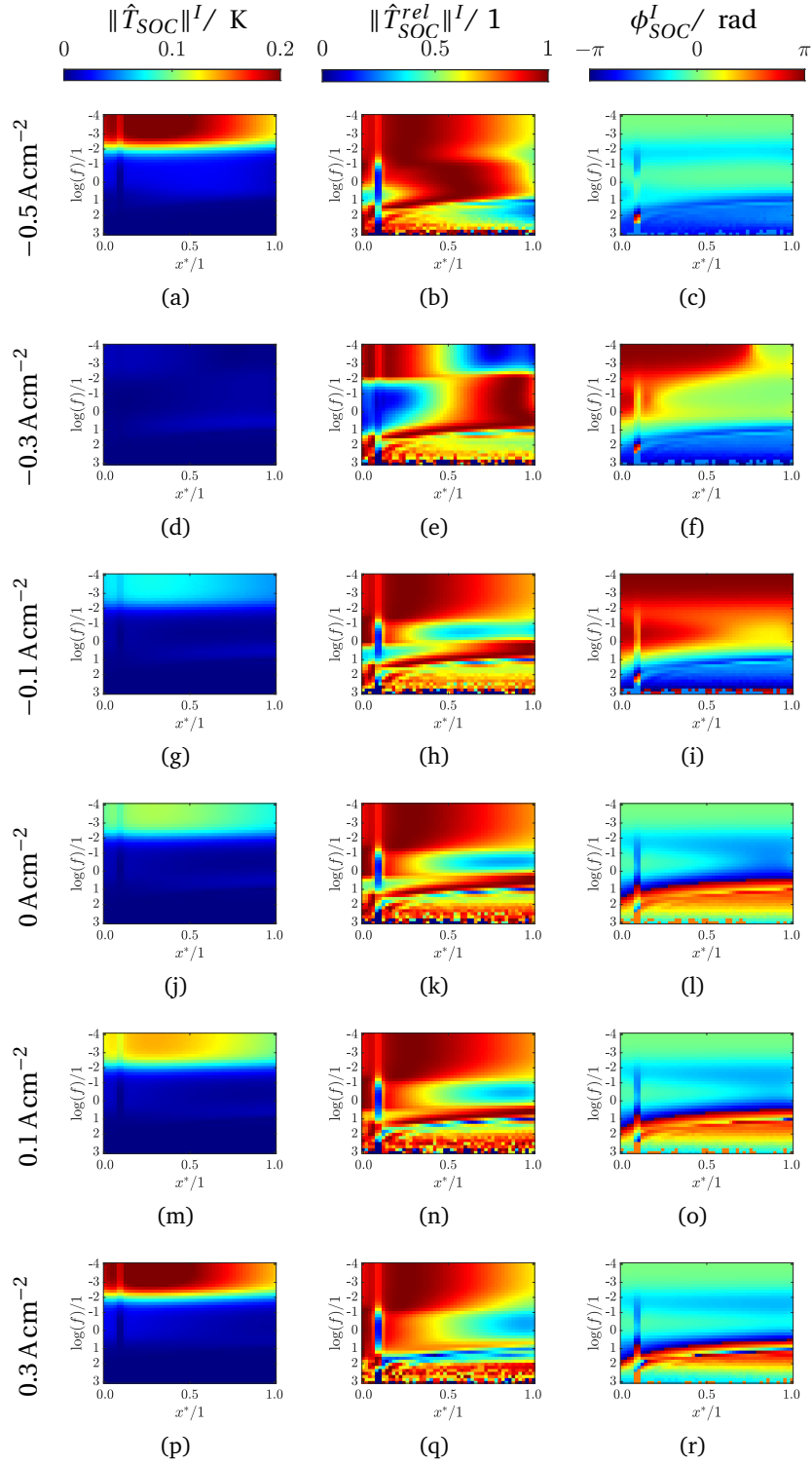


Figure D.1 – The thermal response of the SOC containing a defective area defined by a supplementary local resistance ASR_{def} at $x^* = 0.1-0.12$. From left to right columns: $\|\hat{T}_{SOC}\|^I$, $\|\hat{T}_{SOC}^{rel}\|^I$, and ϕ_{SOC}^I . Each line corresponds to a different applied current density.

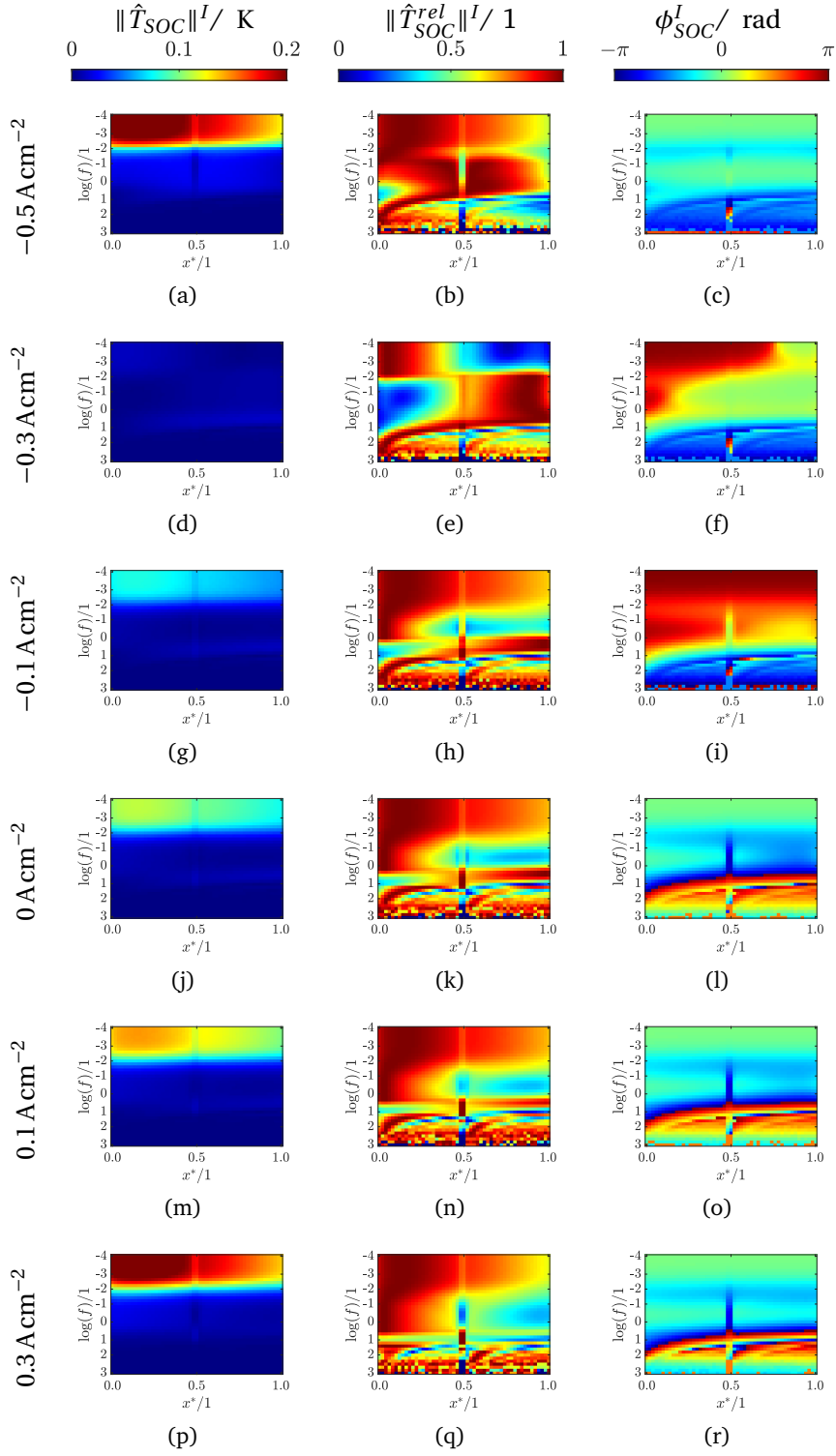


Figure D.2 – The thermal response of the SOC containing a defective area defined by a supplementary local resistance ASR_{def} at $x^* = 0.5-0.52$. From left to right columns: $\|\hat{T}_{SOC}\|^I$, $\|\hat{T}_{SOC}^{rel}\|^I$, and ϕ_{SOC}^I . Each line corresponds to a different applied current density.

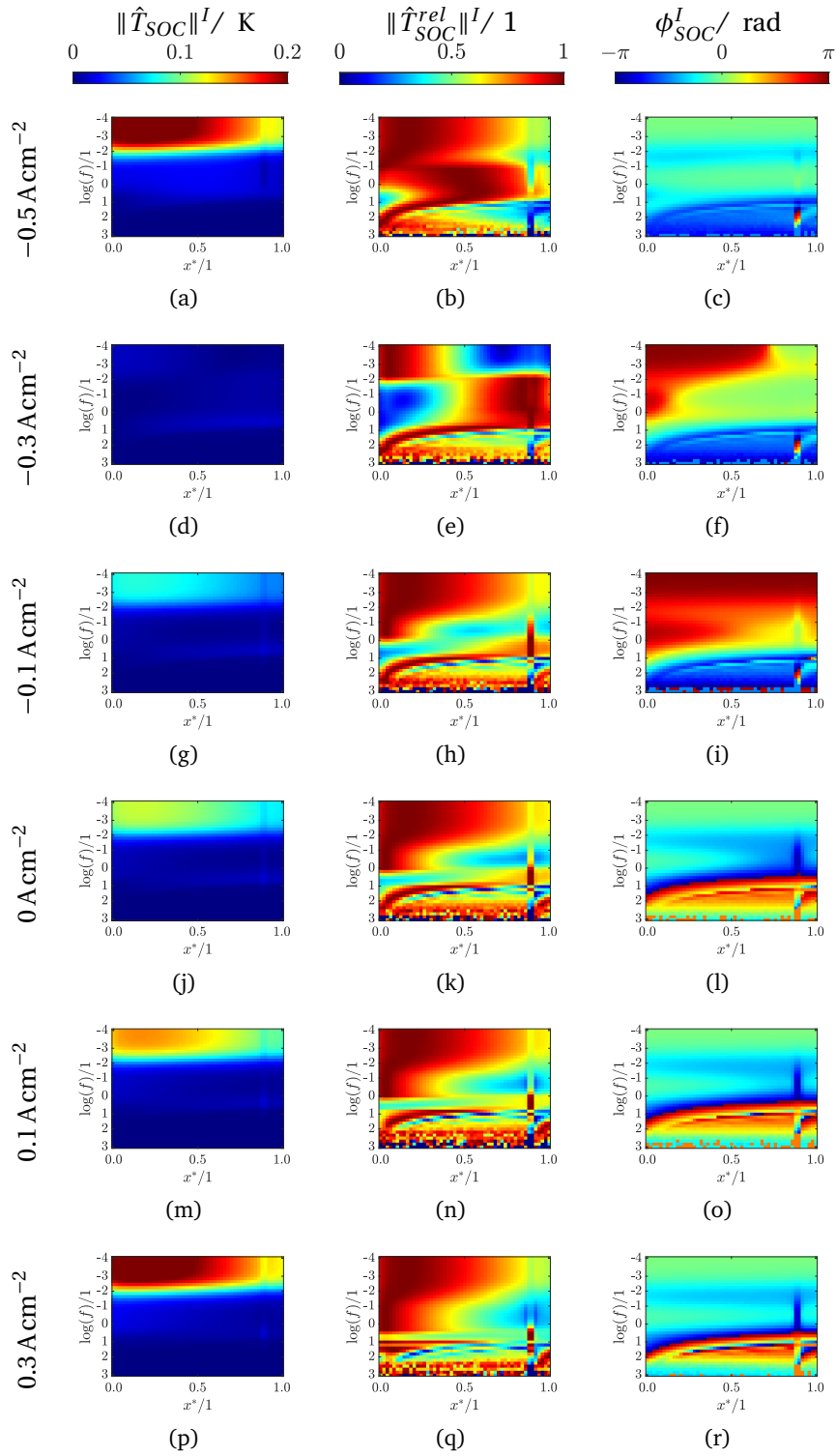


Figure D.3 – The thermal response of the SOC containing a defective area defined by a supplementary local resistance ASR_{def} at $x^* = 0.9-0.92$. From left to right column: $\|\hat{T}_{SOC}\|^I$, $\|\hat{T}_{SOC}^{rel}\|^I$, and ϕ_{SOC}^I . Each line corresponds to a different applied current density.

CHAPTER E

LT data analysis results

Appendix E. LT data analysis results

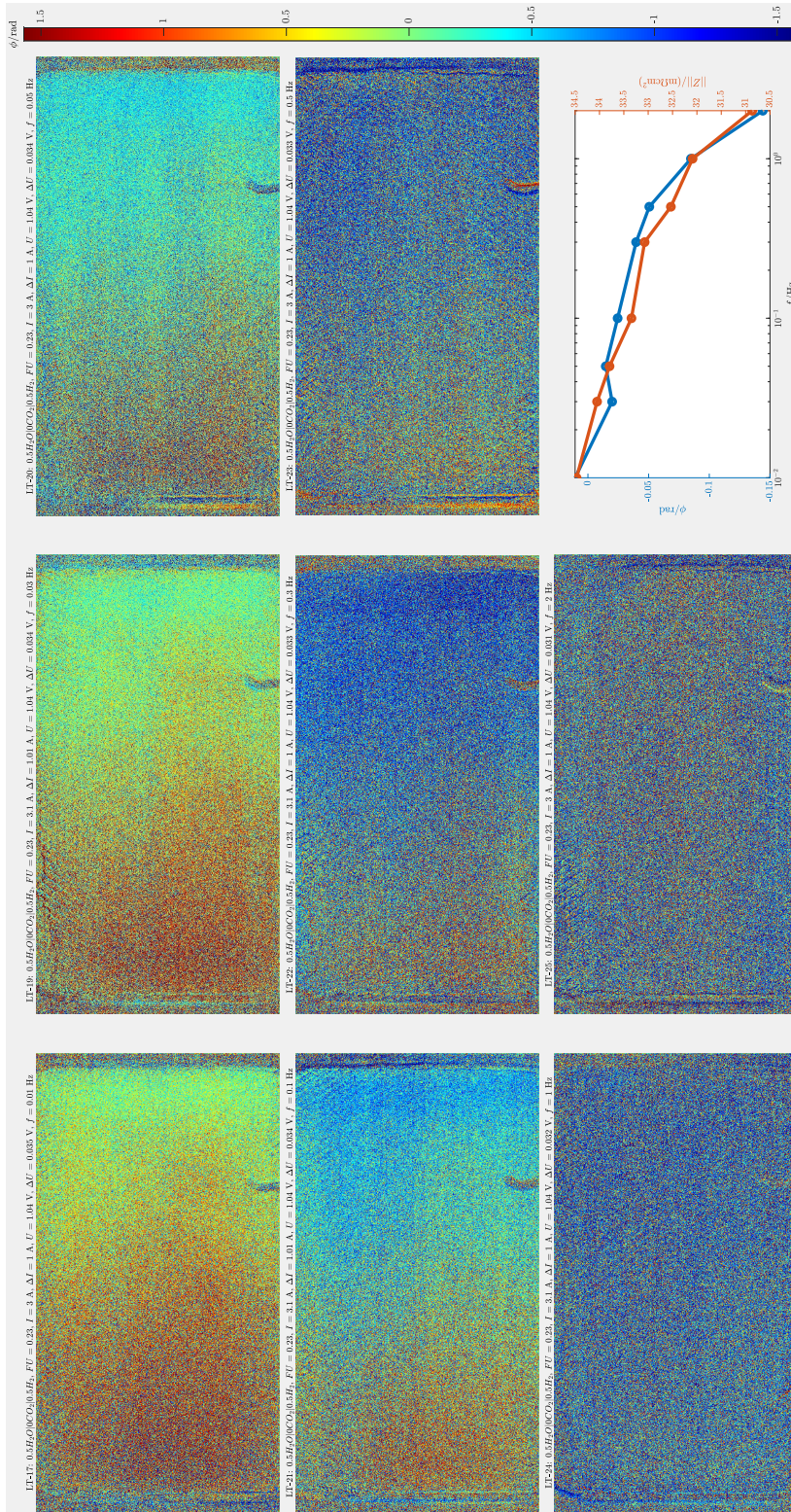


Figure E.1 – The ϕ_{SOC}^I for eight frequencies as well as Z and ϕ in an Bode plot.

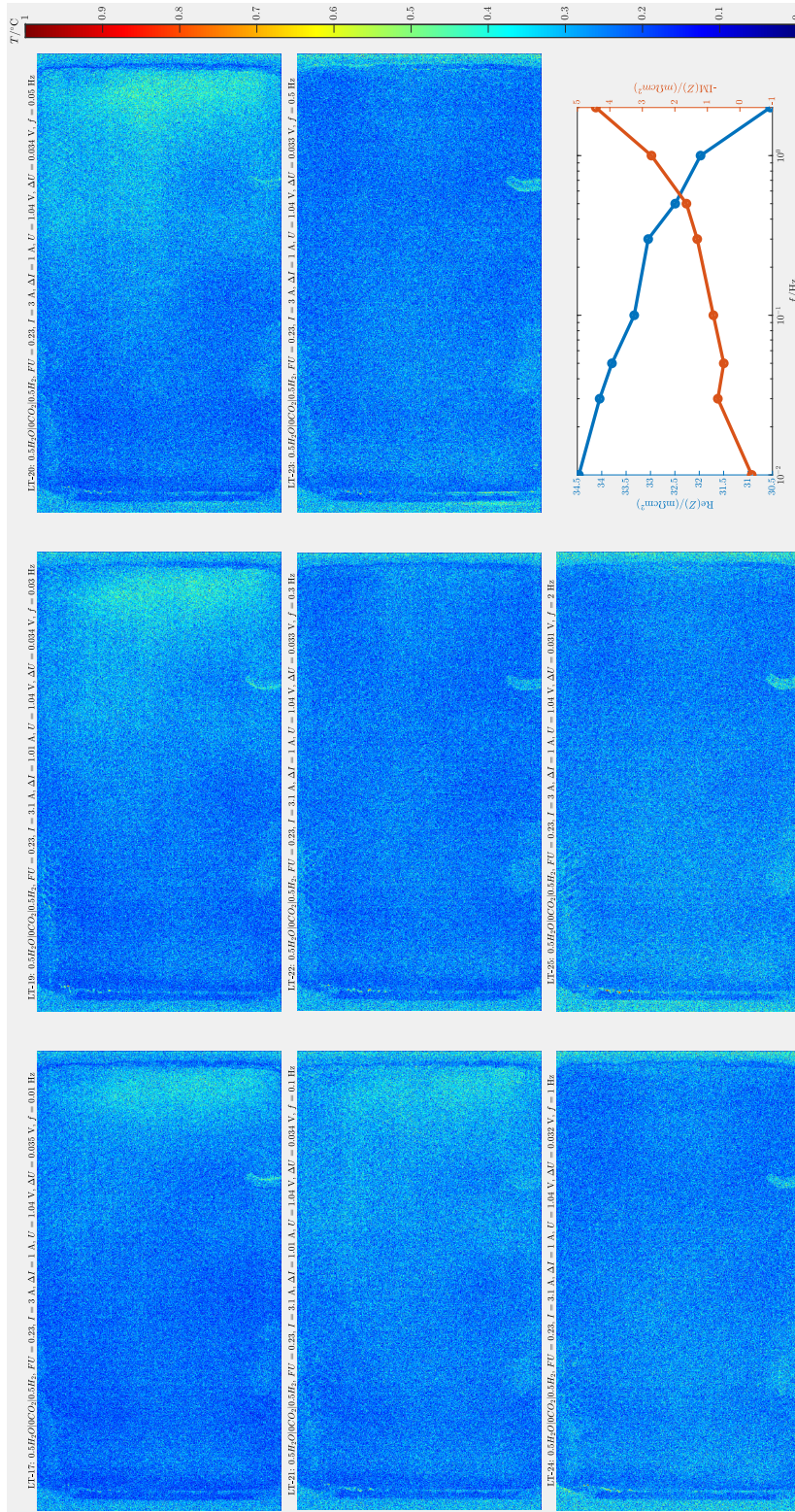


Figure E.2 – The $\|\hat{T}_{\text{SOC}}\|^I$ for eight frequencies as well as Z' and Z'' in an Bode plot.

Bibliography

- [1] Portia Murray. The Role of Power-to-X Technologies in Decentralised Multi-Energy Systems. Doctoral Thesis, ETH Zurich, 2020. URL <https://www.research-collection.ethz.ch/handle/20.500.11850/403923>. Accepted: 2020-03-09T10:43:39Z.
- [2] Roberto Montanini, Antonino Quattrocchi, Sebastiano A. Piccolo, Alessandra Amato, Stefano Trocino, Sabrina C. Zignani, Massimiliano Lo Faro, and Gaetano Squadrito. Real-time thermal imaging of solid oxide fuel cell cathode activity in working condition. Applied Optics, 55(25):7142–7148, 2016.
- [3] L. Rasha, J. I. S. Cho, T. P. Neville, A. Corredera, P. R. Shearing, and D. J. L. Brett. Water distribution mapping in polymer electrolyte fuel cells using lock-in thermography. Journal of Power Sources, 440:227160, November 2019. ISSN 0378-7753. doi: 10.1016/j.jpowsour.2019.227160. URL <http://www.sciencedirect.com/science/article/pii/S037877531931153X>.
- [4] John Howell and Pinar Menüç. Radiation Configuration Factors C-15.html. URL <http://www.thermalradiation.net/sectionc/C-15.html>.
- [5] Allied Vision. Manta Data Sheet G-223_nir V3.7.0.
- [6] J. Schefold, A. Brisse, and M. Zahid. Electronic Conduction of Yttria-Stabilized Zirconia Electrolyte in Solid Oxide Cells Operated in High Temperature Water Electrolysis. J. Electrochem. Soc., 156(8):B897–B904, January 2009. ISSN 0013-4651, 1945-7111. doi: 10.1149/1.3138701. URL <http://jes.ecsdl.org/content/156/8/B897>.
- [7] L. Grond, H. Vlap, and J. Knijp. Integration of Power-to-Gas and biogas supply chain. DNV GL Report No. GCS, 15:R24614, 2015.
- [8] George V. Last and Mary T. Schmick. Identification and Selection of Major Carbon Dioxide Stream Compositions. Technical Report PNNL-20493, 1019211, June 2011. URL <http://www.osti.gov/servlets/purl/1019211-QRxIjN/>.

Bibliography

- [9] Régis Farret, Laurent André, Etienne Brosse, Paul Broutin, Fabrice Chopin, Phillipe Gombert, Simon Jallais, and Samuel Saysset. Substances Annexes au CO₂ pour un Stockage Souterrain (SACSS) – Rapport du groupe de travail du Club CO₂. Technical Report INERIS-DRS-12-127545-07346A., INERIS, 2012.
- [10] Richard T. J. Porter, Michael Fairweather, Mohamed Pourkashanian, and Robert M. Woolley. The range and level of impurities in CO₂ streams from different carbon capture sources. *International Journal of Greenhouse Gas Control*, 36:161–174, May 2015. ISSN 1750-5836. doi: 10.1016/j.ijggc.2015.02.016. URL <http://www.sciencedirect.com/science/article/pii/S1750583615000705>.
- [11] Joo-Youp Lee, Tim C Keener, and Y Jeffery Yang. Impacts of Flue Gas Impurities in Sequestered CO₂ on Groundwater Sources: A Process Analysis and Implications for Risk Management. page 16, 2008.
- [12] P. Caliandro, A. Nakajo, S. Diethelm, and J. Van herle. Model-assisted identification of solid oxide cell elementary processes by electrochemical impedance spectroscopy measurements. *Journal of Power Sources*, 436:226838, October 2019. ISSN 0378-7753. doi: 10.1016/j.jpowsour.2019.226838. URL <http://www.sciencedirect.com/science/article/pii/S0378775319308316>.
- [13] Guillaume Jeanmonod, Ligang Wang, Stefan Diethelm, François Maréchal, and Jan Van herle. Trade-off designs of power-to-methane systems via solid-oxide electrolyzer and the application to biogas upgrading. *Applied Energy*, 247:572–581, August 2019. ISSN 0306-2619. doi: 10.1016/j.apenergy.2019.04.055. URL <http://www.sciencedirect.com/science/article/pii/S0306261919307020>.
- [14] Svante Arrhenius. On the Influence of Carbonic Acid in the Air upon the Temperature of the Ground. page 22, 1896.
- [15] Thomas R. Anderson, Ed Hawkins, and Philip D. Jones. CO₂, the greenhouse effect and global warming: from the pioneering work of Arrhenius and Callendar to today's Earth System Models. *Endeavour*, 40(3):178–187, September 2016. ISSN 0160-9327. doi: 10.1016/j.endeavour.2016.07.002. URL <http://www.sciencedirect.com/science/article/pii/S0160932716300308>.
- [16] Jack C. Pales and Charles D. Keeling. The concentration of atmospheric carbon dioxide in Hawaii. *Journal of Geophysical Research* (1896-1977), 70(24):6053–6076, 1965. ISSN 2156-2202. doi: 10.1029/JZ070i024p06053. URL <https://agupubs.onlinelibrary.wiley.com/doi/abs/10.1029/JZ070i024p06053>. eprint: <https://agupubs.onlinelibrary.wiley.com/doi/pdf/10.1029/JZ070i024p06053>.
- [17] Charles D Keeling. Is Carbon Dioxide from Fossil Fuel Changing Man's Environment? page 9, 2020.

- [18] J. S. Sawyer. Man-made Carbon Dioxide and the “Greenhouse” Effect. *Nature*, 239 (5366):23–26, September 1972. ISSN 1476-4687. doi: 10.1038/239023a0. URL <https://www.nature.com/articles/239023a0>. Number: 5366 Publisher: Nature Publishing Group.
- [19] J. Hansen, D. Johnson, A. Lacis, S. Lebedeff, P. Lee, D. Rind, and G. Russell. Climate Impact of Increasing Atmospheric Carbon Dioxide. *Science*, 213(4511):957–966, August 1981. ISSN 0036-8075, 1095-9203. doi: 10.1126/science.213.4511.957. URL <https://science.sciencemag.org/content/213/4511/957>. Publisher: American Association for the Advancement of Science Section: Articles.
- [20] The origins of the IPCC: How the world woke up to climate change, March 2018. URL <https://council.science/current/blog/the-origins-of-the-ipcc-how-the-world-woke-up-to-climate-change/>. Section: Blog.
- [21] UNITED NATIONS FRAMEWORK CONVENTION ON CLIMATE CHANGE. page 33.
- [22] Joeri Rogelj, Michel den Elzen, Niklas Höhne, Taryn Fransen, Hanna Fekete, Harald Winkler, Roberto Schaeffer, Fu Sha, Keywan Riahi, and Malte Meinshausen. Paris Agreement climate proposals need a boost to keep warming well below 2 °C. *Nature*, 534(7609):631–639, June 2016. ISSN 1476-4687. doi: 10.1038/nature18307. URL <https://www.nature.com/articles/nature18307>. Number: 7609 Publisher: Nature Publishing Group.
- [23] Samuel Randalls. History of the 2°C climate target. *WIREs Climate Change*, 1(4):598–605, 2010. ISSN 1757-7799. doi: 10.1002/wcc.62. URL <https://onlinelibrary.wiley.com/doi/abs/10.1002/wcc.62>. _eprint: <https://onlinelibrary.wiley.com/doi/pdf/10.1002/wcc.62>.
- [24] United Nations Environment Programme. *The emissions gap report 2019*. 2019. ISBN 978-92-807-3766-0. OCLC: 1129598239.
- [25] United Nations Environment Programme. *Lessons from a decade of emissions gap assessments*. 2019. URL <https://www.unenvironment.org/resources/emissions-gap-report-10-year-summary>.
- [26] Paul Denholm and Maureen Hand. Grid flexibility and storage required to achieve very high penetration of variable renewable electricity. *Energy Policy*, 39(3): 1817–1830, March 2011. ISSN 0301-4215. doi: 10.1016/j.enpol.2011.01.019. URL <http://www.sciencedirect.com/science/article/pii/S0301421511000292>.
- [27] Leonardo K. K. Maia and Edwin Zondervan. Optimization of energy storage and system flexibility in the context of the energy transition: Germany’s power grid as a case study. *BMC Energy*, 1(1):9, December 2019. ISSN 2524-4469. doi: 10.1186/s42500-019-0009-2. URL <https://doi.org/10.1186/s42500-019-0009-2>.

Bibliography

- [28] William Zappa, Martin Junginger, and Machteld van den Broek. Is a 100% renewable European power system feasible by 2050? *Applied Energy*, 233-234:1027–1050, January 2019. ISSN 0306-2619. doi: 10.1016/j.apenergy.2018.08.109. URL <http://www.sciencedirect.com/science/article/pii/S0306261918312790>.
- [29] Madeleine McPherson and Samiha Tahseen. Deploying storage assets to facilitate variable renewable energy integration: The impacts of grid flexibility, renewable penetration, and market structure. *Energy*, 145:856–870, February 2018. ISSN 0360-5442. doi: 10.1016/j.energy.2018.01.002. URL <http://www.sciencedirect.com/science/article/pii/S0360544218300021>.
- [30] Mohammed Yekini Suberu, Mohd Wazir Mustafa, and Nouruddeen Bashir. Energy storage systems for renewable energy power sector integration and mitigation of intermittency. *Renewable and Sustainable Energy Reviews*, 35:499–514, July 2014. ISSN 1364-0321. doi: 10.1016/j.rser.2014.04.009. URL <http://www.sciencedirect.com/science/article/pii/S1364032114002366>.
- [31] Francisco Díaz-González, Andreas Sumper, Oriol Gomis-Bellmunt, and Roberto Villafáfila-Robles. A review of energy storage technologies for wind power applications. *Renewable and Sustainable Energy Reviews*, 16(4):2154–2171, May 2012. ISSN 1364-0321. doi: 10.1016/j.rser.2012.01.029. URL <http://www.sciencedirect.com/science/article/pii/S1364032112000305>.
- [32] Omid Palizban and Kimmo Kauhaniemi. Energy storage systems in modern grids—Matrix of technologies and applications. *Journal of Energy Storage*, 6: 248–259, May 2016. ISSN 2352-152X. doi: 10.1016/j.est.2016.02.001. URL <http://www.sciencedirect.com/science/article/pii/S2352152X1630010X>.
- [33] Mathew Aneke and Meihong Wang. Energy storage technologies and real life applications – A state of the art review. *Applied Energy*, 179:350–377, October 2016. ISSN 0306-2619. doi: 10.1016/j.apenergy.2016.06.097. URL <http://www.sciencedirect.com/science/article/pii/S0306261916308728>.
- [34] M. Waidhas. Business opportunities for MW electrolysis and related requirements, 2017.
- [35] Chi-Jen Yang. Chapter 2 - Pumped Hydroelectric Storage. In Trevor M. Letcher, editor, *Storing Energy*, pages 25–38. Elsevier, Oxford, January 2016. ISBN 978-0-12-803440-8. doi: 10.1016/B978-0-12-803440-8.00002-6. URL <http://www.sciencedirect.com/science/article/pii/B9780128034408000026>.
- [36] Xing Luo, Jihong Wang, Mark Dooner, and Jonathan Clarke. Overview of current development in electrical energy storage technologies and the application potential in power system operation. *Applied Energy*, 137:511–536, January 2015. ISSN 0306-2619. doi: 10.1016/j.apenergy.2014.09.081. URL <http://www.sciencedirect.com/science/article/pii/S0306261914010290>.

- [37] Herib Blanco and André Faaij. A review at the role of storage in energy systems with a focus on Power to Gas and long-term storage. Renewable and Sustainable Energy Reviews, 81:1049–1086, January 2018. ISSN 1364-0321. doi: 10.1016/j.rser.2017.07.062. URL <http://www.sciencedirect.com/science/article/pii/S1364032117311310>.
- [38] Lothar Mennicken, Alexander Janz, and Stefanie Roth. The German R&D Program for CO₂ Utilization—Innovations for a Green Economy. Environ Sci Pollut Res, 23(11):11386–11392, June 2016. ISSN 1614-7499. doi: 10.1007/s11356-016-6641-1. URL <https://doi.org/10.1007/s11356-016-6641-1>.
- [39] Sheila Samsatli and Nouri J. Samsatli. The role of renewable hydrogen and inter-seasonal storage in decarbonising heat – Comprehensive optimisation of future renewable energy value chains. Applied Energy, 233-234:854–893, January 2019. ISSN 0306-2619. doi: 10.1016/j.apenergy.2018.09.159. URL <http://www.sciencedirect.com/science/article/pii/S0306261918314715>.
- [40] Sebastian Schiebahn, Thomas Grube, Martin Robinius, Vanessa Tietze, Bhunesh Kumar, and Detlef Stolten. Power to gas: Technological overview, systems analysis and economic assessment for a case study in Germany. International Journal of Hydrogen Energy, 40(12):4285–4294, April 2015. ISSN 0360-3199. doi: 10.1016/j.ijhydene.2015.01.123. URL <http://www.sciencedirect.com/science/article/pii/S0360319915001913>.
- [41] Jakob Zinck Thellufsen and Henrik Lund. Cross-border versus cross-sector inter-connectivity in renewable energy systems. Energy, 124:492–501, April 2017. ISSN 0360-5442. doi: 10.1016/j.energy.2017.02.112. URL <http://www.sciencedirect.com/science/article/pii/S0360544217302943>.
- [42] Karim Ghaib and Fatima-Zahrae Ben-Fares. Power-to-Methane: A state-of-the-art review. Renewable and Sustainable Energy Reviews, 81:433–446, January 2018. ISSN 1364-0321. doi: 10.1016/j.rser.2017.08.004. URL <http://www.sciencedirect.com/science/article/pii/S1364032117311346>.
- [43] Tanay Sıdkı Uyar and Doğançan Beşikci. Integration of hydrogen energy systems into renewable energy systems for better design of 100% renewable energy communities. International Journal of Hydrogen Energy, 42(4):2453–2456, January 2017. ISSN 0360-3199. doi: 10.1016/j.ijhydene.2016.09.086. URL <http://www.sciencedirect.com/science/article/pii/S0360319916315063>.
- [44] Pascal De Buck. Energy transition in Europe: the case for gas and gas infrastructure, 2018.
- [45] Raluca Suciuc, Luc Girardin, and François Maréchal. Energy integration of CO₂ networks and power to gas for emerging energy autonomous cities in Europe. Energy,

Bibliography

- 157:830–842, August 2018. ISSN 0360-5442. doi: 10.1016/j.energy.2018.05.083. URL <http://www.sciencedirect.com/science/article/pii/S0360544218309034>.
- [46] Hella Engerer and Manfred Horn. Natural gas vehicles: An option for Europe. *Energy Policy*, 38(2):1017–1029, February 2010. ISSN 0301-4215. doi: 10.1016/j.enpol.2009.10.054. URL <http://www.sciencedirect.com/science/article/pii/S0301421509008131>.
- [47] Gerda Reiter and Johannes Lindorfer. Evaluating CO₂ sources for power-to-gas applications – A case study for Austria. *Journal of CO₂ Utilization*, 10:40–49, June 2015. ISSN 2212-9820. doi: 10.1016/j.jcou.2015.03.003. URL <http://www.sciencedirect.com/science/article/pii/S2212982015000244>.
- [48] Jay Cheng. *Biomass to renewable energy processes*. CRC press, 2017. ISBN 1-4987-7881-X.
- [49] Wolfgang Köppel, Manuel Götz, and Frank Graf. Quality aspects, technological and ecological consideration. page 11, 2009.
- [50] Truc T. Q. Vo, David M. Wall, Denis Ring, Karthik Rajendran, and Jerry D. Murphy. Techno-economic analysis of biogas upgrading via amine scrubber, carbon capture and ex-situ methanation. *Applied Energy*, 212:1191–1202, February 2018. ISSN 0306-2619. doi: 10.1016/j.apenergy.2017.12.099. URL <http://www.sciencedirect.com/science/article/pii/S0306261917318226>.
- [51] Julia Witte, Adelaide Calbry-Muzyka, Tanja Wieseler, Peter Hottinger, Serge M. A. Biollaz, and Tilman J. Schildhauer. Demonstrating direct methanation of real biogas in a fluidised bed reactor. *Applied Energy*, 240:359–371, April 2019. ISSN 0306-2619. doi: 10.1016/j.apenergy.2019.01.230. URL <http://www.sciencedirect.com/science/article/pii/S0306261919302594>.
- [52] Ligang Wang, Mar Pérez-Fortes, Hossein Madi, Stefan Diethelm, Jan Van herle, and François Maréchal. Optimal design of solid-oxide electrolyzer based power-to-methane systems: A comprehensive comparison between steam electrolysis and co-electrolysis. *Applied Energy*, 211:1060–1079, February 2018. ISSN 0306-2619. doi: 10.1016/j.apenergy.2017.11.050. URL <http://www.sciencedirect.com/science/article/pii/S0306261917316367>.
- [53] Domenico Ferrero, Andrea Lanzini, Massimo Santarelli, and Pierluigi Leone. A comparative assessment on hydrogen production from low- and high-temperature electrolysis. *International Journal of Hydrogen Energy*, 38(9):3523–3536, March 2013. ISSN 0360-3199. doi: 10.1016/j.ijhydene.2013.01.065. URL <http://www.sciencedirect.com/science/article/pii/S0360319913001511>.
- [54] Gurpreet Kaur, Aniruddha P. Kulkarni, Sarbjit Giddey, and Sukhvinder P. S. Badwal. Ceramic composite cathodes for CO₂ conversion to CO in solid oxide electrolysis

- cells. *Applied Energy*, 221:131–138, July 2018. ISSN 0306-2619. doi: 10.1016/j.apenergy.2018.03.176. URL <http://www.sciencedirect.com/science/article/pii/S0306261918305269>.
- [55] Christopher Graves, Sune D. Ebbesen, and Mogens Mogensen. Co-electrolysis of CO₂ and H₂O in solid oxide cells: performance and durability. *Solid State Ionics*, 192(1):398–403, 2011.
- [56] Ligang Wang, Johannes Düll, François Maréchal, and Jan Van herle. Trade-off designs and comparative exergy evaluation of solid-oxide electrolyzer based power-to-methane plants. *International Journal of Hydrogen Energy*, December 2018. ISSN 0360-3199. doi: 10.1016/j.ijhydene.2018.11.151. URL <http://www.sciencedirect.com/science/article/pii/S0360319918337832>.
- [57] Philippe Mocoteguy and Annabelle Brisse. A review and comprehensive analysis of degradation mechanisms of solid oxide electrolysis cells. *International Journal of Hydrogen Energy*, 38(36):15887–15902, December 2013. ISSN 0360-3199. doi: 10.1016/j.ijhydene.2013.09.045. URL <http://www.sciencedirect.com/science/article/pii/S0360319913022684>.
- [58] Yun Zheng, Jianchen Wang, Bo Yu, Wenqiang Zhang, Jing Chen, Jinli Qiao, and Jiujun Zhang. A review of high temperature co-electrolysis of H₂O and CO₂ to produce sustainable fuels using solid oxide electrolysis cells (SOECs): advanced materials and technology. *Chemical Society Reviews*, 46(5):1427–1463, 2017. doi: 10.1039/C6CS00403B. URL <https://pubs.rsc.org/en/content/articlelanding/2017/cs/c6cs00403b>. Publisher: Royal Society of Chemistry.
- [59] Michael C. Tucker. Progress in metal-supported solid oxide electrolysis cells: A review. *International Journal of Hydrogen Energy*, 45(46):24203–24218, September 2020. ISSN 0360-3199. doi: 10.1016/j.ijhydene.2020.06.300. URL <http://www.sciencedirect.com/science/article/pii/S0360319920325106>.
- [60] Siti Munira Jamil, Mohd Hafiz Dzarfan Othman, Mukhlis A. Rahman, Juhana Jaafar, A. F. Ismail, and K. Li. Recent fabrication techniques for micro-tubular solid oxide fuel cell support: A review. *Journal of the European Ceramic Society*, 35(1): 1–22, January 2015. ISSN 0955-2219. doi: 10.1016/j.jeurceramsoc.2014.08.034. URL <http://www.sciencedirect.com/science/article/pii/S0955221914004634>.
- [61] Kevin Huang and John B. Goodenough. Solid Oxide Fuel Cell Technology | ScienceDirect, 2009. URL <https://www.sciencedirect.com/book/9781845696283/solid-oxide-fuel-cell-technology>.
- [62] S.B. Beale. Numerical models for planar solid oxide fuel cells. In B. Sundén and M. Faghri, editors, *WIT Transactions on State of the Art in Science and Engineering*, volume 1, pages 43–82. WIT Press, 1 edition, October 2005. ISBN

Bibliography

- 978-1-85312-840-0. doi: 10.2495/1-85312-840-6/02. URL <http://library.witpress.com/viewpaper.asp?pcode=1853128406-002-1>. ISSN: 1755-8336.
- [63] Marta Boaro and Antonino Salvatore Aricò, editors. Advances in Medium and High Temperature Solid Oxide Fuel Cell Technology. CISM International Centre for Mechanical Sciences. Springer International Publishing, 2017. ISBN 978-3-319-46145-8. doi: 10.1007/978-3-319-46146-5. URL <https://www.springer.com/gp/book/9783319461458>.
- [64] Marie Petitjean, Magali Reytier, André Chatroux, Lionel Bruguière, Aurore Mansuy, Hervé Sassoulas, Stéphane Di Iorio, Bertrand Morel, and Julie Mougín. Performance and Durability of High Temperature Steam Electrolysis: From the Single Cell to Short-Stack Scale. *ECS Trans.*, 35(1):2905–2913, December 2011. ISSN 1938-6737. doi: 10.1149/1.3570290. URL <https://iopscience.iop.org/article/10.1149/1.3570290>.
- [65] J. Schefold, A. Brisse, and F. Tietz. Nine thousand hours of operation of a solid oxide cell in steam electrolysis mode. *Journal of The Electrochemical Society*, 159(2):A137–A144, 2011.
- [66] Josef Schefold, Annabelle Brisse, and Hendrik Poepke. Long-term Steam Electrolysis with Electrolyte-Supported Solid Oxide Cells. *Electrochimica Acta*, 179: 161–168, 2015.
- [67] Josef Schefold, Annabelle Brisse, and Hendrik Poepke. 23,000 h steam electrolysis with an electrolyte supported solid oxide cell. *International Journal of Hydrogen Energy*, 42(19):13415–13426, May 2017. ISSN 0360-3199. doi: 10.1016/j.ijhydene.2017.01.072. URL <http://www.sciencedirect.com/science/article/pii/S0360319917302392>.
- [68] Josef Schefold, Hendrik Poepke, and Annabelle Brisse. Solid Oxide Electrolyser Cell Testing Up to the Above 30,000 h Time Range. *ECS Trans.*, 97(7):553, June 2020. ISSN 1938-5862. doi: 10.1149/09707.0553ecst. URL <https://iopscience.iop.org/article/10.1149/09707.0553ecst/meta>. Publisher: IOP Publishing.
- [69] M. Hubert, J. Laurencin, P. Cloetens, B. Morel, D. Montinaro, and F. Lefebvre-Joud. Impact of Nickel agglomeration on Solid Oxide Cell operated in fuel cell and electrolysis modes. *Journal of Power Sources*, 397:240–251, September 2018. ISSN 0378-7753. doi: 10.1016/j.jpowsour.2018.06.097. URL <http://www.sciencedirect.com/science/article/pii/S0378775318307018>.
- [70] Xiufu Sun, Ming Chen, Yi-Lin Liu, Per Hjalmarsson, Sune Dalgaard Ebbesen, Søren Højgaard Jensen, Mogens Bjerg Mogensen, and Peter Vang Hendriksen. Durability of solid oxide electrolysis cells for syngas production. *Journal of The Electrochemical Society*, 160(9):F1074–F1080, 2013.

- [71] Van Nhu Nguyen, Qingping Fang, Ute Packbier, and Ludger Blum. Long-term tests of a Jülich planar short stack with reversible solid oxide cells in both fuel cell and electrolysis modes. International Journal of Hydrogen Energy, 38(11): 4281–4290, 2013.
- [72] Sune Dalgaard Ebbesen, Xiufu Sun, and Mogens Bjerg Mogensen. Understanding the processes governing performance and durability of solid oxide electrolysis cells. Faraday discussions, 182:393–422, 2015.
- [73] Sune D. Ebbesen, Christopher Graves, Anne Hauch, Søren H. Jensen, and Mogens Mogensen. Poisoning of solid oxide electrolysis cells by impurities. Journal of The Electrochemical Society, 157(10):B1419–B1429, 2010.
- [74] Per Hjalmarsson, Xiufu Sun, Yi-Lin Liu, and Ming Chen. Durability of high performance Ni–yttria stabilized zirconia supported solid oxide electrolysis cells at high current density. Journal of Power Sources, 262:316–322, 2014.
- [75] Kongfa Chen, Shu-Sheng Liu, Na Ai, Michihisa Koyama, and San Ping Jiang. Why solid oxide cells can be reversibly operated in solid oxide electrolysis cell and fuel cell modes? Physical Chemistry Chemical Physics, 17(46):31308–31315, 2015. doi: 10.1039/C5CP05065K. URL <https://pubs.rsc.org/en/content/articlelanding/2015/cp/c5cp05065k>. Publisher: Royal Society of Chemistry.
- [76] Christopher Graves, Sune Dalgaard Ebbesen, Søren Højgaard Jensen, Søren Bredmose Simonsen, and Mogens Bjerg Mogensen. Eliminating degradation in solid oxide electrochemical cells by reversible operation. Nature materials, 14(2): 239–244, 2015.
- [77] Zacharie Wuillemin, Yannik Antonetti, Cédric Beetschen, Olivier Millioud, Sergio Ceschini, and Hossein Madi. Local activation and degradation of electrochemical processes in a SOFC. ECS Transactions, 57(1):561–570, 2013.
- [78] M. Trini, P. S. Jørgensen, A. Hauch, J. J. Bentzen, P. V. Hendriksen, and M. Chen. 3D Microstructural Characterization of Ni/YSZ Electrodes Exposed to 1 Year of Electrolysis Testing. J. Electrochem. Soc., 166(2):F158–F167, January 2019. ISSN 0013-4651, 1945-7111. doi: 10.1149/2.1281902jes. URL <http://jes.ecsdl.org/content/166/2/F158>.
- [79] Yifeng Zheng, Qingshan Li, Tao Chen, Wei Wu, Cheng Xu, and Wei Guo Wang. Comparison of performance and degradation of large-scale solid oxide electrolysis cells in stack with different composite air electrodes. International Journal of Hydrogen Energy, 40(6):2460–2472, February 2015. ISSN 0360-3199. doi: 10.1016/j.ijhydene.2014.12.101. URL <http://www.sciencedirect.com/science/article/pii/S0360319914034983>.

Bibliography

- [80] Yi Wang, Wenyuan Li, Liang Ma, Wei Li, and Xingbo Liu. Degradation of solid oxide electrolysis cells: Phenomena, mechanisms, and emerging mitigation strategies—A review. *Journal of Materials Science & Technology*, 55:35–55, October 2020. ISSN 1005-0302. doi: 10.1016/j.jmst.2019.07.026. URL <http://www.sciencedirect.com/science/article/pii/S1005030219302464>.
- [81] Anne Hauch, Sune Dalgaard Ebbesen, Søren Højgaard Jensen, and Mogens Mogensen. Highly efficient high temperature electrolysis. *J. Mater. Chem.*, 18(20):2331–2340, May 2008. ISSN 1364-5501. doi: 10.1039/B718822F. URL <https://pubs.rsc.org/en/content/articlelanding/2008/jm/b718822f>. Publisher: The Royal Society of Chemistry.
- [82] G. Rinaldi, A. Nakajo, P. Burdet, M. Cantoni, W. K. S. Chiu, and J. Van herle. Characterization of Local Morphology and Availability of Triple-Phase Boundaries in Solid Oxide Cell Electrodes. *Acta Materialia*, July 2019. ISSN 1359-6454. doi: 10.1016/j.actamat.2019.07.027. URL <http://www.sciencedirect.com/science/article/pii/S1359645419304677>.
- [83] M. Chen, J. V. T. Høgh, J. U. Nielsen, J. J. Bentzen, S. D. Ebbesen, and P. V. Hendriksen. High Temperature Co-Electrolysis of Steam and CO₂ in an SOC Stack: Performance and Durability. *Fuel Cells*, 13(4):638–645, 2013. ISSN 1615-6854. doi: 10.1002/fuce.201200169. URL <https://onlinelibrary.wiley.com/doi/abs/10.1002/fuce.201200169>. _eprint: <https://onlinelibrary.wiley.com/doi/pdf/10.1002/fuce.201200169>.
- [84] D. The, S. Grieshammer, M. Schroeder, M. Martin, M. Al Daroukh, F. Tietz, J. Schefold, and A. Brisse. Microstructural comparison of solid oxide electrolyser cells operated for 6100 h and 9000 h. *Journal of Power Sources*, 275:901–911, February 2015. ISSN 0378-7753. doi: 10.1016/j.jpowsour.2014.10.188. URL <http://www.sciencedirect.com/science/article/pii/S0378775314018072>.
- [85] Youkun Tao, Sune Dalgaard Ebbesen, and Mogens Bjerg Mogensen. Degradation of solid oxide cells during co-electrolysis of steam and carbon dioxide at high current densities. *Journal of Power Sources*, 328:452–462, October 2016. ISSN 0378-7753. doi: 10.1016/j.jpowsour.2016.08.055. URL <http://www.sciencedirect.com/science/article/pii/S0378775316310552>.
- [86] Michael Keane, Hui Fan, Minfang Han, and Prabhakar Singh. Role of initial microstructure on nickel-YSZ cathode degradation in solid oxide electrolysis cells. *International Journal of Hydrogen Energy*, 39(33):18718–18726, November 2014. ISSN 0360-3199. doi: 10.1016/j.ijhydene.2014.09.057. URL <http://www.sciencedirect.com/science/article/pii/S0360319914025786>.
- [87] F. Monaco, M. Hubert, J. Vulliet, J. P. Ouweltjes, D. Montinaro, P. Cloetens, P. Piccardo, F. Lefebvre-Joud, and J. Laurencin. Degradation of Ni-YSZ Electrodes

- in Solid Oxide Cells: Impact of Polarization and Initial Microstructure on the Ni Evolution. *J. Electrochem. Soc.*, 166(15):F1229–F1242, 2019. ISSN 0013-4651, 1945-7111. doi: 10.1149/2.1261915jes. URL <https://iopscience.iop.org/article/10.1149/2.1261915jes>.
- [88] G. Rinaldi, S. Diethelm, E. Oveisi, P. Burdet, J. Van Herle, D. Montinaro, Q. Fu, and A. Brisse. Post-test Analysis on a Solid Oxide Cell Stack Operated for 10,700 Hours in Steam Electrolysis Mode. *Fuel Cells*, 17(4):541–549, 2017. ISSN 1615-6854. doi: 10.1002/fuce.201600194. URL <https://onlinelibrary.wiley.com/doi/abs/10.1002/fuce.201600194>. _eprint: <https://onlinelibrary.wiley.com/doi/pdf/10.1002/fuce.201600194>.
- [89] M. B. Mogensen, A. Hauch, X. Sun, M. Chen, Y. Tao, S. D. Ebbesen, K. V. Hansen, and P. V. Hendriksen. Relation Between Ni Particle Shape Change and Ni Migration in Ni-YSZ Electrodes – a Hypothesis. *Fuel Cells*, 17(4):434–441, 2017. ISSN 1615-6854. doi: 10.1002/fuce.201600222. URL <https://onlinelibrary.wiley.com/doi/abs/10.1002/fuce.201600222>. _eprint: <https://onlinelibrary.wiley.com/doi/pdf/10.1002/fuce.201600222>.
- [90] Mogens Bjerg Mogensen, Ming Chen, Henrik Lund Frandsen, Christopher Graves, Anne Hauch, Torben Jacobsen, Søren Højgaard Jensen, Theis Løye Skaftø, and Xiufu Sun. Comprehensive Hypotheses for Degradation Mechanisms in Ni-Stabilized Zirconia Electrodes. *ECS Trans.*, 91(1):613–620, July 2019. ISSN 1938-6737, 1938-5862. doi: 10.1149/09101.0613ecst. URL <https://iopscience.iop.org/article/10.1149/09101.0613ecst>.
- [91] Giorgio Rinaldi, Arata Nakajo, Priscilla Caliandro, Lucie Navratilova, and Jan Van herle. Effects of Polarization on the Microstructural Changes at the YSZ/Ni-YSZ Interface. *ECS Trans.*, 91(1):641–652, July 2019. ISSN 1938-6737, 1938-5862. doi: 10.1149/09101.0641ecst. URL <https://iopscience.iop.org/article/10.1149/09101.0641ecst>.
- [92] M. Trini, A. Hauch, S. De Angelis, X. Tong, P. Vang Hendriksen, and M. Chen. Comparison of microstructural evolution of fuel electrodes in solid oxide fuel cells and electrolysis cells. *Journal of Power Sources*, 450:227599, February 2020. ISSN 0378-7753. doi: 10.1016/j.jpowsour.2019.227599. URL <http://www.sciencedirect.com/science/article/pii/S0378775319315927>.
- [93] Wenying Li, Yixiang Shi, Yu Luo, Yuqing Wang, and Ningsheng Cai. Carbon deposition on patterned nickel/yttria stabilized zirconia electrodes for solid oxide fuel cell/solid oxide electrolysis cell modes. *Journal of Power Sources*, 276:26–31, February 2015. ISSN 03787753. doi: 10.1016/j.jpowsour.2014.11.106. URL <https://linkinghub.elsevier.com/retrieve/pii/S0378775314019636>.

Bibliography

- [94] Youkun Tao, Sune Dalgaard Ebbesen, and Mogens Bjerg Mogensen. Carbon deposition in solid oxide cells during co-electrolysis of H₂O and CO₂. Journal of The Electrochemical Society, 161(3):F337–F343, 2014.
- [95] Xiangling Yue and John T. S. Irvine. Alternative Cathode Material for CO₂ Reduction by High Temperature Solid Oxide Electrolysis Cells. J. Electrochem. Soc., 159(8):F442–F448, 2012. ISSN 0013-4651, 1945-7111. doi: 10.1149/2.040208jes. URL <https://iopscience.iop.org/article/10.1149/2.040208jes>.
- [96] V. Duboviks, M. Lomberg, R. C. Maher, L. F. Cohen, N. P. Brandon, and G. J. Offer. Carbon deposition behaviour in metal-infiltrated gadolinia doped ceria electrodes for simulated biogas upgrading in solid oxide electrolysis cells. Journal of Power Sources, 293:912–921, 2015.
- [97] M. A. Laguna-Bercero, R. Campana, A. Larrea, J. A. Kilner, and V. M. Orera. Electrolyte degradation in anode supported microtubular yttria stabilized zirconia-based solid oxide steam electrolysis cells at high voltages of operation. Journal of Power Sources, 196(21):8942–8947, 2011.
- [98] F. Tietz, D. Sebold, A. Brisse, and J. Schefold. Degradation phenomena in a solid oxide electrolysis cell after 9000 h of operation. Journal of Power Sources, 223: 129–135, February 2013. ISSN 0378-7753. doi: 10.1016/j.jpowsour.2012.09.061. URL <http://www.sciencedirect.com/science/article/pii/S0378775312014826>.
- [99] Ruth Knibbe, Marie Lund Traulsen, Anne Hauch, Sune Dalgaard Ebbesen, and Mogens Mogensen. Solid Oxide Electrolysis Cells: Degradation at High Current Densities. J. Electrochem. Soc., 157(8):B1209, June 2010. ISSN 1945-7111. doi: 10.1149/1.3447752. URL <https://iopscience.iop.org/article/10.1149/1.3447752/meta>. Publisher: IOP Publishing.
- [100] Per Hjalmarsson, Xiufu Sun, Yi-Lin Liu, and Ming Chen. Influence of the oxygen electrode and inter-diffusion barrier on the degradation of solid oxide electrolysis cells. Journal of Power Sources, 223:349–357, February 2013. ISSN 0378-7753. doi: 10.1016/j.jpowsour.2012.08.063. URL <http://www.sciencedirect.com/science/article/pii/S0378775312013614>.
- [101] Jeonghee Kim, Ho-Il Ji, Hari Prasad Dasari, Dongwook Shin, Huesup Song, Jong-Ho Lee, Byung-Kook Kim, Hae-June Je, Hae-Weon Lee, and Kyung Joong Yoon. Degradation mechanism of electrolyte and air electrode in solid oxide electrolysis cells operating at high polarization. International Journal of Hydrogen Energy, 38(3):1225–1235, February 2013. ISSN 0360-3199. doi: 10.1016/j.ijhydene.2012.10.113. URL <http://www.sciencedirect.com/science/article/pii/S0360319912024391>.
- [102] Michael Keane, Manoj K. Mahapatra, Atul Verma, and Prabhakar Singh. LSM–YSZ interactions and anode delamination in solid oxide electrolysis cells. International

- Journal of Hydrogen Energy*, 37(22):16776–16785, November 2012. ISSN 0360-3199. doi: 10.1016/j.ijhydene.2012.08.104. URL <http://www.sciencedirect.com/science/article/pii/S0360319912019544>.
- [103] D. Szymczewska, J. Karczewski, A. Chrzan, and P. Jasinski. CGO as a barrier layer between LSCF electrodes and YSZ electrolyte fabricated by spray pyrolysis for solid oxide fuel cells. *Solid State Ionics*, 302:113–117, April 2017. ISSN 0167-2738. doi: 10.1016/j.ssi.2016.11.008. URL <http://www.sciencedirect.com/science/article/pii/S0167273816305872>.
- [104] M. Morales, V. Miguel-Pérez, A. Tarancón, A. Slodczyk, M. Torrell, B. Ballesteros, J. P. Ouweltjes, J. M. Bassat, D. Montinaro, and A. Morata. Multi-scale analysis of the diffusion barrier layer of gadolinia-doped ceria in a solid oxide fuel cell operated in a stack for 3000 h. *Journal of Power Sources*, 344:141–151, March 2017. ISSN 0378-7753. doi: 10.1016/j.jpowsour.2017.01.109. URL <http://www.sciencedirect.com/science/article/pii/S0378775317301192>.
- [105] Trine Klemensø, Jimmi Nielsen, Peter Blennow, Åsa H. Persson, Tobias Stegk, Bjarke Holl Christensen, and Steffen Sønderby. High performance metal-supported solid oxide fuel cells with Gd-doped ceria barrier layers. *Journal of Power Sources*, 196(22):9459–9466, November 2011. ISSN 0378-7753. doi: 10.1016/j.jpowsour.2011.07.014. URL <http://www.sciencedirect.com/science/article/pii/S0378775311013528>.
- [106] Giorgio Rinaldi, Arata Nakajo, Jan Van herle, Pierre Burdet, Emad Oveisi, and Marco Cantoni. Strontium Migration at the GDC-YSZ Interface of Solid Oxide Cells in SOFC and SOEC Modes. *ECS Trans.*, 78(1):3297–3307, May 2017. ISSN 1938-6737, 1938-5862. doi: 10.1149/07801.3297ecst. URL <https://iopscience.iop.org/article/10.1149/07801.3297ecst>.
- [107] Zehua Pan, Qinglin Liu, Meng Ni, Renzhi Lyu, Ping Li, and Siew Hwa Chan. Activation and failure mechanism of La_{0.6}Sr_{0.4}Co_{0.2}Fe_{0.8}O_{3-δ} air electrode in solid oxide electrolyzer cells under high-current electrolysis. *International Journal of Hydrogen Energy*, 43(11):5437–5450, March 2018. ISSN 0360-3199. doi: 10.1016/j.ijhydene.2018.01.181. URL <http://www.sciencedirect.com/science/article/pii/S0360319918303252>.
- [108] Bo Wei, Kongfa Chen, Ling Zhao, Zhe Lü, and San Ping Jiang. Chromium deposition and poisoning at La_{0.6}Sr_{0.4}Co_{0.2}Fe_{0.8}O₃ oxygen electrodes of solid oxide electrolysis cells. *Phys. Chem. Chem. Phys.*, 17(3):1601–1609, December 2014. ISSN 1463-9084. doi: 10.1039/C4CP05110F. URL <https://pubs.rsc.org/en/content/articlelanding/2015/cp/c4cp05110f>. Publisher: The Royal Society of Chemistry.
- [109] Kongfa Chen, Junji Hyodo, Aaron Dodd, Na Ai, Tatsumi Ishihara, Li Jian, and San Ping Jiang. Chromium deposition and poisoning of La_{0.8}Sr_{0.2}MnO₃ oxygen

Bibliography

- electrodes of solid oxide electrolysis cells. *Faraday Discuss.*, 182(0):457–476, November 2015. ISSN 1364-5498. doi: 10.1039/C5FD00010F. URL <https://pubs.rsc.org/en/content/articlelanding/2015/fd/c5fd00010f>. Publisher: The Royal Society of Chemistry.
- [110] Kongfa Chen, Junji Hyodo, Na Ai, Tatsumi Ishihara, and San Ping Jiang. Boron deposition and poisoning of La 0.8 Sr 0.2 MnO 3 oxygen electrodes of solid oxide electrolysis cells under accelerated operation conditions. *International Journal of Hydrogen Energy*, 41(3):1419–1431, 2016.
- [111] Kongfa Chen, Na Ai, Ling Zhao, and San Ping Jiang. Effect of Volatile Boron Species on the Electrocatalytic Activity of Cathodes of Solid Oxide Fuel Cells: II. (La,Sr)(Co,Fe)O₃ Based Electrodes. *J. Electrochem. Soc.*, 160(3):F301, January 2013. ISSN 1945-7111. doi: 10.1149/2.019304jes. URL <https://iopscience.iop.org/article/10.1149/2.019304jes/meta>. Publisher: IOP Publishing.
- [112] Jinsheng Wang, David Ryan, Edward J. Anthony, Neil Wildgust, and Toby Aiken. Effects of impurities on CO₂ transport, injection and storage. *Energy Procedia*, 4: 3071–3078, January 2011. ISSN 1876-6102. doi: 10.1016/j.egypro.2011.02.219. URL <http://www.sciencedirect.com/science/article/pii/S1876610211004164>.
- [113] Edith Bucher, Christian Gspan, Ferdinand Hofer, and Werner Sitte. Post-test analysis of silicon poisoning and phase decomposition in the SOFC cathode material La_{0.58}Sr_{0.4}Co_{0.2}Fe_{0.8}O₃ by transmission electron microscopy. *Solid State Ionics*, 230:7–11, January 2013. ISSN 0167-2738. doi: 10.1016/j.ssi.2012.08.013. URL <http://www.sciencedirect.com/science/article/pii/S0167273812004808>.
- [114] Takuto Kushi. Effects of sulfur poisoning on degradation phenomena in oxygen electrodes of solid oxide electrolysis cells and solid oxide fuel cells. *International Journal of Hydrogen Energy*, 42(15):9396–9405, 2017.
- [115] Evgenij Barsoukov and J. Ross Macdonald. Impedance Spectroscopy: Theory, Experiment and Applications, A John Wiley & Sons. Inc., Publication, USA, pages 13–20, 2005.
- [116] Ting Hei Wan, Mattia Saccoccio, Chi Chen, and Francesco Ciucci. Influence of the discretization methods on the distribution of relaxation times deconvolution: implementing radial basis functions with DRTtools. *Electrochimica Acta*, 184: 483–499, 2015.
- [117] Dino Klotz, Jan Philipp Schmidt, Alexander Kromp, André Weber, and Ellen Ivers-Tiffée. The Distribution of Relaxation Times as Beneficial Tool for Equivalent Circuit Modeling of Fuel Cells and Batteries. *ECS Trans.*, 41(28):25–33, April 2012. ISSN 1938-6737, 1938-5862. doi: 10.1149/1.3692958. URL <http://ecst.ecsdl.org/content/41/28/25>.

- [118] André Leonide, Volker Sonn, André Weber, and Ellen Ivers-Tiffée. Evaluation and modeling of the cell resistance in anode-supported solid oxide fuel cells. Journal of The Electrochemical Society, 155(1):B36–B41, 2008.
- [119] Bernard A. Boukamp. Derivation of a Distribution Function of Relaxation Times for the (fractal) Finite Length Warburg. Electrochimica Acta, 252:154–163, October 2017. ISSN 0013-4686. doi: 10.1016/j.electacta.2017.08.154. URL <http://www.sciencedirect.com/science/article/pii/S0013468617318145>.
- [120] Priscilla Caliandro. Identification of Solid Oxide Cell Elementary Processes by Electrochemical Impedance Spectroscopy, 2018. URL <https://infoscience.epfl.ch/record/255087>.
- [121] A. Hauch, S. D. Ebbesen, S. H. Jensen, and M. Mogensen. Solid Oxide Electrolysis Cells: Microstructure and Degradation of the Ni/Yttria-Stabilized Zirconia Electrode. J. Electrochem. Soc., 155(11):B1184, September 2008. ISSN 1945-7111. doi: 10.1149/1.2967331. URL <https://iopscience.iop.org/article/10.1149/1.2967331/meta>. Publisher: IOP Publishing.
- [122] K. Thydén, Y. L. Liu, and J. B. Bilde-Sørensen. Microstructural characterization of SOFC Ni-YSZ anode composites by low-voltage scanning electron microscopy. Solid State Ionics, 178(39):1984–1989, March 2008. ISSN 0167-2738. doi: 10.1016/j.ssi.2007.12.075. URL <http://www.sciencedirect.com/science/article/pii/S0167273808000076>.
- [123] Marco Cantoni. Introduction to EDX, 2014.
- [124] A. Nakajo, G. Rinaldi, P. Caliandro, G. Jeanmonod, L. Navratilova, M. Cantoni, and J. Van herle. Evolution of the Morphology Near Triple-Phase Boundaries in Ni-Yttria Stabilized Zirconia Electrodes Upon Cathodic Polarization. J. Electrochem. En. Conv. Stor., 17(4), November 2020. ISSN 2381-6872. doi: 10.1115/1.4046478. URL <https://asmedigitalcollection.asme.org/electrochemical/article/17/4/041102/1074944/Evolution-of-the-Morphology-Near-Triple-Phase>. Publisher: American Society of Mechanical Engineers Digital Collection.
- [125] Arata Nakajo, Alex P. Cocco, M. B. DeGostin, Pierre Burdet, Aldo A. Peracchio, Brice N. Cassenti, Marco Cantoni, Jan Van herle, and Wilson K. S. Chiu. Evolution of 3-D Transport Pathways and Triple-Phase Boundaries in the Ni-YSZ Hydrogen Electrode upon Fuel Cell or Electrolysis Cell Operation. ECS Trans., 78(1):3205–3215, May 2017. ISSN 1938-6737, 1938-5862. doi: 10.1149/07801.3205ecst. URL <https://iopscience.iop.org/article/10.1149/07801.3205ecst>.
- [126] A. Bertei, E. Ruiz-Trejo, F. Tariq, V. Yufit, A. Atkinson, and N. P. Brandon. Validation of a physically-based solid oxide fuel cell anode model combining 3D tomography

Bibliography

- and impedance spectroscopy. International Journal of Hydrogen Energy, 41(47): 22381–22393, 2016.
- [127] Lorenz Holzer and Marco Cantoni. Review of FIB-tomography. Nanofabrication using focused ion and electron beams: Principles and applications, 559201222, 2012.
- [128] Ludwig Reimer. Transmission electron microscopy: physics of image formation and microanalysis, volume 36. Springer, 2013. ISBN 3-662-13553-1.
- [129] D. Waldbillig, A. Wood, and D. G. Ivey. Electrochemical and microstructural characterization of the redox tolerance of solid oxide fuel cell anodes. Journal of Power Sources, 145(2):206–215, August 2005. ISSN 0378-7753. doi: 10.1016/j.jpowsour.2004.12.071. URL <http://www.sciencedirect.com/science/article/pii/S037877530500282X>.
- [130] Q. Jeangros, A. Faes, J. B. Wagner, T. W. Hansen, U. Aschauer, J. Van herle, A. Hessler-Wyser, and R. E. Dunin-Borkowski. In situ redox cycle of a nickel-YSZ fuel cell anode in an environmental transmission electron microscope. Acta Materialia, 58(14):4578–4589, August 2010. ISSN 1359-6454. doi: 10.1016/j.actamat.2010.04.019. URL <http://www.sciencedirect.com/science/article/pii/S1359645410002351>.
- [131] Stéphane Poitel, Zhujun Wang, Marc Willinger, Jan Van herle, and Cécile Hébert. In-Situ Observation of Co-Ce Coated Metallic Interconnect Oxidation Combined with High-Resolution Post Exposure Analysis. ECS Trans., 78(1):1615–1632, May 2017. ISSN 1938-6737, 1938-5862. doi: 10.1149/07801.1615ecst. URL <https://iopscience.iop.org/article/10.1149/07801.1615ecst>.
- [132] Michael B. Pomfret, Jeffrey C. Owrutsky, and Robert A. Walker. In situ optical studies of solid-oxide fuel cells. Annual Review of Analytical Chemistry, 3:151–174, 2010.
- [133] John D. Kirtley, Daniel A. Steinhurst, Jeffery C. Owrutsky, Michael B. Pomfret, and Robert A. Walker. In situ optical studies of methane and simulated biogas oxidation on high temperature solid oxide fuel cell anodes. Physical Chemistry Chemical Physics, 16(1):227–236, 2014. doi: 10.1039/C3CP53278J. URL <https://pubs.rsc.org/en/content/articlelanding/2014/cp/c3cp53278j>.
- [134] Michael B. Pomfret, Jeffrey C. Owrutsky, and Robert A. Walker. High-Temperature Raman Spectroscopy of Solid Oxide Fuel Cell Materials and Processes. J. Phys. Chem. B, 110(35):17305–17308, September 2006. ISSN 1520-6106, 1520-5207. doi: 10.1021/jp063952l. URL <https://pubs.acs.org/doi/10.1021/jp063952l>.
- [135] John D. Kirtley, Michael B. Pomfret, Daniel A. Steinhurst, Jeffrey C. Owrutsky, and Robert A. Walker. Toward a Working Mechanism of Fuel Oxidation in SOFCs: In

- Situ Optical Studies of Simulated Biogas and Methane. *J. Phys. Chem. C*, 119 (23):12781–12791, June 2015. ISSN 1932-7447. doi: 10.1021/jp511304x. URL <https://doi.org/10.1021/jp511304x>. Publisher: American Chemical Society.
- [136] Bryan C. Eigenbrodt, Michael B. Pomfret, Daniel A. Steinhurst, Jeffrey C. Owrutsky, and Robert A. Walker. Direct, In Situ Optical Studies of Ni-YSZ Anodes in Solid Oxide Fuel Cells Operating with Methanol and Methane. *J. Phys. Chem. C*, 115 (6):2895–2903, February 2011. ISSN 1932-7447, 1932-7455. doi: 10.1021/jp109292r. URL <https://pubs.acs.org/doi/10.1021/jp109292r>.
- [137] D. A. Agarkov, I. N. Burmistrov, F. M. Tsybrov, I. I. Tartakovskii, V. V. Kharton, and S. I. Bredikhin. In-situ Raman spectroscopy analysis of the interfaces between Ni-based SOFC anodes and stabilized zirconia electrolyte. *Solid State Ionics*, 302: 133–137, April 2017. ISSN 0167-2738. doi: 10.1016/j.ssi.2016.12.034. URL <http://www.sciencedirect.com/science/article/pii/S0167273816305690>.
- [138] D. A. Agarkov, I. N. Burmistrov, F. M. Tsybrov, I. I. Tartakovskii, V. V. Kharton, and S. I. Bredikhin. In-situ Raman spectroscopy analysis of the interface between ceria-containing SOFC anode and stabilized zirconia electrolyte. *Solid State Ionics*, 319:125–129, June 2018. ISSN 0167-2738. doi: 10.1016/j.ssi.2018.02.006. URL <http://www.sciencedirect.com/science/article/pii/S0167273817307154>.
- [139] D. A. Agarkov, I. N. Burmistrov, G. M. Eliseeva, I. V. Ionov, S. V. Rabotkin, V. A. Semenov, A. A. Solovyev, I. I. Tartakovskii, and S. I. Bredikhin. Comparison of in-situ Raman studies of SOFC with thick single-crystal and thin-film magnetron sputtered membranes. *Solid State Ionics*, 344:115091, January 2020. ISSN 0167-2738. doi: 10.1016/j.ssi.2019.115091. URL <http://www.sciencedirect.com/science/article/pii/S0167273819306885>.
- [140] Michael B. Pomfret, Daniel A. Steinhurst, and Jeffrey C. Owrutsky. Identification of a Methane Oxidation Intermediate on Solid Oxide Fuel Cell Anode Surfaces with Fourier Transform Infrared Emission. *J. Phys. Chem. Lett.*, 4(8):1310–1314, April 2013. ISSN 1948-7185. doi: 10.1021/jz400443m. URL <https://pubs.acs.org/doi/10.1021/jz400443m>.
- [141] Xinyu Lu, Peter W. Faguy, and Meilin Liu. In Situ Potential-Dependent FTIR Emission Spectroscopy : A Novel Probe for High Temperature Fuel Cell Interfaces. *J. Electrochem. Soc.*, 149(10):A1293, August 2002. ISSN 1945-7111. doi: 10.1149/1.1506981. URL <https://iopscience.iop.org/article/10.1149/1.1506981/meta>. Publisher: IOP Publishing.
- [142] Gang Ju, Kenneth Reifsnider, and Xinyu Huang. Infrared Thermography and Thermoelectrical Study of a Solid Oxide Fuel Cell. *J. Fuel Cell Sci. Technol*, 5(3): 031006–031006–6, May 2008. ISSN 2381-6872. doi: 10.1115/1.2894470. URL <http://dx.doi.org/10.1115/1.2894470>.

Bibliography

- [143] D. J. Cumming and R. H. Elder. Thermal imaging of solid oxide cells operating under electrolysis conditions. Journal of Power Sources, 280:387–392, 2015.
- [144] James B. Robinson, Paul R. Shearing, and Daniel J. L. Brett. Thermal Imaging of Electrochemical Power Systems: A Review. Journal of Imaging, 2(1):2, March 2016. doi: 10.3390/jimaging2010002. URL <https://www.mdpi.com/2313-433X/2/1/2>. Number: 1 Publisher: Multidisciplinary Digital Publishing Institute.
- [145] Denis J. Cumming, Rebecca Taylor, Jevgenija Manerova, Derek C. Sinclair, Chris Hardacre, and Rachael H. Elder. In-Situ Monitoring of Solid Oxide Electrolysis Cells. ECS Transactions, 58(2):207–216, 2013.
- [146] Michael B. Pomfret, Daniel A. Steinhurst, David A. Kidwell, and Jeffrey C. Owrutsky. Thermal imaging of solid oxide fuel cell anode processes. Journal of Power Sources, 195(1):257–262, 2010.
- [147] Aaron Geller, Michael Pomfret, Daniel A. Steinhurst, Yi Yu, Zhi Liu, Jeffrey C. Owrutsky, and Bryan W. Eichhorn. Operando Tracking of Electrochemical Activity in Solid Oxide Electrochemical Cells by using Near-Infrared Imaging. ChemElectroChem, 2(10):1527–1534, 2015.
- [148] M. Jasiński, K. Ziewiec, and M. Wojciechowska. Real Time Thermal Imaging of Solid Oxide Fuel Cell. Archives of Metallurgy and Materials, Vol. 64, iss. 4, 2019. URL <http://yadda.icm.edu.pl/baztech/element/bwmeta1.element.baztech-127b8479-ecdc-446f-9104-b71ed4629959>.
- [149] Y. Tachikawa, J. Sugimoto, M. Takada, T. Kawabata, S. M. Lyth, Y. Shiratori, and K. Sasaki. In Operando Visualization of SOFC Electrodes by Thermography and Visible Light Imaging. ECS Electrochem. Lett., 4(11):F61–F64, January 2015. ISSN 2162-8726, 2162-8734. doi: 10.1149/2.0031511eel. URL <http://eel.ecsdl.org/content/4/11/F61>.
- [150] Bryan Eigenbrodt, John Kirtley, and Robert A. Walker. In Situ Optical Studies of Solid Oxide Fuel Cells Operating With Dry and Humidified Oxygenated Fuels. ECS Transactions, 35(1):2789–2798, 2011.
- [151] John D. Kirtley, Michael B. Pomfret, Daniel A. Steinhurst, Jeffrey C. Owrutsky, and Robert A. Walker. In Operando Optical Studies of SOFCs Operating with Butanol. ECS Trans., 68(1):1091–1102, February 2015. ISSN 1938-6737, 1938-5862. doi: 10.1149/06801.1091ecst. URL <http://ecst.ecsdl.org/content/68/1/1091>.
- [152] J. D. Kirtley, S. N. Qadri, D. A. Steinhurst, and J. C. Owrutsky. In situ, simultaneous thermal imaging and infrared molecular emission studies of solid oxide fuel cell electrodes. Journal of Power Sources, 336:54–62, December 2016. ISSN 0378-7753. doi: 10.1016/j.jpowsour.2016.10.047. URL <http://www.sciencedirect.com/science/article/pii/S0378775316314392>.

- [153] Kyle W. Reeping, John D. Kirtley, Jessie M. Bohn, Daniel A. Steinhurst, Jeffrey C. Owrutsky, and Robert A. Walker. Chlorine-Induced Degradation in Solid Oxide Fuel Cells Identified by Operando Optical Methods. *J. Phys. Chem. C*, 121(5): 2588–2596, February 2017. ISSN 1932-7447. doi: 10.1021/acs.jpcc.6b11548. URL <https://doi.org/10.1021/acs.jpcc.6b11548>.
- [154] Michael B. Pomfret, Daniel A. Steinhurst, and Jeffrey C. Owrutsky. Thermal Imaging of Solid Oxide Fuel Cell Anode Degradation with Dry and Wet Ethanol Fuel Flows. *ECS Trans.*, 35(1):1563–1570, April 2011. ISSN 1938-6737, 1938-5862. doi: 10.1149/1.3570141. URL <http://ecst.ecsdl.org/content/35/1/1563>.
- [155] James B. Robinson, Leon D. Brown, Rhodri Jervis, Oluwadamilola O. Taiwo, Thomas M. M. Heenan, Jason Millichamp, Thomas J. Mason, Tobias P. Neville, Ralph Clague, David S. Eastwood, Christina Reinhard, Peter D. Lee, Daniel J. L. Brett, and Paul R. Shearing. Investigating the effect of thermal gradients on stress in solid oxide fuel cell anodes using combined synchrotron radiation and thermal imaging. *Journal of Power Sources*, 288:473–481, August 2015. ISSN 0378-7753. doi: 10.1016/j.jpowsour.2015.04.104. URL <http://www.sciencedirect.com/science/article/pii/S0378775315007612>.
- [156] Arata Nakajo, Zacharie Wullemin, and Daniel Favrat. Simulation of thermal stresses in anode-supported solid oxide fuel cell stacks. Part I: Probability of failure of the cells. *Journal of Power Sources*, 193(1):203–215, 2009.
- [157] Rubén Usamentiaga, Pablo Venegas, Jon Guerediaga, Laura Vega, Julio Molleda, and Francisco G. Bulnes. Infrared Thermography for Temperature Measurement and Non-Destructive Testing. *Sensors*, 14(7):12305–12348, July 2014. doi: 10.3390/s140712305. URL <https://www.mdpi.com/1424-8220/14/7/12305>. Number: 7 Publisher: Multidisciplinary Digital Publishing Institute.
- [158] Daniel L. Balageas, Jean-Michel Roche, François-Henri Leroy, Wei-Min Liu, and Alexander M. Gorbach. The thermographic signal reconstruction method: A powerful tool for the enhancement of transient thermographic images. *Biocybernetics and Biomedical Engineering*, 35(1):1–9, January 2015. ISSN 0208-5216. doi: 10.1016/j.bbe.2014.07.002. URL <http://www.sciencedirect.com/science/article/pii/S0208521614000643>.
- [159] Toscano Cinzia, Meola Carosena, and Carlomagno Giovanni Maria. Porosity distribution in composite structures with infrared thermography. *Journal of Composites*, 2013, 2013.
- [160] Homin Song, Hyung Jin Lim, Sangmin Lee, Hoon Sohn, Wonjun Yun, and Eunha Song. Automated detection and quantification of hidden voids in triplex bonding layers using active lock-in thermography. *NDT & E International*, 74:94–105, September 2015. ISSN 0963-8695. doi: 10.1016/j.ndteint.2015.05.004. URL <http://www.sciencedirect.com/science/article/pii/S0963869515000560>.

Bibliography

- [161] Carosena Meola and Cinzia Toscano. Flash Thermography to Evaluate Porosity in Carbon Fiber Reinforced Polymer (CFRPs). Materials, 7(3):1483–1501, March 2014. doi: 10.3390/ma7031483. URL <https://www.mdpi.com/1996-1944/7/3/1483>. Number: 3 Publisher: Multidisciplinary Digital Publishing Institute.
- [162] Carosena Meola, Giovanni Maria Carlomagno, Antonino Squillace, and Antonio Vitiello. Non-destructive evaluation of aerospace materials with lock-in thermography. Engineering Failure Analysis, 13(3):380–388, April 2006. ISSN 1350-6307. doi: 10.1016/j.engfailanal.2005.02.007. URL <http://www.sciencedirect.com/science/article/pii/S135063070500097X>.
- [163] Patrik Broberg. Surface crack detection in welds using thermography. NDT & E International, 57:69–73, July 2013. ISSN 0963-8695. doi: 10.1016/j.ndteint.2013.03.008. URL <http://www.sciencedirect.com/science/article/pii/S096386951300056X>.
- [164] Claudinei Rezende Calado, F. a. R. Calado, G. Caput, S. C. Gomes, and R. M. Andrade. Porosity and Delamination Defect Detection in Ceramic Materials by Active Infrared Thermography and Optical Digital Microscopy, 2014. URL <https://www.scientific.net/MSF.798-799.671>. Conference Name: Brazilian Ceramic Conference 57 ISBN: 9783038351146 ISSN: 1662-9752 Pages: 671-676 Publisher: Trans Tech Publications Ltd Volume: 798-799.
- [165] P. Wyss, E. Hack, and P. Holtappels. Application of Non-Destructive Testing to Analyse SOFC Cells and Stacks. Fuel Cells, 9(6):907–910, December 2009. ISSN 1615-6854. doi: 10.1002/fuce.200900021. URL <https://onlinelibrary.wiley.com/doi/abs/10.1002/fuce.200900021>.
- [166] J. P. Rakotoniaina, O. Breitenstein, and M. Langenkamp. Localization of weak heat sources in electronic devices using highly sensitive lock-in thermography. Materials Science and Engineering: B, 91-92:481–485, April 2002. ISSN 0921-5107. doi: 10.1016/S0921-5107(01)01011-X. URL <http://www.sciencedirect.com/science/article/pii/S092151070101011X>.
- [167] Ch. Schmidt, F. Altmann, and O. Breitenstein. Application of lock-in thermography for failure analysis in integrated circuits using quantitative phase shift analysis. Materials Science and Engineering: B, 177(15):1261–1267, September 2012. ISSN 0921-5107. doi: 10.1016/j.mseb.2012.02.011. URL <http://www.sciencedirect.com/science/article/pii/S0921510712000931>.
- [168] Otwin Breitenstein. Nondestructive local analysis of current–voltage characteristics of solar cells by lock-in thermography. Solar Energy Materials and Solar Cells, 95(10):2933–2936, October 2011. ISSN 0927-0248. doi: 10.1016/j.solmat.2011.05.049. URL <http://www.sciencedirect.com/science/article/pii/S0927024811003242>.

- [169] Otwin Breitenstein. Local efficiency analysis of solar cells based on lock-in thermography. Solar Energy Materials and Solar Cells, 107:381–389, December 2012. ISSN 0927-0248. doi: 10.1016/j.solmat.2012.07.019. URL <http://www.sciencedirect.com/science/article/pii/S0927024812003820>.
- [170] S. Rißland and O. Breitenstein. High resolution saturation current density imaging at grain boundaries by lock-in thermography. Solar Energy Materials and Solar Cells, 104:121–124, September 2012. ISSN 0927-0248. doi: 10.1016/j.solmat.2012.05.011. URL <http://www.sciencedirect.com/science/article/pii/S092702481200236X>.
- [171] James B. Robinson, Erik Engebretsen, Donal P. Finegan, Jawwad Darr, Gareth Hinds, Paul R. Shearing, and Daniel J. L. Brett. Detection of Internal Defects in Lithium-Ion Batteries Using Lock-in Thermography. ECS Electrochem. Lett., 4(9):A106, January 2015. ISSN 2162-8734. doi: 10.1149/2.0071509eel. URL <https://iopscience.iop.org/article/10.1149/2.0071509eel/meta>. Publisher: IOP Publishing.
- [172] Dana B. Sulas, Steve Johnston, Natalie Seitzman, Heather Platt, Mowafak Al-Jassim, and Harvey Guthrey. Defect Detection in Solid-State Battery Electrolytes Using Lock-In Thermal Imaging. J. Electrochem. Soc., 165(13):A3205–A3211, 2018. ISSN 0013-4651, 1945-7111. doi: 10.1149/2.0131814jes. URL <https://iopscience.iop.org/article/10.1149/2.0131814jes>.
- [173] Erik Engebretsen, James B. Robinson, Oluwamayowa Obeisun, Tom Mason, Donal Finegan, Gareth Hinds, Paul R. Shearing, and Daniel JL Brett. Electro-thermal impedance spectroscopy applied to an open-cathode polymer electrolyte fuel cell. Journal of Power Sources, 302:210–214, 2016.
- [174] G. Jeanmonod, S. Diethelm, and J. Van herle. The effect of SO₂ on the Ni-YSZ electrode of a solid oxide electrolyzer cell operated in co-electrolysis. J. Phys. Energy, 2(3):034002, May 2020. ISSN 2515-7655. doi: 10.1088/2515-7655/ab8b55. URL <https://doi.org/10.1088/2515-7655/ab8b55>. Publisher: IOP Publishing.
- [175] John A Apps. A Review of Hazardous Chemical Species Associated with CO₂ Capture from Coal-Fired Power Plants and their Potential Fate during CO₂ Geologic Storage. page 64, 2006.
- [176] Hélène Lepaumier, Frédéric Mercier, and Guillaume Jeanmonod. D2.4 – Effects of contaminants on durability. European Horizon 2020 - Research and Innovation Framework Programme (H2020-JTI-FCH-2015-1) under grant agreement n° 699892 (ECO project) D2.4, 2019. URL <https://cordis.europa.eu/project/id/699892/results>.

Bibliography

- [177] Xiaojin Zhang, Christian Bauer, Christopher L. Mutel, and Kathrin Volkart. Life Cycle Assessment of Power-to-Gas: Approaches, system variations and their environmental implications. Applied Energy, 190:326–338, March 2017. ISSN 0306-2619. doi: 10.1016/j.apenergy.2016.12.098. URL <http://www.sciencedirect.com/science/article/pii/S0306261916318682>.
- [178] Imran Ullah Khan, Mohd Hafiz Dzarfan Othman, Haslenda Hashim, Takeshi Matsuura, A. F. Ismail, M. Rezaei-DashtArzhandi, and I. Wan Azelee. Biogas as a renewable energy fuel – A review of biogas upgrading, utilisation and storage. Energy Conversion and Management, 150:277–294, October 2017. ISSN 0196-8904. doi: 10.1016/j.enconman.2017.08.035. URL <http://www.sciencedirect.com/science/article/pii/S0196890417307471>.
- [179] Tohid N.Borhani and Meihong Wang. Role of solvents in CO₂ capture processes: The review of selection and design methods. Renewable and Sustainable Energy Reviews, 114:109299, October 2019. ISSN 1364-0321. doi: 10.1016/j.rser.2019.109299. URL <http://www.sciencedirect.com/science/article/pii/S1364032119305076>.
- [180] Ting Shuai Li, He Miao, Tao Chen, Wei Guo Wang, and Cheng Xu. Effect of Simulated Coal-Derived Gas Composition on H₂S Poisoning Behavior Evaluated Using a Disaggregation Scheme. J. Electrochem. Soc., 156(12):B1383–B1388, January 2009. ISSN 0013-4651, 1945-7111. doi: 10.1149/1.3232006. URL <http://jes.ecsdl.org/content/156/12/B1383>.
- [181] Koji Kuramoto, Sou Hosokai, Koichi Matsuoka, Tomohiro Ishiyama, Haruo Kishimoto, and Katsuhiko Yamaji. Degradation behaviors of SOFC due to chemical interaction between Ni-YSZ anode and trace gaseous impurities in coal syngas. Fuel Processing Technology, 160:8–18, June 2017. ISSN 0378-3820. doi: 10.1016/j.fuproc.2017.02.009. URL <http://www.sciencedirect.com/science/article/pii/S0378382017302527>.
- [182] Zia Ud Din and Z. A. Zainal. The fate of SOFC anodes under biomass producer gas contaminants. Renewable and Sustainable Energy Reviews, 72:1050–1066, May 2017. ISSN 1364-0321. doi: 10.1016/j.rser.2016.10.012. URL <http://www.sciencedirect.com/science/article/pii/S1364032116306621>.
- [183] Hossein Madi, Stefan Diethelm, Christian Ludwig, and Jan Van Herle. Organic-sulfur poisoning of solid oxide fuel cell operated on bio-syngas. International Journal of Hydrogen Energy, 41(28):12231–12241, July 2016. ISSN 0360-3199. doi: 10.1016/j.ijhydene.2016.06.014. URL <http://www.sciencedirect.com/science/article/pii/S0360319915302688>.
- [184] Jens R. Rostrup-Nielsen. Chemisorption of hydrogen sulfide on a supported nickel catalyst. Journal of Catalysis, 11(3):220–227, July 1968. ISSN 0021-9517. doi:

- 10.1016/0021-9517(68)90035-3. URL <http://www.sciencedirect.com/science/article/pii/0021951768900353>.
- [185] C. H. Bartholomew, G. D. Weatherbee, and G. A. Jarvi. Sulfur poisoning of nickel methanation catalysts: I. in situ deactivation by H₂S of nickel and nickel bimetallics. *Journal of Catalysis*, 60(2):257–269, November 1979. ISSN 0021-9517. doi: 10.1016/0021-9517(79)90147-7. URL <http://www.sciencedirect.com/science/article/pii/0021951779901477>.
- [186] K. Haga, S. Adachi, Y. Shiratori, K. Itoh, and K. Sasaki. Poisoning of SOFC anodes by various fuel impurities. *Solid State Ionics*, 179(27):1427–1431, September 2008. ISSN 0167-2738. doi: 10.1016/j.ssi.2008.02.062. URL <http://www.sciencedirect.com/science/article/pii/S0167273808002452>.
- [187] Yoshio Matsuzaki and Isamu Yasuda. The poisoning effect of sulfur-containing impurity gas on a SOFC anode: Part I. Dependence on temperature, time, and impurity concentration. *Solid State Ionics*, 132(3):261–269, July 2000. ISSN 0167-2738. doi: 10.1016/S0167-2738(00)00653-6. URL <http://www.sciencedirect.com/science/article/pii/S0167273800006536>.
- [188] Dimitrios K. Niakolas. Sulfur poisoning of Ni-based anodes for Solid Oxide Fuel Cells in H/C-based fuels. *Applied Catalysis A: General*, 486:123–142, September 2014. ISSN 0926-860X. doi: 10.1016/j.apcata.2014.08.015. URL <http://www.sciencedirect.com/science/article/pii/S0926860X14005006>.
- [189] K. Sasaki, K. Susuki, A. Iyoshi, M. Uchimura, N. Imamura, H. Kusaba, Y. Teraoka, H. Fuchino, K. Tsujimoto, Y. Uchida, and N. Jingo. H₂S Poisoning of Solid Oxide Fuel Cells. *J. Electrochem. Soc.*, 153(11):A2023–A2029, January 2006. ISSN 0013-4651, 1945-7111. doi: 10.1149/1.2336075. URL <http://jes.ecsdl.org/content/153/11/A2023>.
- [190] Shaowu Zha, Zhe Cheng, and Meilin Liu. Sulfur Poisoning and Regeneration of Ni-Based Anodes in Solid Oxide Fuel Cells. *J. Electrochem. Soc.*, 154(2):B201–B206, January 2007. ISSN 0013-4651, 1945-7111. doi: 10.1149/1.2404779. URL <http://jes.ecsdl.org/content/154/2/B201>.
- [191] John N. Kuhn, Nandita Lakshminarayanan, and Umit S. Ozkan. Effect of hydrogen sulfide on the catalytic activity of Ni-YSZ cermets. *Journal of Molecular Catalysis A: Chemical*, 282(1):9–21, March 2008. ISSN 1381-1169. doi: 10.1016/j.molcata.2007.11.032. URL <http://www.sciencedirect.com/science/article/pii/S1381116907006759>.
- [192] Whitney S. Jablonski, Stephanie M. Villano, and Anthony M. Dean. A comparison of H₂S, SO₂, and COS poisoning on Ni/YSZ and Ni/K₂O-CaAl₂O₄ during methane steam and dry reforming. *Applied Catalysis A: General*, 502:399–409, August

Bibliography

2015. ISSN 0926-860X. doi: 10.1016/j.apcata.2015.06.009. URL <http://www.sciencedirect.com/science/article/pii/S0926860X15300259>.
- [193] Jens F. B. Rasmussen and Anke Hagen. The effect of H₂S on the performance of Ni-YSZ anodes in solid oxide fuel cells. *Journal of Power Sources*, 191(2): 534–541, June 2009. ISSN 0378-7753. doi: 10.1016/j.jpowsour.2009.02.001. URL <http://www.sciencedirect.com/science/article/pii/S037877530900192X>.
- [194] A. Weber, S. Dierickx, A. Kromp, and E. Ivers-Tiffée. Sulfur Poisoning of Anode-Supported SOFCs under Reformate Operation. *Fuel Cells*, 13(4):487–493, 2013. ISSN 1615-6854. doi: 10.1002/fuce.201200180. URL <https://onlinelibrary.wiley.com/doi/abs/10.1002/fuce.201200180>.
- [195] A. Kromp, S. Dierickx, A. Leonide, A. Weber, and E. Ivers-Tiffée. Electrochemical Analysis of Sulfur-Poisoning in Anode Supported SOFCs Fuelled with a Model Reformate. *J. Electrochem. Soc.*, 159(5):B597–B601, January 2012. ISSN 0013-4651, 1945-7111. doi: 10.1149/2.015206jes. URL <http://jes.ecsdl.org/content/159/5/B597>.
- [196] Jeng-Han Wang and Meilin Liu. Computational study of sulfur–nickel interactions: A new S–Ni phase diagram. *Electrochemistry Communications*, 9(9):2212–2217, September 2007. ISSN 1388-2481. doi: 10.1016/j.elecom.2007.06.022. URL <http://www.sciencedirect.com/science/article/pii/S1388248107002536>.
- [197] Davide Papurello and Andrea Lanzini. SOFC single cells fed by biogas: Experimental tests with trace contaminants. *Waste Management*, 72:306–312, February 2018. ISSN 0956-053X. doi: 10.1016/j.wasman.2017.11.030. URL <http://www.sciencedirect.com/science/article/pii/S0956053X17308577>.
- [198] Davide Papurello, Andrea Lanzini, Sonia Fiorilli, Federico Smeacetto, Rahul Singh, and Massimo Santarelli. Sulfur poisoning in Ni-anode solid oxide fuel cells (SOFCs): Deactivation in single cells and a stack. *Chemical Engineering Journal*, 283:1224–1233, January 2016. ISSN 1385-8947. doi: 10.1016/j.cej.2015.08.091. URL <http://www.sciencedirect.com/science/article/pii/S1385894715011730>.
- [199] Anke Hagen. Sulfur Poisoning of the Water Gas Shift Reaction on Anode Supported Solid Oxide Fuel Cells. *J. Electrochem. Soc.*, 160(2):F111–F118, January 2013. ISSN 0013-4651, 1945-7111. doi: 10.1149/2.060302jes. URL <http://jes.ecsdl.org/content/160/2/F111>.
- [200] Kazunari Sasaki, S. Adachi, K. Haga, M. Uchikawa, J. Yamamoto, A. Iyoshi, J.-T. Chou, Y. Shiratori, and K. Itoh. Fuel Impurity Tolerance of Solid Oxide Fuel Cells. *ECS Trans.*, 7(1):1675–1683, May 2007. ISSN 1938-6737, 1938-5862. doi: 10.1149/1.2729277. URL <http://ecst.ecsdl.org/content/7/1/1675>.

- [201] Hossein Madi, Stefan Diethelm, and Christian Ludwig. The impact of toluene on the performance of anode-supported Ni-YSZ SOFC operated on hydrogen and biosyngas. *ECS Transactions*, 68(1):2811–2818, 2015. ISBN: 1938-6737 Publisher: The Electrochemical Society.
- [202] John Bøgild Hansen. Correlating Sulfur Poisoning of SOFC Nickel Anodes by a Temkin Isotherm. *Electrochem. Solid-State Lett.*, 11(10):B178–B180, January 2008. ISSN 1099-0062, 1944-8775. doi: 10.1149/1.2960521. URL <http://esl.ecsdl.org/content/11/10/B178>.
- [203] Yifeng Zheng, Juan Zhou, Lan Zhang, Qinglin Liu, Zehua Pan, and Siew Hwa Chan. High-temperature electrolysis of simulated flue gas in solid oxide electrolysis cells. *Electrochimica Acta*, 280:206–215, August 2018. ISSN 0013-4686. doi: 10.1016/j.electacta.2018.05.117. URL <http://www.sciencedirect.com/science/article/pii/S0013468618311629>.
- [204] Theis Løye Skafte, Peter Blennow, Johan Hjelm, and Christopher Graves. Carbon deposition and sulfur poisoning during CO₂ electrolysis in nickel-based solid oxide cell electrodes. *Journal of Power Sources*, 373:54–60, January 2018. ISSN 0378-7753. doi: 10.1016/j.jpowsour.2017.10.097. URL <http://www.sciencedirect.com/science/article/pii/S0378775317314593>.
- [205] K. Haga, Y. Shiratori, K. Ito, and K. Sasaki. Chlorine Poisoning of SOFC Ni-Cermet Anodes. *J. Electrochem. Soc.*, 155(12):B1233–B1239, January 2008. ISSN 0013-4651, 1945-7111. doi: 10.1149/1.2980521. URL <http://jes.ecsdl.org/content/155/12/B1233>.
- [206] Ting Shuai Li, Cheng Xu, Tao Chen, He Miao, and Wei Guo Wang. Chlorine contaminants poisoning of solid oxide fuel cells. *J Solid State Electrochem*, 15(6): 1077–1085, June 2011. ISSN 1433-0768. doi: 10.1007/s10008-010-1166-x. URL <https://doi.org/10.1007/s10008-010-1166-x>.
- [207] Davide Papurello, Andrea Lanzini, Davide Drago, Pierluigi Leone, and Massimo Santarelli. Limiting factors for planar solid oxide fuel cells under different trace compound concentrations. *Energy*, 95:67–78, January 2016. ISSN 0360-5442. doi: 10.1016/j.energy.2015.11.070. URL <http://www.sciencedirect.com/science/article/pii/S0360544215016333>.
- [208] O. A. Marina, L. R. Pederson, E. C. Thomsen, C. A. Coyle, and K. J. Yoon. Reversible poisoning of nickel/zirconia solid oxide fuel cell anodes by hydrogen chloride in coal gas. *Journal of Power Sources*, 195(20):7033–7037, October 2010. ISSN 0378-7753. doi: 10.1016/j.jpowsour.2010.05.006. URL <http://www.sciencedirect.com/science/article/pii/S037877531000786X>.
- [209] Chunchuan Xu, Mingyang Gong, John W. Zondlo, XingBo Liu, and Harry O. Finklea. The effect of HCl in syngas on Ni-YSZ anode-supported solid oxide

Bibliography

- fuel cells. *Journal of Power Sources*, 195(8):2149–2158, April 2010. ISSN 0378-7753. doi: 10.1016/j.jpowsour.2009.09.079. URL <http://www.sciencedirect.com/science/article/pii/S0378775309018205>.
- [210] Alessandro Cavalli, Roberta Bernardini, Tommaso Del Carlo, and Purushothaman Vellayani Aravind. Effect of H₂S and HCl on solid oxide fuel cells fed with simulated biosyngas containing primary tar. *Energy Science & Engineering*, 7(6):2456–2468, 2019. ISSN 2050-0505. doi: 10.1002/ese3.434. URL <https://onlinelibrary.wiley.com/doi/abs/10.1002/ese3.434>. _eprint: <https://onlinelibrary.wiley.com/doi/pdf/10.1002/ese3.434>.
- [211] Gerhard Buchinger, Paul Hinterreiter, Thomas Raab, Stefan Griesser, Richard Claassen, Dirk Peter Claassen, Werner Sitte, and Dieter Meissner. Operating Microtubular SOFCs With Hydrogen Chloride and Hydrogen Sulfide Containing Fuels and Synthetic Wood Gas. *Journal of Fuel Cell Science and Technology*, 3(3):280–283, August 2006. ISSN 1550-624X, 1551-6989. doi: 10.1115/1.2205361. URL <https://asmedigitalcollection.asme.org/electrochemical/article/3/3/280/475311/Operating-Microtubular-SOFCs-With-Hydrogen>.
- [212] Marcin Błesznowski, Janusz Jewulski, and Agata Zieleniak. Determination of H₂S and HCl concentration limits in the fuel for anode supported SOFC operation. *Open Chemistry*, 11(6):960–967, 2013. ISSN 2391-5420. doi: 10.2478/s11532-013-0228-1. URL <https://www.degruyter.com/view/j/chem.2013.11.issue-6/s11532-013-0228-1/s11532-013-0228-1.xml>.
- [213] JianEr Bao, Gopala N. Krishnan, Palitha Jayaweera, Jordi Perez-Mariano, and Angel Sanjurjo. Effect of various coal contaminants on the performance of solid oxide fuel cells: Part I. Accelerated testing. *Journal of Power Sources*, 193(2):607–616, September 2009. ISSN 0378-7753. doi: 10.1016/j.jpowsour.2009.04.034. URL <http://www.sciencedirect.com/science/article/pii/S0378775309006983>.
- [214] J. P. Trembly, R. S. Gemmen, and D. J. Bayless. The effect of coal syngas containing HCl on the performance of solid oxide fuel cells: Investigations into the effect of operational temperature and HCl concentration. *Journal of Power Sources*, 169(2):347–354, June 2007. ISSN 0378-7753. doi: 10.1016/j.jpowsour.2007.03.018. URL <http://www.sciencedirect.com/science/article/pii/S0378775307005678>.
- [215] Hossein Madi, Andrea Lanzini, Davide Papurello, Stefan Diethelm, Christian Ludwig, and Massimo Santarelli. Solid oxide fuel cell anode degradation by the effect of hydrogen chloride in stack and single cell environments. *Journal of Power Sources*, 326:349–356, 2016.
- [216] JianEr Bao, Gopala N. Krishnan, Palitha Jayaweera, Kai-Hung Lau, and Angel Sanjurjo. Effect of various coal contaminants on the performance of solid oxide fuel cells: Part II. ppm and sub-ppm level testing. *Journal of*

- Power Sources, 193(2):617–624, September 2009. ISSN 0378-7753. doi: 10.1016/j.jpowsour.2009.04.035. URL <http://www.sciencedirect.com/science/article/pii/S0378775309006995>.
- [217] N. Coute, J. D. Ortego, J. T. Richardson, and M. V. Twigg. Catalytic steam reforming of chlorocarbons: trichloroethane, trichloroethylene and perchloroethylene. Applied Catalysis B: Environmental, 19(3):175–187, December 1998. ISSN 0926-3373. doi: 10.1016/S0926-3373(98)00075-7. URL <http://www.sciencedirect.com/science/article/pii/S0926337398000757>.
- [218] Kyle W. Reeping and Robert A. Walker. In Operando Vibrational Raman Studies of Chlorine Contamination in Solid Oxide Fuel Cells. J. Electrochem. Soc., 162(12):F1310–F1315, January 2015. ISSN 0013-4651, 1945-7111. doi: 10.1149/2.0191512jes. URL <http://jes.ecsdl.org/content/162/12/F1310>.
- [219] Kyle Wyatt Reeping. Chlorine induced degradation of SOFCs operating on carbon containing fuels. pages 1–230, 2017. URL <https://scholarworks.montana.edu/xmlui/handle/1/15060>. Accepted: 2019-02-05T15:17:51Z Publisher: Montana State University - Bozeman, College of Letters & Science.
- [220] S. J. Xia and V. I. Birss. Deactivation and Recovery of Ni-YSZ Anode in H₂ Fuel Containing H₂S. ECS PV, 2005-07:1275–1283, January 2005. ISSN 1938-6737, 1938-5862. doi: 10.1149/200507.1275PV. URL <http://ecst.ecsdl.org/content/ecstpv/2005-07/1275>.
- [221] Zhe Cheng, Shaowu Zha, and Meilin Liu. Influence of cell voltage and current on sulfur poisoning behavior of solid oxide fuel cells. Journal of Power Sources, 172(2):688–693, October 2007. ISSN 0378-7753. doi: 10.1016/j.jpowsour.2007.07.052. URL <http://www.sciencedirect.com/science/article/pii/S0378775307015121>.
- [222] Anke Hagen, Jens F. B. Rasmussen, and Karl Thydén. Durability of solid oxide fuel cells using sulfur containing fuels. Journal of Power Sources, 196(17):7271–7276, September 2011. ISSN 0378-7753. doi: 10.1016/j.jpowsour.2011.02.053. URL <http://www.sciencedirect.com/science/article/pii/S0378775311004800>.
- [223] A. Hauch, A. Hagen, J. Hjelm, and T. Ramos. Sulfur Poisoning of SOFC Anodes: Effect of Overpotential on Long-Term Degradation. J. Electrochem. Soc., 161(6):F734–F743, January 2014. ISSN 0013-4651, 1945-7111. doi: 10.1149/2.080406jes. URL <http://jes.ecsdl.org/content/161/6/F734>.
- [224] Hossein Madi. Investigations into the Effects of Biofuel Contaminants on Solid Oxide Fuel Cells. 2016. doi: 10.5075/epfl-thesis-7161. URL <https://infoscience.epfl.ch/record/221169>.

Bibliography

- [225] Hossein Madi, Andrea Lanzini, Stefan Diethelm, Davide Papurello, Jan Van herle, Matteo Lualdi, Jørgen Gutzon Larsen, and Massimo Santarelli. Solid oxide fuel cell anode degradation by the effect of siloxanes. *Journal of Power Sources*, 279: 460–471, April 2015. ISSN 0378-7753. doi: 10.1016/j.jpowsour.2015.01.053. URL <http://www.sciencedirect.com/science/article/pii/S0378775315000658>.
- [226] Anne Hauch, Søren Højgaard Jensen, Jørgen B. Bilde-Sørensen, and Mogens Mogensen. Silica Segregation in the Ni / YSZ Electrode. *J. Electrochem. Soc.*, 154 (7):A619, May 2007. ISSN 1945-7111. doi: 10.1149/1.2733861. URL <https://iopscience.iop.org/article/10.1149/1.2733861/meta>. Publisher: IOP Publishing.
- [227] Youkun Tao, Jing Shao, and Shiyang Cheng. Electrochemically Scavenging the Silica Impurities at the Ni–YSZ Triple Phase Boundary of Solid Oxide Cells. *ACS Appl. Mater. Interfaces*, 8(27):17023–17027, July 2016. ISSN 1944-8244. doi: 10.1021/acsami.6b04723. URL <https://doi.org/10.1021/acsami.6b04723>. Publisher: American Chemical Society.
- [228] T. S. Li, C. Gao, M. Xu, B. Li, M. Wu, and W. G. Wang. Effects of PH₃ and CH₃Cl Contaminants on the Performance of Solid Oxide Fuel Cells. *Fuel Cells*, 14(6):999–1005, 2014. ISSN 1615-6854. doi: 10.1002/fuce.201300248. URL <https://onlinelibrary.wiley.com/doi/abs/10.1002/fuce.201300248>. _eprint: <https://onlinelibrary.wiley.com/doi/pdf/10.1002/fuce.201300248>.
- [229] Davide Pumiglia, Simone Vaccaro, Andrea Masi, Stephen J. McPhail, Mauro Falconieri, Serena Gagliardi, Livia Della Seta, and Maurizio Carlini. Aggravated test of Intermediate temperature solid oxide fuel cells fed with tar-contaminated syngas. *Journal of Power Sources*, 340:150–159, February 2017. ISSN 0378-7753. doi: 10.1016/j.jpowsour.2016.11.065. URL <http://www.sciencedirect.com/science/article/pii/S0378775316315622>.
- [230] Felix Fischer, Michael Hauser, Maximilian Hauck, Stephan Herrmann, Sebastian Fendt, Hyeondeok Jeong, Christian Lenser, Norbert H. Menzler, and Hartmut Spliethoff. Effect of internal hydrocarbon reforming during coupled operation of a biomass gasifier with hot gas cleaning and SOFC stacks. *Energy Sci Eng*, page ese3.334, April 2019. ISSN 2050-0505, 2050-0505. doi: 10.1002/ese3.334. URL <https://onlinelibrary.wiley.com/doi/abs/10.1002/ese3.334>.
- [231] Hyeondeok Jeong, Michael Hauser, Felix Fischer, Maximilian Hauck, Sandra Lobe, Roland Peters, Christian Lenser, Norbert H. Menzler, and Olivier Guillon. Utilization of Bio-Syngas in Solid Oxide Fuel Cell Stacks: Effect of Hydrocarbon Reforming. *J. Electrochem. Soc.*, 166(2):F137–F143, 2019. ISSN 0013-4651, 1945-7111. doi: 10.1149/2.1191902jes. URL <https://iopscience.iop.org/article/10.1149/2.1191902jes>.

- [232] Davide Papurello, Andrea Lanzini, Pierluigi Leone, and Massimo Santarelli. The effect of heavy tars (toluene and naphthalene) on the electrochemical performance of an anode-supported SOFC running on bio-syngas. *Renewable Energy*, 99:747–753, December 2016. ISSN 0960-1481. doi: 10.1016/j.renene.2016.07.029. URL <http://www.sciencedirect.com/science/article/pii/S0960148116306255>.
- [233] Arianna Baldinelli, Giovanni Cinti, Umberto Desideri, and Francesco Fantozzi. Biomass integrated gasifier-fuel cells: Experimental investigation on wood syngas tars impact on NiYSZ-anode Solid Oxide Fuel Cells. *Energy Conversion and Management*, 128:361–370, November 2016. ISSN 0196-8904. doi: 10.1016/j.enconman.2016.09.048. URL <http://www.sciencedirect.com/science/article/pii/S019689041630838X>.
- [234] Martin Hauth, Werner Lerch, Karlheinz König, and Jürgen Karl. Impact of naphthalene on the performance of SOFCs during operation with synthetic wood gas. *Journal of Power Sources*, 196(17):7144–7151, September 2011. ISSN 0378-7753. doi: 10.1016/j.jpowsour.2010.09.007. URL <http://www.sciencedirect.com/science/article/pii/S0378775310016101>.
- [235] Chunchuan Xu, John W. Zondlo, Harry O. Finklea, Oktay Demircan, Mingyang Gong, and XingBo Liu. The effect of phosphine in syngas on Ni-YSZ anode-supported solid oxide fuel cells. *Journal of Power Sources*, 193(2):739–746, September 2009. ISSN 0378-7753. doi: 10.1016/j.jpowsour.2009.04.044. URL <http://www.sciencedirect.com/science/article/pii/S0378775309007307>.
- [236] Mingjia Zhi, Xinqi Chen, Harry Finklea, Ismail Celik, and Nianqiang Q. Wu. Electrochemical and microstructural analysis of nickel–yttria-stabilized zirconia electrode operated in phosphorus-containing syngas. *Journal of Power Sources*, 183(2):485–490, September 2008. ISSN 0378-7753. doi: 10.1016/j.jpowsour.2008.05.055. URL <http://www.sciencedirect.com/science/article/pii/S0378775308010495>.
- [237] Chunchuan Xu, John W. Zondlo, Mingyang Gong, and XingBo Liu. Effect of PH₃ poisoning on a Ni-YSZ anode-supported solid oxide fuel cell under various operating conditions. *Journal of Power Sources*, 196(1):116–125, January 2011. ISSN 0378-7753. doi: 10.1016/j.jpowsour.2010.07.018. URL <http://www.sciencedirect.com/science/article/pii/S0378775310011675>.
- [238] Fatma Nihan Cayan, Mingjia Zhi, Suryanarayana Raju Pakalapati, Ismail Celik, Nianqiang Wu, and Randall Gemmen. Effects of coal syngas impurities on anodes of solid oxide fuel cells. *Journal of Power Sources*, 185(2):595–602, December 2008. ISSN 0378-7753. doi: 10.1016/j.jpowsour.2008.06.058. URL <http://www.sciencedirect.com/science/article/pii/S0378775308012664>.
- [239] C. A. Coyle, O. A. Marina, E. C. Thomsen, D. J. Edwards, C. D. Cramer, G. W. Coffey, and L. R. Pederson. Interactions of nickel/zirconia solid oxide fuel cell anodes

Bibliography

- with coal gas containing arsenic. *Journal of Power Sources*, 193(2):730–738, September 2009. ISSN 0378-7753. doi: 10.1016/j.jpowsour.2009.04.042. URL <http://www.sciencedirect.com/science/article/pii/S0378775309007289>.
- [240] J. P. Trembly, R. S. Gemmen, and D. J. Bayless. The effect of coal syngas containing AsH₃ on the performance of SOFCs: Investigations into the effect of operational temperature, current density and AsH₃ concentration. *Journal of Power Sources*, 171(2):818–825, September 2007. ISSN 0378-7753. doi: 10.1016/j.jpowsour.2007.06.087. URL <http://www.sciencedirect.com/science/article/pii/S0378775307013614>.
- [241] Olga A. Marina, Larry R. Pederson, Christopher A. Coyle, Ed C. Thomsen, and Greg W. Coffey. Ni/YSZ Anode Interactions with Impurities in Coal Gas. *ECS Trans.*, 25(2):2125–2130, December 2019. ISSN 1938-6737. doi: 10.1149/1.3205760. URL <https://iopscience.iop.org/article/10.1149/1.3205760>.
- [242] J. Mermelstein, M. Millan, and N. P. Brandon. The impact of carbon formation on Ni–YSZ anodes from biomass gasification model tars operating in dry conditions. *Chemical Engineering Science*, 64(3):492–500, February 2009. ISSN 0009-2509. doi: 10.1016/j.ces.2008.09.020. URL <http://www.sciencedirect.com/science/article/pii/S0009250908005174>.
- [243] Joshua Mermelstein, Marcos Millan, and Nigel Brandon. The impact of steam and current density on carbon formation from biomass gasification tar on Ni/YSZ, and Ni/CGO solid oxide fuel cell anodes. *Journal of Power Sources*, 195(6):1657–1666, March 2010. ISSN 0378-7753. doi: 10.1016/j.jpowsour.2009.09.046. URL <http://www.sciencedirect.com/science/article/pii/S0378775309017030>.
- [244] J. Mermelstein, M. Millan, and N. P. Brandon. The interaction of biomass gasification syngas components with tar in a solid oxide fuel cell and operational conditions to mitigate carbon deposition on nickel-gadolinium doped ceria anodes. *Journal of Power Sources*, 196(11):5027–5034, June 2011. ISSN 0378-7753. doi: 10.1016/j.jpowsour.2011.02.011. URL <http://www.sciencedirect.com/science/article/pii/S037877531100365X>.
- [245] Ming Liu, M. G. Millan, P. V. Aravind, and N. Brandon. Influence of Operating Conditions on Carbon Deposition in SOFCs Fuelled by Tar-Containing Biosyngas. *J. Electrochem. Soc.*, 158(11):B1310, October 2011. ISSN 1945-7111. doi: 10.1149/2.027111jes. URL <https://iopscience.iop.org/article/10.1149/2.027111jes/meta>. Publisher: IOP Publishing.
- [246] Tygue S. Doyle, Zahir Dehouche, P. V. Aravind, Ming Liu, and Sinisa Stankovic. Investigating the impact and reaction pathway of toluene on a SOFC running on syngas. *International Journal of Hydrogen Energy*, 39(23):12083–12091, August 2014. ISSN 0360-3199. doi: 10.1016/j.ijhydene.2014.05.148. URL <http://www.sciencedirect.com/science/article/pii/S0360319914015602>.

- [247] Michael Geis, Stephan Herrmann, Sebastian Fendt, Hyeondeok Jeong, Christian Lenser, Norbert H. Menzler, and Hartmut Spliethoff. Coupling SOFCs to biomass gasification - The influence of phenol on cell degradation in simulated bio-syngas. Part I: Electrochemical analysis. International Journal of Hydrogen Energy, 43(45):20417–20427, November 2018. ISSN 0360-3199. doi: 10.1016/j.ijhydene.2018.07.155. URL <http://www.sciencedirect.com/science/article/pii/S0360319918323796>.
- [248] Hde Coninck, M. Loos, B. Metz, O. Davidson, and L. Meyer. IPCC special report on carbon dioxide capture and storage. Intergovernmental Panel on Climate Change, 2005.
- [249] Bin Liu, Hiroki Muroyama, Toshiaki Matsui, Kazuo Tomida, Tatsuo Kabata, and Koichi Eguchi. Analysis of Impedance Spectra for Segmented-in-Series Tubular Solid Oxide Fuel Cells. J. Electrochem. Soc., 157(12):B1858, 2010. ISSN 00134651. doi: 10.1149/1.3494214. URL <https://iopscience.iop.org/article/10.1149/1.3494214>.
- [250] Ellen Ivers-Tiffée and André; Weber. Evaluation of electrochemical impedance spectra by the distribution of relaxation times. J. Ceram. Soc. Japan, 125(4): 193–201, 2017. ISSN 1348-6535, 1882-0743. doi: 10.2109/jcersj2.16267. URL https://www.jstage.jst.go.jp/article/jcersj2/125/4/125_16267/_article.
- [251] A. L. Gavriluk, D. A. Osinkin, and D. I. Bronin. The use of Tikhonov regularization method for calculating the distribution function of relaxation times in impedance spectroscopy. Russ J Electrochem, 53(6):575–588, June 2017. ISSN 1023-1935, 1608-3342. doi: 10.1134/S1023193517060040. URL <http://link.springer.com/10.1134/S1023193517060040>.
- [252] Mattia Saccoccio, Ting Hei Wan, Chi Chen, and Francesco Ciucci. Optimal Regularization in Distribution of Relaxation Times applied to Electrochemical Impedance Spectroscopy: Ridge and Lasso Regression Methods - A Theoretical and Experimental Study. Electrochimica Acta, 147:470–482, November 2014. ISSN 0013-4686. doi: 10.1016/j.electacta.2014.09.058. URL <http://www.sciencedirect.com/science/article/pii/S0013468614018763>.
- [253] Harald Brandstätter, Ilie Hanzu, and Martin Wilkening. Myth and Reality about the Origin of Inductive Loops in Impedance Spectra of Lithium-Ion Electrodes — A Critical Experimental Approach. Electrochimica Acta, 207:218–223, July 2016. ISSN 0013-4686. doi: 10.1016/j.electacta.2016.03.126. URL <http://www.sciencedirect.com/science/article/pii/S0013468616306971>.
- [254] Ivan Pivac and Frano Barbir. Inductive phenomena at low frequencies in impedance spectra of proton exchange membrane fuel cells – A review. Journal of Power Sources, 326:112–119, September 2016. ISSN 0378-7753. doi: 10.1016/j.

Bibliography

- jpowsour.2016.06.119. URL <http://www.sciencedirect.com/science/article/pii/S037877531630831X>.
- [255] B Vanhassel, B Boukamp, and A Burggraaf. Electrode polarization at the Au, O₂(g)/yttria stabilized zirconia interface. Part I: Theoretical considerations of reaction model. *Solid State Ionics*, 48(1-2):139–154, October 1991. ISSN 01672738. doi: 10.1016/0167-2738(91)90210-3. URL <https://linkinghub.elsevier.com/retrieve/pii/0167273891902103>.
- [256] Aziz Nechache, Bernard A. Boukamp, Michel Cassir, and Armelle Ringuedé. Premature degradation study of a cathode-supported solid oxide electrolysis cell. *J Solid State Electrochem*, 23(1):109–123, January 2019. ISSN 1433-0768. doi: 10.1007/s10008-018-4116-7. URL <https://doi.org/10.1007/s10008-018-4116-7>.
- [257] Aziz Nechache, Bernard A. Boukamp, Michel Cassir, and Armelle Ringuedé. Accelerated degradation of yttria stabilized zirconia electrolyte during high-temperature water electrolysis. *J Solid State Electrochem*, 23(3):871–881, March 2019. ISSN 1433-0768. doi: 10.1007/s10008-018-04184-3. URL <https://doi.org/10.1007/s10008-018-04184-3>.
- [258] J. P. Diard, B. Le Gorrec, and C. Montella. Calculation, simulation and interpretation of electrochemical impedances: Part 3. Conditions for observation of low frequency inductive diagrams for a two-step electron transfer reaction with an adsorbed intermediate species. *Journal of Electroanalytical Chemistry*, 326(1): 13–36, May 1992. ISSN 1572-6657. doi: 10.1016/0022-0728(92)80500-4. URL <http://www.sciencedirect.com/science/article/pii/0022072892805004>.
- [259] Dino Klotz. Characterization and Modeling of Electrochemical Energy Conversion Systems by Impedance Techniques, 2012. URL <https://publikationen.bibliothek.kit.edu/1000029318>.
- [260] Andre Leonide, Yannick Apel, and Ellen Ivers-Tiffée. SOFC Modeling and Parameter Identification by Means of Impedance Spectroscopy. *ECS Trans.*, 19(20):81–109, February 2009. ISSN 1938-6737, 1938-5862. doi: 10.1149/1.3247567. URL <http://ecst.ecsdl.org/content/19/20/81>.
- [261] A. Schiefer, M. Heinzmann, and A. Weber. Inductive Low-Frequency Processes in PEMFC-Impedance Spectra. *Fuel Cells*, 20(4):499–506, 2020. ISSN 1615-6854. doi: 10.1002/fuce.201900212. URL <https://onlinelibrary.wiley.com/doi/abs/10.1002/fuce.201900212>. _eprint: <https://onlinelibrary.wiley.com/doi/pdf/10.1002/fuce.201900212>.
- [262] H. Schichlein, A.C. Müller, M. Voigts, A. Krügel, and E. Ivers-Tiffée. Deconvolution of electrochemical impedance spectra for the identification of electrode reaction mechanisms in solid oxide fuel cells. *Journal of Applied Electrochemistry*, 32(8):

- 875–882, August 2002. ISSN 1572-8838. doi: 10.1023/A:1020599525160. URL <https://doi.org/10.1023/A:1020599525160>.
- [263] A Roine. HSC Chemistry® [Software], 2015. URL www.outotec.com/HSC.
- [264] Ruth Knibbe, Anne Hauch, Johan Hjelm, Sune D. Ebbesen, and Mogens Mogensen. Durability of Solid Oxide Cells. *Green*, 1(2):141–169, July 2011. ISSN 1869-876X, 1869-8778. doi: 10.1515/green.2011.015. URL <https://www.degruyter.com/view/journals/green/1/2/article-p141.xml>. Publisher: De Gruyter Section: Green.
- [265] Anke Hagen, Gregory B. Johnson, and Per Hjalmarsson. Electrochemical evaluation of sulfur poisoning in a methane-fuelled solid oxide fuel cell: Effect of current density and sulfur concentration. *Journal of Power Sources*, 272:776–785, December 2014. ISSN 0378-7753. doi: 10.1016/j.jpowsour.2014.08.125. URL <http://www.sciencedirect.com/science/article/pii/S0378775314014001>.
- [266] H. P. He, A. Wood, D. Steedman, and M. Tilleman. Sulphur tolerant shift reaction catalysts for nickel-based SOFC anode. *Solid State Ionics*, 179(27):1478–1482, September 2008. ISSN 0167-2738. doi: 10.1016/j.ssi.2007.11.009. URL <http://www.sciencedirect.com/science/article/pii/S0167273807003505>.
- [267] E. Brightman, D. G. Ivey, D. J. L. Brett, and N. P. Brandon. The effect of current density on H₂S-poisoning of nickel-based solid oxide fuel cell anodes. *Journal of Power Sources*, 196(17):7182–7187, September 2011. ISSN 0378-7753. doi: 10.1016/j.jpowsour.2010.09.089. URL <http://www.sciencedirect.com/science/article/pii/S0378775310016952>.
- [268] T. Yoshizumi, S. Taniguchi, Y. Shiratori, and K. Sasaki. Sulfur Poisoning of SOFCs: Voltage Oscillation and Ni Oxidation. *J. Electrochem. Soc.*, 159(11):F693–F701, January 2012. ISSN 0013-4651, 1945-7111. doi: 10.1149/2.032211jes. URL <http://jes.ecsdl.org/content/159/11/F693>.
- [269] André Leonide. *SOFC modelling and parameter identification by means of impedance spectroscopy*. 10.5445/KSP/1000019173, 2010. URL <http://dx.doi.org/10.5445/KSP/1000019173>.
- [270] J. I. Gazzarri and O. Kesler. Non-destructive delamination detection in solid oxide fuel cells. *Journal of Power Sources*, 167(2):430–441, May 2007. ISSN 0378-7753. doi: 10.1016/j.jpowsour.2007.02.042. URL <http://www.sciencedirect.com/science/article/pii/S0378775307004533>.
- [271] Dino Klotz. Negative capacitance or inductive loop? – A general assessment of a common low frequency impedance feature. *Electrochemistry Communications*, 98:58–62, January 2019. ISSN 1388-2481. doi: 10.1016/j.elecom.2018.11.017. URL <http://www.sciencedirect.com/science/article/pii/S1388248118303084>.

Bibliography

- [272] Otwin Breitenstein, Wilhelm Warta, and Martin C. Schubert. Lock-in Thermography: Basics and Use for Evaluating Electronic Devices and Materials, volume 10 of Springer Series in Advanced Microelectronics. Springer International Publishing, Cham, 2018. ISBN 978-3-319-99824-4 978-3-319-99825-1. doi: 10.1007/978-3-319-99825-1. URL <http://link.springer.com/10.1007/978-3-319-99825-1>.
- [273] Michael F. Modest. Radiative heat transfer. Academic press, 2013. ISBN 0-12-386990-0.
- [274] Frank P. Incropera and Frank P. Incropera, editors. Fundamentals of heat and mass transfer. John Wiley, Hoboken, NJ, 6th ed edition, 2007. ISBN 978-0-471-45728-2. OCLC: ocm62532755.
- [275] Michael Vollmer and Klaus-Peter Möllmann. Infrared Thermal Imaging | Wiley Online Books. 2018. doi: 10.1002/9783527693306. URL <https://onlinelibrary.wiley.com/doi/book/10.1002/9783527693306>.
- [276] J.-J. Orteu, Y. Rotrou, T. Sentenac, and L. Robert. An Innovative Method for 3-D Shape, Strain and Temperature Full-Field Measurement Using a Single Type of Camera: Principle and Preliminary Results. Exp Mech, 48(2):163–179, April 2008. ISSN 0014-4851, 1741-2765. doi: 10.1007/s11340-007-9071-7. URL <http://link.springer.com/10.1007/s11340-007-9071-7>.
- [277] Yann Rotrou, Thierry Sentenac, Yannick Le Maoult, Pierre Magnan, and Jean Farré. Near infrared thermography with silicon FPA - Comparison to MWIR and LWIR thermography. Quantitative InfraRed Thermography Journal, 3(1):93–115, June 2006. ISSN 1768-6733, 2116-7176. doi: 10.3166/qirt.3.93-115. URL <http://www.tandfonline.com/doi/abs/10.3166/qirt.3.93-115>.
- [278] Yann Rotrou, Thierry Sentenac, Yannick Le Maoult, Pierre Magnan, and Jean A. Farre. Demonstration of near-infrared thermography with silicon image sensor cameras. In Thermosense XXVII, volume 5782, pages 9–19. International Society for Optics and Photonics, March 2005. doi: 10.1117/12.605894. URL <https://www.spiedigitallibrary.org/conference-proceedings-of-spie/5782/0000/Demonstration-of-near-infrared-thermography-with-silicon-image-sensor-cameras/10.1117/12.605894.short>.
- [279] Dave Litwiller. CCD vs. CMOS: Facts and Fiction. page 4, 2001.
- [280] A. Amato, A. S. Aricò, M. Lo Faro, R. Montanini, S. A. Piccolo, A. Quattrocchi, G. Squadrito, S. Trocino, and S. C. Zignani. Infrared thermography applied to solid oxide fuel cells at operating temperatures. Advanced Infrared Technology & Applications, page 119, 2015.

- [281] Vladimir P. Vavilov and Douglas D. Burleigh. Review of pulsed thermal NDT: Physical principles, theory and data processing. NDT & E International, 73:28–52, July 2015. ISSN 0963-8695. doi: 10.1016/j.ndteint.2015.03.003. URL <http://www.sciencedirect.com/science/article/pii/S0963869515000389>.
- [282] Hernán D. Benítez, Clemente Ibarra-Castanedo, AbdelHakim Bendada, Xavier Maldague, Humberto Loaiza, and Eduardo Caicedo. Definition of a new thermal contrast and pulse correction for defect quantification in pulsed thermography. Infrared Physics & Technology, 51(3):160–167, January 2008. ISSN 1350-4495. doi: 10.1016/j.infrared.2007.01.001. URL <http://www.sciencedirect.com/science/article/pii/S135044950700014X>.
- [283] O. Breitenstein, M. Langenkamp, F. Altmann, D. Katzer, A. Lindner, and H. Eggers. Microscopic lock-in thermography investigation of leakage sites in integrated circuits. Rev. Sci. Instrum., 71(11):4155, 2000. ISSN 00346748. doi: 10.1063/1.1310345. URL <http://scitation.aip.org/content/aip/journal/rsi/71/11/10.1063/1.1310345>.
- [284] N Rajic. Principal component thermography for flaw contrast enhancement and flaw depth characterisation in composite structures. Composite Structures, 58(4):521–528, December 2002. ISSN 0263-8223. doi: 10.1016/S0263-8223(02)00161-7. URL <http://www.sciencedirect.com/science/article/pii/S0263822302001617>.
- [285] S. Marinetti, E. Grinzato, P. G. Bison, E. Bozzi, M. Chimenti, G. Pieri, and O. Salvetti. Statistical analysis of IR thermographic sequences by PCA. Infrared Physics & Technology, 46(1):85–91, December 2004. ISSN 1350-4495. doi: 10.1016/j.infrared.2004.03.012. URL <http://www.sciencedirect.com/science/article/pii/S1350449504000532>.
- [286] Yuxia Duan, Stefanie Huebner, Ulf Hassler, Ahmad Osman, Clemente Ibarra-Castanedo, and Xavier P. V. Maldague. Quantitative evaluation of optical lock-in and pulsed thermography for aluminum foam material. Infrared Physics & Technology, 60:275–280, September 2013. ISSN 1350-4495. doi: 10.1016/j.infrared.2013.05.009. URL <http://www.sciencedirect.com/science/article/pii/S1350449513001114>.
- [287] Qingju Tang, Chiwu Bu, Yuanlin Liu, Litao Qi, and Zongyan Yu. A new signal processing algorithm of pulsed infrared thermography. Infrared Physics & Technology, 68:173–178, January 2015. ISSN 1350-4495. doi: 10.1016/j.infrared.2014.12.002. URL <http://www.sciencedirect.com/science/article/pii/S1350449514002709>.
- [288] X. Maldague and S. Marinetti. Pulse phase infrared thermography. Journal of Applied Physics, 79(5):2694–2698, March 1996. ISSN 0021-8979. doi: 10.1063/

Bibliography

- 1.362662. URL <https://aip.scitation.org/doi/abs/10.1063/1.362662>. Publisher: American Institute of Physics.
- [289] X Maldague, F Galmiche, and A Ziadi. Advances in pulsed phase thermography. *Infrared Physics & Technology*, 43(3):175–181, June 2002. ISSN 1350-4495. doi: 10.1016/S1350-4495(02)00138-X. URL <http://www.sciencedirect.com/science/article/pii/S135044950200138X>.
- [290] Clemente Ibarra-Castanedo, Marc Genest, Jean-Marc Piau, Stéphane Guibert, Abdelhakim Bendada, and Xavier P. V. Maldague. Active infrared thermography techniques for the nondestructive testing of materials. In *Ultrasonic and Advanced Methods for Nondestructive Testing and Material Characterization*, pages 325–348. WORLD SCIENTIFIC, May 2007. ISBN 978-981-270-409-2. doi: 10.1142/9789812770943_0014. URL https://www.worldscientific.com/doi/abs/10.1142/9789812770943_0014.
- [291] Clemente Ibarra-Castanedo, Marc Genest, Stéphane Guibert, Jean-Marc Piau, Xavier P. V. Maldague, and Abdelhakim Bendada. Inspection of aerospace materials by pulsed thermography, lock-in thermography, and vibrothermography: a comparative study. In *Thermosense XXIX*, volume 6541, page 654116. International Society for Optics and Photonics, April 2007. doi: 10.1117/12.720097. URL <https://www.spiedigitallibrary.org/conference-proceedings-of-spie/6541/654116/Inspection-of-aerospace-materials-by-pulsed-thermography-lock-in-thermography/10.1117/12.720097.short>.
- [292] F.J. Madruga, C. Ibarra-Castanedo, O.M. Conde, J.M. Lopez-Higuera, and X. Maldague. Automatic data processing based on the skewness statistic parameter for subsurface defect detection by active infrared thermography. In *Proceedings of the 2008 International Conference on Quantitative InfraRed Thermography*. QIRT Council, 2008. doi: 10.21611/qirt.2008.12_16_16. URL http://qirt.gel.ulaval.ca/archives/qirt2008/papers/12_16_16.pdf.
- [293] Francisco J. Madruga, Clemente Ibarra-Castanedo, Olga M. Conde, Xavier P. Maldague, and José M. López-Higuera. Enhanced contrast detection of subsurface defects by pulsed infrared thermography based on the fourth order statistic moment, kurtosis. In *Thermosense XXXI*, volume 7299, page 72990U. International Society for Optics and Photonics, April 2009. doi: 10.1117/12.818684. URL <https://www.spiedigitallibrary.org/conference-proceedings-of-spie/7299/72990U/Enhanced-contrast-detection-of-subsurface-defects-by-pulsed-infrared-thermography/10.1117/12.818684.short>.
- [294] Arata Nakajo, Zacharie Wullemmin, Patrick Metzger, Stefan Diethelm, Günter Schiller, Jan Van herle, and Daniel Favrat. Electrochemical Model of Solid Oxide Fuel Cell for Simulation at the Stack Scale I. Calibration Procedure on Experimental

- Data. *J. Electrochem. Soc.*, 158(9):B1083, 2011. ISSN 00134651. doi: 10.1149/1.3596433. URL <https://iopscience.iop.org/article/10.1149/1.3596433>.
- [295] Process Systems Enterprise Ltd. gPROMS® ModelBuilder 4.2.0 (x64). 1997.
- [296] Matlab. MATLAB, 2020.
- [297] David S. Smith, Arnaud Alzina, Julie Bourret, Benoît Nait-Ali, Fabienne Pennec, Nicolas Tessier-Doyen, Kodai Otsu, Hideaki Matsubara, Pierre Elser, and Urs T. Gonzenbach. Thermal conductivity of porous materials. *Journal of Materials Research*, 28(17):2260–2272, September 2013. ISSN 0884-2914, 2044-5326. doi: 10.1557/jmr.2013.179. URL <https://www.cambridge.org/core/journals/journal-of-materials-research/article/thermal-conductivity-of-porous-materials/305483B7FD8E920537C7D97453738FF1>. Publisher: Cambridge University Press.
- [298] Bruce E. Poling, J. M. Prausnitz, and John P. O’Connell. *The properties of gases and liquids*. McGraw-Hill, New York, 5th ed edition, 2001. ISBN 978-0-07-011682-5.
- [299] J. R. Ehlert and T. F. Smith. View factors for perpendicular and parallel rectangular plates. *Journal of Thermophysics and Heat Transfer*, 7(1):173–175, 1993. doi: 10.2514/3.11587. URL <https://doi.org/10.2514/3.11587>. Publisher: American Institute of Aeronautics and Astronautics _eprint: <https://doi.org/10.2514/3.11587>.
- [300] A. Bertei and C. Nicolella. Common inconsistencies in modeling gas transport in porous electrodes: The dusty-gas model and the Fick law. *Journal of Power Sources*, 279:133–137, April 2015. ISSN 0378-7753. doi: 10.1016/j.jpowsour.2015.01.007. URL <http://www.sciencedirect.com/science/article/pii/S0378775315000087>.
- [301] Huayang Zhu, Robert J. Kee, Vinod M. Janardhanan, Olaf Deutschmann, and David G. Goodwin. Modeling Elementary Heterogeneous Chemistry and Electrochemistry in Solid-Oxide Fuel Cells. *J. Electrochem. Soc.*, 152(12):A2427, 2005. ISSN 00134651. doi: 10.1149/1.2116607. URL <https://iopscience.iop.org/article/10.1149/1.2116607>.
- [302] S. B. Adler, J. A. Lane, and B. C. H. Steele. Electrode Kinetics of Porous Mixed-Conducting Oxygen Electrodes. *J. Electrochem. Soc.*, 143(11):3554, November 1996. ISSN 1945-7111. doi: 10.1149/1.1837252. URL <https://iopscience.iop.org/article/10.1149/1.1837252/meta>. Publisher: IOP Publishing.
- [303] Ann Mari Svensson, Svein Sunde, and Kemal Nisşancioğlu. Mathematical Modeling of Oxygen Exchange and Transport in Air-Perovskite-YSZ Interface Regions: I. Reduction of Intermediately Adsorbed Oxygen. *J. Electrochem. Soc.*, 144(8):2719, August 1997. ISSN 1945-7111. doi: 10.1149/1.1837887. URL <https://iopscience.iop.org/article/10.1149/1.1837887/meta>. Publisher: IOP Publishing.

Bibliography

- [304] Ann Mari Svensson, Svein Sunde, and Kemal Nişancıoğlu. Mathematical Modeling of Oxygen Exchange and Transport in Air-Perovskite-Yttria-Stabilized Zirconia Interface Regions: II. Direct Exchange of Oxygen Vacancies. J. Electrochem. Soc., 145(4):1390, April 1998. ISSN 1945-7111. doi: 10.1149/1.1838471. URL <https://iopscience.iop.org/article/10.1149/1.1838471/meta>. Publisher: IOP Publishing.
- [305] A.F. Robertson and D. Gross. An electrical-analog method for transient heat-flow analysis. J. RES. NATL. BUR. STAN., 61(2):105, August 1958. ISSN 0091-0635. doi: 10.6028/jres.061.016. URL https://nvlpubs.nist.gov/nistpubs/jres/61/jresv61n2p105_A1b.pdf.
- [306] Moussa Chnani, Marie-Cécile Marion-Péra, Raynal Glises, J.M. Kauffmann, and Daniel Hissel. Transient thermal behaviour of a solid oxide fuel cell. Transient thermal behaviour of a solid oxide fuel cell, June 2007.
- [307] Steven W Ellingson. Electromagnetics. Volume 1 Volume 1. 2018. ISBN 978-0-9979201-9-2. OCLC: 1061533384.
- [308] EMVA. EMVA Standard 1288, 2010.
- [309] Charles S. Williams. Discussion of the Theories of Cavity-Type Sources of Radiant Energy. J. Opt. Soc. Am., JOSA, 51(5):564–571, May 1961. doi: 10.1364/JOSA.51.000564. URL <https://www.osapublishing.org/josa/abstract.cfm?uri=josa-51-5-564>.
- [310] Yann Rotrou. Thermographie courtes longueurs d'onde avec des caméras silicium: contribution à la modélisation radiométrique. page 181.
- [311] Alejandro Ferrero, Joaquin Campos, and Alicia Pons. Correction of photoresponse nonuniformity for matrix detectors based on prior compensation for their nonlinear behavior. Appl. Opt., AO, 45(11):2422–2427, April 2006. ISSN 2155-3165. doi: 10.1364/AO.45.002422. URL <https://www.osapublishing.org/ao/abstract.cfm?uri=ao-45-11-2422>.
- [312] Ole Stenzel, Omar Pecho, Lorenz Holzer, Matthias Neumann, and Volker Schmidt. Big data for microstructure-property relationships: A case study of predicting effective conductivities. AIChE Journal, 63(9):4224–4232, 2017. ISSN 1547-5905. doi: 10.1002/aic.15757. URL <https://aiche.onlinelibrary.wiley.com/doi/abs/10.1002/aic.15757>.
- [313] Jong-Hee Park and Robert N. Blumenthal. Electronic Transport in 8 Mole Percent Y₂O₃ - ZrO₂. J. Electrochem. Soc., 136(10):2867–2876, January 1989. ISSN 0013-4651, 1945-7111. doi: 10.1149/1.2096302. URL <http://jes.ecsdl.org/content/136/10/2867>.

- [314] Robert J. Kee, Huayang Zhu, Brett W. Hildenbrand, Einar Vøllestad, Michael D. Sanders, and Ryan P. O'Hayre. Modeling the Steady-State and Transient Response of Polarized and Non-Polarized Proton-Conducting Doped-Perovskite Membranes. *J. Electrochem. Soc.*, 160(3):F290–F300, January 2013. ISSN 0013-4651, 1945-7111. doi: 10.1149/2.016304jes. URL <http://jes.ecsdl.org/content/160/3/F290>.
- [315] Huayang Zhu, Sandrine Ricote, W. Grover Coors, Christodoulos Chatzichristodoulou, and Robert J. Kee. Equilibrium and transient conductivity for gadolinium-doped ceria under large perturbations: II. Modeling. *Solid State Ionics*, 268:198–207, December 2014. ISSN 0167-2738. doi: 10.1016/j.ssi.2014.07.009. URL <http://www.sciencedirect.com/science/article/pii/S0167273814003142>.
- [316] Ming Chen, Yi-Lin Liu, Janet Jonna Bentzen, Wei Zhang, Xiufu Sun, Anne Hauch, Youkun Tao, Jacob R. Bowen, and Peter Vang Hendriksen. Microstructural Degradation of Ni/YSZ Electrodes in Solid Oxide Electrolysis Cells under High Current. *J. Electrochem. Soc.*, 160(8):F883–F891, 2013. ISSN 0013-4651, 1945-7111. doi: 10.1149/2.098308jes. URL <http://jes.ecsdl.org/lookup/doi/10.1149/2.098308jes>.

Publications

Journal papers

Jeanmonod, G., Diethelm, S., Van herle, J., 2020. The effect of SO₂ on the Ni-YSZ electrode of a solid oxide electrolyzer cell operated in co-electrolysis. *J. Phys. Energy* 2, 034002. <https://doi.org/10.1088/2515-7655/ab8b55>

Nakajo, A., Rinaldi, G., Caliandro, P., Jeanmonod, G., Navratilova, L., Cantoni, M., Van herle, J., 2020. Evolution of the Morphology Near Triple-Phase Boundaries in Ni–Yttria Stabilized Zirconia Electrodes Upon Cathodic Polarization. *Journal of Electrochemical Energy Conversion and Storage* 17. <https://doi.org/10.1115/1.4046478>

Jeanmonod, G., Wang, L., Diethelm, S., Maréchal, F., Van herle, J., 2019b. Trade-off designs of power-to-methane systems via solid-oxide electrolyzer and the application to bio-gas upgrading. *Applied Energy* 247, 572–581. <https://doi.org/10.1016/j.apenergy.2019.04.055>

Conference papers

Jeanmonod, G., Van herle, J., Active thermography applied to solid oxide cells, *Proceedings of 15th European Fuel Cell Forum*, October 2020.

Jeanmonod, G., Diethelm, S., Van herle, J., 2019a. Active Near-Infrared Imaging for Spatio-Temporal Monitoring of a Solid Oxide Cell in Operation. *ECS Trans.* 91, 437. <https://doi.org/10.1149/09101.0437ecst>

Jeanmonod, G., Wang, L., Diethelm, S., Maréchal, F., Van herle, J., Trade-off designs of power-to-methane systems via solid-oxide electrolyzer and the application to biogas upgrading, *ICAE2018*, August 2019, Pages 572-581

Jeanmonod, G., Diethelm, S., Van herle, J., Durability testing of SOCs in single cell and short-stack configurations operated in steam-electrolysis and co-electrolysis mode, *Proceedings of 13th European Fuel Cell Forum*, July 2018

Conference presentation

Active thermography applied to solid oxide cells. EFCF 15, Luzern-Switzerland, October, 2020

Active Near-Infrared Imaging for Spatio-Temporal Monitoring of a Solid Oxide Cell in Operation. SOFC-XVI, Kyoto-Japan, July, 2019

Trade-off designs of power-to-methane systems via solid-oxide electrolyzer and the application to biogas upgrading, ICAE2018, Hong-kong, August, 2019

Conference poster

Durability testing of SOCs in single cell and short-stack configurations operated in steam-electrolysis and co-electrolysis mode. EFCF 13, Luzern-Switzerland, July, 2018

Optimal selection of design points for power-to-methane system with solid-oxide electrolyzer swept by oxygen, MODVAL 15, Aarau-Switzerland, April, 2018

Guillaume Jeanmonod

16.09.1990, Suisse

Avenue des Crosets 33
1800 Vevey, Switzerland

☎ (+41) 79 394 67 27

✉ jeanmonodg@gmail.com

🌐 www.linkedin.com/in/guillaume-jeanmonod/

ORCID iD: 0000-0003-2390-1138



Education

- 2016 – 2021 **PhD**, *École Polytechnique Fédérale de Lausanne (EPFL)*, Suisse.
Title: « Effects of impurities and local behavior characterization using active thermography on solid oxide electrolysis cells ». Electrochemical characterization and analysis of solid oxide electrolysis cell exposed to impurities. Developed a dedicated test-bench and applied active thermography to solid oxide cells. Analysis of experimental measurements using a numerical model. Under the supervision of MER Jan Van herle. Oral exam date : 04.02.2021
- 2013 – 2016 **Master of Science in Mechanical Engineering**, *École Polytechnique Fédérale de Lausanne (EPFL)*, Suisse.
Semester project : « Étude d'un Flush Airdata Sensing System (FADS) », modelization of Matlab and investigation of the calibration procedure. Master Thesis : « Parametric investigation of a flexible oscillating thin plate for power extraction », Coupled fluid-structure numeric simulation. Published work. Performed at l'Université LAVAL (Québec). Supervisors: Prof. Mathieu Olivier and Prof. John Richard Thome.
- 2013 – 2016 **Bachelor of Science in Mechanical Engineering**, *École Polytechnique Fédérale de Lausanne (EPFL)*, Suisse.

Experience

- 2016 – 2020 **Assistant**, *École Polytechnique Fédérale de Lausanne (EPFL)*, Switzerland.
Preparation and coaching of exercise sessions for the "thermodynamic II", "renewable energies", and "engine and fuel cell" for Bachelor and Master students. Directed two Master's level semester projects.
- 2018 – 2020 **PhD representative**, *École Polytechnique Fédérale de Lausanne (EPFL)*, Switzerland.
PhD representative of the doctoral program in energy.
- 2015 **Internship**, *Power Vision Engineering*, (4 month).
Implementation in the commercial software SIMSEN, validation and sensitivity study of a mixed flow model applied to a prismatic pipe. Independent work within a team, delivery of a final report to the company and an intermediate and final presentation.
- 2013 – 2015 **Student representative**, *École Polytechnique Fédérale de Lausanne (EPFL)*, Switzerland.
Representative of the Master student in mechanical engineering.
- 2012 **Internship**, *Emile Egger & Cie SA*, (1 month).
Handling of different machine tools for the realization of a poly-mechanic examination piece. Computer modeling of a pump casing (SolidWorks). Initiation to welding (TIG, MIG).

Publications

- 2020 Jeanmonod, G., Diethelm, S. & Herle, J. V. The effect of SO₂ on the Ni-YSZ electrode of a solid oxide electrolyzer cell operated in co-electrolysis. en. *Journal of Physics: Energy* **2**. Publisher: IOP Publishing, 034002.
- Nakajo, A. et al. Evolution of the Morphology Near Triple-Phase Boundaries in Ni-Yttria Stabilized Zirconia Electrodes Upon Cathodic Polarization. *Journal of Electrochemical Energy Conversion and Storage* **17**. ISSN: 2381-6872. <https://doi.org/10.1115/1.4046478> (2020).
- 2019 Jeanmonod, G., Diethelm, S. & Herle, J. V. Active Near-Infrared Imaging for Spatio-Temporal Monitoring of a Solid Oxide Cell in Operation. en. *ECS Transactions* **91**. Publisher: IOP Publishing, 437.
- Jeanmonod, G., Wang, L., Diethelm, S., Maréchal, F. & Van herle, J. Trade-off designs of power-to-methane systems via solid-oxide electrolyzer and the application to biogas upgrading. *Applied Energy* **247**, 572–581.
- 2017 Jeanmonod, G. & Olivier, M. Effects of chordwise flexibility on 2D flapping foils used as an energy extraction device. en. *Journal of Fluids and Structures* **70**, 327–345.

Skills

- Programming MATLAB, L^AT_EX, gProms, Labview; Technical software: HSC, Catia, SolidWorks
- Languages French: mother tongue; English: advanced, German: basic
- Technique Impedance spectroscopy, relaxation time distribution, thermal imaging, electron microscopy, frequency analysis
- Hobbies Swimming, mountain sports, and bike touring